Photoswitchable Fluorescent Dyes for RESOLFT Super-Resolution Microscopy



Kathryn Leslie

Magdalen College, University of Oxford

A thesis submitted for the degree of Doctor of Philosophy

Hilary Term 2023

Abstract

Super-resolution fluorescence microscopy, which allows the resolution of features below the diffraction limit of light, has transformed our ability to investigate cellular processes on the nanoscale. This thesis describes the synthesis, characterisation and testing of photoswitchable fluorescent dyes for application in RESOLFT super-resolution microscopy.

Chapter 1 introduces super-resolution fluorescence microscopy and the many different techniques for resolving below the diffraction limit. It goes on to explore the differences in the chemical tools (fluorescent dyes) required for each of these techniques. Finally, it focuses on the requirements for photoswitchable dyads for RESOLFT in particular, and explores some molecular design principles.

Chapter 2 describes a dyad which combines environmental polarity sensing with RESOLFT super-resolution imaging. Polarity sensing below the diffraction limit is demonstrated in synthetic vesicles, a first for RESOLFT microscopy.

Chapter 3 reports the synthesis and characterisation of a new FRET quenching photoswitchable dyad based on a diazocine photoswitch, in an attempt to improve the fatigue of previous FRET dyad designs. The photophysical properties of this dyad are thoroughly characterised, and a more complete model for photoswitching is developed based off its unexpected behaviour.

Chapter 4 explores PET quenching as a mechanism for photoswitchable dyads, exploiting distance changes between a quencher and a dye to modulate electron transfer rates in competition with fluorescence. The synthesised dyads show important proof of concept results, which inform the development of more rigid and close-packed designs towards this goal.

Acknowledgements

I would like to firstly thank Professor Harry Anderson for being a supportive, encouraging and kind supervisor throughout the duration of my PhD, and in particular during the challenging pandemic years. I am very grateful for all I have learnt and been challenged by as a member of your group. Thanks also to my fellow team RESOLFT members, Dr Andrew Frawley, Dr Virginia Wycisk, and Bobby Qiu for being great scientists and collaborators. My thanks also go to Dr Silvia Galiani, and Professor Christian Eggeling for their support and microscopy expertise, and Professor Fernanda Duarte and Dr Alistair Sterling for guidance in the computational aspects of this work. I am very grateful for a Commonwealth Scholarship and the support of the SBM CDT, without which I would not have been able to study at Oxford.

The HLA group has been a fountain of joy over the years, and I would like to acknowledge excellent science discussions and lots of fun had with Dr Andrew Frawley, Dr James Thomas, Dr Keith Andrews, Dr Virginia Wycisk, Josh Field and Jake Holmes. In particular, I would like to thank Andrew for all the support and for proof reading this thesis, and Keith for video documenting the most important part of my PhD. Thank you also to the unstoppable Daniella Cheang and Pernille Bols for helping to shape (my experience in) Oxford Chemistry for the better.

A PhD is always a huge undertaking, but especially so in the unusual circumstances of the last few years. I'm not sure I would have made it without the key UK support crew of Jo Mitchell, Annie Withecombe, Susie Heywood and Hannah Webster. Or without the fun times and support from Stuart, Gil, Ali, Kayleigh, Lillian, Tristan, and especially the inimitable Howard St Hotties (Dani, Charlie, Pearse and Zac).

Equally I must thank the Australian support crew, including the bestest friends Rachel Anderson and Katie and Daniel Batchen. I also thank Alex Leslie for constant laughs and Ellie updates, Phillip Leslie for genuinely believing there is nothing I can't do, and Sandra Moore for being the best mum in the entire universe bar none. *Ad maiorem Dei gloriam*.

List of Publications

1. Super-resolution RESOLFT microscopy of lipid bilayers using a fluorophore-switch dyad. A. T. Frawley, V. Wycisk, Y. Xiong, S. Galiani, E. Sezgin, I. Urbančič, A. Vargas Jentzsch, K. G. Leslie, C. Eggeling and H. L. Anderson, *Chemical Science*, **2020**, *11*, 8955.

2. A Photoswitchable Solvatochromic Dye for Probing Membrane Ordering by RESOLFT Super-resolution Microscopy. A. T. Frawley[‡], K. G. Leslie[‡], V. Wycisk, S. Galiani, D. Shrestha, C. Eggeling, H. L. Anderson, *ChemPhysChem* **2023**, e202300125.

3. How do donor and acceptor substituents change the photophysical and photochemical behavior of dithienylethenes? The search for a water-soluble visible-light photoswitch. S. Qiu, A. T. Frawley, K. G. Leslie, H. L. Anderson, *chemrxiv,* **2023**, 10.26434/chemrxiv-2023-f5102.

List of Abbreviations

aq.	aqueous
Boc	*tert*-butoxycarbonyl
b	broad
Bu	butyl
CW	continuous wave
δ	chemical shift
d	deuterated
d	doublet
Δ	difference
DCM	dichloromethane
dd	doublet of doublets
DFT	density functional theory
DIPEA	*N,N*-diisopropylethylamine
DMF	dimethylformamide
DMSO	dimethylsulfoxide
DOPC	1,2-dioleoyl-*sn*-glycero-3-phosphocholine
ε	molar absorption coefficient
ESI	electrospray ionisation
ϕ	quantum yield
Fc	ferrocene
FRET	Förster resonance energy transfer
FHWM	full width at half maximum
GUV	giant unilamellar vesicle

GPMV	giant plasma membrane vesicle
h	hours
HBTU	*N,N,N',N'*-tetramethyl-*O*-(1*H*-benzotriazol-1-yl)uronium hexafluorophosphate
HR	high resolution
Hz	Hertz
J	coupling constant; spectral overlap integral
K	Kelvin
k	kinetic rate constant
L_d	lipid disordered
LED	light emitting diode
L_o	lipid ordered
m	multiplet
Me	methyl
MINFLUX	maximally informative luminescence excitation probing
MS	mass spectrometry
NA	numerical aperture
NBS	*N*-bromosuccinimde
NIS	*N*-iodosuccinimde
NMR	nuclear magnetic resonance
PAINT	points accumulation for imaging in nanoscale topography
PALM	photoativated localisation microscopy
PBS	phosphate buffered saline
PET	photoinduced electron transfer
PLL	polylysine

POI	protein of interest
ppm	parts per million
PSD	photostationary state distribution
PSF	point spread function
PSS	photostationary state
q	quartet
R_0	Förster radius
RESOLFT	Reversible saturable optical fluorescence transitions
s	singlet
SCE	standard calomel electrode
SIM	structured illumination microscopy
SMLM	single molecule localisation microscopy
SO	spironaphthoxazine
st. dev.	standard deviation
STED	stimulated emission depletion
STORM	stochastic optical reconstruction microscopy
τ	lifetime
t	triplet
$t_{1/2}$	half life
TFA	trifluoroacetic acid
THF	tetrahydrofuran
UV-vis	ultraviolet-visible
λ	wavelength

Contents

Chapter 1: Introduction

1. Super-resolution microscopy 2
   1.1 Fluorescence for imaging 2
   1.2 Diffraction-limited microscopy 4
   1.3 Resolving below the diffraction limit 6
   1.4 Single molecule localisation methods 8
   1.5 Ensemble methods 9
      1.5.1 Structured Illumination Microscopy (SIM) 10
      1.5.2 Stimulated Emission Depletion Microscopy (STED) 10
      1.5.3 Reversible Saturable Optical Fluorescence Transitions Microscopy (RESOLFT) 12
   1.6 Recent super-resolution techniques 13
2. Chemical tools for super-resolution microscopy 15
   2.1 STORM dyes 15
   2.2 PAINT dyes 17
   2.3 STED dyes 18
   2.4 RESOLFT tools 19
      2.4.1 Proteins 20
      2.4.2 Small molecule dyes 21
3. Design principals for photoswitchable RESOLFT dyes 27
   3.1 Introduction 27
   3.2 FRET quenching 27
   3.3 PET quenching 29
   3.4 Photoswitches 33
   3.5 Dyes 36
4. Project aims 38
5. References 39

Chapter 2: A Nile Red dyad for polarity sensing below the diffraction limit

1. Introduction 45
   1.1 Sensing and Super-resolution 45
   1.2 Nile Red Polarity Sensing 49

2. Results and Discussion 54
2.1 Synthesis and photophysical characterisation 54
2.2 Investigating PET quenching 56
2.3 RESOLFT imaging 59
2.4 Resolution Analysis 62
2.5 Polarity Sensing 68
2.6 Polarity Sensing Below the Diffraction Limit 70
2.7 Translation to biological systems 76
3. Conclusions and Future Work 78
4. Experimental Methods 80
4.1 Optical analysis 80
4.2 Experimental redox potential measurements 80
4.3 Calculated redox potentials 81
4.4 Preparation of GUVs for imaging 81
4.5 Preparation of GPMVs for imaging 82
4.6 Preparation of THP-1 cells for imaging 82
4.7 RESOLFT Microscopy 82
4.8 Confocal microscopy (for colocalization and spectral imaging) 83
5. References 85
6. Appendix 87
6.1 Super-resolution image analysis script 87

Chapter 3: Diazocine as a FRET quencher for photoswitchable dyads

1. Introduction 93
1.1 Improving RESOLFT dyes 93
1.2 Choosing a photoswitch 94
2. Results and Discussion 100
2.1 Photoswitch synthesis and characterisation 100
2.2 Choosing a fluorophore 102
2.3 Dyad synthesis 105
2.4 Dyad testing 107
2.5 A model for dyad switching 113
2.6 Switch modifications 116

3. Conclusions and Future Work 120
4.Experimental Methods 122
4.1 General Synthetic Methods 122
4.2 mCPBA titration 122
4.3 Synthesis and Characterisation 123
4.4 Photophysical characterisation 131
4.4 Preparation of GUVs for imaging 132
4.5 RESOLFT microscopy 132
5. References 133

Chapter 4: Photoswitchable PET quenching for RESOLFT dyads

1. Introduction 136
2. Results and Discussion 141
2.1 First design phase 141
2.1.1 Photoswitch synthesis and characterisation 141
2.1.2 Choosing a fluorophore and quencher 144
2.1.3 Modelling geometric changes 149
2.1.4 Dyad synthesis 153
2.1.5 Dyad testing 156
2.1.6 Conclusions from this design 161
2.2 Second Design Phase 164
2.2.1 Modelling geometry changes 164
2.2.2 Choosing a dye and quencher 165
2.2.3 Synthesis of the photoswitch 166
2.2.4 Characterisation of the photoswitch 173
2.2.5 Synthesis of the Dyad 174
3. Conclusions and Future Work 176
4. Experimental Methods 178
4.1 General Synthetic Methods 178
4.2 Synthesis and Characterisation 178
4.3 Computational Methods 201
4.4 Photophysical Methods and electrochemical methods 202
5. References 203

Chapter 1

Introduction

1. Super-resolution microscopy

1.1 Fluorescence for imaging

Since Robert Hooke first coined the term 'cell' in 1665 to describe the 'microscopical pores' he observed in cork with a simple compound microscope,[1] scientists have been using increasingly advanced methods to make visible the microscopic, and now nanoscopic, features and functions of biological systems. The first microscopes relied on the contrast from the difference in light absorption to differentiate features in cells, often aided by coloured stains. Fluorescence as a means of observation and detection in biological imaging was not introduced to microscopy until the early 1900s, when German scientists developed microscopes to observe the autofluorescence in tissues excited with UV light.[2] By using exogenously applied fluorophores which are excited in the visible region, the contrast is greatly improved, as the majority of biological matter is not excited and does not emit in this region. The field of fluorescence imaging has exploded with dyes that can be used to label proteins of interest,[3] target specific organelles,[4] sense chemical species[5] and probe the local microenvironment,[6] contributing to an ever more detailed picture of cellular behaviour in conditions of health and disease.

Fluorescence microscopy depends on collecting light emitted by a fluorophore after excitation. A Jabłoński diagram[7] shows the various excited states and processes which can occur in organic fluorophores[a] (Figure 1.1), where S_0 refers to the ground state, S_1 and S_2 to singlet excited states and T_1 to the first triplet excited state. Upon absorption of a photon, excitation can occur to different excited states (on a femtosecond timescale), however rapid internal conversion and vibrational relaxation occur (on a picosecond timescale), which populates the lowest vibrational level of the S_1 excited state. Most emission processes occur from this level, a phenomenon known as Kasha's rule.[8] From the excited state, non-radiative decay *via* vibrational relaxation can occur,

[a] Aleksander Jabłoński first proposed the classical energy level picture we now refer to as a Jablonski diagram in his honour in 1933.[7] His name is pronounced 'jaˈbwɔ̃nski' (similar to 'yaboinski') demonstrating the possible pitfalls of having an internationally-recognised scientific concept named after you.

as can emission of a photon to return directly to the ground state. Intersystem crossing to a triplet state can also occur, which is often slow in comparison to emission as it is formally spin forbidden for organic fluorophores. From a triplet state, both non-radiative decay and emission (phosphorescence) can occur to return the molecule to the ground state.

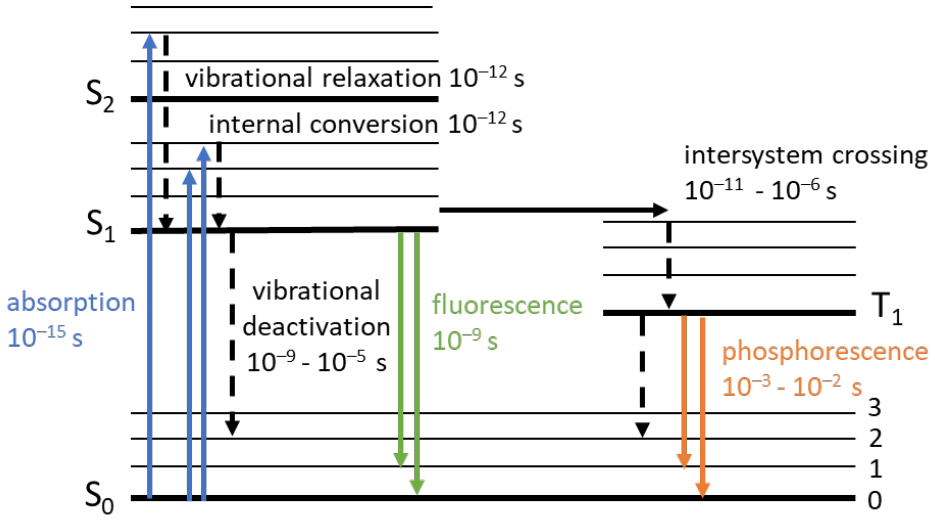


Figure 1.1: A Jablonski diagram, showing the timescales of excited state processes upon absorption of a photon.

Internal conversion relaxation processes mean the emission energy is always lower than the absorbed energy. The difference between the excitation and emission wavelengths is called the Stokes shift. Fluorescent molecules can be characterised in a number of ways, most commonly by their quantum yield and lifetime.

The ratio of the photons emitted as fluorescence over the total number absorbed is the quantum yield, which can also be expressed as the ratio of rates of radiative and non-radiative processes according to Equation 1:

$$\Phi_{\mathrm{f}} = \frac{photons\ emitted}{photons\ absorbed} = \frac{k_{\mathrm{r}}}{k_{\mathrm{r}} + k_{\mathrm{nr}}} \qquad \text{(Equation 1)}$$

Where k_{r} is the emission rate constant and k_{nr} is the collective non-radiative rate constant. When the quantum yield is 1, fluorescence is much faster than all non-radiative processes, and every photon absorbed leads to a photon emitted.

The fluorescence lifetime is the decay constant for the exponential depopulation of the S_1 electronic excited state, and can be expressed as the inverse of the sum of radiative and non-radiative rate constants according to Equation 2:

$$\tau = \frac{1}{k_{\mathrm{r}} + k_{\mathrm{nr}}} \qquad \text{(Equation 2)}$$

Many organic fluorophores have lifetimes on the nanosecond timescale.

1.2 Diffraction-limited microscopy

As described above, fluorescence microscopy utilises the emission of applied organic fluorophores to image biological samples. It is a commonly-used method of microscopy as its minimal invasiveness allows the observation of structures and processes in live cells. Widefield and confocal fluorescence microscopy are the two most common types of fluorescence imaging and will be briefly explained here.

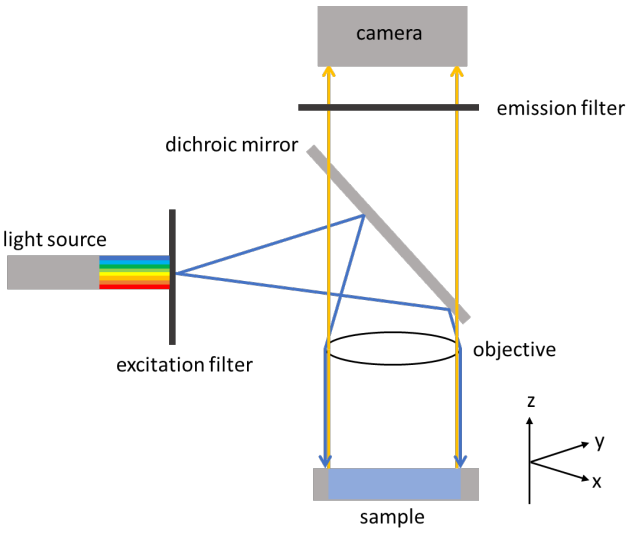


Figure 1.2: Widefield fluorescence microscope set-up.

Widefield fluorescence microscopy utilises a broad-spectrum light source combined with various filters to allow for excitation with different light colours (Figure 1.2).[9] The excitation reflects off a dichroic mirror – a filter which uses interference to reflect some light wavelengths and allow others to pass through – into the sample. This reflected light illuminates the entire sample volume in the

x,y and z planes. Fluorescent dyes emit light which passes back through the objective and the dichroic mirror, and an image is captured on a camera. Because light is coming from many layers within the sample, including above and below the focal plane, samples thicker than 10 µm can cause significant blurring. However, a key advantage to this technique is the fast acquisition, as a whole field of view can be imaged at once.

Confocal fluorescence microscopy was first invented in 1957 by Marvin Minsky, and has been a mainstream research tool since the 1980s.[10] Unlike widefield microscopy, confocal microscopy is a scanning technique – it illuminates only a single 'pixel' of the field-of-view at a time rather than the whole sample (Figure 1.3A), and uses lasers as the excitation source.[11] In order to build up a whole image, the focused spot of light is scanned across the x,y plane of the sample (Figure 1.3B), and emission is collected back through the objective and measured by a photomultiplier tube (PMT) detector. PMTs convert photons into current, and the intensity value is stored for each pixel.

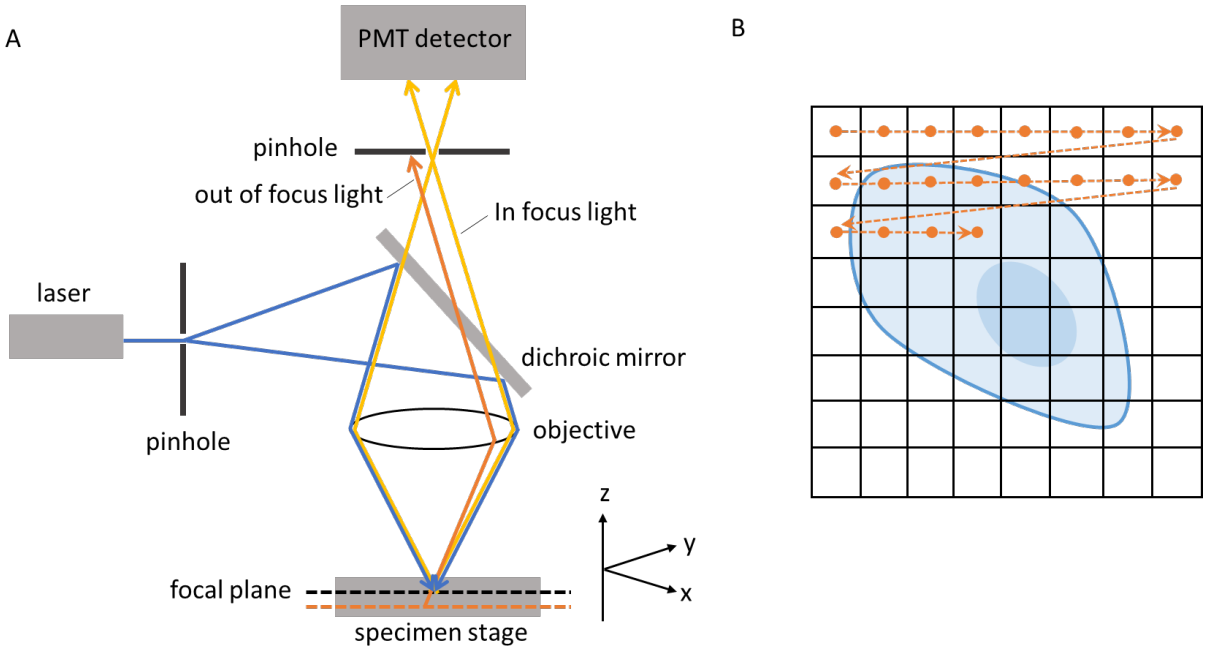


Figure 1.3: The standard set-up for a confocal microscope, showing light focused through an objective a specific point in a sample x,y plane, and pinholes used to filter out light from out of focus planes in the z axis (A). A schematic of a pixel-by-pixel beam scanning path.

The second major difference between confocal and widefield is that although the excitation spot excites fluorophores through the entire depth of the sample, emission from all but the desired focal

plane is filtered out through a pinhole in the detector. This greatly improves resolution in the z axis, and allows 'optical sectioning' whereby specific z planes of a sample can be imaged, and built into a 3D data set by acquiring images at many focus depths.

1.3 Resolving below the diffraction limit

The role of the objective lens in the microscope techniques discussed above is to collect and focus light. Objectives are characterised by their numerical aperture (*NA*), which describes the range of angles over which it can accept and focus light, in media with a particular refractive index (*n*), according to Equation 3:

$$NA = n\,sin\theta \qquad \text{(Equation 3)}$$

where θ is the half-angle of the largest light cone that can pass into the objective (Figure 1.4).

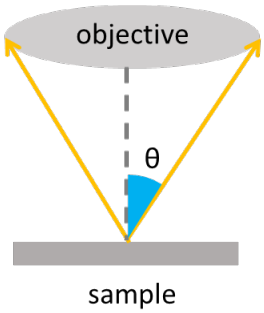


Figure 1.4: A schematic of an objective lens focusing light from an emitted sample of angle θ.

Due to the way light diffracts as it interacts with lenses and moves through apertures, light from an infinitesimally small point can only be recorded as a much larger ellipsoid pattern diffraction spot – known as a point spread function (PSF) (Figure 1.5). This places a limit on how closely we can resolve two objects, which was defined as a function of the wavelength and the numerical aperture of the microscope according to Equation 4 (x,y plane) and Equation 5 (z-axis) by Ernst Abbe in 1873[12]:

$$d_{x,y} = \frac{\lambda}{2NA} \qquad \text{(Equation 4)}$$

$$d_z = \frac{2\lambda}{NA^2} \qquad \text{(Equation 5)}$$

where *d* is the minimum resolvable distance, λ is the wavelength of light, and *NA* is the numerical aperture of the instrument. On modern microscopes, with numerical apertures around 1.4, the maximum achievable x,y resolution for green light (500 nm) excitation is 178 nm, and for red light (700 nm) excitation, 250 nm. The maximum achievable z axis resolution in these cases is 510 and 714 nm respectively. This is much smaller than the size of a cell (10 – 100 µm) but still on the same order of magnitude as some organelles (eg. lysosomes which range from 100 – 1000 nm), and much larger than proteins or individual molecules (1 – 5 nm).

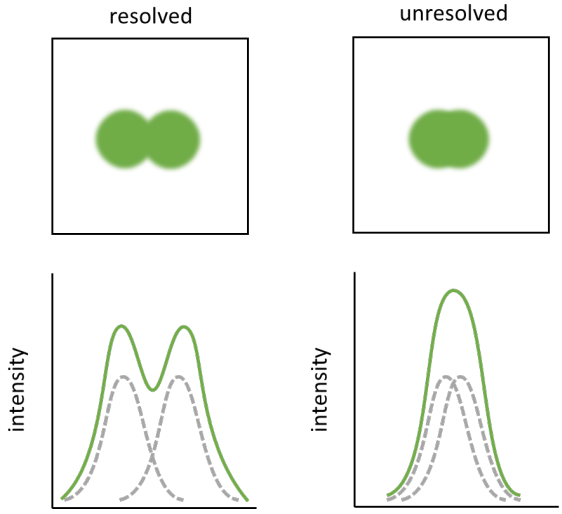


Figure 1.5: The ellipsoid point spread functions of two emitters, far enough apart to be resolved (left) and too close to be resolved (right).

It was thought that this fundamental diffraction barrier was impenetrable, however in the late 1990s, super-resolution microscopy techniques to surpass it were first proposed. These techniques aimed to use the properties of fluorescent molecules themselves to overcome the diffraction barrier. By using photoswitching to turn molecules on and off either stochastically or with specific irradiation, localisation of fluorophores below the diffraction limit was possible. In 2014 Stefan Hell, Eric Betzig and William Moerner were awarded the Nobel Prize in chemistry for their development of these technologies.[13-15]

Super-resolution microscopy methods can be broadly broken down into two types of techniques: single molecule methods, utilising stochastic switching, and ensemble methods, utilising deterministic switching with lasers. These techniques are continuously improving, pushing resolution down towards the single nanometre regime and allowing unprecedented insight into biological structure and function, while maintaining the classical advantages of fluorescence microscopy including specificity, sensitivity and live cell observation. Each technique comes with its own strengths, based on the inherent compromises between spatial resolution and temporal resolution, efficiency, photodamage, imaging depth and multicolour ability.[16] In short – different techniques are best chosen to answer different questions depending on what is required from an experiment.

1.4 Single molecule localisation methods

Single molecule localisation methods (SMLM) resolve below the diffraction limit by localising the coordinates of sparsely distributed emissive dyes, through an accurate computational determination of the centre of the point spread function, which is not possible if multiple neighbouring dyes are emitting at the same time. By keeping dyes in a dynamic equilibrium where they are predominantly turned off, individual localisations are built up over thousands of frames, which are then reconstructed into the final image (Figure 1.6).

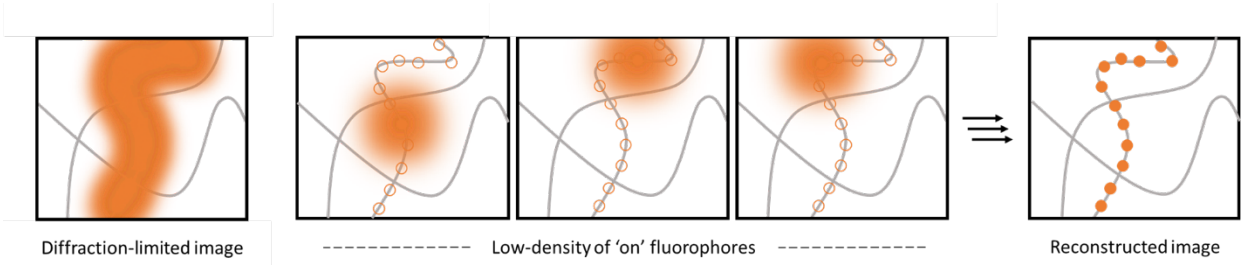


Figure 1.6: The principal behind single molecule localisation techniques. Although the emission collected is diffraction-limited, if it can be assumed to be from a single dye, its coordinates can be localised at the centre of the PSF.

The resolutions achievable by this technique are routinely around 20 nm in the x,y plane (Figure 1.7). The image reconstruction process does, however, limit the temporal resolution that is possible with these techniques, making them unsuitable for imaging fast dynamic processes. There are

different SMLM techniques, which are differentiated by the way the imaging agents are switched between the off and on states. Stochastic optical reconstruction microscopy (STORM) uses reducing buffers to drive organic dyes into long-lived dark states, where they sporadically photoswitch back on (discussed further below).[17] Photoactivated localisation microscopy (PALM) works in a similar way to STORM, but uses fluorescent proteins rather than small molecule fluorophores.[18] These proteins are non-emissive in the resting state, and are switched on via a light-triggered isomerisation to a bright form. By activating and then bleaching a subset of the total population at a time, high resolution images can be built up over many cycles. Points accumulation for imaging in nanoscale topography (PAINT) is another SMLM technique that uses organic dyes, but relies on transient associations of the dyes with a target (discussed further below).[19]

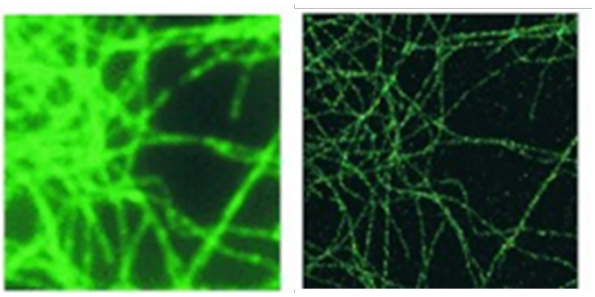


Figure 1.7: Comparison of a diffraction-limited TIRF (left) and super-resolution STORM (right) microscope image of the cytoskeletal microtubule network of mammalian cells, stained with Atto520. Reproduced with permission.[20]

Single-molecule localisation methods are generally wide-field techniques, which illuminate the entire sample and record an entire field-of-view output on CCD cameras. Although this is faster than beam scanning, the requirement for many thousands of images to build up a single frame often means the time resolution is not much improved, and makes imaging dynamic process in live cells difficult.

1.5 Ensemble methods

There are also a variety of techniques which aim to resolve fluorophores in space rather than in time, by using different excitation laser patterns. Structured illumination microscopy (SIM) – a

widefield method – as well as stimulated emission depletion (STED) and Reversible Saturable Optical Fluorescence Transitions (RESOLFT) – both laser scanning methods – will be discussed.

1.5.1 Structured Illumination Microscopy (SIM)

SIM takes advantage of the large scale interference (moiré) patterns generated when two patterned objects are overlaid. Using patterned excitation irradiation generated by a grating, the sub-diffraction features in samples form moiré patterns in the recorded emission.[21] Multiple images and moiré patterns are captured by rotation and translation of the patterned illumination, and processing can (back)-extract information and more precise localisation of the sub-diffraction details in the sample than is possible with fluorescence microscopy. A schematic is given in Figure 1.8.

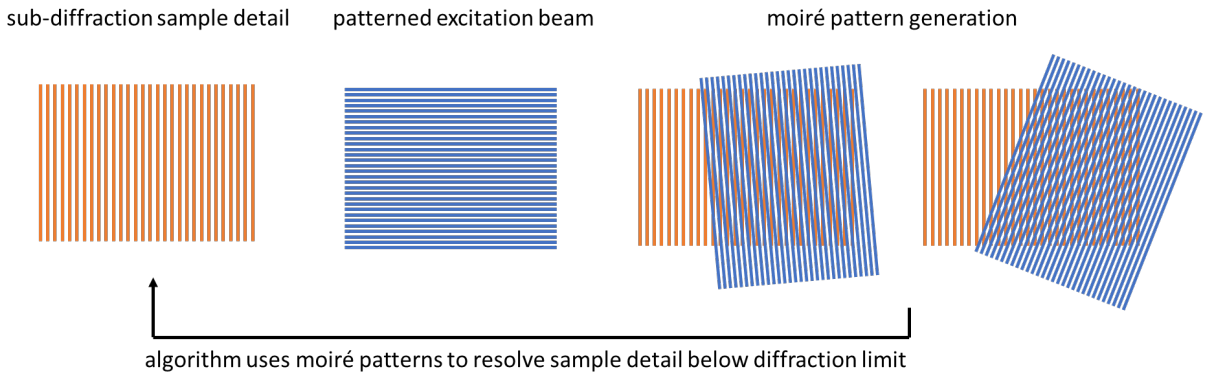


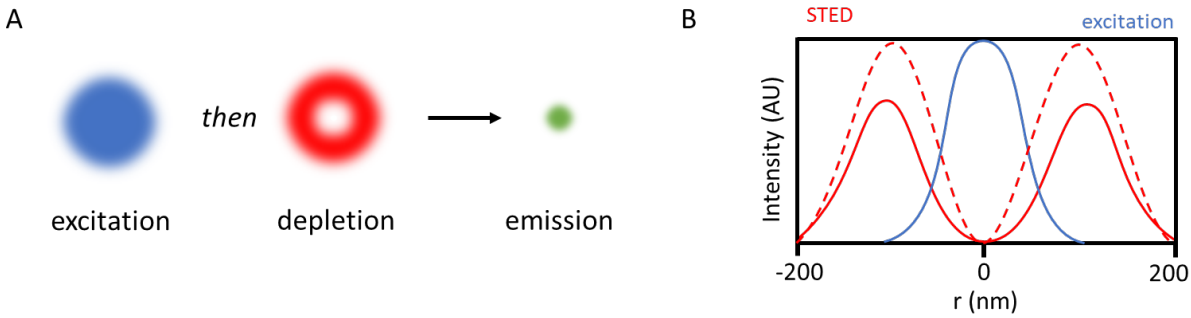
Figure 1.8: Idealised sample detail and excitation pattern showing that different moiré patterns are produced due to the interference between the sample and the patterned illumination as their relative orientation is changed in SIM.

One of the main advantages of SIM is that is can be used directly on dyes and samples that have been prepared for non-super resolution methods, and can do multi-colour and relatively high speed imaging.[22] It does, however, normally only provide a two-fold enhancement in resolution, with typical resolution around 100 – 120 nm laterally.[23]

1.5.2 Stimulated Emission Depletion Microscopy (STED)

Stimulated emission depletion microscopy uses stimulated emission to force populations of fluorophores into a dark state, leaving a sub-diffraction sized irradiation spot of fluorophores

active. It is a scanning method, so at each pixel a sequence of lasers is applied (Figure 1.9A). First, fluorophores are excited to a singlet excited state with a diffraction-limited laser beam. Then, a donut-shaped red laser, with a (diffraction-unlimited) central node of zero intensity stimulates emission from the excited state back to the ground state faster than fluorescence emission can occur (10^{-9} s). The emission from the fluorophores at the centre of the donut laser can then be



collected. The more intense the laser power of the depletion donut, the smaller the effective central zero point is, therefore depletion laser power is positively correlated with resolution (Figure 1.9B).[24]

Figure 1.9: The laser sequence for STED microscopy (A): excitation (blue) is followed by depletion with a donut-shaped red laser, resulting in diffraction unlimited emission at the central node of zero intensity. (B) The effective size of the central node decreases with increasing depletion beam intensity as it creates a steeper well (solid to dotted line).

The donut shaped depletion beam is formed by passing the depletion laser through a vortex phase plate, which shifts the phase of the laser beam in a spiral around the centre, causing a hollow central cylinder in the intensity distribution.[25] As STED is a scanning technique, the out-of-focus emission can be filtered out through a pinhole, and the optical sectioning of tissues into different focal planes is possible. The emission is collected as an intensity in each pixel using photodetectors, and can be filtered by wavelength and sent to different detectors for multi-colour imaging. The main limitation to STED microscopy is the high intensity laser irradiation required to deplete the excited state before spontaneous emission occurs, with photobleaching and phototoxicity being major issues.[26] Nevertheless, resolution with STED microscopy is routinely in the range of 30 – 80 nm laterally and 100 nm axially.[27]

1.5.3 Reversible Saturable Optical Fluorescence Transitions Microscopy (RESOLFT)

RESOLFT is a closely-related technique to STED, utilising the same overlaid donut laser beam concept to allow only small populations of fluorophores to emit (Figure 1.10A). The first report of RESOLFT microscopy came 10 years after STED, and utilised photochemical switching rather than stimulated emission from the excited state as a method for turning molecules off.[28] The main advantage of this method is that the intensity of light required for photoswitching is similar to excitation in confocal fluorescence microscopy, and up to six orders of magnitude lower than those required for STED microscopy.[29] This gives RESOLFT microscopy a distinct advantage as a super-resolution technique in live cell imaging experiments over long timeframes, reducing the phototoxicity and photobleaching associated with STED depletion lasers.[30]

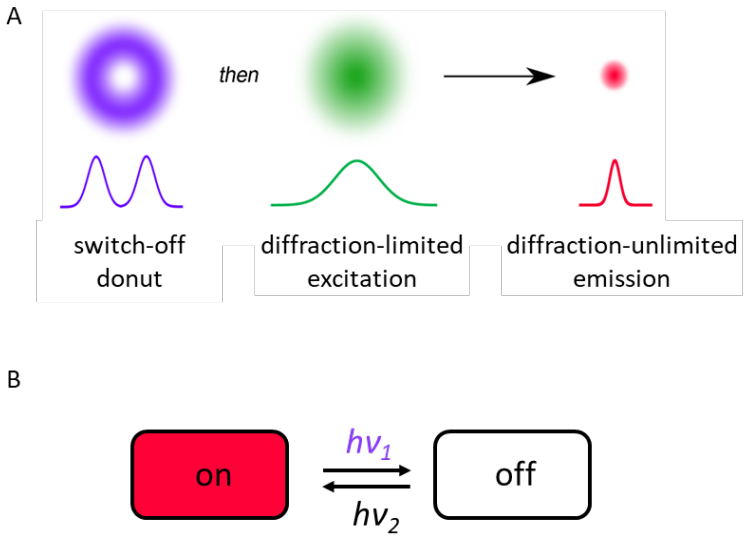


Figure 1.10: RESOLFT laser illumination pattern (A): the switch-off donut triggers photochemical switching to an off state, so that when the excitation laser is applied (green), only emission from the central node is observed. (B) Photochemical switching required in dyes or proteins applied to RESOLFT microscopy.

RESOLFT microscopy requires fluorophores which can be photochemically switched between a bright 'on' state and a dark 'off' state (Figure 1.10B), which are described further in Introduction Section 2.4. Although using photochemical switching rather than stimulated depletion reduces the required laser power, it introduces new challenges for the design of fluorescent dyes and proteins[31] required for the technique to work.

Recent development to RESOLFT microscopes and image acquisitions methods have seen parallelisation of illumination to increase acquisition speed,[32,b] algorithms utilising real-time feedback to optimise imaging parameters,[33] and enhancements in the 3D nature of off-switching depletion patterns to afford resolutions below 80 nm in all three dimensions.[34] The best lateral resolutions in RESOLFT are often around 30 – 40 nm.[35]

1.6 Recent super-resolution techniques

In recent years, Stefan Hell has developed new super-resolution microscopy techniques called MINFLUX[36] and MINSTED[37] which combine aspects of single molecule localisation methods and the laser patterns of ensemble methods. In MINFLUX, a donut-shaped excitation laser is used to localise a fluorophore by irradiation at several points around the location of the dye (Figure 1.11A). Algorithms then use the variation in emission intensity as a result of the Gaussian intensity of the donut to localise the dye. The usual paradigm of localising fluorophores at the point of maximum emission (see Figure 1.5 and 1.6, above), was flipped on its head, meaning that small differences between no emission at the centre of the donut and a weak emission close to the minimum are larger than the Poissonian Noise (ie $\Delta N > N_1^{1/2}$ moving from position N_1 to N_2) (Figure 1.11B), giving high localisation confidence from much lower photon flux.[38] This requires first knowing a fluorophore is actually there, as low or no emission could be a result of no molecule present, but this check can be done with conventional imaging techniques and requires few photons. MINFLUX technology can now be used for 3D, multicolour imaging with resolutions from 1 to 3 nm in fixed and living cells.[39]

MINSTED operates with a similar concept, however this time the donut beam is a *depletion* laser, which is moved to coordinates around a fluorophore to be localised. Rather than using high laser powers like in STED to completely deplete fluorophores everywhere except the central donut

[b] This technique is called MoNaLISA (Molecular Nanoscale Live Imaging with Sectioning Ability), proving that RESOLFT could be bettered both in its resolution capabilities and the contrived nature of its acronym.

position, lower laser powers are used and the corresponding variations in intensity are used to localise fluorophores. By using a blue-shifted STED beam and separating individual fluorophores by on/off switching, ångström precision localisation has been achieved.[40]

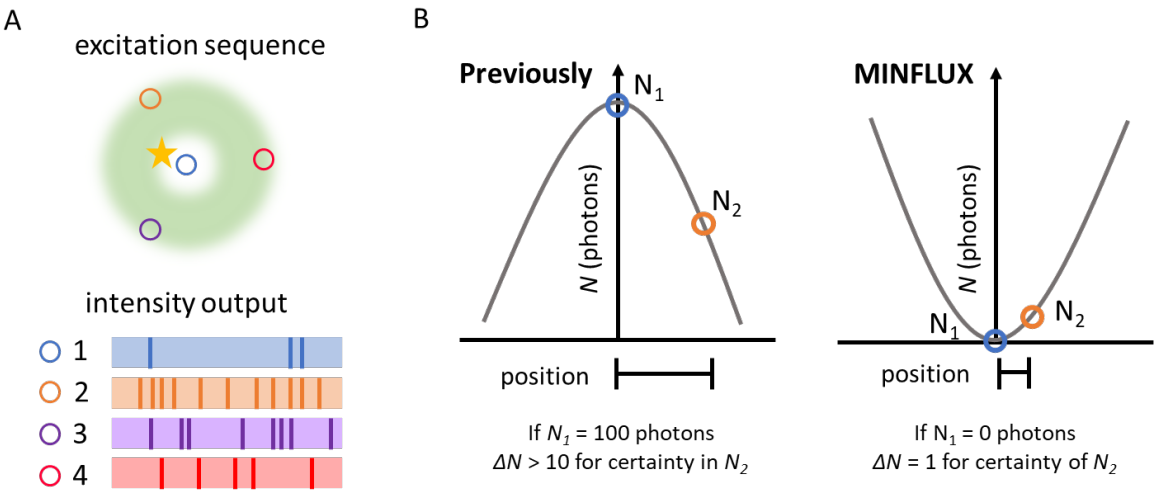


Figure 1.11: (A) The donut excitation pattern in MINSTED moves to different coordinates around a fluorescent dye (star), delivering different excitation intensities around the Gaussian distribution of the donut. This generates different output photon intensity levels, which can be used to calculate the position of the fluorophore. (B) Representation of the fundamental difference between previous localisation techniques and MINFLUX/MINSTED. At low intensity, the distance between two locations at which we can be certain the recorded intensity difference is real and not noise becomes much smaller. Figure adapted from reference 32 (A) and reference 34 (B).

The main advantage of both MINSTED and MINFLUX techniques is that they minimise the requirement for large numbers of photons to deliver precise localisations (a downside of SMLM) and minimise the requirement for high laser powers to remove signal from local molecules (a downside of STED and other ensemble methods). Currently, these new super-resolution techniques suffer from complex illumination and scanning regimes requiring specialist equipment and analysis, small fields of view, and relatively long acquisition times.[41] However, it is expected that they will become more widely implemented and user-friendly in the future and give way to many new insights into biological processes on a genuinely molecular scale.

2. Chemical tools for super-resolution microscopy

Most super-resolution techniques require photoswitchable dyes with high contrast between their dark and bright states, and good resistance to photodegredation.[42] The desirable properties required for excellent imaging fluorophores also remain the same – high brightness (the product of the extinction coefficient and fluorescence quantum yield), red-shifted absorption and emission wavelengths, low susceptibility to photobleaching, and solubility. Other aspects of the dye structure and function depend on the specific type of microscopy.

2.1 STORM dyes

Single-molecule stochastic switching methods require dyes that are predominantly in a dark 'off' state, with sporadic turn-on events. The process by which fluorophores are maintained in the dark state is generally by modulation of the external conditions, for example through chemical buffers or laser irradiation.[43] This means the fluorophores used are generally the same as those applied in confocal microscopy, as no further chemical modification is necessary to achieve switching. This is a key advantage of STORM microscopy. The photochemical mechanism by which the dark state is formed is debated, but in the case of cyanine dyes it is proposed to be the formation of an encounter complex between the dye and a nucleophilic thiol (Figure 1.12).[44]

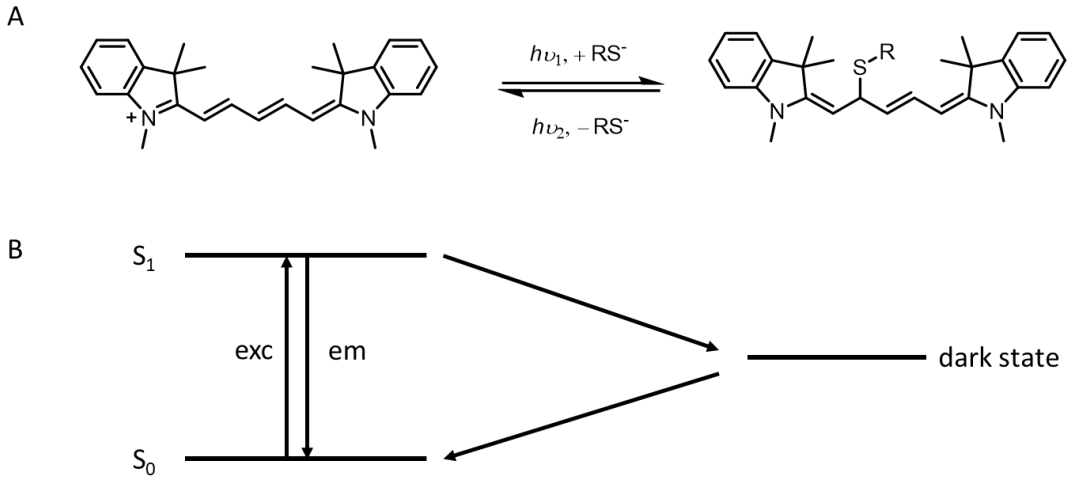


Figure 1.12: Suggested mechanism of thiol buffer quenching of cyanine dyes (A) and schematic of cyanine dark state utilised in STORM imaging (B).

Spatial resolution in STORM microscopy is fundamentally limited by the signal to noise ratio, rather than the pixel size or the wavelength of excitation. Therefore, bright dyes are crucially important, as this makes the localisation process more accurate. The certainty in a fluorophore's position scales approximately with the inverse square root of the number of detected photons,[45] so bright emitters are more precisely localised. Bright and photostable dyes have been a focus of much research for this purpose.[46,47]

The resolution of the labelled objects also depends on the duty cycle of a fluorophore – how long it spends in the emissive state before returning to dark. The turn-on process must occur at rates low enough that neighbouring molecules do not emit at the same time, which would obfuscate the computational localisation of the spatial coordinates of a single emitter from its point spread function. A low (and optimum) duty cycle means the rates of switching between the states are balanced so that only a small fraction of dyes are emitting at one time.[48]

Together, the duty cycle and the signal to noise ratio are the key defining factors in the maximum achievable resolution for STORM imaging. Despite these well-characterised parameters, there is little insight into what *structural* features correlate with high level performance for a fluorophore in STORM imaging.[42] However, a systematic study has characterised the 26 commercially available fluorophores and identified ideal buffer conditions for imaging.[49]

Some synthetic efforts have been made towards dyes that photoswitch spontaneously by making them susceptible to thiol addition in the ground state rather than the excited state, thereby averting the need for intense laser irradiation and very specific buffer conditions. Approaches to this include designs with electronically tailored intramolecular nucleophile/electrophile pairs (Figure 1.13),[50-53] or reducing steric hindrance around electrophilic sites.[54]

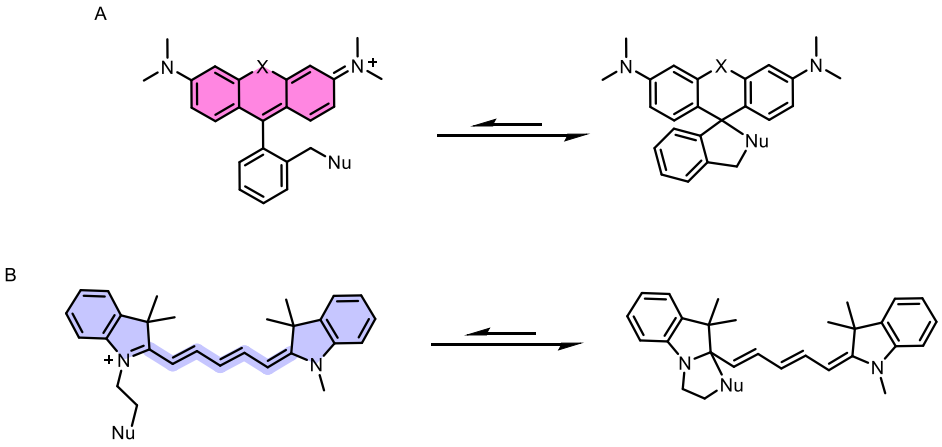


Figure 1.13: Examples of rhodamine[50,51] (A) and cyanine[52,53] (B) dyes with internal nucleophiles capable of disrupting the conjugation of the chromophore and switching them from a fluorescent state (left) to a dark state (right).

2.2 PAINT dyes

PAINT microscopy works in a similar way to STORM, by imaging small subsets of the total fluorophore population to achieve precise individual molecule localisation. However, rather than using chemical buffers or lasers to keep dyes in the dark state, fluorophores are designed to associate transiently with a target through chemical binding. This leads to a large 'turn-on' in emission by slowing down the diffusion rate and allowing their emission to be localised. This means dyes for PAINT microscopy must be chemically modified with a binding group of appropriate affinity for the target, or designed with emission properties that are environmentally-sensitive to the target environment. PAINT was originally reported with the Nile Red dye, which was able to interact transiently with vesicle membranes from a bulk aqueous solution, resulting in a large turn-on in emission due to the fluorogenic properties of the dye.[19] Modifications of the lipophilicity of Nile Red through attachment of alkyl groups can improve the reversible binding behaviour (for more discussion of this, see Chapter 2).[55] Fluorescent ligands for proteins of interest have also been utilised in PAINT,[56] but perhaps the most widespread method is DNA-PAINT, where a protein of interest is labelled with a docking strand of DNA, and a dye is labelling with the corresponding imager strand (Figure 1.14).[57] The binding kinetics can be controlled by the length of the complementary strands, and the binding event results in a slowing down of freely-diffusing dye

such that enough emitted photos can be localised.[58] Antibody kits for DNA-PAINT are commercially available.

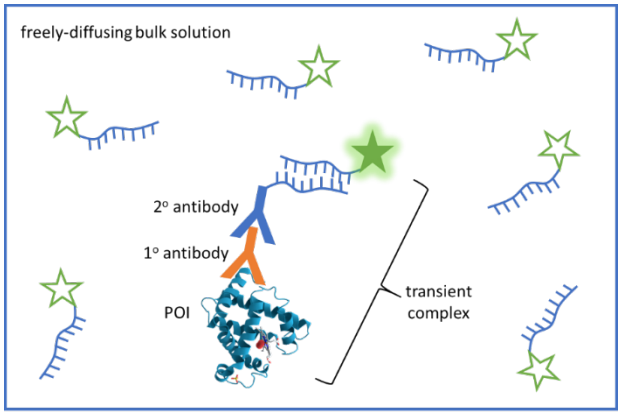


Figure 1.14: the principle of DNA-PAINT microscopy: dyes form transient complexes with a labelled protein of interest (POI) *via* DNA base-pair interactions, slowing down their diffusion and allowing their signal to be localised.

2.3 STED dyes

Due to the nature of the laser depletion method, STED is theoretically applicable to all fluorescent dyes, so long as they emit in the red to infrared region where the depletion laser beam lies (Figure 1.15A,B).[59] Due to the high intensity depletion beam, which induces transitions from S_1 into higher excited states that are associated with photobleaching, photostability is an important characteristic of STED dyes.[60] It is currently unclear what structural features lead to the photostability and depletion characteristics that make a dye well-suited to application in STED, and reported resolutions differ between 16 to 140 nm for different dyes.[42] Well-known commercial dyes include the Abberior STAR line which are rhodamine derivatives (Figure 1.15C).

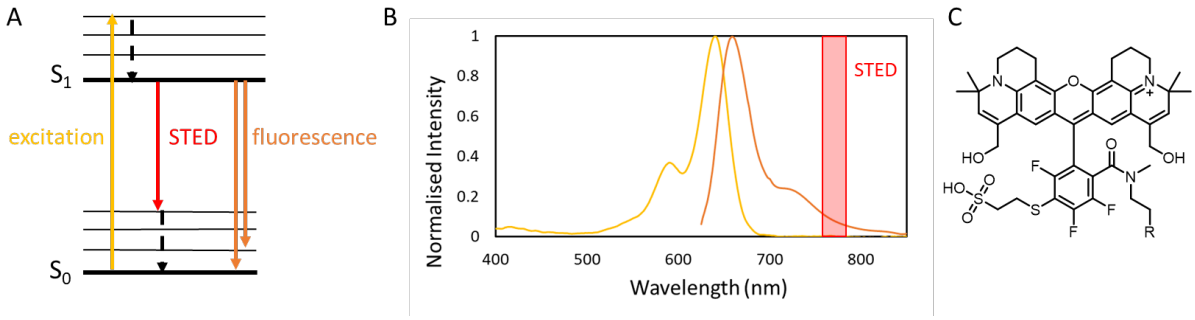


Figure 1.15: Energy diagram of a fluorophore showing the stimulated emission depletion (STED) process (A), with ideal range for the STED depletion beam on the tail of fluorescence emission (B) for the commercially-available dye Abberior STAR 635 (C).

2.4 RESOLFT tools

As discussed above, RESOLFT microscopy uses a donut-shaped quenching laser to photochemically isomerise dyes into a dark 'off' state, using much lower laser powers than the analogous STED depletion beam. In order for this technique to work efficiently, dyes must posess the following properties:

- Photochemical switching between a bright 'on' and a dark 'off' state.
- High contrast between the bright 'on' and dark 'off' state – this normally depends on having high photostationary distributions of a photoswitch at chosen irradiation wavelengths. It is also dependent on the photochemical quantum yields and the molar absorption coefficients of the two forms (discussed in Section 3.4).
- Fatigue resistant – an ideal RESOLFT imaging dye must do thousands of switching cycles without showing fatigue.
- Visible light switching – commercial microscopes do not tend to have UV lasers, and irradiation with UV can cause damage to biological systems, faster dye fatigue, and has poor penetration through tissue.
- Rapid photoswitching kinetics on a microsecond timescale, to allow for the fast acquisition of images and the capturing of dynamic biological processes.
- High brightness – the product of the molar extinction coefficient and the fluorescence quantum yield of a dye.
- Low toxicity
- Solubility and cellular membrane permeability (for an organic dye)
- Emission in the red for the best transparency in tissues and minimal cellular background autofluorescence.

These criteria apply to both fluorescent proteins and organic dyes for RESOLFT microscopy. In this next section I will discuss the current available tools for protein and organic dye tools for RESOFLT.

2.4.1 Proteins

The first application of the RESOLFT microscopy concept used photoswitchable proteins, demonstrating the advantage of utilising photochemical switching over stimulated emission, with laser intensities eight orders of magnitude lower than the comparable STED intensities at the time.[28] Photoswitchable proteins contain a chromophore that can adopt either a fluorescent 'on' state or a dark 'off' state through a photochemical *trans* – *cis* isomerisation.[61] They are derivatives of the green fluorescent protein (GFP) family, comprising a central chromophore on an alpha helix, surrounded by a barrel of beta sheets (Figure 1.16A).[29] The emission properties of the chromophores are dependent on their protonation state, isomeric form, and interactions with the surrounding amino acid residues (Figure 1.16B). This ability to tune the chromophore environment has given rise to the development of many mutants with varying spectral properties, often from the rational design of structural changes.[62] Like with any super-resolution dye, the properties of photoswitchable fluorescent proteins that are important for their application include brightness and switching speed, background (off state fluorescence), and fatigue. These parameters are often the target of optimisation mutation studies, with around 30 reported photoswitchable proteins,[29] and variants produced to have improved photostability,[63] switching kinetics (and therefore imaging speed),[64,65] switching direction (and therefore laser sequence),[66] red-shifted emission,[67,68] and lifetime.[69]

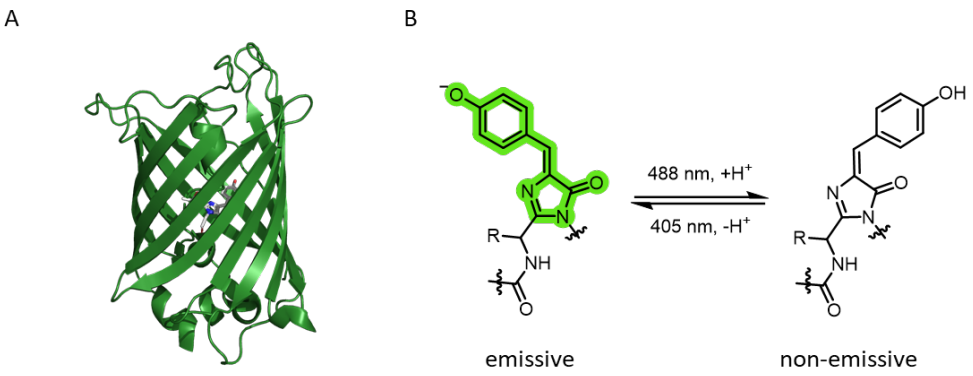


Figure 1.16A: The structure of enhanced green fluorescent protein (pdb 2Y0G)[70] showing the barrel of beta sheets around a central alpha helix and B: structure of the central chromophore. Isomerisation of the central chromophore exposes the phenol to residues with different pKa values, resulting in different protonation states.

There are some downsides to using photoswitchable proteins for RESOLFT microscopy, which limit their application in various ways. These include their relatively large size, sensitivity to local pH and oxygen dependence. They also require genetic mutation in order to introduce them to cells, as well as often having slow switching kinetics and in particular, poor photostability. Importantly, there is only so much improvement of these parameters that can be introduced by protein modification, as the core scaffold and chromophore cannot easily be altered.

2.4.2 Small molecule dyes

By using synthetic dyes, the range of photoswitching mechanisms and chromophores that can be explored is much greater. However, few organic dyes for RESOLFT have been reported.[42] Developing organic dyes for RESOLFT would also give the ability to include organelle targeting and chemical sensing moieties, furthering the application of this technique.

One design strategy for photoswitchable RESOLFT dyes is to use an intrinsically fluorescent photoswitch. There are several examples based around the diarylethene sulfone chromophore, which undergoes a ring-closing 6 π electrocyclization to give a conjugated, fluorescent form (Figure 1.17A). Attachment of poly carboxylic acid groups to give the tetra-acid (Figure 1.17B) was reported as the first water-soluble derivative,[71] and was applied to RESOLFT microscopy with

immunostaining to image α-tubulin with full-width-at-half-maxima of 75 nm.[c] However, these dyes photobleach relatively quickly, with 50% intensity lost after 20 imaging cycles, possibly due to the need to activate the system with UV light. Other studies on these chromophores found that asymmetric push-pull derivatives had increased fatigue resistance in organic solvents,[72] as well as impacting the fluorescence quantum yield and the photochemical switching quantum yield.[73] Functionalisation with 12 carboxylic acids was necessary to impart aqueous fatigue resistance (Figure 1.17C), however this highly-charged compound is no longer cell permeable, limiting its application to RESOLFT.[74]

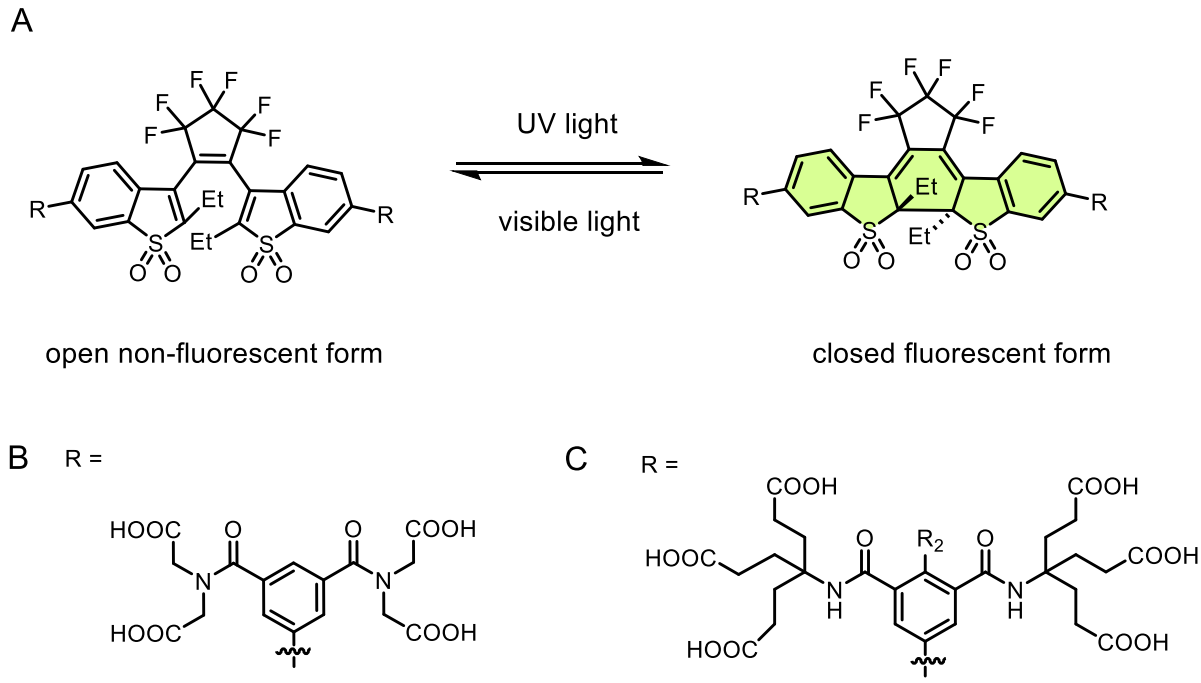


Figure 1.17: Example fluorescent sulfone diarylethenes.

[c] Full-width-at-half-maximum (FWHM) is the width of an object's line profile at half the maximum intensity, and often used to demonstrate the resolution rather than the distance between two objects – this is discussed further in Chapter 2.

Another design strategy for photoswitchable RESOLFT dyes is to make a dyad, whereby a photoswitchable quenching unit is attached to a fluorescent dye.[75,76] This allows the optimisation of the photoswitching component of the molecule, and the emissive component of the molecule separately. Commonly, these dyads are made to utilise Förster Resonant Engery Transfer as a reliable and predictable method of quenching emission (Figure 1.18). This requires using a photoswitch with a large change in its absorbance between the two forms, such that one overlaps with the dye and quenches emission *via* FRET, and the other does not.

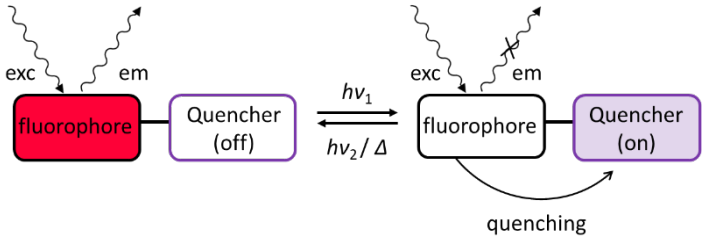


Figure 1.18: Dyad strategy for photoswitchable RESOLFT dyes. When the quencher is in its non-absorbing form (off), the dye emits light as fluorescence. When the quencher is isomerised to its coloured form (on), energy from the excited dye is no longer emitted but instead transferred to the quencher.

Reversible diarylethene photoswitches paired with a rhodamine dye were the first proposed FRET dyads for RESOLFT (eg. Figure 1.19A).[77] In later work, these dyads were attached to silica nanoparticles and imaged with a RESOLFT microscope,[78] distinguishing particles ~230 nm apart. In these experiments photobleaching was the main issue limiting better resolution. In a separate early system, a coumarin-based dyad with a furyl-fulgide photoswitch was used in RESOLFT imaging (Figure 1.19B). These compounds were not synthetically tethered, but rather both were doped into a polymer matrix, and the photoswitching allowed resolution of grooves in the matrix ~50 nm apart.[79] Finally, a cyanine pair (Cy3 and Cy5) was reported which combined buffer-induced turn-off of cyanines from STORM imaging with a FRET process to make a photoswitchable dyad for RESOLFT.[80] It was capable of resolving labelled tubulin strands ~130 nm apart, however the resolution was limited to due to photobleaching and therefore pixel size.

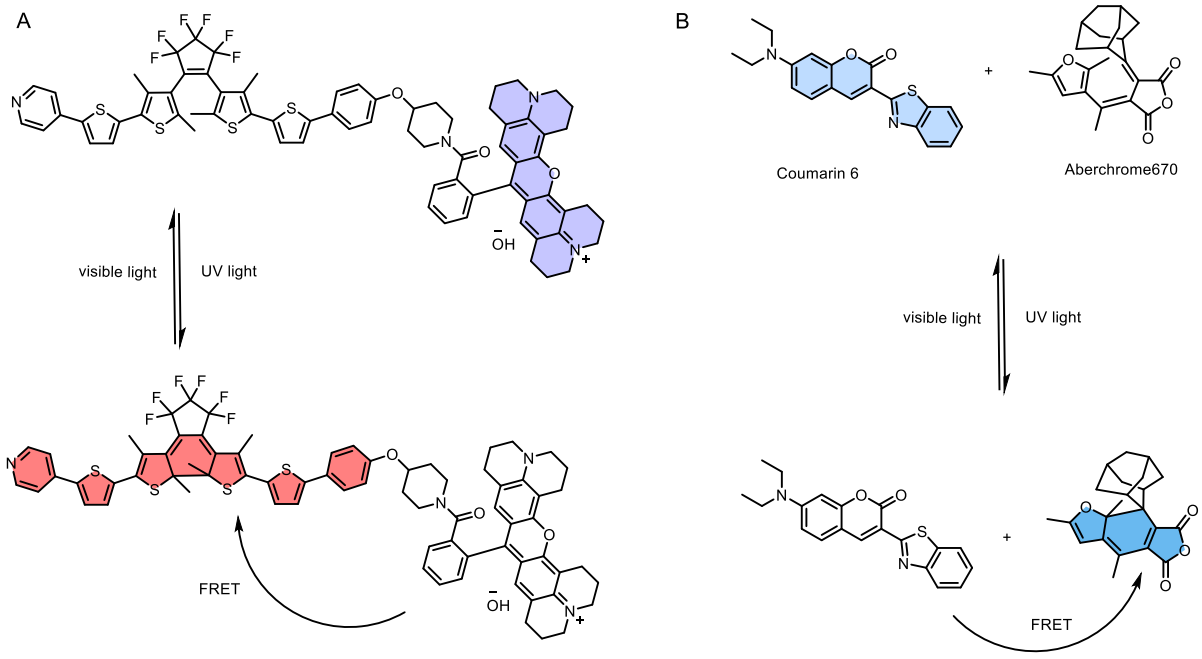


Figure 1.19: Previously reported RESOLFT FRET-quenched pairs.

There are several reported photoswitchable dyads based around perylene dyes and diarylethene photoswitches, however these are often tested with single molecule localisation microscopy techniques rather than RESOLFT.[81-83] One example of a photoswitchable dyad applied to a cellular environment was a polymeric naphthalimide dye and diarylethene photoswitch.[84] The naphthalimide dye that was chosen incorporated a lysosome targeting group, and the polymer was used to image lysosomes ~40 nm apart with single molecule localisation microscopy.

In previous work by our group, a FRET dyad composed of a silicon rhodamine dye and a spiropyran photoswitch[85] was shown to have good switching properties and high brightness in confocal experiments, however the fatigue resistance was not good enough to perform RESOLFT microscopy (Figure 1.20A). A better optimised visible light spironaphthoxazine photoswitch was then developed by our group[86] which allowed successful RESOLFT FRET dyads to be made with Atto590 and cyanine dyes (Figure 1.20B).[87]

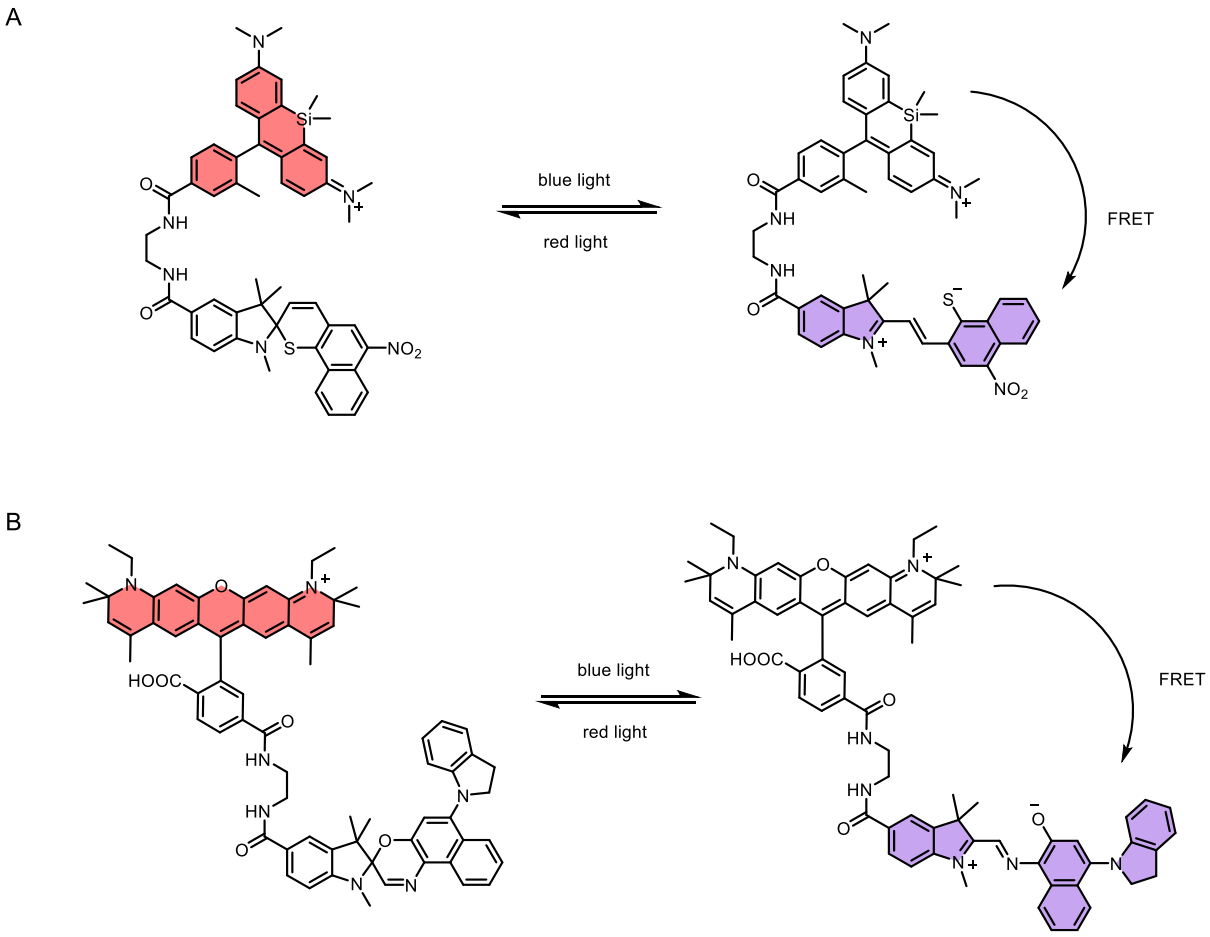


Figure 1.20: spiropyran (A) and spironaphthxazine (B) dyads reported by our group.

These dyads were imaged in giant unilamellar vesicle membranes (GUVs), with FWHM around 100 nm (Figure 1.21), showing average enhancements compared to confocal images of 2. The best resolutions are around 80 nm with enhancements compared to confocal of 2.7.

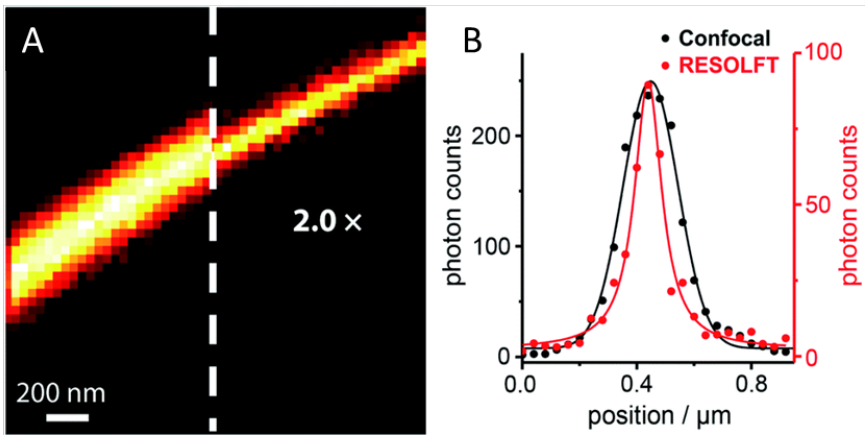


Figure 1.21: (A) RESOLFT and confocal image of a DOPC giant unilamellar vesicle membrane stained with spironaphthoxazine dyad (Figure 1.20B, above), and (B) line profiles of confocal and RESOLFT images.

Both the spiropyran and spironaphthoxazine dyads are an improvement on almost all the previously-reported dyads as they use visible light to switch in both directions, which is of key importance both for application with available microscope lasers, cell health, and dye photobleaching. However, despite these steps forward, key limitations still remain. Fatigue resistance is still an issue for high resolution images over long-term imaging, as the spironaphthoxazine switch degrades at a significant rate. The reverse isomerisation with red light to re-set the dyad each pixel is also quite slow, which limits the size of the field of view and rate of imaging.

3. Design principles for photoswitchable RESOLFT dyes

3.1 Introduction

The key design requirement for a RESOLFT dye is the ability to trigger a change in fluorescence emission from a bright "on" state to a dark "off" state with light.[88] Photoswitches, molecules which isomerise between two different forms when irradiated with light (see section 3.4), are attractive functional molecules to incorporate into the design as they provide a mechanism for initiating light-triggered changes, which are uncoupled from a fluorophore. This allows the use of existing fluorophores with optimised properties for imaging. A photoswitch therefore, must be chosen for its ability to modulate fluorescence intensity by causing quenching in one form, and not in another. There are multiple excited state processes that can compete with fluorescence to cause quenching, including Förster Resonant Engery Transfer (FRET) and photoinduced electron transfer (PET). Both FRET and PET are well-established methods of quenching fluorescence, and will be discussed further here.

3.2 FRET quenching

FRET is the process by which the energy of an excited state donor fluorophore is non-radiatively transferred to an acceptor molecule, which can go on to emit itself or decay non-radiatively (Figure 1.22). The requirements for FRET quenching to occur include physical proximity, the alignment of the donor and acceptor transition dipole moments, and spectral overlap between the donor emission and the acceptor absorption.[89]

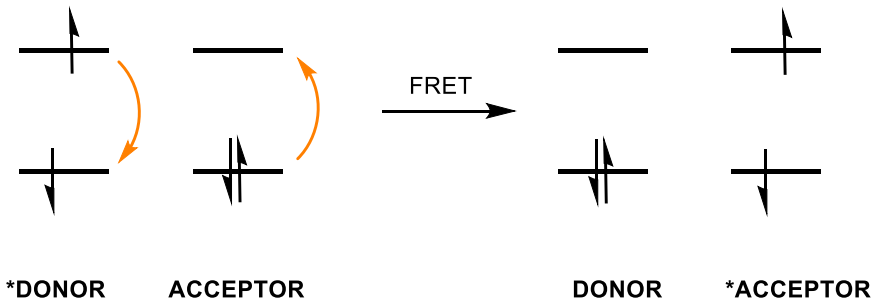


Figure 1.22: Schematic representation of FRET between an excited state donor molecule and an acceptor.

The efficiency of the FRET process can be calculated for a given donor and acceptor pair. The Förster radius R_0, is the distance at which FRET is 50% efficient, and can be approximated with Equation 6:

$$R_0 = 0.2108 \left[\frac{\kappa^2 \varphi_D J(\lambda)}{n^4}\right]^{\frac{1}{6}} \quad \text{(Equation 6)}$$

In equation 6, κ^2 is the dipole orientation factor, which describes the relative orientation of the transition dipoles of the donor and acceptor. The value can range from 0 to 4, (0 for perpendicular, 1 for parallel, 4 for antiparallel) but is assumed to be an average of 2/3 given free rotation between the donor and acceptor. φ_D is the fluorescence quantum yield of the donor, *n* is the refractive index of the solvent, and $J(\lambda)$ is the spectral overlap integral, which is given by Equation 7.

$$J(\lambda) = \int f_D \varepsilon_A(\lambda) \lambda^4 \, d\lambda \quad \text{(Equation 7)}$$

where f_D is the normalised donor emission spectrum, $\varepsilon_A(\lambda)$ is the acceptor molar absorption coefficient at wavelength λ.

From the Förster radius, the FRET efficiency at a given distance between a donor and acceptor (*r*) can then be calculated according to Equation 8:

$$E = \frac{1}{1 + (\frac{r}{R_0})^6} \quad \text{(Equation 8)}$$

The rate constant of FRET at a given distance between donor and acceptor (*r*) can be calculated using Equation 9:

$$k(r) = \frac{1}{\tau_D}(\frac{R_0}{r})^6 \quad \text{(Equation 9)}$$

Where τ_D is the fluorescence lifetime of the donor (without the acceptor) and (R_0) is the Förster radius.

FRET quenching has been employed extensively as a design strategy in small molecule fluorescent sensors,[90] and fluorescent proteins as biomolecular research tools.[91] Assuming good spectral overlap, FRET is normally highly efficient over a distance of several nanometres, and its strong

distance dependence has resulted in its common use as a 'spectroscopic ruler' to measure distances on the molecular scale.[92]

3.3 PET quenching

Photoinduced electron transfer is a redox process by which an electron is exchanged either inter- or intramolecularly between the excited state of one molecule and the ground state of another, *via* a charge separated intermediate. This electron transfer can occur either to (Figure 1.23A) or from (Figure 1.23B) the excited state molecule, giving rise to two possible pairs of charged intermediates. Relaxation by a further electron transfer occurs in both cases to regain the neutral forms.

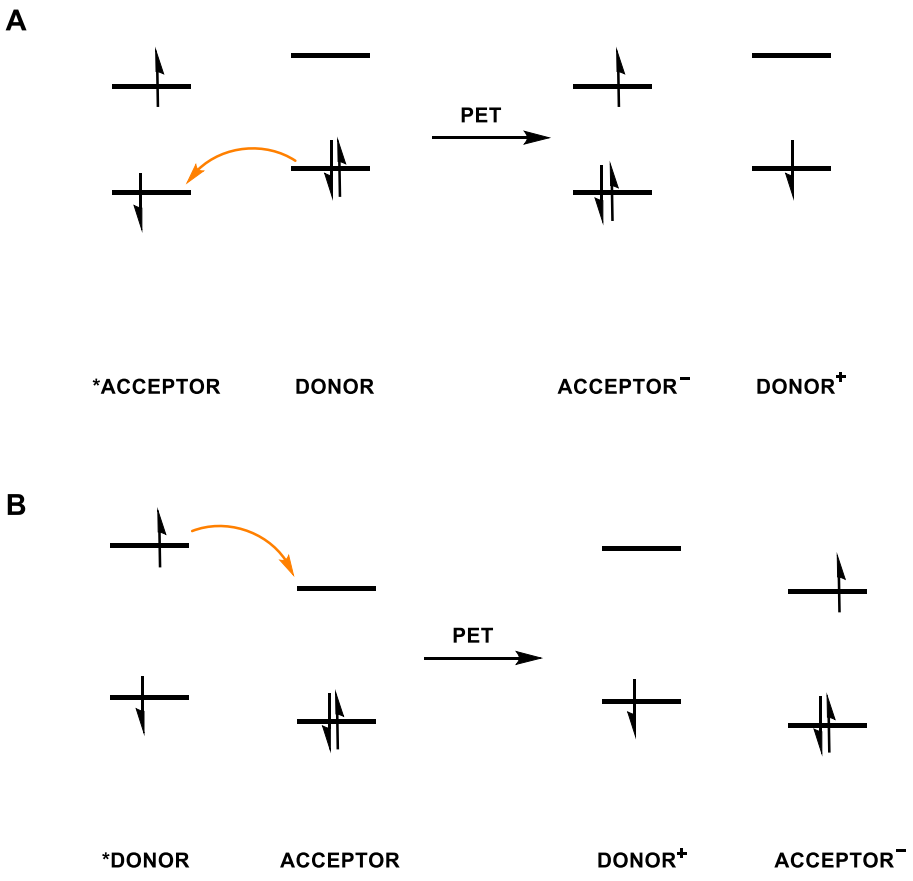


Figure 1.23: PET quenching between (A) an excited state acceptor and donor, or (B) excited state donor and acceptor, forming the charge separated, radical anion acceptor and radical cation donor in both cases.

Photoinduced electron transfers are strongly distance dependent, with their rate described by the Marcus equation:

$$k_{\mathrm{ET}} = \frac{2\pi}{\hbar}|H_{AB}|^2 \frac{1}{\sqrt{4\pi\lambda k_{\mathrm{B}}T}} e^{\left(\frac{-(\lambda+\Delta G^{\circ})^2}{4\lambda k_{\mathrm{B}}T}\right)} \qquad \text{(Equation 10)}$$

where $|H_{AB}|$ is the electronic coupling between the initial and final (charge separate) states, λ is the reorganisation energy for the solvent and species once charge is redistributed, ΔG° is the thermodynamic driving force for the rearrangement, $\hbar$ is the reduced Planck constant, k_{B} is Boltzmann's constant and T is temperature.

It is a complex endeavour to accurately analyse systems with this equation. Some experimentalists use large approximations for many of the terms to estimate electron transfer rates,[93] and in contrast theoreticians provide complex treatments of small systems to take into account how electronic coupling changes with both distance and orientation (for example with singlet fission between two ethylene molecules[94]). It will suffice to say here that both electronic coupling and the outer sphere reorganisation energy are distance-dependent, and rates of electron transfer decay exponentially with an increase in distance between a donor and an acceptor.[95] Generally, we know the distance at which PET occurs is much shorter than FRET, as the wavefunctions of the donor and acceptor must overlap for an electron to be transferred. The rate of the electron transfer process must out-compete fluorescence (10^{-9} s) and other non-radiative excited state processes. This will be further discussed in Chapter 4.

In addition to rate considerations, the electron transfer process must be thermodynamically favourable. The thermodynamics of a PET reaction can be predicted with the Weller equation (Equation 11).[96]

$$\Delta G_{PET} = E(D/D^+) - \Delta E(A) - E(A^-/A) - \frac{e^2}{\varepsilon r} \qquad \text{(Equation 11)}$$

In this equation $E(D/D^+)$ is the oxidation potential of the donor, and $E(A^-/A)$ and $\Delta E(A)$ are the reduction potential and singlet excitation energy of the acceptor respectively. The final term ($e^2/\varepsilon r$) accounts for the free energy gained by bringing the ions together in solution, where e is the elemental charge, r is the distance between the donor and acceptor, and ε is the relative

permittivity of the solvent. This term, however, is generally much smaller than the errors in the redox potentials (both measured and calculated), so it is generally neglected.[96]

An analogous equation exists for systems where the acceptor is in the excited state for photoinduced electron transfer. All the terms remain the same but the excitation energy is the absorption maximum of the donor, as in Equation 12.

$$\Delta G_{PET} = E(D/D^{+}) - \Delta E(D) - E(A^{-}/A) - \frac{e^2}{\varepsilon r} \qquad \text{(Equation 12)}$$

Sometimes it is not feasible to measure the redox potentials of a system experimentally.[97] In the case of photoswitching molecules, often one form of the switch is thermally unstable and only exists on timescales shorter than voltammetry experiments. Another obstacle to the measurement of redox potentials occurs when electron transfer catalyses the conversion between the two isomers as well as light, as is the case with many otherwise thermally stable photoswitches.[98] There are also the standard barriers to experimental measurement including finding a solvent with the correct electrochemical window to observe your molecule, and solubility requirements.[99]

A simple estimation of the difference in oxidation and reduction potentials can be made using Koopman's theorem,[100] where the oxidation potential is equal to the negative of the energy of the highest occupied molecular orbital, and the reduction potential is equal to the negative of the energy of the lowest unoccupied molecular orbital. This estimation is not particularly accurate as it neglects the change in orbital energies or geometries between the neutral and charged forms of the molecule. In order to incorporate computational results into thermodynamic analysis it is important to calculate the redox potentials more accurately. This can be done by calculating the change in Gibbs free energy between the neutral and the charged forms from their respective optimised geometries, and then converting to a potential using the Nernst equation.[101] These types of DFT calculations are sensitive to choices in functionals and basis sets,[102] so it is important to use an appropriate level of theory and benchmark according to relevant experimental results.

PET can be validated experimentally using transient absorption spectroscopy, allowing the direct observation of the short-lived charge separated form of the redox pair.[103] Transient absorption spectroscopy experiments can capture processes and dynamics on the femtosecond timescale.[104] Time-resolved spectra can be further analysed by fitting collected data to models in order to understand the reaction kinetics.[105]

In the absence of the specialist equipment required to perform these measurements, solvation polarity studies can be performed as evidence of PET quenching. This is because the charged nature of the redox pair intermediates in PET quenching processes means their stability is very sensitive to polarity. Generally, as molecules are studied in solvents with increasing dielectric constants, PET quenching becomes more efficient as the charge separated intermediate is better stabilised.

There are many fluorescent sensors in the literature based on the principle that electron-rich moieties (such as tertiary amine lone pairs), are highly competent at participating in photoinduced electron transfers as donors when coupled with electron-poor dyes. When these lone pairs are protonated or interact with a metal, this electron transfer is inhibited, and fluorescence is allowed, providing turn-on sensors for pH and a variety of metals including Zn^{2+} and Cu^{2+}. This design concept is the subject of many reviews for various fluorescent sensors.[106,107] Protonation studies are therefore sometimes used as evidence of a PET process, whereby if addition of a proton source restores fluorescence, it provides some evidence that the deprotonated, electron rich species was a PET donor.

3.4 Photoswitches

Photoswitches are molecules which can be reversibly converted between two isomers that have different absorption spectra using light, or in some cases thermally (Figure 1.24).

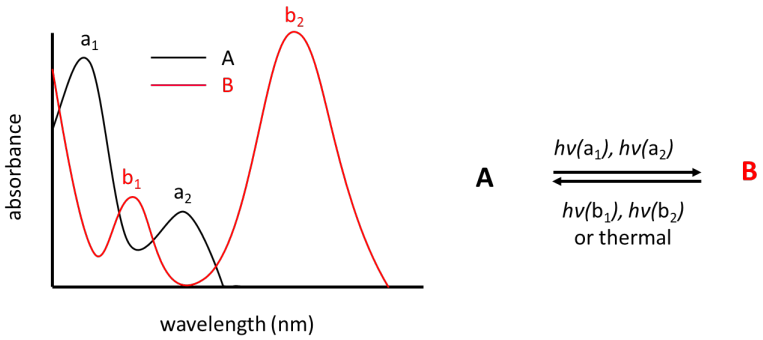


Figure 1.24: Example absorption spectra of a photoswitch in form A and form B.

Upon absorption of light (for example *hν*(a_1) *or hν*(a_2)), a molecule in its thermodynamically stable form A is able to photochemically isomerise to form B. The reverse reaction can then be triggered by light absorbed by the molecule in form B (for example *hν*(b_1) or *hν*(b_2), or can occur thermally. There are a number of terms and parameters that allow us to define the nature of these transformations:

(a) The photochemical quantum yield ($\varphi_{A\rightarrow B}$) relates to the efficiency of the isomerisation reaction in a similar way to a fluorescence quantum yield – *i.e.* of the number of photons absorbed, how many trigger an isomerisation.

(b) The thermal half-life ($t_{1/2}$) refers to the half-life of the thermal relaxation from a meta-stable isomer back to its thermodynamic minimum. This reaction follows mono-exponential decay kinetics, and is dependent on the solvent and temperature.

(c) The photostationary state (PSS) refers to the photoequilibrium reached under constant irradiation by a particular light source.

(d) At the photostationary state, there is a photostationary distribution (PSD), which refers to the relative composition of isomers A and B. The photostationary distribution varies with

the wavelength of irradiation, as it depends both on the relative intensity of the absorption of each isomer at a given wavelength, as well as the photochemical quantum yields of switching. In the example above, you would expect larger PSDs of each isomer by irradiation at $hv(a_2)$ and $hv(b_2)$, as opposed to irradiation with $hv(a_1)$ and $hv(b_1)$, due to the ability to selectively address a single isomer without competing absorption and reverse reaction of the other isomer. In most applications, the ability to reach 100% PSD of each isomer is desirable for precise control of a responsive material.

(e) The fatigue resistance refers to the rate of photodegradation over multiple switching cycles, caused by excited state side-reactions.

The two forms of photoswitches often have different physical and chemical properties, leading to the ability to induce changes in geometry, excited state properties, redox potentials, and charge distribution with light.[108] The applications for systems that can trigger these changes are almost limitless, and include catalysis, supramolecular assembly, molecular walkers and motors, and biological applications such as controlling protein-protein interactions or ligand binding.[109]

Different classes of photoswitch undergo different types of isomerisation reactions when excited, and differ greatly in the described parameters (Figure 1.25). Some photoswitches, such as azobenzenes,[110,111] stilbenes,[112] (thio)indigos,[113] and acylhydrazones[114,115] undergo an E-Z isomerisation around a C=C or N=C bond. These molecules are often fairly small chromophores, and induce large geometric changes in the systems in which they are incorporated upon photosiomerisation.

Other molecules, such as diarylethenes[116,117] and dihyrdopyrenes,[118] undergo a 6π electrocyclization reaction in response to light. These molecules show a large change in the conjugation of the system upon cyclisation, which leads to significant changes in the absorption wavelengths and intensity between the two forms. In the case of diarylethene cyclisation, the conjugation becomes greatly extended, generating a highly coloured chromophore, whereas in the

case of dihydropyrenes the 14 π-electron aromatic system of the thermally stable state is ring opened upon irradiation to give a less coloured form.

Finally, there are photoswitches with more complex mixed mechanisms,[119] which undergo ring-closing and opening reactions in conjuction with other isomerisation reactions, such as spiropyrans[120] and spiroxazines,[86] fulgides[121] and fulgimides,[122] and chromenes.[123]

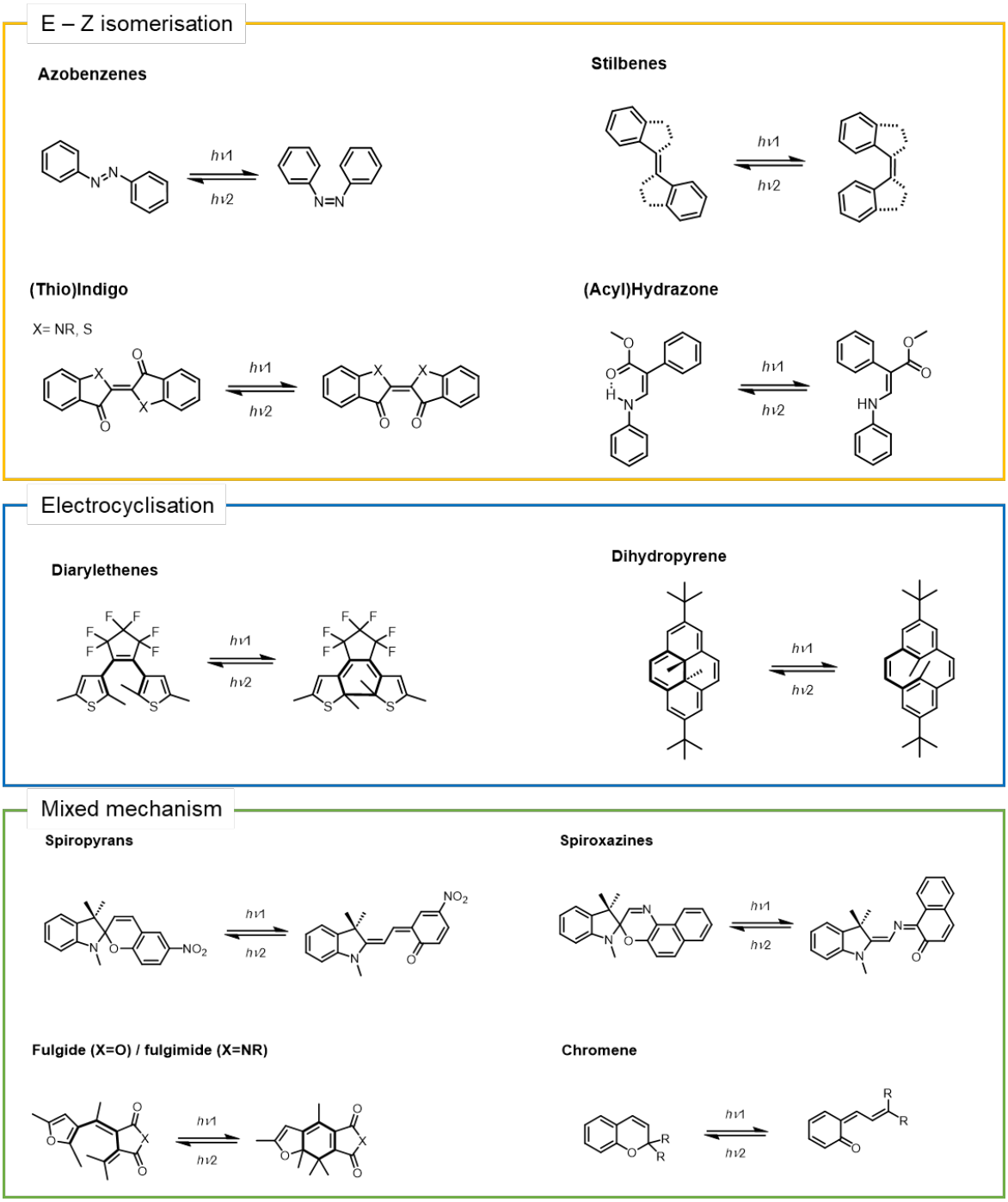


Figure 1.25: Different classes of photoswitches, grouped by photoisomerisation mechanism.

3.5 Dyes

There are a broad range of fluorescent dyes which are commercially available or readily synthesised in the laboratory. In general, the range of photoswitches is significantly more limited than fluorophores, and the demands on their performance greater for most RESOLFT designs. Therefore, designs usually start with the selection of the best photoswitch, followed by picking a suitable dye to match. There are a few main classes of fluorophore which are commonly employed in biological imaging (Figure 1.26).[124,125] These core scaffolds have often been extensively manipulated in order to improve upon their photophysical and chemical properties.

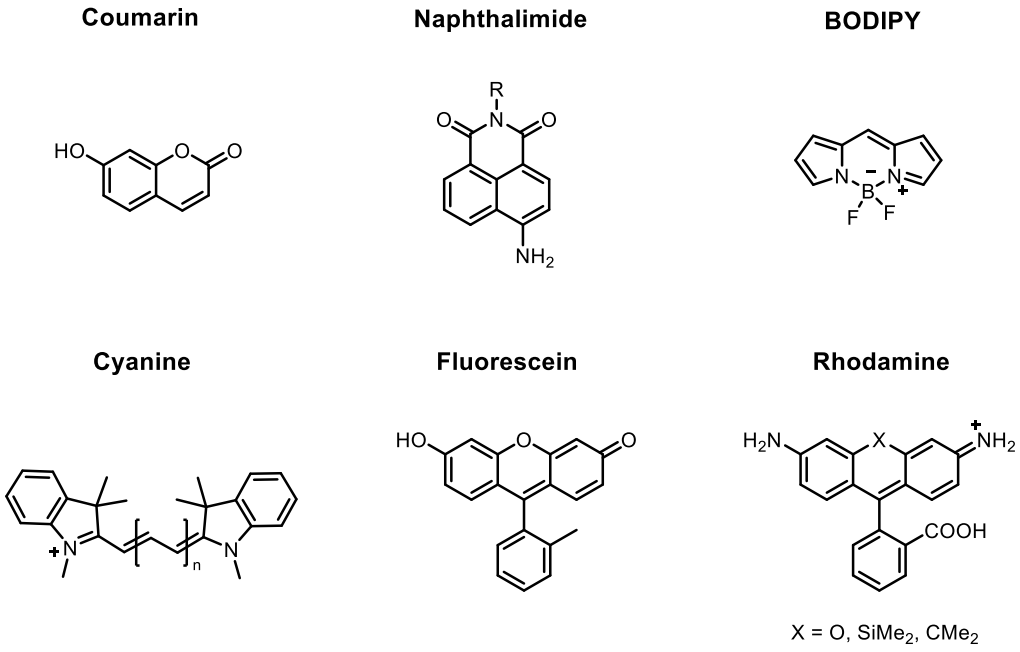


Figure 1.26: The core structures of some common classes of fluorescent dye

Coumarins, for example, are small, photostable, readily synthesised and fairly soluble.[126] They are generally quite blue-emitting dyes, and it takes significant structural modifications to extend their emission wavelengths into the red.[127] Naphthalimides are also bright and photostable, and offer synthetic flexibility with multiple points for the attachment of targeting or switching moieties. They are generally green-orange emitters, with no red/NIR emitters known.[128] BODIPY dyes have high

quantum yields and fairly red-shifted absorption and emission, however they are often non-trivial to synthesise.[129]

Cyanines have high extinction coefficients, and have easily shifted absorption and emission into the far red through extension of the conjugation by addition of further ethylene groups.[130] However, they tend to have lower quantum yields than other dyes, and they are difficult to functionalise asymmetrically. Fluorescein was first synthesised in 1871, and was one of the earliest applied immunofluorescence microscopy labels.[130] They are bright and synthetically modifiable dyes, however they have a strong pH dependence, and are most fluorescent above the pKa of the phenolic oxygen (~6.4).[131] While this has been exploited for the development of pH sensors, it can lead to non-uniform emission within different cellular environments.[d]

Finally, rhodamine derivatives are prevalent commercial dyes, featuring high extinction coefficients and high fluorescence quantum yields. Substitution of silicon or carbon for oxygen in the xanthene core has led to a variety of derivatives with emission in the red to near-IR,[132,133] and varying the substituents on the aniline groups to 4-membered azetidine rings inhibits excited state deactivation through twisting and improves brightness.[46]

One of the main design concerns guiding choice of dye in this thesis is the wavelength of emission, either to maximise FRET overlap (see Chapter 3), or minimise the chance of FRET (see Chapter 4). In both cases, red-emitting fluorophores were considered most advantageous for pairing with the studied photoswitches.

[d] Fluorescein was used in one of the first fluorescence sensing applications in 1877, when 10 kg of the dye was dumped in the river Danube to appear 60 hours later in the Rhine, proving the two rivers were linked by underground water systems.

4. Project aims

Based on the potential for small organic dyes to create useful tools for RESOLFT imaging, and the current limitations in the applications of RESOLFT, my broad project aim is to improve upon the properties of photoswitchable dyes to increase their applicability to RESOLFT imaging.

In Chapter 2, I investigate the feasibility of incorporating environmental sensing into a super-resolution RESOLFT dye, to develop a tool with the ability to report on the local polarity at resolution below the diffraction limit. The potential of this dyad is tested in synthetic vesicle membranes, as well as live cells.

In Chapter 3, I investigate a new FRET dyad based on the diazocine photoswitch and rhodamine B, in an attempt to improve on the fatigue observed in previous generations of dyads incorporating a spironaphthoxazine photoswitch. An investigation of the unexpected photophysical and photochemical properties is performed, allowing an improved model for dyad design to be developed.

In Chapter 4, I investigate dyads with a PET-quenching mechanism, in order to attempt to make a more generalisable design for RESOLFT switchable dyes. The first generation of investigated dyads show proof-of-concept quenching, and informed the second generation of more rigid dyad designs.

5. References

1. H. Gest, *Notes Rec. Roy. Soc.*, **2004**, *58*, 187.
2. A. C. Croce and G. Bottiroli, *Eur. J. Histochem.*, **2014**, *58,* 2461.
3. C. P. Toseland, *J. Chem. Bio.*, **2013**, *6*, 85.
4. H. Zhu, J. Fan, J. Du and X. Peng, *Acc. Chem. Res.*, **2016**, *49*, 2115.
5. D. Wu, A. C. Sedgwick, T. Gunnlaugsson, E. U. Akkaya, J. Yoon and T. D. James, *Chem. Soc. Rev.*, **2017**, *46*, 7105.
6. S. Wang, W. X. Ren, J.-T. Hou, M. Won, J. An, X. Chen, J. Shu and J. S. Kim, *Chem. Soc. Rev.*, **2021**, *50*, 8887.
7. A. Jablonski, *Nature*, **1933**, *131*, 839.
8. M. Kasha, *Discuss. Faraday Soc.*, **1950**, *9*, 14.
9. C. A. Combs and H. Shroff, *Curr. Protoc. Neurosci.*, **2017**, *79*, 2.1.1.
10. M. Minsky, *Scanning*, **1988**, *10*, 128.
11. J. Jonkman and C. M. Brown, *J. Biomol. Tech.*, **2015**, *26*, 54.
12. E. Abbe, *Archiv F. Mikrosk. Anatomie.,* **1873**, *9*, 413.
13. S. W. Hell, *Angew. Chem. Int. Ed.*, **2015**, *54*, 8054.
14. E. Betzig, *Angew. Chem. Int. Ed.*, **2015**, *54*, 8034.
15. W. E. Moerner, *Angew. Chem. Int. Ed.*, **2015**, *54*, 8067.
16. L. Schermelleh, A. Ferrand, T. Huser, C. Eggeling, M. Sauer, O. Biehlmaier and G. P. C. Drummen, *Nat. Cell Biol.*, **2019**, *21*, 72.
17. M. J. Rust, M. Bates and X. Zhuang, *Nat. Methods*, **2006**, *3*, 793.
18. E. Betzig, G. H. Patterson, R. Sougrat, O. W. Lindwasser, S. Olenych, J. S. Bonifacino, M. W. Davidson, J. Lippincott-Schwartz and H. F. Hess, *Science*, **2006**, *313*, 1642.
19. A. Sharonov and R. M. Hochstrasser, *P. Nat. Acad. Sci.*, **2006**, *103*, 18911.
20. M. Heilemann, S. Van De Linde, A. Mukherjee and M. Sauer, *Angew. Chem. Int. Ed.*, **2009**, *48*, 6903.
21. Y. Ma, K. Wen, M. Liu, J. Zheng, K. Chu, Z. J. Smith, L. Liu and P. Gao, *J. Phys. Photonics*, **2021**, *3*, 024009.
22. R. Heintzmann and T. Huser, *Chem. Rev.*, **2017**, *117*, 13890.
23. J. D. Manton, *Philos. T, R. Soc. A*, **2022**, *380*, 20210109.
24. G. Vicidomini, P. Bianchini and A. Diaspro, *Nat. Methods*, **2018**, *15*, 173.
25. H. Blom and J. Widengren, *Chem. Rev.*, **2017**, *117*, 7377.
26. T. Müller, C. Schumann and A. Kraegeloh, *ChemPhysChem*, **2012**, *13*, 1986.
27. H. Blom and J. Widengren, *Curr. Opin. Chem. Biol.*, **2014**, *20*, 127.
28. M. Hofmann, C. Eggeling, S. Jakobs and S. W. Hell, *P. Nat. Acad. Sci.* **2005**, *102*, 17565.
29. N. A. Jensen, I. Jansen, M. Kamper and S. Jakobs, *Nanoscale Photonic Imaging*, 1st Ed. T. Salditt, A. Egner and D. R. Luke, Springer International Publishing, **2020**.
30. S. Wäldchen, J. Lehmann, T. Klein, S. van de Linde and M. Sauer, *Sci. Rep.*, **2015**, *5*, 15348.
31. P. Dedecker, J.-i. Hotta, C. Flors, M. Sliwa, H. Uji-i, M. B. J. Roeffaers, R. Ando, H. Mizuno, A. Miyawaki and J. Hofkens, *J. Am. Chem. Soc.*, **2007**, *129*, 16132.
32. L. A. Masullo, A. Bodén, F. Pennacchietti, G. Coceano, M. Ratz and I. Testa, *Nat. Commun.*, **2018**, *9*, 3281.
33. J. Dreier, M. Castello, G. Coceano, R. Cáceres, J. Plastino, G. Vicidomini and I. Testa, *Nat. Commun.*, **2019**, *10*, 556.
34. A. Bodén, F. Pennacchietti, G. Coceano, M. Damenti, M. Ratz and I. Testa, *Nat. Biotech.*, **2021**, *39*, 609.
35. S. W. Hell, S. J. Sahl, M. Bates, X. Zhuang, R. Heintzmann, M. J. Booth, J. Bewersdorf, G. Shtengel, H. Hess and P. Tinnefeld, *J. Phys. D*, **2015**, *48*, 443001.
36. F. Balzarotti, Y. Eilers, K. C. Gwosch, A. H. Gynnå, V. Westphal, F. D. Stefani, J. Elf and S. W. Hell, *Science*, **2017**, *355*, 606.

37. M. Weber, M. Leutenegger, S. Stoldt, S. Jakobs, T. S. Mihaila, A. N. Butkevich and S. W. Hell, *Nat. Photonics*, **2021**, *15*, 361.
38. J. Xiao and T. Ha, *Science*, **2017**, *355*, 582.
39. K. C. Gwosch, J. K. Pape, F. Balzarotti, P. Hoess, J. Ellenberg, J. Ries and S. W. Hell, *Nat. Methods*, **2020**, *17*, 217.
40. M. Weber, H. von der Emde, M. Leutenegger, P. Gunkel, S. Sambandan, T. A. Khan, J. Keller-Findeisen, V. C. Cordes and S. W. Hell, *Nat. Biotech.*, **2022**, 10.1038/s41587-022-01519-4.
41. J. Alvelid and I. Testa, *Curr. Opin. Biomed. Eng.*, **2019**, *12*, 34.
42. T. J. Chozinski, L. A. Gagnon and J. C. Vaughan, *FEBS Lett.*, **2014**, *588*, 3603.
43. M. Lelek, M. T. Gyparaki, G. Beliu, F. Schueder, J. Griffié, S. Manley, R. Jungmann, M. Sauer, M. Lakadamyali and C. Zimmer, *Nat. Rev. Methods Primers*, **2021**, *1*, 39.
44. G. T. Dempsey, M. Bates, W. E. Kowtoniuk, D. R. Liu, R. Y. Tsien and X. Zhuang, *J. Am. Chem. Soc*, **2009**, *131*, 18192.
45. K. Kikuchi, L. D. Adair, J. Lin, E. J. New and A. Kaur, *Angew. Chem. Int. Ed.*, **2023**, *62*, e202204745.
46. J. B. Grimm, B. P. English, J. Chen, J. P. Slaughter, Z. Zhang, A. Revyakin, R. Patel, J. J. Macklin, D. Normanno, R. H. Singer, T. Lionnet and L. D. Lavis, *Nat Methods*, **2015**, *12*, 244.
47. J. B. Grimm, B. P. English, H. Choi, A. K. Muthusamy, B. P. Mehl, P. Dong, T. A. Brown, J. Lippincott-Schwartz, Z. Liu, T. Lionnet and L. D. Lavis, *Nat. Methods*, **2016**, *13*, 985.
48. H. Li and J. C. Vaughan, *Chem. Rev.*, **2018**, *118*, 9412.
49. G. T. Dempsey, J. C. Vaughan, K. H. Chen, M. Bates and X. Zhuang, *Nat. Methods*, **2011**, *8*, 1027.
50. S.-n. Uno, M. Kamiya, T. Yoshihara, K. Sugawara, K. Okabe, M. C. Tarhan, H. Fujita, T. Funatsu, Y. Okada, S. Tobita and Y. Urano, *Nat. Chem.*, **2014**, *6*, 681.
51. N. Lardon, L. Wang, A. Tschanz, P. Hoess, M. Tran, E. D'Este, J. Ries and K. Johnsson, *J. Am. Chem. Soc*, **2021**, *143*, 14592.
52. H. Fujioka, S.-n. Uno, M. Kamiya, R. Kojima, K. Johnsson and Y. Urano, *Chem. Commun.*, **2020**, *56*, 5617.
53. K. Miki, K. Kojima, K. Oride, H. Harada, A. Morinibu and K. Ohe, *Chem. Commun.*, **2017**, *53*, 7792.
54. A. Morozumi, M. Kamiya, S.-n. Uno, K. Umezawa, R. Kojima, T. Yoshihara, S. Tobita and Y. Urano, *J. Am. Chem. Soc*, **2020**, *142*, 9625.
55. D. I. Danylchuk, S. Moon, K. Xu and A. S. Klymchenko, *Angew. Chem. Int. Ed.*, **2019**, *58*, 14920.
56. G. Giannone, E. Hosy, F. Levet, A. Constals, K. Schulze, Alexander I. Sobolevsky, M. P. Rosconi, E. Gouaux, R. Tampé, D. Choquet and L. Cognet, *Biophys. J.*, **2010**, *99*, 1303.
57. R. Jungmann, C. Steinhauer, M. Scheible, A. Kuzyk, P. Tinnefeld and F. C. Simmel, *Nano Lett.*, **2010**, *10*, 4756.
58. J. Schnitzbauer, M. T. Strauss, T. Schlichthaerle, F. Schueder and R. Jungmann, *Nat. Protocols*, **2017**, *12*, 1198.
59. J. Tam and D. Merino, *J. Neurochem.,* **2015**, *135*, 643.
60. A. Stockhammer and F. Bottanelli, *J. Phys. D*, **2020**, *54*, 033001.
61. J. Woodhouse, G. Nass Kovacs, N. Coquelle, L. M. Uriarte, V. Adam, T. R. M. Barends, M. Byrdin, E. de la Mora, R. Bruce Doak, M. Feliks, M. Field, F. Fieschi, V. Guillon, S. Jakobs, Y. Joti, P. Macheboeuf, K. Motomura, K. Nass, S. Owada, C. M. Roome, C. Ruckebusch, G. Schirò, R. L. Shoeman, M. Thepaut, T. Togashi, K. Tono, M. Yabashi, M. Cammarata, L. Foucar, D. Bourgeois, M. Sliwa, J.-P. Colletier, I. Schlichting and M. Weik, *Nat. Commun.*, **2020**, *11*, 741.
62. V. Adam, K. Hadjidemetriou, N. Jensen, R. L. Shoeman, J. Woodhouse, A. Aquila, A.-S. Banneville, T. R. M. Barends, V. Bezchastnov, S. Boutet, M. Byrdin, M. Cammarata, S. Carbajo, N. Eleni Christou, N. Coquelle, E. De la Mora, M. El Khatib, T. Moreno Chicano, R.

Bruce Doak, F. Fieschi, L. Foucar, O. Glushonkov, A. Gorel, M. L. Grünbein, M. Hilpert, M. Hunter, M. Kloos, J. E. Koglin, T. J. Lane, M. Liang, A. Mantovanelli, K. Nass, G. Nass Kovacs, S. Owada, C. M. Roome, G. Schirò, M. Seaberg, M. Stricker, M. Thépaut, K. Tono, K. Ueda, L. M. Uriarte, D. You, N. Zala, T. Domratcheva, S. Jakobs, M. Sliwa, I. Schlichting, J.-P. Colletier, D. Bourgeois and M. Weik, *ChemPhysChem*, **2022**, *23*, e202200192.

63. T. Grotjohann, I. Testa, M. Leutenegger, H. Bock, N. T. Urban, F. Lavoie-Cardinal, K. I. Willig, C. Eggeling, S. Jakobs and S. W. Hell, *Nature*, **2011**, *478*, 204.
64. T. Grotjohann, I. Testa, M. Reuss, T. Brakemann, C. Eggeling, S. W. Hell and S. Jakobs, *eLife*, **2012**, *1*, e00248.
65. C. Gregor, S. C. Sidenstein, M. Andresen, S. J. Sahl, J. G. Danzl and S. W. Hell, *Sci. Rep.*, **2018**, *8*, 2724.
66. T. Konen, D. Stumpf, T. Grotjohann, I. Jansen, M. Bossi, M. Weber, N. Jensen, S. W. Hell and S. Jakobs, *ACS Nano*, **2021**, *15*, 9509.
67. F. Lavoie-Cardinal, N. A. Jensen, V. Westphal, A. C. Stiel, A. Chmyrov, J. Bierwagen, I. Testa, S. Jakobs and S. W. Hell, *ChemPhysChem*, **2014**, *15*, 655.
68. F. Pennacchietti, E. O. Serebrovskaya, A. R. Faro, I. I. Shemyakina, N. G. Bozhanova, A. A. Kotlobay, N. G. Gurskaya, A. Bodén, J. Dreier, D. M. Chudakov, K. A. Lukyanov, V. V. Verkhusha, A. S. Mishin and I. Testa, *Nat. Methods*, **2018**, *15*, 601.
69. I. Testa, E. D'Este, N. T. Urban, F. Balzarotti and S. W. Hell, *Nano Letters*, **2015**, *15*, 103.
70. A. Royant and M. Noirclerc-Savoye, *J. Struct. Biol.*, **2011**, *174*, 385.
71. B. Roubinet, M. L. Bossi, P. Alt, M. Leutenegger, H. Shojaei, S. Schnorrenberg, S. Nizamov, M. Irie, V. N. Belov and S. W. Hell, *Angew. Chem. Int. Ed.*, **2016**, *55*, 15429.
72. K. Uno, M. L. Bossi, T. Konen, V. N. Belov, M. Irie and S. W. Hell, *Adv. Opt. Mat.*, **2019**, *7*, 1801746.
73. O. Nevskyi, D. Sysoiev, J. Dreier, S. C. Stein, A. Oppermann, F. Lemken, T. Janke, J. Enderlein, I. Testa, T. Huhn and D. Wöll, *Small*, **2018**, *14*, 1703333.
74. K. Uno, M. L. Bossi, M. Irie, V. N. Belov and S. W. Hell, *J. Am. Chem. Soc*, **2019**, *141*, 16471.
75. I. Yildiz, E. Deniz and F. M. Raymo, *Chem. Soc. Rev.*, **2009**, *38*, 1859.
76. F. M. Raymo and M. Tomasulo, *J. Phys. Chem. A*, **2005**, *109*, 7343.
77. M. Bossi, V. Belov, S. Polyakova and S. W. Hell, *Angew. Chem. Int. Ed.*, **2006**, *45*, 7462.
78. J. Fölling, S. Polyakova, V. Belov, A. van Blaaderen, M. L. Bossi and S. W. Hell, *Small*, **2008**, *4*, 134.
79. M. Bossi, J. Fölling, M. Dyba, V. Westphal and S. W. Hell, *New J. Phys.*, **2006**, *8*, 275.
80. J. Kwon, J. Hwang, J. Park, G. R. Han, K. Y. Han and S. K. Kim, *Sci. Rep.*, **2015**, *5*, 17804.
81. T. Fukaminato, T. Doi, N. Tamaoki, K. Okuno, Y. Ishibashi, H. Miyasaka and M. Irie, *J. Am. Chem. Soc*, **2011**, *133*, 4984.
82. C. Li, H. Yan, L.-X. Zhao, G.-F. Zhang, Z. Hu, Z.-L. Huang and M.-Q. Zhu, *Nat. Commun.*, **2014**, *5*, 5709.
83. J.-X. Liu, B. Xin, C. Li, N.-H. Xie, W.-L. Gong, Z.-L. Huang and M.-Q. Zhu, *ACS Appl. Mat. & Interfaces*, **2017**, *9*, 10338.
84. C. Li, Z. Hu, M. P. Aldred, L.-X. Zhao, H. Yan, G.-F. Zhang, Z.-L. Huang, A. D. Q. Li and M.-Q. Zhu, *Macromolecules*, **2014**, *47*, 8594.
85. Y. Xiong, P. Rivera-Fuentes, E. Sezgin, A. Vargas Jentzsch, C. Eggeling and H. L. Anderson, *Org. Lett.*, **2016**, *18*, 3666.
86. Y. Xiong, A. Vargas Jentzsch, Johannes W. M. Osterrieth, E. Sezgin, I. V. Sazanovich, K. Reglinski, S. Galiani, A. W. Parker, C. Eggeling and H. L. Anderson, *Chem. Sci.*, **2018**, *9*, 3029.
87. A. T. Frawley, V. Wycisk, Y. Xiong, S. Galiani, E. Sezgin, I. Urbančič, A. Vargas Jentzsch, K. G. Leslie, C. Eggeling and H. L. Anderson, *Chem. Sci.*, **2020**, *11*, 8955.
88. S. W. Hell, *NanoBiotech.*, **2005**, *1*, 296.
89. J. R. Lakowicz, *Principles of fluorescence spectroscopy*, Springer Science & Business Media, **2013**.

90. L. Yuan, W. Lin, K. Zheng and S. Zhu, *Acc. Chem. Res.*, **2013**, *46*, 1462.
91. W. R. Algar, N. Hildebrandt, S. S. Vogel and I. L. Medintz, *Nat. Methods*, **2019**, *16*, 815.
92. B. Hellenkamp, S. Schmid, O. Doroshenko, O. Opanasyuk, R. Kühnemuth, S. Rezaei Adariani, B. Ambrose, M. Aznauryan, A. Barth, V. Birkedal, M. E. Bowen, H. Chen, T. Cordes, T. Eilert, C. Fijen, C. Gebhardt, M. Götz, G. Gouridis, E. Gratton, T. Ha, P. Hao, C. A. Hanke, A. Hartmann, J. Hendrix, L. L. Hildebrandt, V. Hirschfeld, J. Hohlbein, B. Hua, C. G. Hübner, E. Kallis, A. N. Kapanidis, J.-Y. Kim, G. Krainer, D. C. Lamb, N. K. Lee, E. A. Lemke, B. Levesque, M. Levitus, J. J. McCann, N. Naredi-Rainer, D. Nettels, T. Ngo, R. Qiu, N. C. Robb, C. Röcker, H. Sanabria, M. Schlierf, T. Schröder, B. Schuler, H. Seidel, L. Streit, J. Thurn, P. Tinnefeld, S. Tyagi, N. Vandenberk, A. M. Vera, K. R. Weninger, B. Wünsch, I. S. Yanez-Orozco, J. Michaelis, C. A. M. Seidel, T. D. Craggs and T. Hugel, *Nat. Methods*, **2018**, *15*, 669.
93. M. G. Neumann, I. A. Pastre and C. M. Previtali, *J Photochem. Photobiol. A*, **1991**, *61*, 91.
94. A. Zaykov, P. Felkel, E. A. Buchanan, M. Jovanovic, R. W. A. Havenith, R. K. Kathir, R. Broer, Z. Havlas and J. Michl, *J. Am. Chem. Soc*, **2019**, *141*, 17729.
95. M. Kuss-Petermann and O. S. Wenger, *Phys. Chem. Chem. Phys.*, **2016**, *18*, 18657.
96. A. Weller, *Pure Applied Chem.*, **1968**, *16*, 115.
97. O. O'Mari and V. I. Vullev, *Curr. Opin. Electrochem.*, **2022**, *31*, 100862.
98. A. Goulet-Hanssens, M. Utecht, D. Mutruc, E. Titov, J. Schwarz, L. Grubert, D. Bléger, P. Saalfrank and S. Hecht, *J. Am. Chem. Soc*, **2017**, *139*, 335.
99. N. Elgrishi, K. J. Rountree, B. D. McCarthy, E. S. Rountree, T. T. Eisenhart and J. L. Dempsey, *J. Chem. Ed.*, **2018**, *95*, 197.
100. T. Koopmans, *Physica*, **1934**, *1*, 104.
101. Lindsay E. Roy, Elena Jakubikova and E. R. Batista, Accurate Calculation of Redox Potentials Using Density Functional Methods, https://www.lanl.gov/orgs/adtsc/publications/science_highlights_2009/3roy.pdf, (accessed May 20th, 2020).
102. M. Isegawa, F. Neese and D. A. Pantazis, *J. Chem. Theory Comp.*, **2016**, *12*, 2272.
103. R. Berera, R. van Grondelle and J. T. M. Kennis, *Photosynthesis Research*, **2009**, *101*, 105.
104. A. Stolow, A. E. Bragg and D. M. Neumark, *Chem. Rev.*, **2004**, *104*, 1719.
105. C. Ruckebusch, M. Sliwa, P. Pernot, A. de Juan and R. Tauler, *J. Photochem. Photobiol. C*, **2012**, *13*, 1.
106. A. P. de Silva, T. S. Moody and G. D. Wright, *Analyst*, **2009**, *134*, 2385.
107. B. Daly, J. Ling and A. P. de Silva, *Chem. Soc. Rev.*, **2015**, *44*, 4203.
108. A. Goulet-Hanssens, F. Eisenreich and S. Hecht, *Adv. Mater.*, **2020**, 32, 1905966.
109. Z. L. Pianowski, *Chem. Eur. J.*, **2019**, *25*, 5128.
110. H. M. D. Bandara and S. C. Burdette, *Chem. Soc. Rev.*, **2012**, *41*, 1809.
111. S. Crespi, N. A. Simeth and B. König, *Nat. Rev. Chem.*, **2019**, *3*, 133.
112. D. Villarón and S. J. Wezenberg, *Angew. Chem. Int. Ed.*, **2020**, *59*, 13192.
113. C. Petermayer and H. Dube, *Acc. Chem. Res.*, **2018**, *51*, 1153.
114. X. Su and I. Aprahamian, *Chem. Soc. Rev.*, **2014**, *43*, 1963.
115. L. A. Tatum, X. Su and I. Aprahamian, *Acc. Chem. Res.*, **2014**, *47*, 2141.
116. M. Irie, *Chem. Rev.*, **2000**, *100*, 1685.
117. M. Irie, T. Fukaminato, K. Matsuda and S. Kobatake, *Chem. Rev.*, **2014**, *114*, 12174.
118. K. Klaue, W. Han, P. Liesfeld, F. Berger, Y. Garmshausen and S. Hecht, *J. Am. Chem. Soc*, **2020**, *142*, 11857.
119. J. Volarić, W. Szymanski, N. A. Simeth and B. L. Feringa, *Chem. Soc. Rev.*, **2021**, *50*, 12377.
120. L. Kortekaas and W. R. Browne, *Chem. Soc. Rev.*, **2019**, *48*, 3406.
121. F. Renth, R. Siewertsen and F. Temps, *International Rev. Phys. Chem.*, **2013**, *32*, 1.
122. R. Matsushima and H. Sakaguchi, *J. Photochem. Photobiol. A*, **1997**, *108*, 239.
123. H. Durr and H. Bouas-Laurent, *Photochromism: molecules and systems*, Elsevier, **2003**.
124. L. D. Lavis and R. T. Raines, *ACS Chem. Biol.*, **2008**, *3*, 142.

125. L. D. Lavis and R. T. Raines, *ACS Chem. Biol*, **2014**, *9*, 855.
126. D. Cao, Z. Liu, P. Verwilst, S. Koo, P. Jangjili, J. S. Kim and W. Lin, *Chem. Rev.*, **2019**, *119*, 10403.
127. S. S. Matikonda, J. Ivanic, M. Gomez, G. Hammersley and M. J. Schnermann, *Chem. Sci.*, **2020**, *11*, 7302.
128. K. G. Leslie, D. Jacquemin, E. J. New and K. A. Jolliffe, *Chem. Eur. J.*, **2018**, *24*, 5569.
129. A. Loudet and K. Burgess, *Chem. Rev.*, **2007**, *107*, 4891.
130. J. B. Grimm, L. M. Heckman and L. D. Lavis, *Prog. Mol. Biol. Translational Sci.*, C. M. May, Academic Press, **2013**.
131. L. D. Lavis, T. J. Rutkoski and R. T. Raines, *Anal. Chem.*, **2007**, *79*, 6775.
132. Y. Kushida, T. Nagano and K. Hanaoka, *Analyst*, **2015**, *140*, 685.
133. J. B. Grimm, A. J. Sung, W. R. Legant, P. Hulamm, S. M. Matlosz, E. Betzig and L. D. Lavis, *ACS Chem. Biol.*, **2013**, *8*, 1303.

Chapter 2

A Nile Red dyad for polarity sensing below the diffraction limit

1. Introduction

1.1 Sensing and Super-resolution

There have been countless environmental fluorescent sensors developed for biological imaging,[1] reporting on the presence of reactive oxygen species,[2,3] metal ions,[4,5] and oxygen levels,[6] as well as pH,[7] viscosity,[8] and polarity[9] in cells and tissue. These environmental parameters are of interest as they often play important roles in cellular function, with specific cellular organelles varying significantly in their microenvironment.[10] The malfunction of these tightly-controlled parameters is often a hallmark of disease, and they have been associated with pathophysiological processes such as tumorigenesis and inflammation, well before clinical symptoms emerge.[11]

Despite the advance in super-resolution microscopy techniques, environmental fluorescent sensors are largely designed for confocal microscopy, and the challenge of combining quantitative cellular sensing with super-resolution remains a nascent field. The information provided by improved super-resolution methods is largely structural,[12] allowing insight into the location, stoichiometry and movement of cellular proteins and structures. For example, the application of STED using Cep164-labelled centrioles allows the identification of the 9-fold circular arrangement of centriole proteins (Figure 2.1).[13]

In contrast, there have been few advances in probing microenvironmental variation below the diffraction limit, due to a lack of chemical tools with which to do so. The design requirements for fluorescent sensors that can be used in super-resolution microscopy are complex and multimodal. As well as fulfilling the usual requirements for a biological imaging agent (bright, photostable, non-toxic, visible light excitation, soluble) they must also meet the demands for super-resolution, which involve molecular switching between dark 'off' and bright 'on' states, and the demands for sensors, which require a change in fluorescent output dependent upon their interaction with their environment.

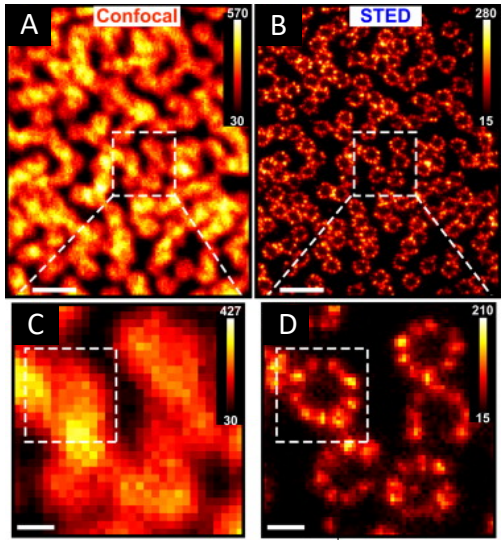


Figure 2.1: Confocal (A) and STED (B) images of Cep164 antibody-labelled centrioles, with closer views of dashed boxes in (C) and (D) respectively. It is possible to identify the 9-fold symmetry and circular arrangement of the proteins in the STED image (d). Reproduced with permission from Elsevier.[13]

Fluorescent sensors often report on analyte presence by changes in fluorescence intensity or excited state lifetime, which could be obfuscated as a read-out by the need for dyes to switch between bright and dark states as required in STORM, STED, and RESOLFT techniques. Fluorescent sensors that change their emission wavelength in response to their environment are better suited to super-resolution, as this output is separate to on-off switching, although even this mechanism could be problematic for techniques such as STED, as the quenching efficiency of the switch-off laser depends on the emission wavelength.[14]

Some recent examples of super-resolution fluorescent sensors include a Zn^{2+} sensor for multi-organelle zinc tracking,[15] and a mitochondrial glutathione probe.[16] Both of these probes have been applied to structured illumination microscopy (SIM – outlined in Introduction Section 1.5.1), which has the advantage of being compatible with fluorophores designed for confocal microscopy, without requiring synthetic design adjustments. Although SIM has limited resolution enhancement compared to other techniques, it can give resolution on the scale of many organelles of interest -

for example lysosomes (100-1200 nm), mitochondria (500-5000 nm) and autophagosomes (150-1500 nm).[15]

A reaction-based turn-on probe that labels nitroreductase enzymes has been described for live-cell STORM imaging, which reports on the distribution of nitroreductase enzymes in the mitrochondria (Figure 2.2A). The probe can achieve resolutions around 63 nm, but once it is reacted, it cannot turn off again, and therefore it cannot report on dynamic changes.[17]

Additionally, there have been a few examples of protein-based sensing systems, including a protein-dye fusion which acts as a ratiometric endosome pH sensor for STED (Figure 2.2B).[18] This sensor combines an intensity-based pH-sensitive fluorescent protein covalently linked to an Abberior STAR fluorophore which has emission properties optimised for STED. As the STAR dye is less sensitive to pH changes, it was bright enough to be used to image clusters of endosomes below the diffraction limit, and the change in emission ratio between the two fluorescent components reported on the local pH. This ratiometric design requires more synthetic effort, however it overcomes some limitations of single dye systems, such as the turn-on, reversible H_2O_2-sensing fluorescent protein HyPer2 which has been applied to STED.[19] It shows a 3-fold resolution enhancement compared to confocal images and was used to identify microdomains of peroxide concentration 100-200 nm in size, however the signal-to-noise ratio and therefore the STED resolution is correlated to the brightness of the dye, and at low concentrations of analyte this means the resolution is detrimentally affected.

Finally, the first example of a reversibly switchable fluorescent protein being used for sensing in RESOLFT was reported in 2022 by Steil and coworkers.[20] The probe was developed by combining a photoswitchable fluorescent protein with a calcium sensing domain, and performing mutations to arrive at derivatives that only photoswitch when bound to Ca^{2+}, and otherwise remain in a dark state (Figure 2.2C). This probe was somewhat hampered by low brightness, however further

mutation cycles were shown to improve properties and the concept could be broadly applied to proteins for different analytes, such as maltose and dopamine.

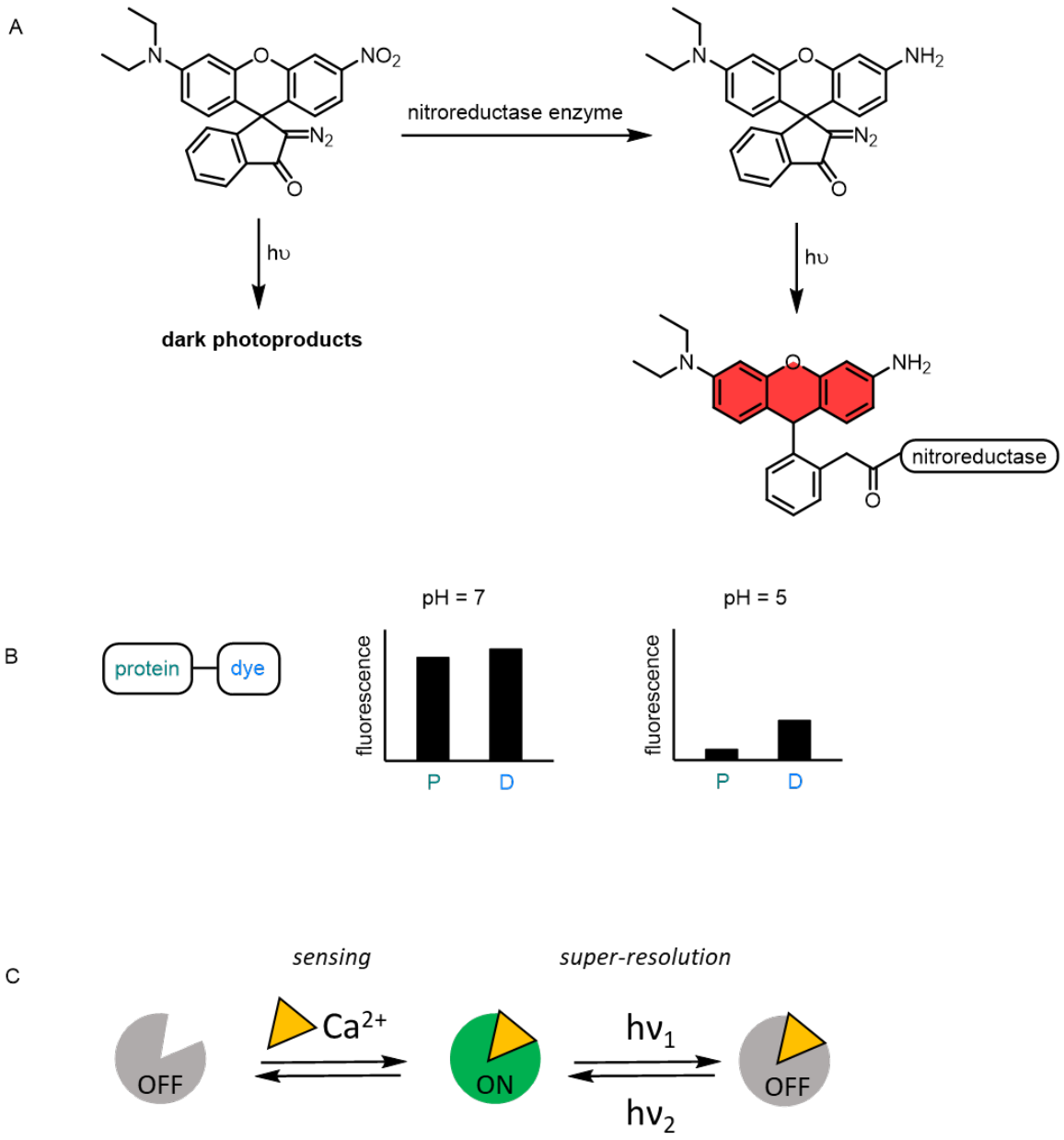


Figure 2.2: Examples of dyes for super-resolution fluorescence imaging incorporating a sensing element.

These examples of fluorescent sensors for super-resolution all take very different approaches to making tools for their respective microscopies, with various advantages and disadvantages. Combining environmental sensing with live-cell super-resolution imaging remains a challenge for chemists designing small-molecule tools to aid the investigation of biological systems, in particular

for RESOLFT. RESOLFT microscopy is well-suited to live-cell imaging, as it does not require the addition of exogenous buffers or complex post-acquisition processing, and uses lower laser powers than the analogous depletion laser in stimulated emission (STED) techniques.[12] It is therefore desirable to develop small-molecule dyes for RESOLFT that incorporate environmental sensing capabilities, as well as fluorescence switching.

1.2 Nile Red Polarity Sensing

The FRET dyads previously developed by our group (Figure 2.3A) switch between a bright 'on' and a dark 'off' state for use with RESOLFT donut lasers.[21] The dyad is comprised of a fluorophore covalently tethered to a spironaphthoxazine photoswitch,[22] which can be isomerised with 405 nm light into a conjugated, broadly-absorbing coloured form (Figure 2.3B) that turns the dyad 'off' by FRET quenching. In the reverse direction, the photoswitch can be closed to its colourless form thermally or with red light, turning the fluorescent dye back 'on'.

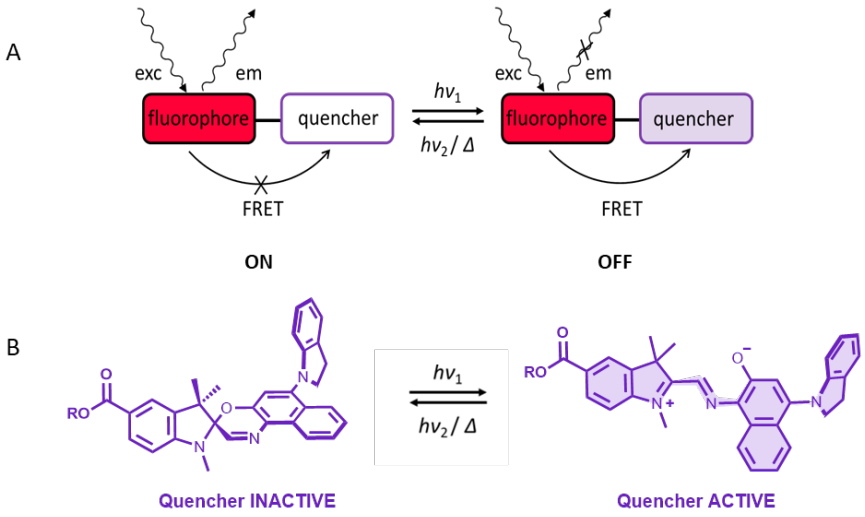


Figure 2.3: (A) Schematic diagram of a photoswitchable FRET dyad where a fluorophore is covalently linked to a reversibly switchable quencher. (B) The structures of the closed inactive and open quenching forms of the spironaphthoxazine photoswitch.

We sought to build upon this design by incorporating a polarity-sensitive Nile Red dye as the fluorescent reporter, combining RESOLFT super-resolution capability with environmental polarity sensing in **NR-dyad** (Figure 2.4A). We calculated that the dyad would have a high level of FRET efficiency (98.5%), based on the high spectral overlap between Nile Red emission and the photoswitch absorption (Figure 2.4B), leading to a FRET distance of over 45 Å in acetonitrile. In the fully-extended conformation of the molecule, the distance of the Nile Red dye from the spironaphthoxazine switch is 21.6 Å, therefore we can expect highly efficient FRET-quenching.

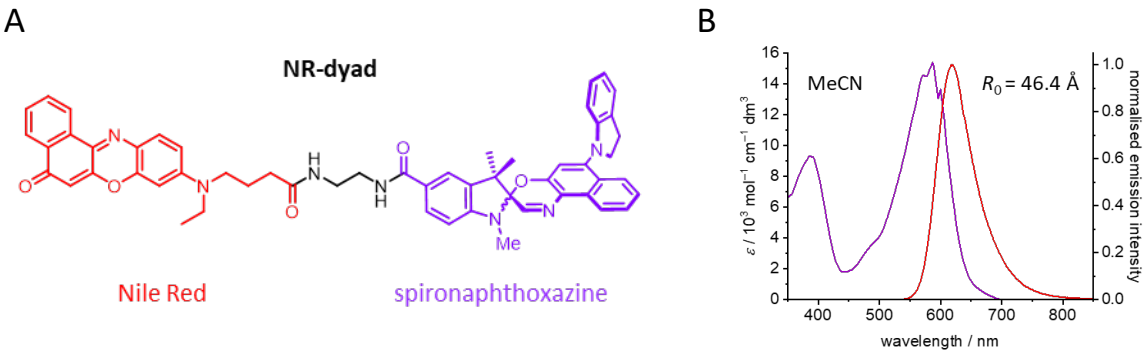


Figure 2.4: (A) Structure of the Nile Red-spironaphthoxazine dyad **NR-Dyad**, and (B) the spectral overlap between the fluorophore donor emission (red) and switch acceptor absorption (purple) in acetonitrile (298 K).

Nile Red has been used extensively to report on lipid packing in biological membranes through the solvatochromism of its emission.[9,23-29] It has been previously applied in PAINT,[30,31] STORM,[32] and STED[33] super-resolution microscopy techniques, but never in RESOLFT. The Nile Red dye was first used in spectrally-resolved PAINT (sPAINT) by Lee and co-workers in 2016,[31] and in spectrally-resolved STORM (SR-STORM) by Xu and co-workers in 2017,[32] in cellular plasma membranes. This proof of concept was extended in work by Klymchenko and co-workers in 2019,[30] where Nile Red was chemically modified to improve its switching properties. Derivatives NR4A and NR12A (Figure 2.5A) were synthesised with anionic sulfonate groups to improve plasma membrane localisation and reduce diffusion into internal organelle membranes. They were also functionalised with alkyl chains of varying lengths in order to modulate the affinity for the membrane. The reversible binding of the dyes in exchange with the bulk aqueous medium leads to on/off switching as Nile Red is

effectively quenched in aqueous environments[34] compared to in the non-polar membrane environment (Figure 2.5B). They found NR4A to have the right properties for reversible membrane binding, leading to an on/off blinking rate suitable for PAINT microscopy. This same molecule was later applied by Eggeling and co-workers to STED,[33] where the reversible binding reduced the photobleaching rate that is often a downside to high-energy STED imaging. In these later papers, polarity was analysed as a ratio between two emission detection windows, rather than through spectral imaging.[30,33]

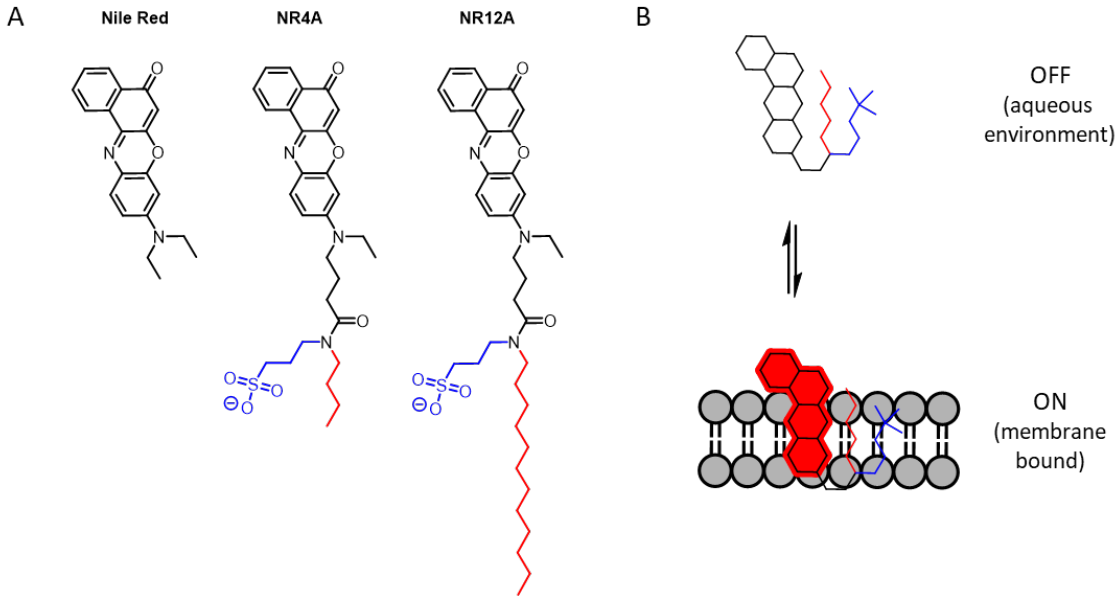


Figure 2.5: (A) The structures of Nile Red and modified analogues NR4A and NR12A. (B) Reversible binding to the membrane induces on/off emission switching in Nile Red.

The solvatochromism of Nile Red that underpins its environmental sensing capability is common among donor-π-acceptor systems, and occurs as a result of the internal charge transfer in the excited state, leading to the formation of a large dipole (Figure 2.6).[35] This dipole is stabilised by surrounding solvent molecules; the stabilisation is greater in more polar media, lowering the excited state energy and causing a red-shift of the resulting emission. In contrast, less-stabilising, non-polar solvents result in higher energy (shorter wavelength) emission. By spectrally separating emitted photons to collect the emission from the dye in shorter (blue) and longer (red) wavelength

channels, the ratio between the two can be calculated, with the output value giving a measurement of the local environment polarity.

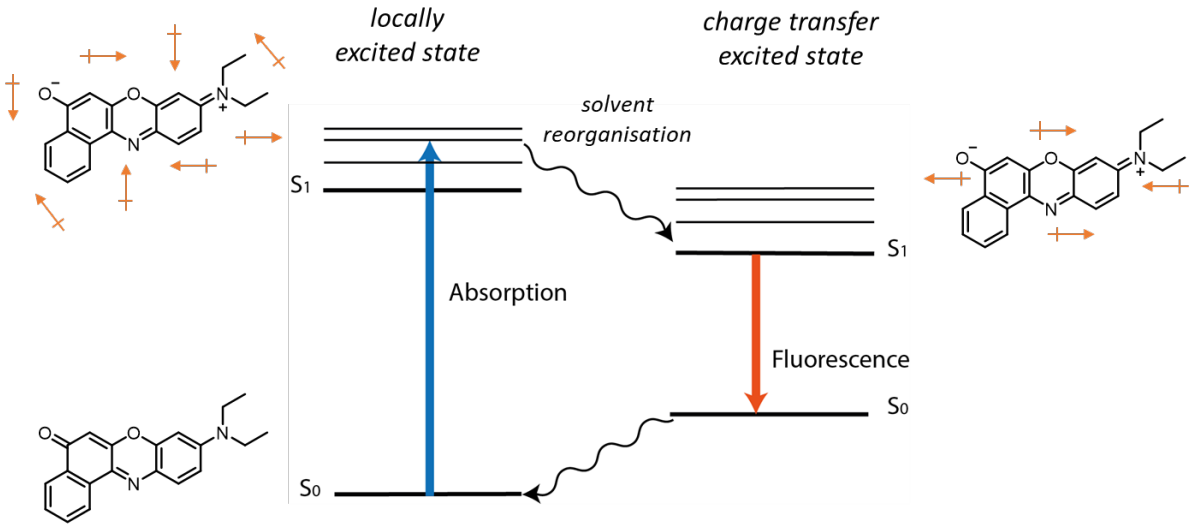


Figure 2.6: Nile Red undergoes an internal charge transfer in the excited state leading to an increase in the dipole. Stabilisation by surrounding molecules lowers the energy of fluorescence emission. The polarity of the environment determines the extent of this stabilisation, leading to a change in emission wavelengths.

Biological membranes are dynamic and heterogenous environments, with areas of distinct lipid compositions[36] that participate in many processes such as membrane signalling[37-40] and host-pathogen interactions.[41-43] Different compositions of lipids, cholesterol, and proteins give more or less ordered membranes, which directly correlates to the amount of water at the bilayer interface, and therefore the environment polarity.[44-47] The rigid fused ring system of cholesterol limits phosopholipid movement and leads to less fluid and less water-permeable membranes at physiological temperatures (Figure 2.7).

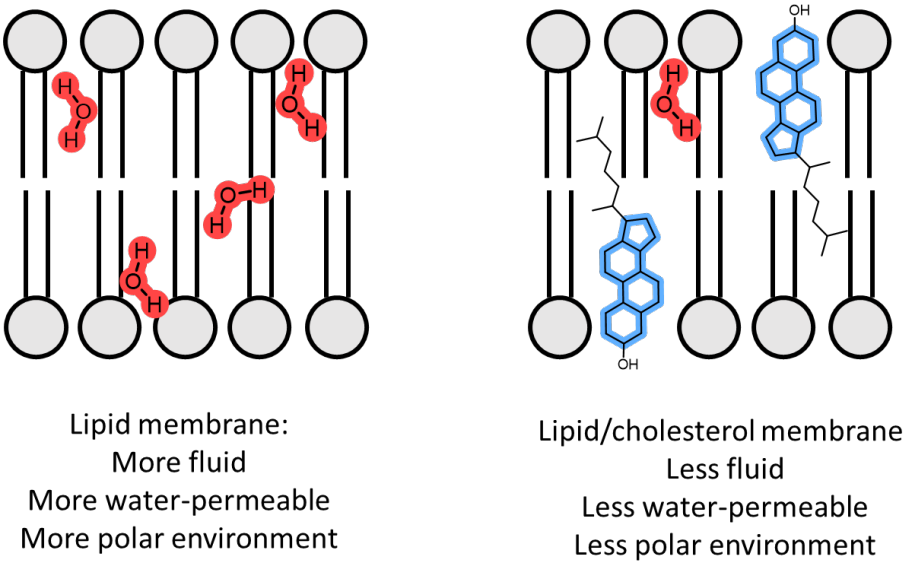


Figure 2.7: Schematic of different membrane compositions and their characteristics.

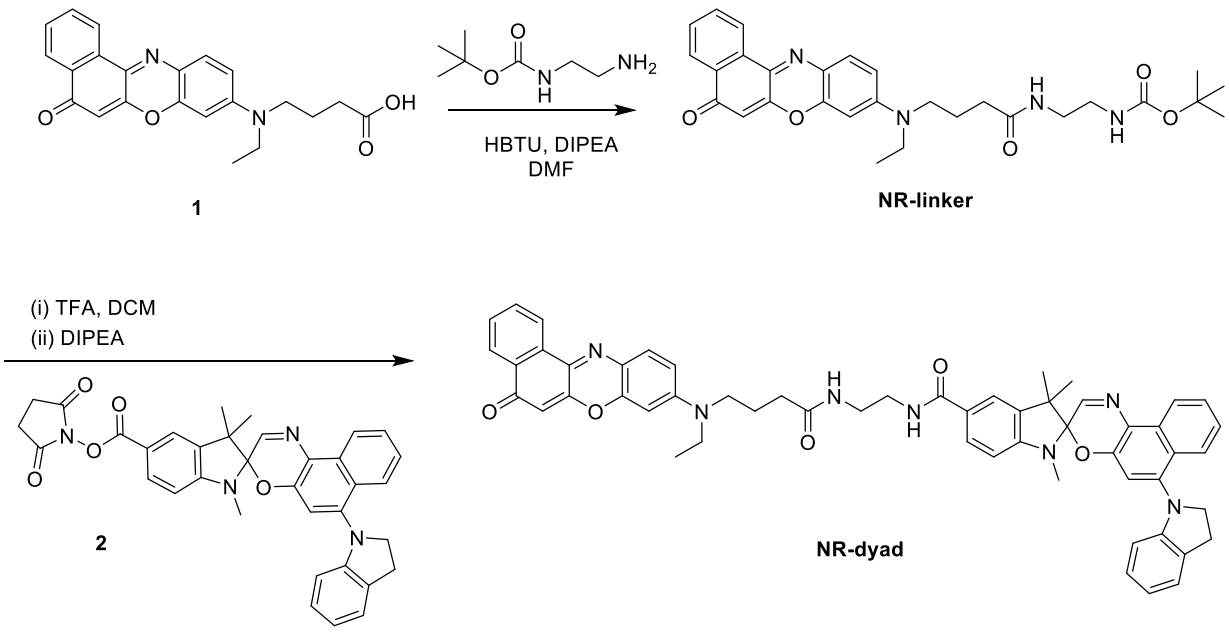
By recording the RESOLFT diffraction-unlimited emission of **NR-dyad** in two separate spectral windows, we envisaged the dyad could act as a super-resolution ratiometric probe for membrane ordering, a tool which has previously been unrealised for RESOLFT microscopy.

2. Results and Discussion

2.1 Synthesis and photophysical characterisation

NR-Dyad was synthesised by my colleague Dr Virginia Wycisk. I carried out all the microscopy experiments and analysis discussed here in collaboration with Dr Andrew Frawley. Absorption and emission spectra, and photophysical properties were recorded by Dr Andrew Frawley. Preparation of GPMVs and cell lines for imaging was done by Dr Dilip Shrestha. I carried out the automated image analysis and script writing, electrochemical measurements and DFT redox calculations independently. This work has been published.[48]

NR-Dyad was synthesised from precursor and control molecule **NR-linker** (Scheme 2.1). Nile Red derivative **1,** was synthesised according to literature procedure which allowed functionalisation through the aniline.[30] Amide coupling with Boc-ethylenediame gave **NR-linker**. A Boc deprotection followed by coupling with an NHS-ester functionalised spiroxazine photoswitch **2** (described previously)[21] gave **NR-dyad**.



Scheme 2.1: The synthesis of **NR-Dyad** from precursor **NR-linker**.

The photophysical properties of **NR-Dyad** were measured in a variety of solvents (Figure 2.8), and compared to the precursor compound **NR-linker**, demonstrating that addition of the spironaphthoxazine photoswitch does not affect the solvatochromism of the fluorophore. In the absorption spectrum, it is evident that the non-quenching form of the switch (absorption around 390 nm) does not display any solvatochromism. The photophysical properties of both **NR-linker** and **NR-dyad**, including the molar extinction coefficients, the fluorescence quantum yields, and the fluorescence lifetimes are shown in Table 2.1. The values for **NR-dyad** are for the closed state of the switch.

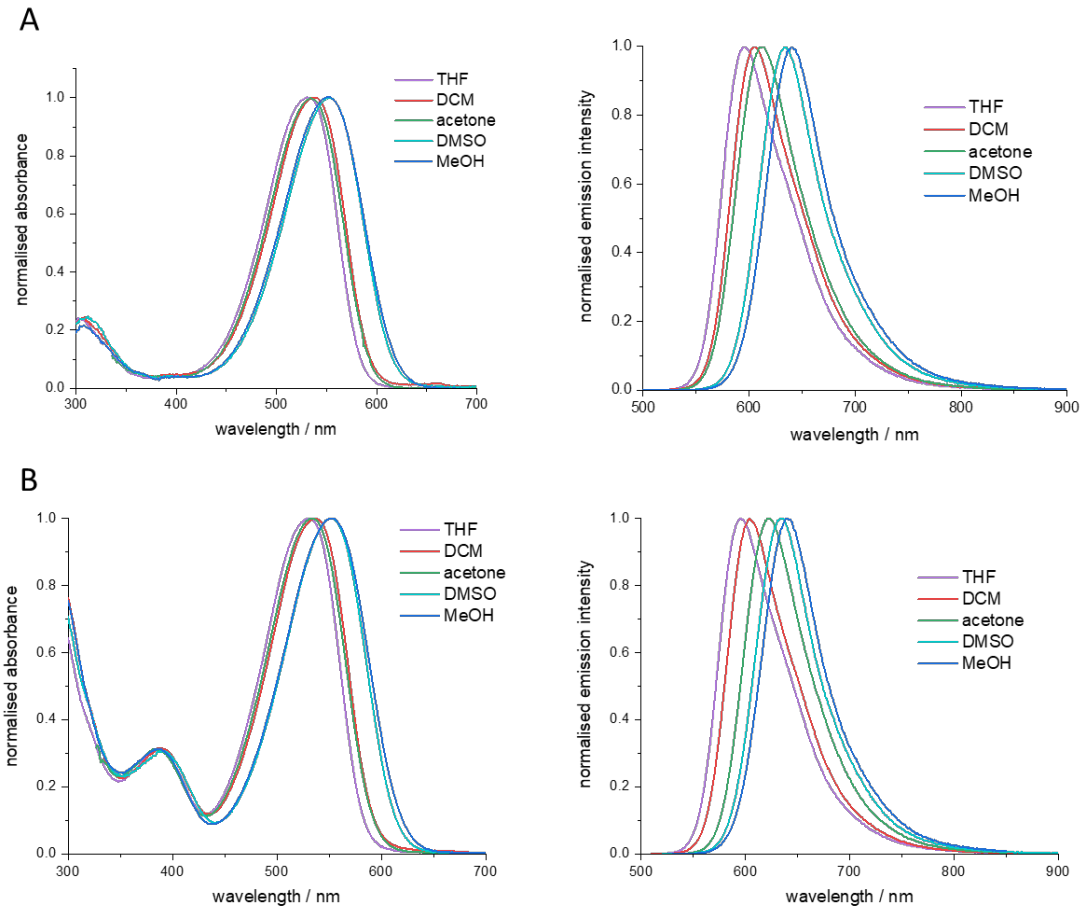


Figure 2.8: Normalised absorption (left) and emission (right) spectra of **NR-linker** (A) and **NR-dyad** (B) in solvents of varying polarity (298 K, 1 µM).

Table 2.1: Photophysical properties of NR-dyad in various solvents (298 K, 1 μM).

	Solvent	E_N^T Reichardt polarity parameter[49]	λ_{max} (abs) / nm	ε (λ_{max}) / mol^{-1} dm^3 cm^{-1}	λ_{max} (em) / nm	Φ_f	τ / ns
NR-linker	THF	0.207	533	72300	596	0.85	4.3
	DCM	0.309	540	70200	605	0.64	4.4
	Acetone	0.355	534	65400	611	0.55	4.6
	DMSO	0.444	552	69600	635	0.48	4.2
	MeOH	0.762	549	65500	641	0.35	3.3
NR-dyad	THF	0.207	531	109000	596	0.59	3.2
	DCM	0.309	536	111000	604	0.34	3.7
	Acetone	0.355	534	120000	612	0.36	3.9
	DMSO	0.444	552	92000	634	0.54	3.6
	MeOH	0.762	554	162000	639	0.15	1.9

The photophysical properties of **NR-dyad** with the photoswitch in the open form were not measured, as the short lifetime of the spironaphthoxazine photoswitch (ms to s) renders cuvette measurements non-trivial. In particular, an accurate measurement of the extent of fluorescence quenching with the photoswitch in its open form is difficult, so **NR-dyad** was taken next to the microscope to assess whether it would fully quench the emission of the Nile Red dye, and therefore perform well as a super-resolution imaging tool (see Section 2.3). It was assumed that the photoswitch behaviour in **NR-dyad** would be similar to our previously-reported dyads.[21,22]

2.2 Investigating PET quenching

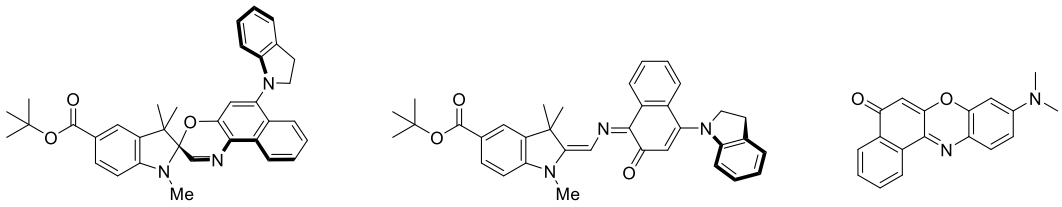
Although the design of this dyad is based on a presumed FRET quenching process, it is also possible that a photoinduced electron transfer is responsible for the observed quenching behaviour when the spironaphthoxazine is in its coloured form. In order to investigate whether this was possible,

the change in Gibbs free energy, ΔG°, of electron transfer was estimated using the Rehm-Weller equation (Equation 1).[50]

$$\Delta G_{PET} = E(D/D^{+}) - \Delta E(D) - E(A^{-}/A) - \frac{e^2}{\varepsilon r} \qquad \text{(Equation 1)}$$

In this equation, $E(\mathrm{D}/\mathrm{D}^{+})$ and $\Delta E(\mathrm{D})$ refer to the oxidation potential of the donor and singlet excitation energy of the fluorophore, respectively, and $E(\mathrm{A}^{-}/\mathrm{A})$ is the reduction potential of the acceptor. The final term ($e^2/\varepsilon r$) accounts for the free energy gained by bringing the ions together in solution, however it is much smaller than the errors in the redox potentials (both measured and calculated), so it can be neglected for this calculation.[50] In this analysis, an excited state energy of 2.15 eV for Nile Red was estimated from experimental data as the midpoint between the absorption and emission maxima in acetonitrile.

Electrochemical measurements were performed on NR-linker and the photoswitch (**SO,** Figure 2.8). However, as the open switch does not persist in solution long enough to measure accurately, we also used calculated values on simplified structures (Figure 2.9) (PBE0/def2-TZVPP/SMD-MeCN//PBE/def2-SVP/SMD-MeCN) for a more complete analysis of the thermodynamic favorability of photoinduced electron transfer reactions.



tert-butyl ester of **SO**$_{closed}$ | *tert*-butyl ester of **SO**$_{open}$ | Nile Red analogue

Figure 2.9: Structures of the dye derivatives and spironaphthoxazine used for calculations. The nile red ethyl groups have been simplified to methyl groups for the calculation.

Free energies (ΔG^{o}) were calculated for redox processes as per the example for reduction in Equation 2, where $G^{o}X^{-}$ is the free energy of a compound X in the reduced state, and $G^{o}X$ is the free energy in the neutral state, using optimised geometries for all redox states. Redox potentials

were calculated from free energies using Equation 3, where z is the number of transferred electrons (z = 1) and F is the Faraday constant, and referenced to the SCE electrode with an absolute E^0 of 4.429 V, corrected for the liquid junction potential in acetonitrile.[51] These values were further corrected to ferrocene (0.40 V vs. SCE)[52] for comparison with experimental values. A comparison of the calculated and experimental values for the redox potentials of each compound is shown in Table 2.2. The calculated values are in good agreement with the obtained experimental values and were used in further analysis.

$$\Delta G^o = G^o X^-(MeCN) - G^o X(MeCN) \quad \text{(Equation 2)}$$

$$E^o = -\Delta G^o(redox)/zF \quad \text{(Equation 3)}$$

Table 2.2: Calculated and measured oxidation and reduction potentials of the measured compounds in acetonitrile. I calculated the values of the switch for an analogous analysis in a previous publication using an identical method.[21]

		Calculated		Experimental
Compound	Process	ΔG° / kJ mol^{-1}	E° / V (*vs.* Fc)	E° / V (*vs.* Fc)
Nile Red	Oxidation	-495	+0.30	+0.44
	Reduction	-316	-1.55	-1.39
SO closed	Oxidation	–476	+0.11	+0.35
	Reduction	–231	–2.44	-[a]
SO open	Oxidation	–472	+0.06	-[b]
	Reduction	–315	–1.56	-[b]

[a] Not observable within the solvent window. [b] The oxidation and reduction potentials of the spironaphthoxazine in its open form cannot be calculated as it does not persist in solution.

Taking the calculated values and applying them to Equation 1 allows the calculation of ΔG_{PET}. We have considered both the case where the switch is acting as the electron donor and the case where Nile Red is the electron donor. In each scenario, we have calculated values for the open

photoswitch and the closed photoswitch, corresponding to the on and off forms of the dyad. The calculated values of the four possible photoinduced electron transfer processes are shown in Table 2.3.

As might be expected for the relatively electron-rich photoswitch, electron transfer is more favourable when the switch acts as the donor, in both open and closed forms. The negative ΔG_{PET} values in these scenarios imply that PET quenching of fluorescence is thermodynamically favourable in **NR-dyad**. Such a process may account for the decrease in the fluorescence quantum yield of Nile Red when it is conjugated to the switch (Table 2.1, above).

Table 2.3: Calculated ΔG_{PET} values for different donor and acceptor pairs.

Donor	Acceptor	Calculated $\Delta \boldsymbol{G}_{\mathbf{PET}}$ / eV
SO closed	Nile Red	–0.49
SO open	Nile Red	–0.54
Nile Red	**SO** closed	+0.59
Nile Red	**SO** open	–0.29

The difference in ΔG_{PET} between open and closed switch is probably not large enough to account for the magnitude of the observed quenching when the switch is in its active form (this idea is more thoroughly explored in Chapter 4). Therefore, while PET may have a minor contribution, it is likely that FRET is the main mechanism by which the open spironaphthoxazine quenches the Nile Red.

2.3 RESOLFT imaging

We first sought to confirm that we could use **NR-dyad** for effective RESOLFT super-resolution imaging. We chose to use giant unilamellar vesicles (GUVs) consisting of 1,2-dioleoyl-*sn-glycero*-3-phosphocholine (DOPC) as a simple model membrane to stain for imaging (Figure 2.10). The

membrane ordering in the vesicles can be altered by combining the DOPC lipid with varying proportions of cholesterol; increasing the cholesterol content produces more ordered vesicles. The vesicles were prepared by electroformation[53] and then incubated with **NR-dyad**.

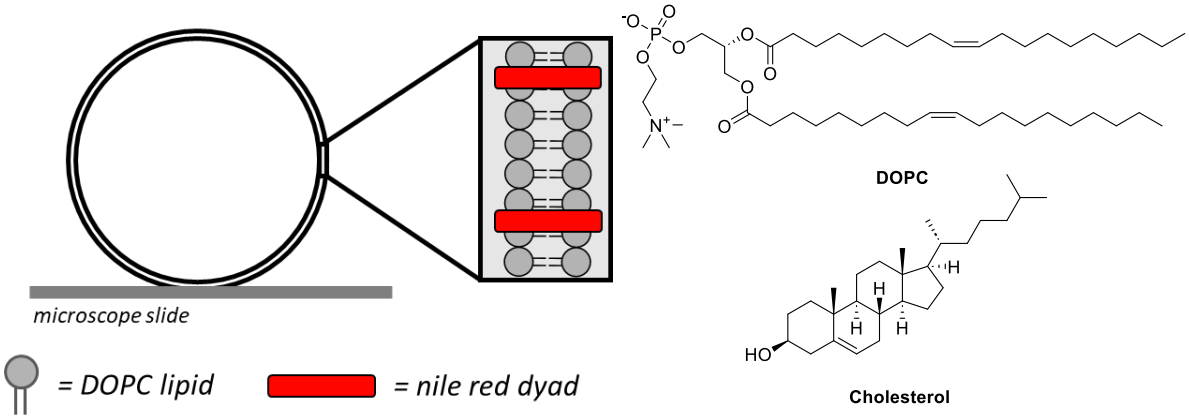


Figure 2.10: Schematic of GUVs on a microscope slide, and the structures of DOPC and cholesterol.

RESOLFT images were acquired in pixel-by-pixel mode, using a diffraction-limited Gaussian-shaped 594 nm excitation spot (providing a confocal control read-out), followed by a donut-shaped 405 nm irradiation to activate the quencher and turn fluorescence off. Then, a second diffraction-limited Gaussian-shaped 594 nm irradiation spot was applied to record a RESOLFT super-resolution image. Finally, the photoswitch was recovered to its closed form and the dye molecules switched back on by irradiation at 640 nm (Figure 2.11). Optimum laser powers for these irradiations were previously determined and based on preceding dyads.[21] For solvatochromic imaging, emission from this excitation was recorded in all the available detectors, however at this stage only the emission in the range 650-755 nm was analysed to compare the output resolution with the confocal control.

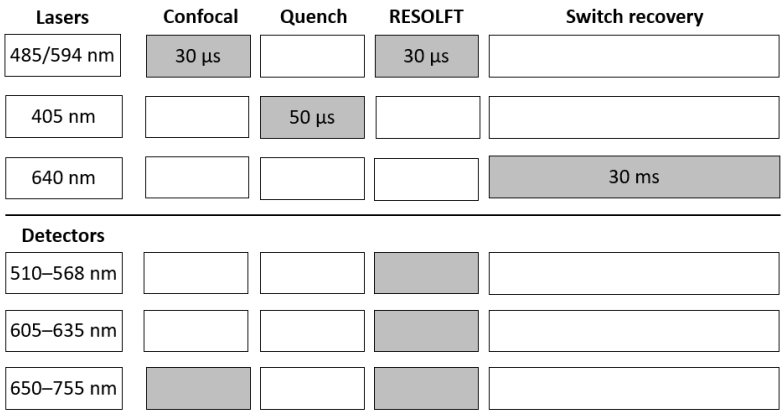


Figure 2.11: Laser and detector sequence for solvatochromic RESOLFT imaging.

We defined the resolution as the full-width-at-half-maximum (FWHM) of a line profile perpendicular to the membrane. The confocal images are well described by Gaussian functions (Equation 4),

$$I = I_0 + I_p\, e^{\frac{-4(ln2)(x-x_p)^2}{w_{con}^2}} \qquad \text{(Equation 4)}$$

where I is the signal intensity (photon counts), I_0 is a baseline correction, I_p is the peak intensity, x is the position along the line, x_p is the center of the peak, and w_{con} is the peak full-width-at-half-maximum (FWHM).

We have previously shown[21] that RESOLFT line profiles are well described by a double Gaussian model (Equation 5), which incorporates the confocal background remaining in the RESOLFT image caused by incomplete quenching of the dyad,

$$I = I_0 + I_{con}\, e^{\frac{-4(ln2)(x-x_p)^2}{w_{con}^2}} + I_{SRM}\, e^{\frac{-4(ln2)(x-x_p)^2}{w_{SRM\text{-}2G}^2}} \qquad \text{(Equation 5)}$$

where w_{con} is fixed as the peak width from the corresponding confocal profile and $w_{SRM\text{-}2G}$ is the fitted FWHM of the RESOLFT component. We then report our observed resolution enhancement as $w_{con}/w_{SRM\text{-}2G}$.

Using this fitting process, we showed that **NR-dyad** can be successfully applied to RESOLFT microscopy to image vesicle membranes of varying composition below the diffraction limit (DOPC, 80:20 DOPC:cholesterol, 50:50 DOPC:cholesterol; representative images in Figure 2.12).

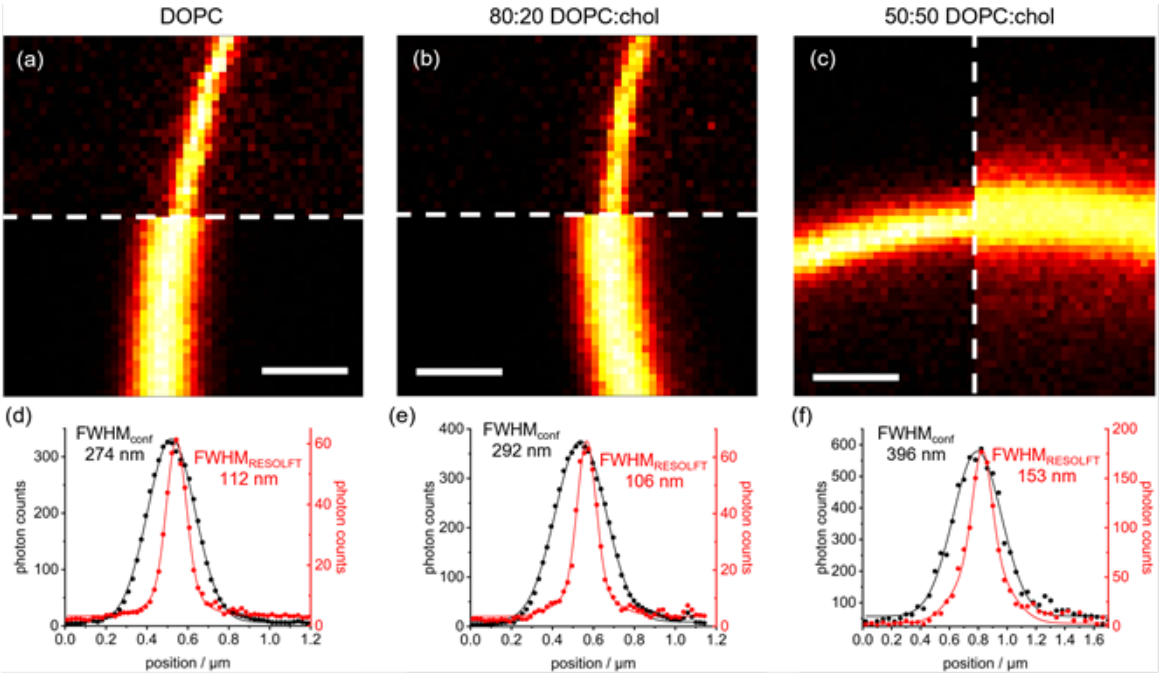


Figure 2.12. Demonstration of RESOLFT resolution enhancement in GUV membranes composed of (a) DOPC, (b) 80:20 DOPC:cholesterol and (c) 50:50 DOPC:cholesterol, all stained with **NR-dyad**; the fitted line profiles through the membranes used to measure FWHM are shown in (d–f). The red and black curves show the fitted line profiles from RESOLFT and confocal imaging, respectively.

2.4 Resolution Analysis

In order to analyse all our images consistently, we developed a Python script to automatically analyse the full-width-at-half-maximum of the membrane in our images (Appendix). An ImageJ macro script was used to convert images with a confocal and RESOLFT channel into .txt images (arrays of pixel intensities), and then the Python numpy module was used to handle the arrays (Figure 2.13). Firstly, a threshold was applied to the image arrays to discard pixels with intensity below 0.3× the maximum intensity (an empirically-determined value), and the matrix locations of the pixels above this threshold were stored as an array. Then, these locations were plotted on an x,y graph and a 2nd degree polynomial fitted to the shape of the 'membrane'. The tangent and normal were calculated at specific points along the membrane, and the normal vectors overlaid

with the original image array to sample the pixel intensities along the line. The pixel intensities were plotted against the distance along the normal and fitted with Gaussian or double Gaussian functions (as described above) to extract the full-width-at-half-maximum of the line profile, which we use as a proxy for resolution.

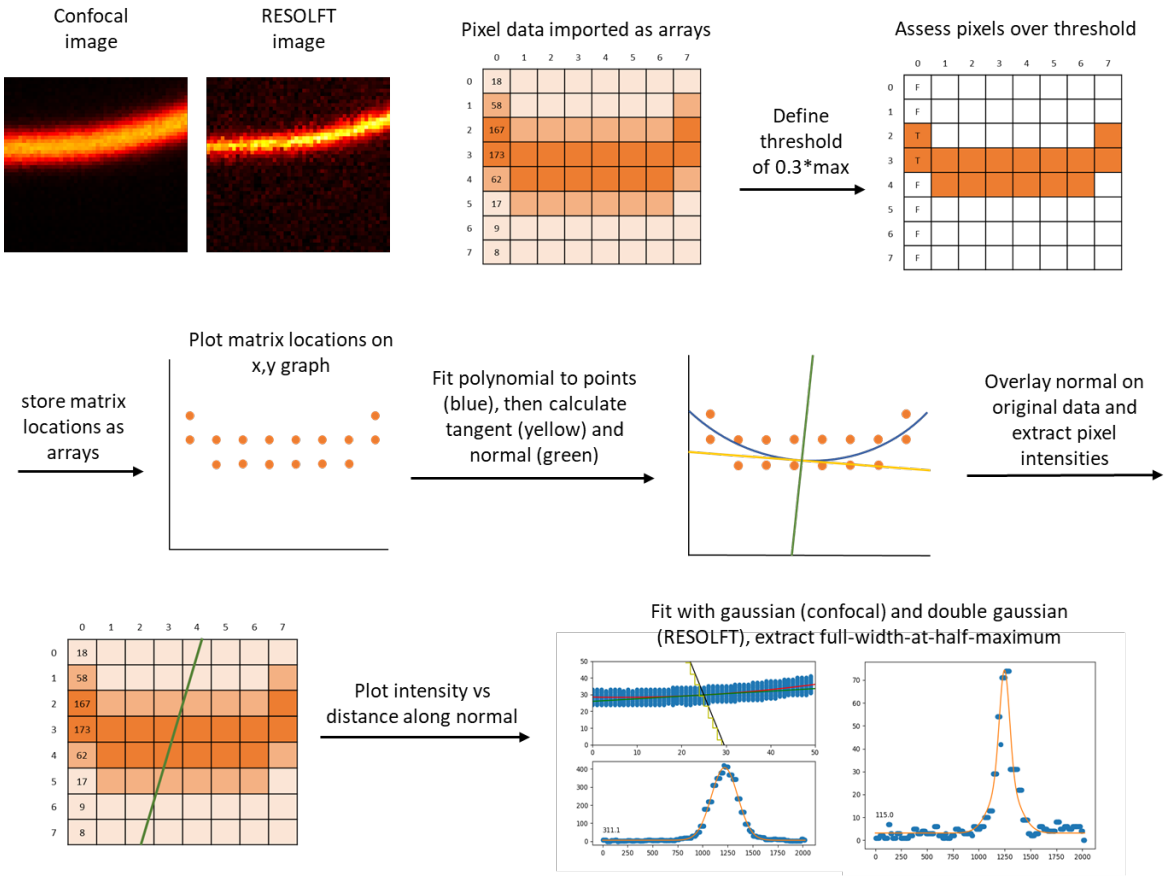


Figure 2.13: Schematic workflow for automatic analysis of FWHM in RESOLFT images.

We observed significant variation in the Gaussian fits between images of vesicles with identical compositions, with FHWM $\pm$ 45 nm ($\pm$ 1 st. dev.). To explore this variation and ensure that we used as much of a data as possible, we chose to measure the FWHM along line profiles at 7 positions across each image, 3 pixels apart, distributed around the central point. An example output in show in Figure 2.14.

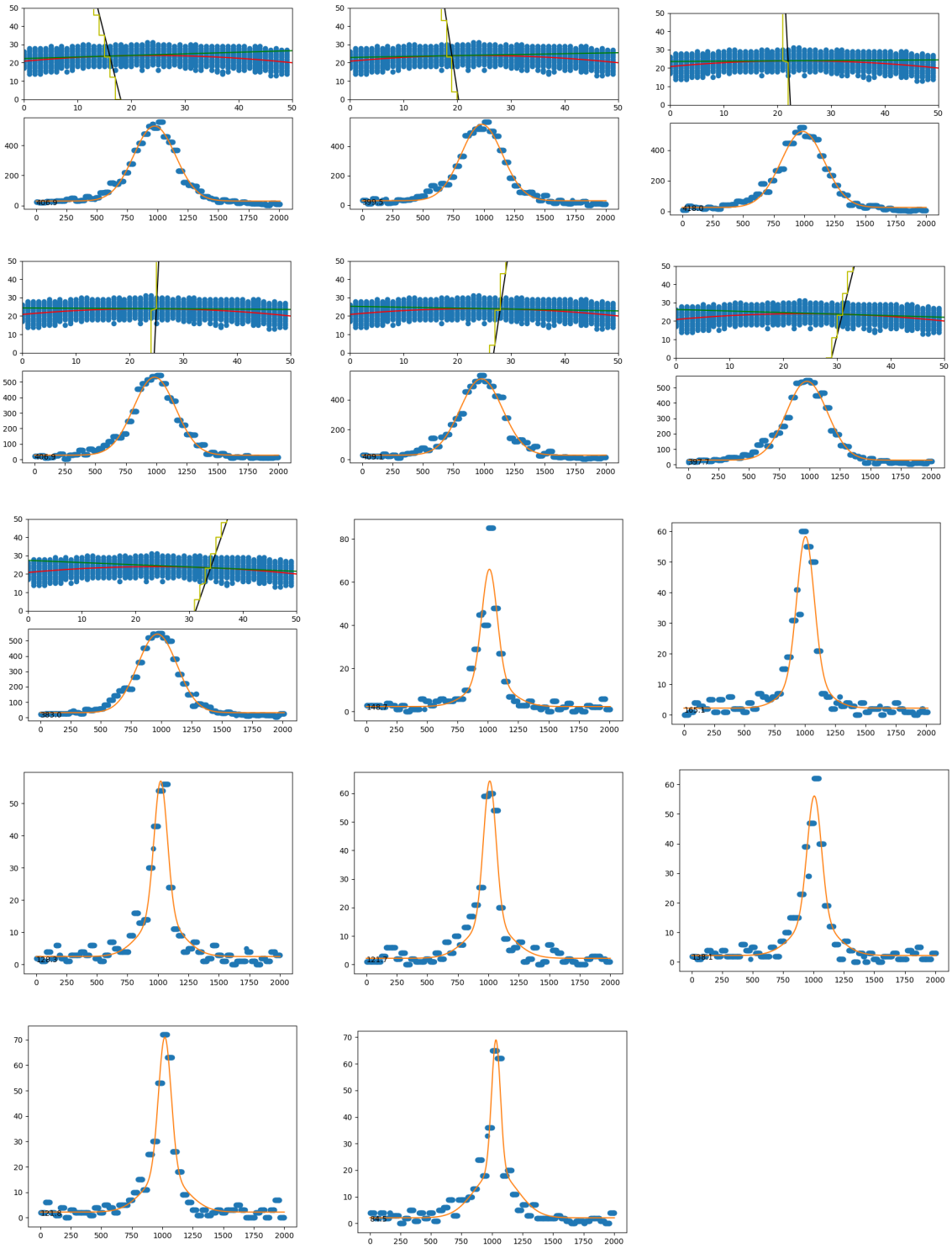


Figure 2.14: Example outputs from the automated script for multiple line profiles through a single image, showing 7 normals to the membrane and their confocal fits, and the 7 corresponding RESOLFT fits.

Using the automated analysis, we fitted 7 line profiles to 336 images of membranes of different polarity. Some data cleaning was performed to remove fits where the RESOLFT Gaussian contribution was small ($\frac{I_{\text{SRM}}}{I_{\text{con}}+ I_{\text{SRM}}}$ < 0.4 ie. less than 40% contribution), as these tended to correlate with poor visual fits of noisy data. The mean resolutions for confocal and RESOLFT images, alongside mean enhancements are shown in Table 2.4.

Table 2.4: Mean confocal, RESOLFT resolutions and enhancements for the different vesicle compositions.

Membrane composition	# line profiles	Mean confocal res / nm	Mean RESOLFT res / nm	Mean RESOLFT Gaussian contribution	Mean enhancement	Enhancement standard deviation
DOPC	1399	377	157	0.78	2.53	0.66
80:20 DOPC:chol	315	322	146	0.79	2.52	0.52
50:50 DOPC:chol	592	387	212	0.57	1.91	0.46

In all three membrane compositions, we observed resolution enhancement by RESOLFT microscopy, with a mean resolution enhancement factor of 2.5 for both DOPC (SD=0.66) and 80:20 DOPC:cholesterol (SD=0.52) membranes. Interestingly, the resolution enhancement was not as good for the 50:50 DOPC:cholesterol membranes, with a mean enhancement factor of 1.9 (SD=0.46). The average resolution enhancements achieved with **NR-dyad** are better than those we achieved with the previous generation of switchable spironaphthoxazine dyads bearing Atto590 or Cy3.5 fluorophores.[21] We attribute this improvement to a reduction in the competing absorption by Nile Red at the switching wavelength of 405 nm compared to fluorophores used previously.

The variation across the 7 line profiles *within* an image led to average FHWM estimates $\pm$ 24 nm ($\pm$ 1 st. dev.). This indicates that a significant contribution to the variation between vesicles of the

same composition comes from the data sampling and fitting process, assuming the membrane width across a 2 μm image is physically constant. This shows the use of multiple line profiles in a single image is genuinely extending the amount of data sampled, which would not be the case if all 7 FHWM within an image were the same. The vesicles themselves, and the variation in their curvature, membrane thickness, movement during imaging, and image plane selection probably also contributes to the variation in FWHM *between* images.

To further investigate why poorer resolution enhancements were observed in the 50:50 DOPC:cholesterol membranes (which are expected to be the most ordered), we considered the relative weighting of the confocal contribution to the super-resolution line profile fit. In most cases, there was a larger confocal contribution in the RESOLFT fits for the 50:50 membranes (more than 40%) than for the DOPC or 80:20 DOPC:cholesterol membranes (approximately 20%, Table 2.5). This suggests that the dye emission is less efficiently quenched following 405 nm irradiation in the 50:50 DOPC:cholesterol membrane environment.

We considered whether the more blue-shifted emission of Nile Red led to poorer spectral overlap with the quencher, in turn leading to poorer FRET efficiency in the more ordered environments. However, the absorption of the open form of the spironaphthoxazine also displays solvatochromism.[22] FRET overlap calculations performed using spectra acquired in toluene and DCM (Table 2.5) showed that the FRET efficiency remains high, actually increasing in more non-polar environments (Figure 2.15).

Table 2.5: Effect of solvent on calculated FRET distances and efficiencies.

Solvent	FRET distance, R_0 / Å	FRET efficiency / %
Toluene	53.1	99.5
Dichloromethane	47.2	99.1
Acetonitrile	43.4	98.5

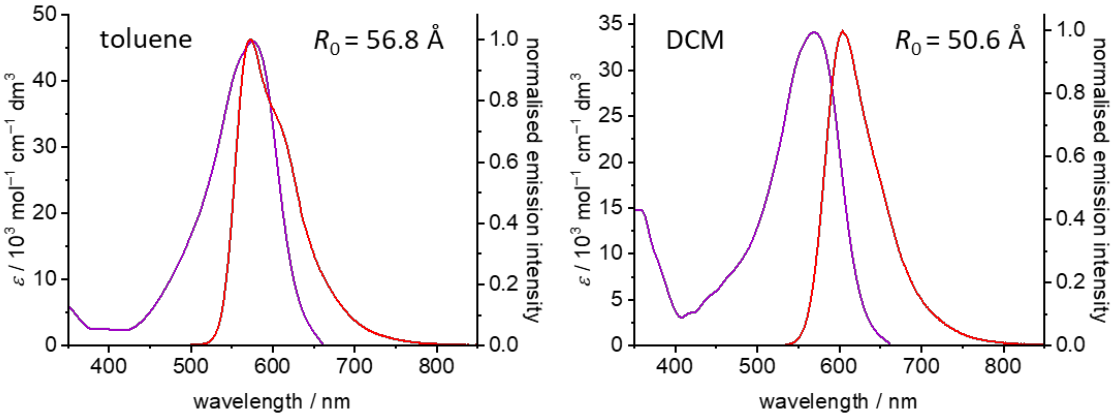


Figure 2.15: Spectra showing FRET overlap in different solvents: the absorption spectra (purple) of the open spironaphthoxazine switch and the emission spectra (red) of **NR-linker** in toluene and DCM (all 298 K).

As well as spectral overlap, FRET efficiency depends on the relative orientation of the donor and acceptor transition dipole moments. In our system, the linker is sufficiently flexible that we do not restrict the relative rotation of the donor and acceptor to the extent that FRET is disrupted, as it can explore a large percentage of transition dipole moment orientations. However, in highly ordered membrane environments, we considered the possibility that molecular rotation is restricted, meaning that the donor and acceptor are less likely to spend time in a conformation where the transition dipole moments are well-aligned. We observed that when imaging **NR-dyad** using a polarized excitation laser, 50:50 DOPC cholesterol, and regions of membrane formed entirely of the L_o phase of 2:2:1 DOPC:sphingomyelin:cholesterol (see below for more discussion) appear bright on one axis and dark on the perpendicular axis, indicating that the transition dipole moments of the dyes are well-aligned with the excitation laser on one axis but not the other. This feature is not observed in disordered DOPC membranes (Figure 2.16). We therefore hypothesise

that **NR-dyad** does not freely rotate on the timescale of the excited state in ordered membranes, which could be the cause of a poorer FRET efficiency, and therefore worse RESOLFT resolution.

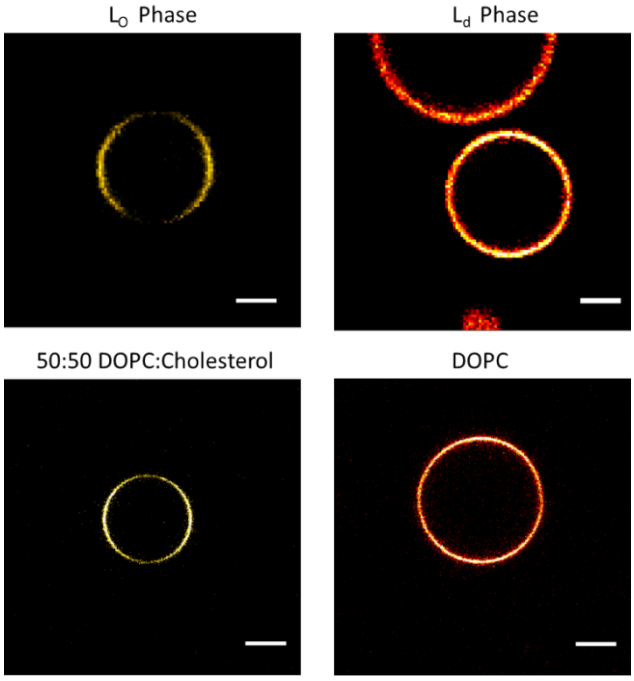


Figure 2.16: Images of various vesicle types stained with **NR-dyad**. λ_{exc} 488 nm with polarized laser, λ_{em} 613 nm (L_o phase), 631 nm (L_d phase), 579 nm (50:50 DOPC:Cholesterol), 659 nm (DOPC). Emission wavelengths represent the center of an 8.9 nm spectral imaging window. Images are falsely colored to approximate their maximum emission. Scale bars represent 2 µm (L_o and L_d phase) and 5 µm (50:50 DOPC:Cholesterol and DOPC).

2.5 Polarity Sensing

Having confirmed that **NR-dyad** can be used to image membranes below the diffraction limit, we next investigated whether the solvent sensitivity recorded in the cuvette could be exploited during microscopy. We first performed confocal spectral imaging experiments in GUVs of varying lipid composition to observe the effect of lipid ordering on the dyad emission. We compared **NR-dyad** to the Nile Red derivative **NR12A** as a model solvatochromic dye, which has previously-reported confocal spectral imaging (Figure 2.17).[30] We compared GUVs consisting of DOPC or the more ordered (less polar) 50:50 DOPC:cholesterol lipid composition. We also made phase-separated GUVs formed from a 2:2:1 DOPC:sphingomyelin:cholesterol mixture, which separate into ordered (L_o) and disordered (L_d) phases.[54] Confocal spectral imaging shows that the emission from the dyad

is blue-shifted in the more ordered lipid membranes, consistent with our hypothesis and with the NR12A reference.

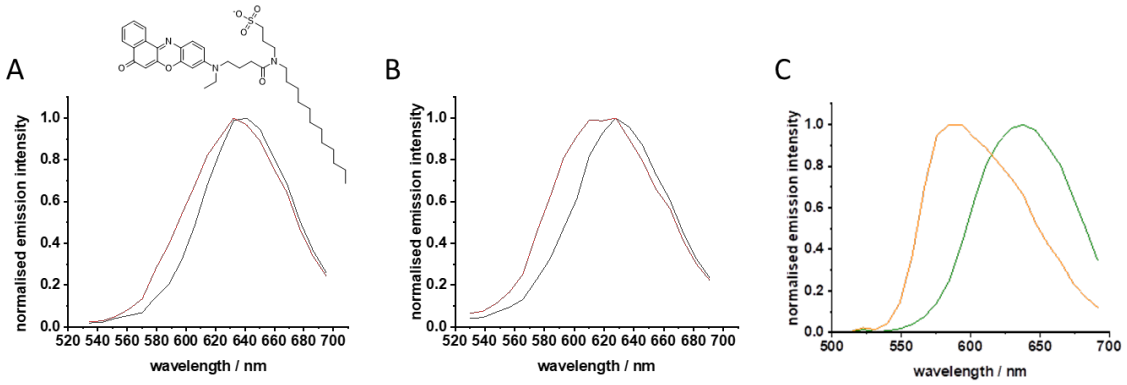


Figure 2.17: Spectral imaging of (A) **NR12A** and (B) **NR-dyad** in GUV membranes comprising DOPC (black) or 50:50 DOPC:cholesterol (red) and (C) spectral imaging of **NR-dyad** in the disordered (L_d, green) and ordered (L_o, orange) domains of phase separated GUV membranes comprising 2:2:1 DOPC:sphingomyelin:cholesterol.

We next developed an imaging sequence capable of recording super-resolution images in multiple spectral regions simultaneously. Comparing the ratio of emission intensity in the whole image in different spectral windows provides information about the polarity in the membranes, and hence the lipid ordering. Due to hardware restrictions, our detection windows were limited to 510–568 nm, 605–635 nm and 650–755 nm. Based on the spectral imaging data, we chose to use the 605–635 nm and 650–755 nm windows, to provide the largest discrimination between different membrane compositions. We expanded our existing RESOLFT imaging sequence to incorporate simultaneous detection in these windows, and compared the output in the two channels for vesicles with different lipid compositions. Using a macro-based automated analysis process developed in ImageJ, 290 images were analysed and the ratio of emission intensity in the two spectral windows was compared. Vesicles with different lipid compositions gave reproducible and highly statistically significant differences in the ratio of emission intensity in the two spectral windows (Figure 2.18).

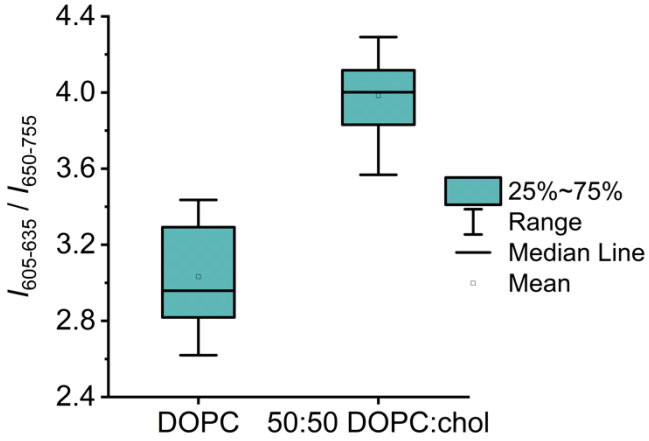


Figure 2.18: Box-and-whisker plot showing a population analysis of the ratio between the pixel intensity in the 605–635 and 650–755 nm channels in DOPC and 50:50 DOPC:cholesterol GUV membranes (λ_{exc} 594 nm). Three stars indicates the p value for paired t-test assessing the difference between these populations is < 0.001, ie. the probability that these observed population differences are statistically significant and did not occur by chance is > 0.999.

2.6 Polarity Sensing Below the Diffraction Limit

In order to realise our goal of being able to discriminate between regions of different membrane ordering within the same super-resolution image, an analysis of polarity in individual pixels is required. We developed a workflow for pixel-by-pixel analysis of images, and applied it to images recorded in multiple detection windows. An example workflow is shown in Figure 2.19.

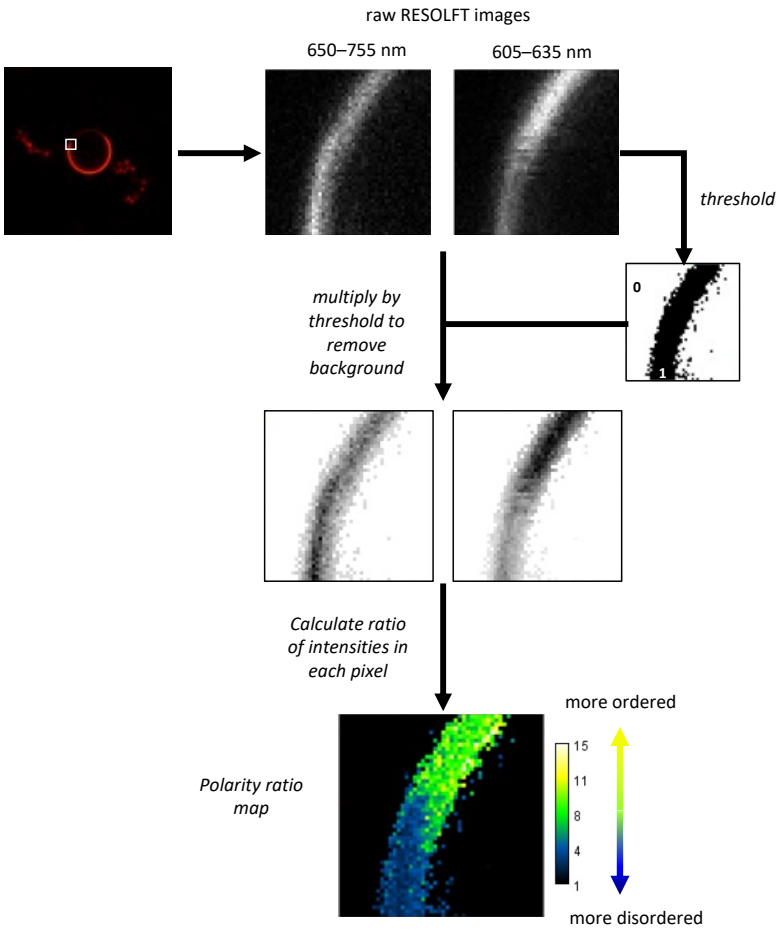


Figure 2.19: Example workflow for analysis of images of phase separated GUVs stained with polarity-sensitive dyes.

This process generates polarity maps where the color scale represents the ratio of intensity in the two spectral windows. Similarly to the whole-image analysis, the pixel-by-pixel analysis shows that DOPC and 50:50 DOPC:cholesterol membranes can be distinguished from each other easily (Figure 2.20).

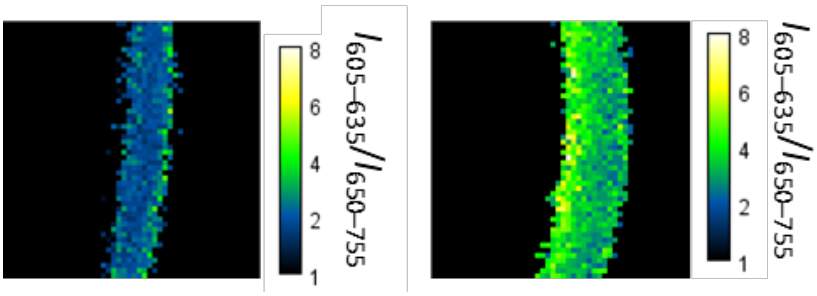


Figure 2.20: Examples of super-resolution images of membranes with pixel-by-pixel analysis showing polarity for DOPC (left) and 50:50 DOPC:cholesterol (right) membranes (higher number = more ordered; images 2 × 2 µm).

We then sought to demonstrate the polarity sensing and RESOLFT capabilities of **NR-dyad** within a single image using phase-separated GUVs as a model membrane. These vesicles are formed from a 2:2:1 DOPC:sphingomyelin:cholesterol lipid mixture, which separates into ordered (L_o) and disordered (L_d) phases. When they were incubated with **NR-dyad,** we found clear preferential localisation in a single phase (Figure 2.21).

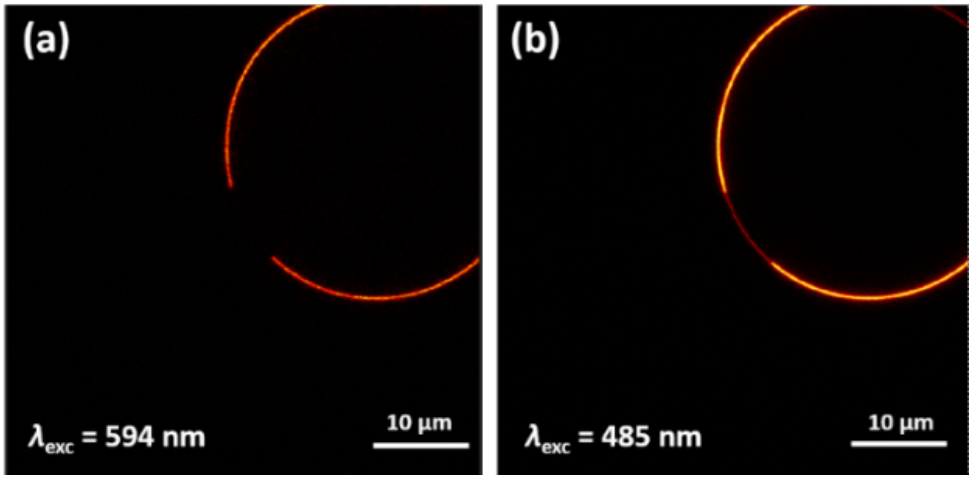


Figure 2.21: Confocal images of 2:2:1 DOPC:sphingomyelin:cholesterol phase-separated GUVs stained with **NR-dyad** excited with (a) 594 nm and (b) 485 nm (detection 650–755 nm, 80 × 80 nm pixels) showing selective excitation of **NR-dyad** in a single phase.

We performed colocalisation experiments with the L_d phase marker FAST DiO (a commercial dye known to localise in the disordered phase) to confirm in which phase **NR-dyad** was preferentially localising. The two dyes could be separated spectrally into a green and red channel in control experiments (Figure 2.22), allowing us to excite each one selectively without crosstalk. We applied the same parameters from the control experiments to image vesicles stained with both dyes, and confirmed colocalisation of NR-dyad and FAST DiO in the L_d phase (Figure 2.23).

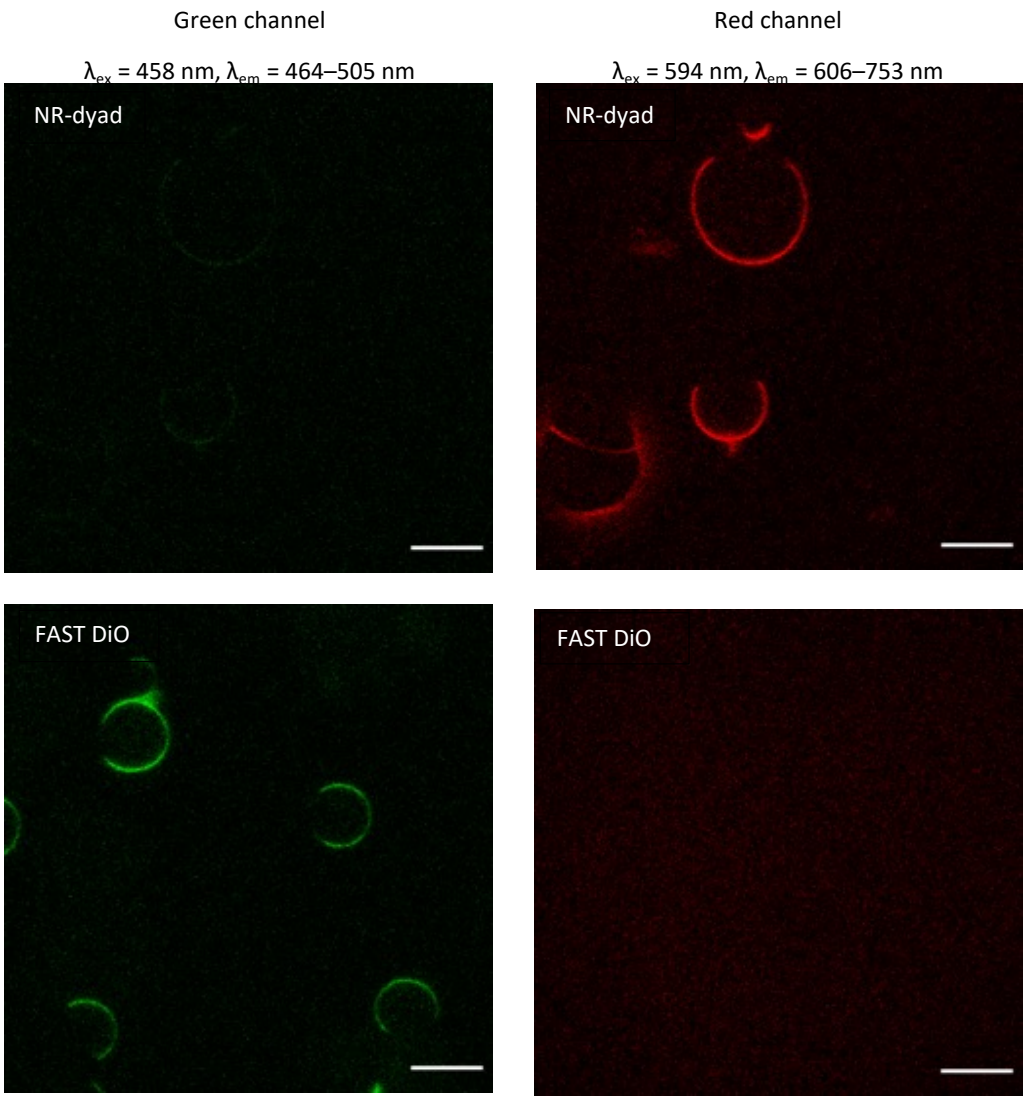


Figure 2.22: Control images for **NR-dyad**/**FAST-DiO** colocalisation experiments in 2:2:1 DOPC:sphingomyelin:cholesterol phase separated GUVs (scale bar = 10 μm). Excitation and detection wavelengths as shown in figure.

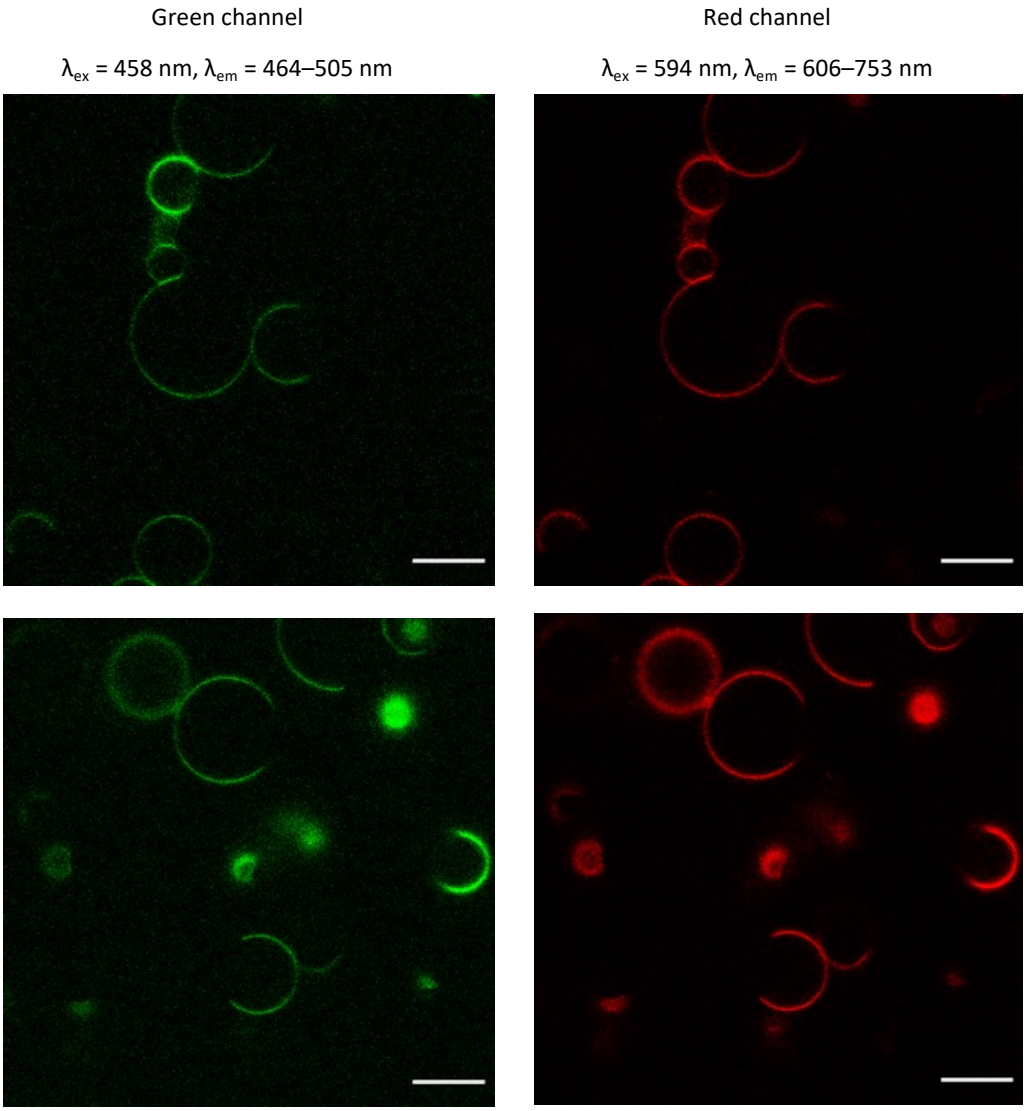


Figure 2.23: Confocal images of phase separated GUVs stained with both NR-dyad and FAST-DiO showing colocalisation in the Ld phase (scale bar = 10 μm). Excitation and detection wavelengths as shown in figure.

Acquisition of RESOLFT images at the phase boundary with our standard image acquisition sequence using 594 nm excitation showed that it is difficult to measure the polarity ratio in the ordered phase due to a lack of signal from dyad accumulated there. However, excitation at 485 nm gives significantly more signal in the L_o phase, probably due to more efficient excitation of the more blue-shifted dyes in this phase, indicating not just a localisation preference but also selective excitation for **NR-dyad** in the disordered phase. By averaging the intensity of emission in the ordered and disordered phases, we can quantify this preference. The $\%L_o$ partitioning coefficients[55] are 8 ± 3% for 594 nm excitation and 33 ± 4% for 485 nm excitation, showing that changing

excitation wavelength has a large effect on the populations we are able to excite in the two phases of the membranes.

We sought to confirm that the polarity ratio collected in our two emission channels could still discriminate between different membrane types (as in Figure 2.20 experiments, above) using the alternative excitation wavelength. We found that with 485 nm excitation, **NR-dyad** could still differentiate environmental polarity through a change in the emission ratio, showing larger ratio differences between our DOPC and 50:50 DOPC:cholesterol vesicles than with 594 nm (Figure 2.24).

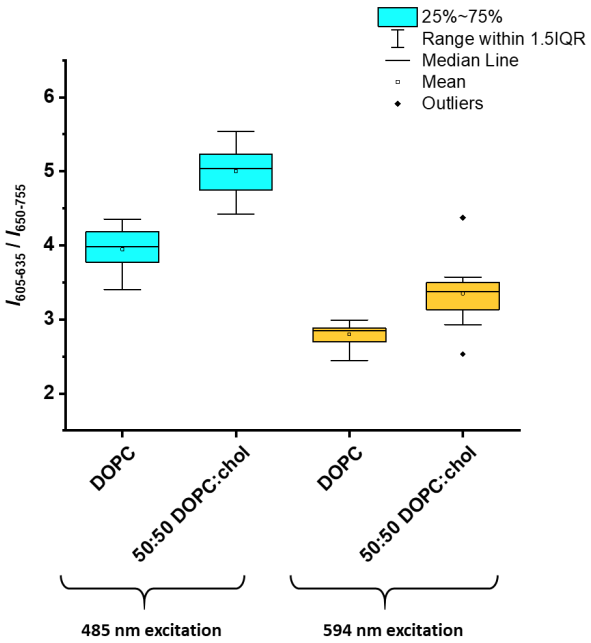


Figure 2.24: Comparison of ratiometric polarity measurements in DOPC and 50:50 DOPC:cholesterol GUV membranes with 485 nm (blue) and 594 nm (orange) excitation. Range within 1.5IQR refers to the range 1.5 x the interquartile range (between Q1 and Q3, shown in blue) further from the Q1 and Q3 limit, and neglects the outliers shown as black diamonds.

Using the pixel-by-pixel analysis workflow, and 485 nm excitation, we were able to produce polarity 'maps' of the phase-separated vesicles, which show where the L_o and L_d phases of the membrane meet at resolution below the diffraction limit, thus demonstrating that the photoswitchable **NR-dyad** can be used as a super-resolution probe for membrane ordering (Figure 2.25).

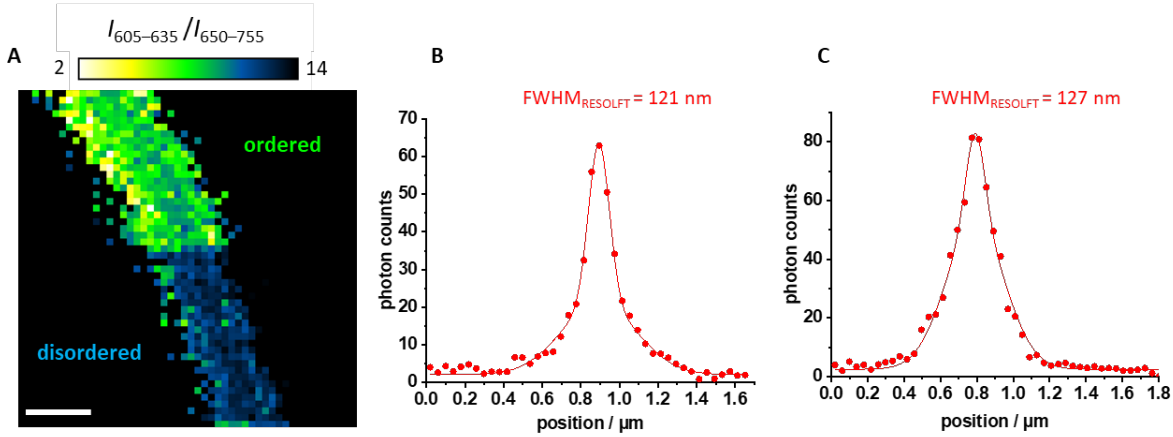


Figure 2.25: RESOLFT polarity sensitive imaging. (A) RESOLFT image polarity map of of phase-separated GUV membranes labelled with **NR-dyad** showing discrimination of regions of different lipid ordering; and fitted line profiles through the (B) disordered and (C) ordered phases of the membrane with RESOLFT FWHMs as shown. Scale bar = 400 nm.

2.7 Translation to biological systems

Following extensive validation in synthetic membranes, and this successful demonstration of polarity imaging below the diffraction limit, we sought to test **NR-dyad** in biological systems. First, we investigated their behavior in giant plasma membrane vesicles (GPMVs), which are isolated from living cells and include many of the proteins and complex lipids in plasma membranes, making them more realistic models of cellular membranes.[56] GPMVs are formed by incubating cells with buffers that stress them and encourage membrane budding.

When we imaged **NR-dyad** in THP-1[e] cell-derived GPMVs, we observed the dyad was taken up and labelled the membranes. However, there was also significant dye visible in the inside of the vesicles, which made fitting line profiles of membranes very challenging (Figure 2.26). Additionally, because the GPMVs are not fixed to the surface of the imaging chamber (unlike GUVs), they are much more mobile. The increased mobility and membrane 'wobbling' meant that super-resolved images could not be acquired reliably.

[e] THP-1 cells are a human monocytic cell line (a type of white blood cell).

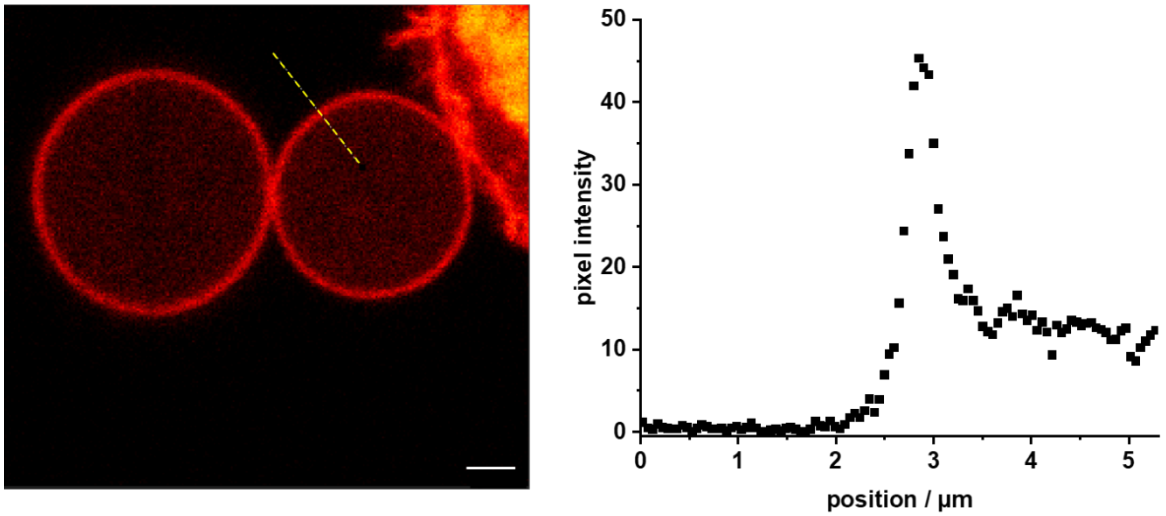


Figure 2.26: (A) Confocal image of GPMVs labelled with **NR-dyad** (λ_{exc} 594 nm, λ_{em} 655–750 nm, 80 × 80 nm pixels, scale bar = 2 µm); (B) pixel intensity along line profile shown in left panel (yellow dotted line).

We also attempted to image THP-1 cells with **NR-dyad**, however it showed no discernible sub-cellular localisation pattern, either in the plasma membrane or any particular organelle (Figure 2.27); rather it was incorporated into all subcellular membranes. This made the acquisition of super-resolution images of particular membranes difficult. Additional experiments were carried out with 0.02% sodium azide (a known inhibitor of endocytosis) in order to slow down spreading of **NR-dyad**. This reduced the uptake rate but did not affect the localisation.

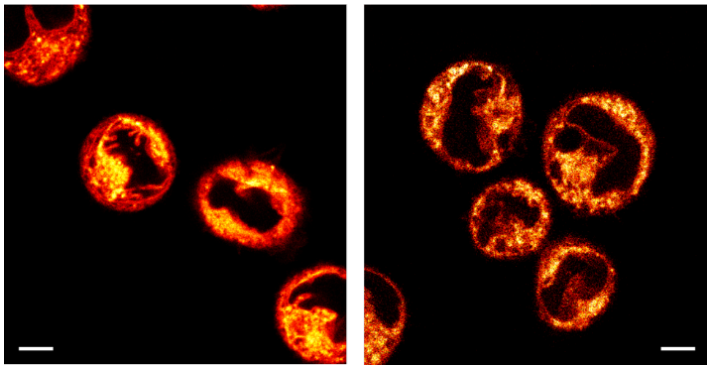


Figure 2.27: Representative images of THP-1 cells stained with **NR-dyad** (λ_{exc} 594 nm, λ_{em} 605–635 nm, 80 × 80 nm pixels, scale bars 5 µm). Left: 5 µM dye loading, 15 min incubation at 37 °C; right: 1 µM dye loading, 1 min incubation at 4 °C.

3. Conclusions and Future Work

In this work, I have investigated a photoswitchable **NR-dyad** comprising a solvatochromic Nile Red dye unit and a spironaphthoxazine quencher, which can be addressed in both directions by visible light. **NR-dyad** shows efficient quenching (94%) due to the high switching ability of the spironaphthoxazine and the excellent FRET efficiency between the Nile Red donor and switch acceptor. It is incorporated efficiently into GUV and cell-derived membranes and can be used to acquire super-resolved fluorescence microscopy images using RESOLFT with resolution enhancements around 2.5-fold in GUVs. Additionally, the emission of **NR-dyad** is sensitive to polarity, and this can be used as a proxy for probing lipid ordering in membranes. Emission from the dyad can be used to distinguish regions of membranes with varying composition, both in membranes of a single composition and in phase-separated vesicles. As a result, **NR-dyad** is capable of reporting on local lipid ordering environments below the diffraction limit, the first tool for RESOLFT which is able to do so.

The nature of RESOLFT imaging makes it necessary to image in a pixel-by-pixel manner, applying the image acquisition sequence to each pixel in succession, and this limits the speed of image acquisition. However, this technique does give super-resolved images in a single acquisition, in contrast to other recent examples of super-resolution membrane probes utilising PAINT microscopy, which requires tens of thousands of frames to construct the final super-resolution image.[31] As a result of the relatively slow recovery of the spironaphthoxazine switch to its closed form, the current temporal resolution of imaging (approx. 75 s) is comparable to the timescale required by PAINT (1 min).[30] Future development of these systems requires switches that can be transformed between their two states in a shorter time.

Unfortunately, in its current form, this dyad is unable to be effectively used in live-cell imaging of plasma membranes as it is efficiently taken into cells and accumulates in many cellular organelles. To probe specific membranes with high resolution, it will be necessary to synthesise organelle-

targeted versions of **NR-dyad**, to direct localisation to membranes of interest within the cells. There has been much work on sub-cellular targeting of small molecule dyes, which could be synthetically incorporated into the dyad. For example, including a sulfonate group may restrict internalisation of the probe, and limit its localisation to the cell membrane (Figure 2.28). Other commonly-used organelle targeting groups[10] such as triphenylphosphonium (for mitochondria) and morpholine (for lysosomes) could be considered. This will allow membrane ordering to be compared in different cellular environments below the diffraction limit.

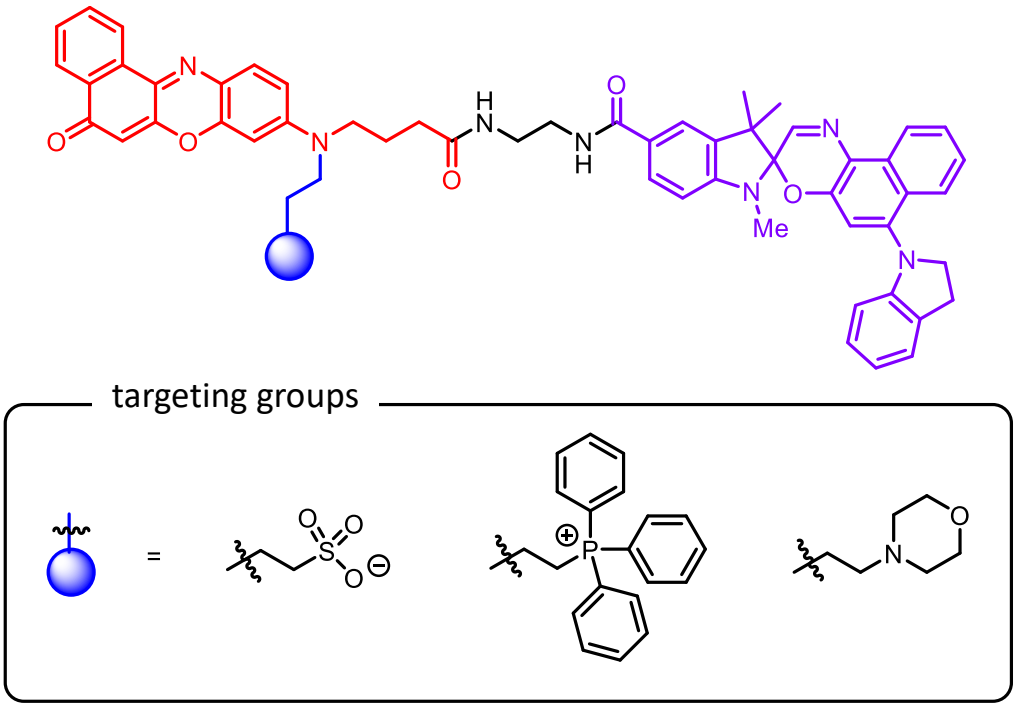


Figure 2.28: Targeting groups for cellular localisation of **NR-dyad**.

We have also shown that judicious choice of excitation wavelength is required for good ratiometric imaging. Improved contrast between the L_d and L_o phases could probably be achieved with other excitation wavelengths and better tuned detection windows, which could be achieved through hardware modifications.

4. Experimental Methods

4.1 Optical analysis

All spectroscopic measurements were conducted in HPLC grade solvents using fused silica cuvettes (10 mm path length, Starna Scientific Ltd, UK). UV-vis absorption spectra were acquired on a Perkin Elmer Lambda 20 spectrometer. Unless otherwise stated, all absorption spectra were recorded at 298 K, with temperature control by a PTP-1 Peltier unit from Perkin Elmer. Fluorescence spectra were acquired at 298 K using an Edinburgh Instruments FS5 spectrofluorometer operating Fluoracle® software, and equipped with a xenon arc lamp (providing 230–1000 nm excitation range), a thermostatic sample holder (SC-20) and both an R13456 PMT detector (200–950 nm spectral coverage, Hamamatsu) and an InGaAs analogue NIR detector (850–1650 nm spectral coverage). Quantum yields were measured by an absolute method using an integrating sphere (SC-30). Lifetimes were measured in time-correlated single photon counting (TCSPC) mode using a picosecond pulsed diode laser (EPL-475; 475 nm, pulse width 100 ps) as the excitation source.

4.2 Experimental redox potential measurements

Redox potentials of the Nile Red dye with linker **2** were measured using square-wave voltammetry. Redox potentials for the spironaphthoxazine switch **SO** were previously measured in a similar analysis.[21] Electrochemical experiments were performed in acetonitrile at compound concentrations of 0.1–1.0 mM with tetrabutylammonium hexafluorophosphate as the electrolyte (0.1 M). Square-wave voltammograms were collected with a modulation amplitude of 50 mV and a frequency of 2 Hz. Glassy carbon (Ø = 1 mm), platinum wire and $Ag|AgNO_3$ (10 mM) were used as working, counter and reference electrodes, respectively. The potentials were referenced at the end of each experiment by addition of ferrocene.

4.3 Calculated redox potentials

Density functional theory (DFT) calculations were carried out using the ORCA 4.1.1 program,[6] using previously-published data for the switch.[21] Tight optimisation criteria were used for all geometries, and numerical frequency calculations used to confirm stationary points as minima, and to calculate thermal energy corrections. Resolution of identity was used to speed up the SCF process employing the RIJCOSX approximation. Grid6 and GridX6 were used in all calculations. Implicit solvation was introduced employing the SMD model.

Redox potentials were calculated from free energies using Equation 3 (discussed in Section 2.2), where *z* is the number of transferred electrons (*z* = 1) and *F* is the Faraday constant, and referenced to the SCE electrode with an absolute E° of 4.429 V, corrected for the liquid junction potential in acetonitrile.[7] These values were further corrected to ferrocene (0.40 V vs. SCE)[8] for comparison with experimental values. Free energies can be calculated for redox processes as per the example of a reduction in Equation 2 (discussed in Section 2.2). Calculations were performed at the PBE0 level of theory in combination with the def2-TZVPP basis set and the SMD solvation model (acetonitrile), using the optimised PBE/def2-SVP geometries.

4.4 Preparation of GUVs for imaging

GUVs were freshly prepared on the same day as imaging, according to the following electroformation procedure.[53] The electroformation chamber was cleaned with ethanol and dried thoroughly under N_2 flow. A solution of lipid (5 µL of a 1 mg mL^{-1} solution in $CHCl_3$) was spread evenly over two Pt electrodes and dried under N_2 flow. A solution of sucrose (370 µL, 300 mM aqueous) was placed in the electroformation chamber and the Pt electrodes were inserted into this solution. For single lipids, the electroformation was carried out at room temperature. For mixed DOPC/cholesterol vesicles, the chamber was heated to 45 °C and to 60 °C for 2:2:1 DOPC:sphingomyelin:cholesterol phase separated GUVs. Using a function generator (frequency 10 Hz, amplitude 5.7 $V_{peak\text{-}to\text{-}peak}$ = 2 V_{RMS}) an electrical potential was applied to the sample for 1 h

to form the GUVs. After 1 h, the frequency was reduced to 2 Hz and left for a further 30 min to detach the GUVs from the electrodes, before being left to cool to room temperature if necessary. Meanwhile, the wells of a glass ibidi µ-Slide 8-well plates were passivated with poly-L-lysine for 1 h, before washing with PBS three times. For confocal and RESOLFT imaging, some of the GUV solution (75 µL) was transferred into an Eppendorf tube and a solution of dyad (1 µL, 1 mM in DMSO for **NR-dyad**, 200 nM in EtOH for **NR12A**) was added and left to incubate for 15 min. The vesicle solution was then placed into PBS (250 µL) in the well of the 8-well plate for imaging. All transfers of GUVs were carried out using trimmed pipette tips. Phosphate buffered saline was made by dissolution of tablets (ThermoFisher) in deionised water. The concentrations of the components are as follows: NaCl at 8.0 g L^{-1}, KCl at 0.2 g L^{-1}, Na_2HPO_4 at 1.15 g L^{-1}, KH_2PO_4 at 0.2 g L^{-1}.

4.5 Preparation of GPMVs for imaging

THP-1 cells grown in RPMI (Roswell Park Memorial Institute) medium suspended in growth medium were washed with an isotonic GPMV buffer (150 mM NaCl, 10 mM HEPES, 2 mM $CaCl_2$, pH 7.4), followed by incubation for 90 minutes at 37 °C with dithiothreitol (final concentration 1 mM) and paraformaldehyde (final concentration 25 mM). GPMVs were labelled in the same GPMV buffer with **NR-dyad** (final concentration 5 µM) and imaged directly.

4.6 Preparation of THP-1 cells for imaging

THP-1 (human monocytic) cells were centrifuged, and the pellet was washed with L15 three times. The cells were then re-suspended in PBS and **NR-dyad** was added (final concentration either 2 or 5 µM). The cells were then incubated with **NR-dyad** at either 37 °C or 4 °C for between 1 min and 15 min, then washed with L15 to remove the unbound dye and suspended in L15 buffer for imaging. In some examples, 0.02% sodium azide was added to the incubation step to minimise endocytosis.

4.7 RESOLFT Microscopy

RESOLFT microscopy was performed on a modified Abberior Instruments RESOLFT microscope (Abberior Instruments, Gottingen, Germany), equipped with excitation lasers at 485 594 nm

(pulsed 80 ps at 80 MHz, LightUp594, Abberior Instruments) and 640 nm (pulsed (80 ps at 80 MHz) or CW, LDH-D-C-640P, Picoquant), and customised to provide a 405 nm doughnut shaped laser via a vortex phase mask (VPP-1b, RPC Photonics, Rochester, NY), placed in the path of the 405 nm source (Cobolt diode laser, CW). Shuttering of the lasers was achieved with acousto-optical modulators (MT110-A1.5-VIS, Photon Lines, Banbury, UK). Images were acquired with 100×/1.4 NA oil immersion objective lens (UPlanSApo 100×/1.4 oil, Olympus, Japan) and detected with photon counting avalanche photo diodes (restricted to detection ranges of 510–568 nm, 605– 635 nm or 650–755 nm). The microscope was operated with Imspector software (Abberior Instruments, Gottingen, Germany) and image analysis was carried out in Imspector and FIJI ImageJ. Lookup tables for the images are based on min/max pixel intensities for each image, with no correction for background. Zero on the lookup table corresponds to a zero-photon count. Laser powers, P, were measured at the back focal plane of the objective. Together with the FWHM of the focal laser intensity distribution, they allow for the calculation of the time-averaged intensity $I = P$ / [π(FWHM/2)2] and a pulse peak intensity $I_{peak} = I/(\tau f)$ with pulse width τ = 80 ps and repetition rate f = 80 MHz. The FWHM of the laser spot can be calibrated from images of 100 nm TetraSpeck beads taken with each laser, and are approximately 205 nm for the 405 nm laser, 225 nm for the 594 nm laser, and 235 nm for the 640 nm laser. These measurements give intensities for each laser as follows: 405 nm (P = 34–466 μW corresponds to I = 0.10–1.41 MW cm^{-2}); 594 nm (P = 0.46–3.96 μW corresponds to I = 1.2–10.0 kW cm^{-2}); 640 nm (P = 0.66–3.9 μW corresponds to I = 1.5–8.9 kW cm^{-2}).

4.8 Confocal microscopy (for colocalisation and spectral imaging)

Confocal images were obtained using a Zeiss LSM780 inverted laser scanning confocal microscope equipped with various excitation sources: 405 nm (diode laser, CW, 815 μW at 100%), 458/488/514 nm (multiline Ar-Ion laser, CW) and 594 nm (HeNe laser, CW, 84 μW at 100%). Detection was achieved with PMT non-descanned detectors or high sensitivity GaAsP arrays. Images were

acquired with a Plan Apochromat 63×/1.40 NA DIC M27 oil immersion objective. The microscope was operated via a PC running Zen software. Image analysis was carried out in FIJI ImageJ.

For spectral imaging, images were taken with 8.9 nm windows in the range 500–696 nm using excitation at 488 nm. The intensity in each window was used to construct an emission spectrum. For each vesicle composition, multiple sets of data were recorded, and the spectra averaged.

5. References

1. Z. Yang, J. Cao, Y. He, J. H. Yang, T. Kim, X. Peng and J. S. Kim, *Chem. Soc. Rev.*, **2014**, *43*, 4563.
2. B. J. Bezner, L. S. Ryan and A. R. Lippert, *Anal. Chem.*, **2020**, *92*, 309.
3. D. Wu, L. Chen, Q. Xu, X. Chen and J. Yoon, *Acc. Chem. Res.*, **2019**, *52*, 2158.
4. K. P. Carter, A. M. Young and A. E. Palmer, *Chem. Rev.*, **2014**, *114*, 4564.
5. X. Qian and Z. Xu, *Chem. Soc. Rev.*, **2015**, *44*, 4487.
6. A. Kaur and E. J. New, *Acc. Chem. Res.*, **2019**, *52*, 623.
7. W. Chen, X. Ma, H. Chen, S. Hua Liu and J. Yin, *Coord. Chem. Rev.*, **2021**, *427*, 213584.
8. S.-C. Lee, J. Heo, H. C. Woo, J.-A. Lee, Y. H. Seo, C.-L. Lee, S. Kim and O.-P. Kwon, *Chem. Eur. J.*, **2018**, *24*, 13706.
9. A. S. Klymchenko, *Acc. Chem. Res.*, **2017**, *50*, 366.
10. H. Zhu, J. Fan, J. Du and X. Peng, *Acc. Chem. Res.*, **2016**, *49*, 2115.
11. S. Wang, W. X. Ren, J.-T. Hou, M. Won, J. An, X. Chen, J. Shu and J. S. Kim, *Chem. Soc. Rev.*, **2021**, *50*, 8887.
12. Y. M. Sigal, R. Zhou and X. Zhuang, *Science*, **2018**, *361*, 880.
13. L. Lau, Yin L. Lee, Steffen J. Sahl, T. Stearns and W. E. Moerner, *Biophys. J.*, **2012**, *102*, 2926.
14. G. Vicidomini, G. Moneron, C. Eggeling, E. Rittweger and S. W. Hell, *Opt. Express*, **2012**, *20*, 5225.
15. H. Fang, S. Geng, M. Hao, Q. Chen, M. Liu, C. Liu, Z. Tian, C. Wang, T. Takebe, J.-L. Guan, Y. Chen, Z. Guo, W. He and J. Diao, *Nat. Commun.*, **2021**, *12*, 109.
16. J. Chen, X. Jiang, C. Zhang, K. R. MacKenzie, F. Stossi, T. Palzkill, M. C. Wang and J. Wang, *ACS Sensors*, **2017**, *2*, 1257.
17. Z. Thiel and P. Rivera-Fuentes, *Angew. Chem. Int. Ed.*, **2019**, *58*, 11474.
18. D. S. Richardson, C. Gregor, F. R. Winter, N. T. Urban, S. J. Sahl, K. I. Willig and S. W. Hell, *Nat. Commun.*, **2017**, *8*, 577.
19. N. M. Mishina, A. S. Mishin, Y. Belyaev, E. A. Bogdanova, S. Lukyanov, C. Schultz and V. V. Belousov, *Nano Lett.*, **2015**, *15*, 2928.
20. K. Mishra, J. P. Fuenzalida-Werner, F. Pennacchietti, R. Janowski, A. Chmyrov, Y. Huang, C. Zakian, U. Klemm, I. Testa, D. Niessing, V. Ntziachristos and A. C. Stiel, *Nat. Biotech.*, **2022**, *40*, 598.
21. A. T. Frawley, V. Wycisk, Y. Xiong, S. Galiani, E. Sezgin, I. Urbančič, A. Vargas Jentzsch, K. G. Leslie, C. Eggeling and H. L. Anderson, *Chem. Sci.*, **2020**, *11*, 8955.
22. Y. Xiong, A. Vargas Jentzsch, Johannes W. M. Osterrieth, E. Sezgin, I. V. Sazanovich, K. Reglinski, S. Galiani, A. W. Parker, C. Eggeling and H. L. Anderson, *Chem. Sci.*, **2018**, *9*, 3029.
23. O. A. Kucherak, S. Oncul, Z. Darwich, D. A. Yushchenko, Y. Arntz, P. Didier, Y. Mély and A. S. Klymchenko, *J. Am. Chem. Soc.*, **2010**, *132*, 4907.
24. S. Chiantia, P. Schwille, A. S. Klymchenko and E. London, *Biophys. J.*, **2011**, *100*, L1.
25. Z. Darwich, A. S. Klymchenko, D. Dujardin and Y. Mély, *RSC Adv.*, **2014**, *4*, 8481.
26. R. Kreder, K. A. Pyrshev, Z. Darwich, O. A. Kucherak, Y. Mély and A. S. Klymchenko, *ACS Chem. Biol.*, **2015**, *10*, 1435.
27. E. Sezgin, F. Schneider, V. Zilles, I. Urbančič, E. Garcia, D. Waithe, A. S. Klymchenko and C. Eggeling, *Biophys. .J*, **2017**, *113*, 1321.
28. J. H. Kim, A. Singh, M. Del Poeta, D. A. Brown and E. London, *J. Cell Sci.*, **2017**, *130*, 2682.
29. D. B. Iaea and F. R. Maxfield, *PLoS One*, **2017**, *12*, e0188041.
30. D. I. Danylchuk, S. Moon, K. Xu and A. S. Klymchenko, *Angew. Chem. Int. Ed.*, **2019**, *58*, 14920.
31. M. N. Bongiovanni, J. Godet, M. H. Horrocks, L. Tosatto, A. R. Carr, D. C. Wirthensohn, R. T. Ranasinghe, J.-E. Lee, A. Ponjavic, J. V. Fritz, C. M. Dobson, D. Klenerman and S. F. Lee, *Nat. Commun.*, **2016**, *7*, 13544.

32. S. Moon, R. Yan, S. J. Kenny, Y. Shyu, L. Xiang, W. Li and K. Xu, *J. Am. Chem. Soc.*, **2017**, *139*, 10944.
33. P. Carravilla, A. Dasgupta, G. Zhurgenbayeva, D. I. Danylchuk, A. S. Klymchenko, E. Sezgin and C. Eggeling, *Biophys. Rep.*, **2021**, *1*, 100023.
34. P. Greenspan and S. D. Fowler, *J. Lipid Res.*, **1985**, *26*, 781.
35. J. Levitt, P.-H. Chung and K. Suhling, *J. Biomed. Opt.*, **2015**, *20*, 096002.
36. D. Lingwood and K. Simons, *Science*, **2010**, *327*, 46.
37. K. Weise, S. Kapoor, C. Denter, J. Nikolaus, N. Opitz, S. Koch, G. Triola, A. Herrmann, H. Waldmann and R. Winter, *J. Am. Chem. Soc.*, **2011**, *133*, 880.
38. H. Sunshine and M. L. Iruela-Arispe, *Curr. Opin. Lipid.*, **2017**, *28*, 408.
39. S. Sengupta, R. Karsalia, A. Morrissey and A. K. Bamezai, *Sci. Rep.*, **2021**, *11*, 13970.
40. Y. Bagheri, A. A. Ali, P. Keshri, J. Chambers, A. Gershenson and M. You, *Angew. Chem. Int. Ed.*, **2022**, *61*, e202112033.
41. E. Teissier and E. I. Pécheur, *Eur. Biophys. J.*, **2007**, *36*, 887.
42. M. Lorizate, T. Sachsenheimer, B. Glass, A. Habermann, M. J. Gerl, H. G. Kräusslich and B. Brügger, *Cell Microbiol.*, **2013**, *15*, 292.
43. R. A. Dick, S. L. Goh, G. W. Feigenson and V. M. Vogt, *P. Nat. Acad. Sci.*, **2012**, *109*, 18761.
44. O. H. Griffith, P. J. Dehlinger and S. P. Van, *J. Membrane Biol.*, **1974**, *15*, 159.
45. D. L. Worcester and N. P. Franks, *J. Mol. Biol.*, **1976**, *100*, 359.
46. S. A. Simon, T. J. McIntosh and R. Latorre, *Science*, **1982**, *216*, 65.
47. T. Parasassi, G. De Stasio, A. d'Ubaldo and E. Gratton, *Biophys. J.*, **1990**, *57*, 1179.
48. A. T. Frawley, K. G. Leslie, V. Wycisk, S. Galiani, D. Shrestha, C. Eggeling and H. L. Anderson, *ChemPhysChem*, ***2023***, e202300125.
49. C. Reichardt, *Solvents and Solvent Effects in Organic Chemistry*, Wiley, **2002**.
50. A. Weller, *Pure Appl. Chem.*, **1968**, *16*, 115.
51. T. B. Demissie, K. Ruud and J. H. Hansen, *Organometallics*, **2015**, *34*, 4218.
52. N. G. Connelly and W. E. Geiger, *Chem. Rev.*, **1996**, *96*, 877.
53. F. Schneider, D. Waithe, M. P. Clausen, S. Galiani, T. Koller, G. Ozhan, C. Eggeling and E. Sezgin, *Mol. Biol. Cell*, **2017**, *28*, 1507.
54. T. Baumgart, S. T. Hess and W. W. Webb, *Nature*, **2003**, *425*, 821.
55. E. Sezgin, I. Levental, M. Grzybek, G. Schwarzmann, V. Mueller, A. Honigmann, V. N. Belov, C. Eggeling, U. Coskun, K. Simons and P. Schwille, *Biochim. Biophys. Acta.*, **2012**, *1818*, 1777.
56. Z. Gerstle, R. Desai and S. L. Veatch, *Methods. Enzymol.*, **2018**, *603*, 129.

6. Appendix

6.1 Super-resolution image analysis script

```
import numpy as np
import scipy as sp
from scipy import stats
from scipy.optimize import curve_fit
import matplotlib.pyplot as plt
import math
import os


wd = os.getcwd()
file_list = []
for file in os.listdir(wd):
   if file.endswith('.txt'):
      file_list.append(file)
number_of_files = len(file_list)
channel_array_size = (int(number_of_files)/3) +3
print(channel_array_size)

conf_array = [0] * int(channel_array_size)
apd2_array = [0] * int(channel_array_size)
apd3_array = [0] * int(channel_array_size)


for file in file_list:
   im_id = file.split('_')
   im_id = im_id[8].split('.')
   image_number = im_id[0]
   ch_id = file.split('=')
   ch_id = ch_id[1].split('.')
   channel_number = ch_id[0]
   membrane_id = image_number + "_" + channel_number


   if channel_number == "0-C1":
      conf_array[int(image_number)] = file
   if channel_number == "0-C4":
      apd2_array[int(image_number)] = file
   if channel_number == "0-C5":
      apd3_array[int(image_number)] = file

print(apd2_array)
print(apd3_array)
print(conf_array)

with open('fitting.out', 'a') as outputfile:
   print("filename", ",", "confocal res", "," , "APD2 res", "," , "APD2 contr", ",", "APD2 enh", ",",
"APD3 res" , ",", "APD3 contr" , ",", "APD3 enh", file=outputfile)
```

```
for i in range(0, len(conf_array)):
    file1 = conf_array[i]
    file2 = apd2_array[i]
    file3 = apd3_array[i]
    if file1 == 0:
        print('no file', file=outputfile)
    else:
        print('\n', file1, ',' , end = ' ', file=outputfile)
        fit_array = []
        #import text file as array
        array = np.loadtxt(file1)

        #define min threshold for pixels to count
        threshold = 0.3*array.max()

        #define new array b as coordinates of pixels over threshold
        arrayb = np.nonzero(array > threshold)

        dev0 = np.std(arrayb[0])
        dev1 = np.std(arrayb[1])

        #fit curve to thresholded membrane making sure horizontal

        if dev0 < dev1:
            coefs = np.polyfit(arrayb[1], arrayb[0], deg=2)
        else:
            coefs = np.polyfit(arrayb[0], arrayb[1], deg=2)

        poly = np.poly1d(coefs)
        #create data from poly to plot
        x_model = np.linspace(0, 50, 50)

        #find tangent at x = 16, 19, 22, 25, 28, 31, 34
        deriv = np.polyder(coefs)
        pointval_list = [16, 19, 22, 25, 28, 31, 34]
        for xx in pointval_list:


            fig, axs = plt.subplots(2)
            if dev0 < dev1:
                axs[0].scatter(arrayb[1], arrayb[0])
            else:
                axs[0].scatter(arrayb[0], arrayb[1])
            axs[0].plot(x_model, poly(x_model), color='r')
            axs[0].set_xlim([0, 50])
            axs[0].set_ylim([0, 50])



            y_val_at_point = np.polyval(coefs, xx)
            slope_at_point = np.polyval(deriv, xx)
```

```
minX = 0
maxX = 50

ylow = (minX -xx) * slope_at_point + y_val_at_point
yhigh = (maxX -xx) * slope_at_point + y_val_at_point

#find normal at x = xx and define equation
norm_slope = -1 / slope_at_point
norm_yint = y_val_at_point - ((norm_slope)*xx)
minY = 0
maxY = 50
norm_xlow = -norm_yint/norm_slope
norm_xhigh = (maxY - norm_yint)/norm_slope

#normal equation: slope = norm_slope, yint = norm_yint

#extract data for gaussian fitting along normal line
gauss_array_x = []
gauss_array_y = []

for i in np.arange(0, 50, 0.1):
    x = np.floor((i - norm_yint) / norm_slope)
    if int(x) < 0 or int(x) > 49:
        pass
    else:
       gauss_array_x.append(int(x))
       gauss_array_y.append(int(np.floor(i)))

len_gauss_int_x_y = len(gauss_array_x)

#update matplotlib
axs[0].plot([minX, maxX], [ylow, yhigh], color='g')
axs[0].plot([norm_xlow, norm_xhigh], [minY, maxY], color='k')
axs[0].plot(gauss_array_x, gauss_array_y, color='y')


#find length of normal to plot gaussian along using pythagoras
gauss_intensity = []
A = ((-norm_yint)/norm_slope)
B = ((50 - norm_yint)/norm_slope)
b2 = (A-B)**2
a2 = (50)**2
c = math.sqrt((b2 + a2))
c_nm = c*40
c_ongraph = c_nm*len_gauss_int_x_y/500
gauss_dist = np.linspace(0, c_ongraph, len_gauss_int_x_y)

for (i,j) in zip(gauss_array_x, gauss_array_y):
   if dev0 < dev1:
      gauss_intensity.append(array[j, i])
   else:
```

```
                gauss_intensity.append(array[i, j])

            #define guassian fit and parameters
            def gauss(x, h, a, x0, sigma):
              y = h + a*np.exp(-(x-x0)**2/(2*sigma**2))
              return y
            #give good guesses for p0
            a_0 = np.amax(gauss_intensity)
            a_0_i = np.argmax(gauss_intensity)
            x_0 = gauss_dist[a_0_i]
            parameters, covariance = curve_fit(gauss, gauss_dist, gauss_intensity, p0=[30, a_0, x_0,
150])

            fit_h = parameters[0]
            fit_a = parameters[1]
            fit_x0 = parameters[2]
            fit_sigma = parameters[3]

            fit_y = gauss(gauss_dist, fit_h, fit_a, fit_x0, fit_sigma)
            FWHM = 2.35482*fit_sigma
            roundFWHM = round(FWHM, 1)
            posFWHM = abs(roundFWHM)
            print(posFWHM, ',', end = ' ', file= outputfile)

            axs[1].plot(gauss_dist, gauss_intensity, 'o')
            axs[1].plot(gauss_dist, fit_y, '-')
            axs[1].text(0.8, 0.8, posFWHM)
            plt.savefig(file1 + "point" + str(xx) + ".png", format='png')
            plt.close()

    # DOUBLE GAUSSIAN FITS

            double_gauss_files = [file2, file3]
            for k in double_gauss_files:
              arrayd = np.loadtxt(k)

              #define arrayb so that array is oriented the correct way around to extract data
              threshold = 0.3*arrayd.max()

              #define new array bd as coordinates of pixels over threshold
              arraybd = np.nonzero(arrayd > threshold)

              dev0 = np.std(arraybd[0])
              dev1 = np.std(arraybd[1])

              gauss_intensity_d = []

              for (i,j) in zip(gauss_array_x, gauss_array_y):
                if dev0 < dev1:
                  gauss_intensity_d.append(arrayd[j, i])
                else:
```

```
                gauss_intensity_d.append(arrayd[i, j])

        print(len(gauss_dist))
        print(len(gauss_intensity))
        #define double guassian fit and parameters
        def gauss(x, h, a1, x0, a2, w2):
            y = h + a1*np.exp((-4*np.log(2)*(x-x0)**2)/(posFWHM**2)) + a2*np.exp((-
4*np.log(2)*(x-x0)**2)/(w2**2))
            return y
        #give good guesses for p0
        a_0 = np.amax(gauss_intensity_d)
        a_0_i = np.argmax(gauss_intensity_d)
        x_0 = gauss_dist[a_0_i]
        print(a_0)
        print(a_0_i)
        print(x_0)

        parameters, covariance = curve_fit(gauss, gauss_dist, gauss_intensity_d, p0=[30, a_0,
x_0, a_0, 150])

        fit_h = parameters[0]
        fit_a1 = parameters[1]
        fit_x0 = parameters[2]
        fit_a2 = parameters[3]
        fit_w2 = parameters[4]

        fit_y = gauss(gauss_dist, fit_h, fit_a1, fit_x0, fit_a2, fit_w2)
        FWHM_resolft = fit_w2
        RESOLFT_contr = fit_a2/(fit_a1 + fit_a2)
        roundFWHM_resolft = round(FWHM_resolft, 1)
        posFWHM_resolft = abs(roundFWHM_resolft)
        RESOLFT_enh = posFWHM/posFWHM_resolft
        print(posFWHM_resolft, ',', RESOLFT_contr, ',' , RESOLFT_enh , ',' , end = ' ', file=
outputfile)

        plt.plot(gauss_dist, gauss_intensity_d, 'o')
        plt.plot(gauss_dist, fit_y, '-')
        plt.text(0.8, 0.8, posFWHM_resolft)
        plt.savefig(k + "point" + str(xx) + ".png", format='png')
        plt.close()
```

Chapter 3

Diazocine as a FRET quencher for photoswitchable dyads

1. Introduction

1.1 Improving RESOLFT dyes

As discussed in the Introduction (Chapter 1, Section 2.4.2), reversible FRET quenching of fluorophores can be achieved effectively *via* isomerisation of a photoswitch to a highly absorbing, coloured form. (Figure 3.1A). Our group has previously reported dyads comprising cyanine and Atto fluorophores with a spironaphthoxazine photoswitch as a quencher (Figure 3.1B), for use as RESOLFT dyes. Upon isomerisation with 405 nm light, the photoswitch becomes broadly absorbing in the visible region, turning the dyad 'off' by FRET quenching. In the reverse direction, the photoswitch can be closed to its colourless form thermally or with red light, turning the fluorescent dye back 'on'.

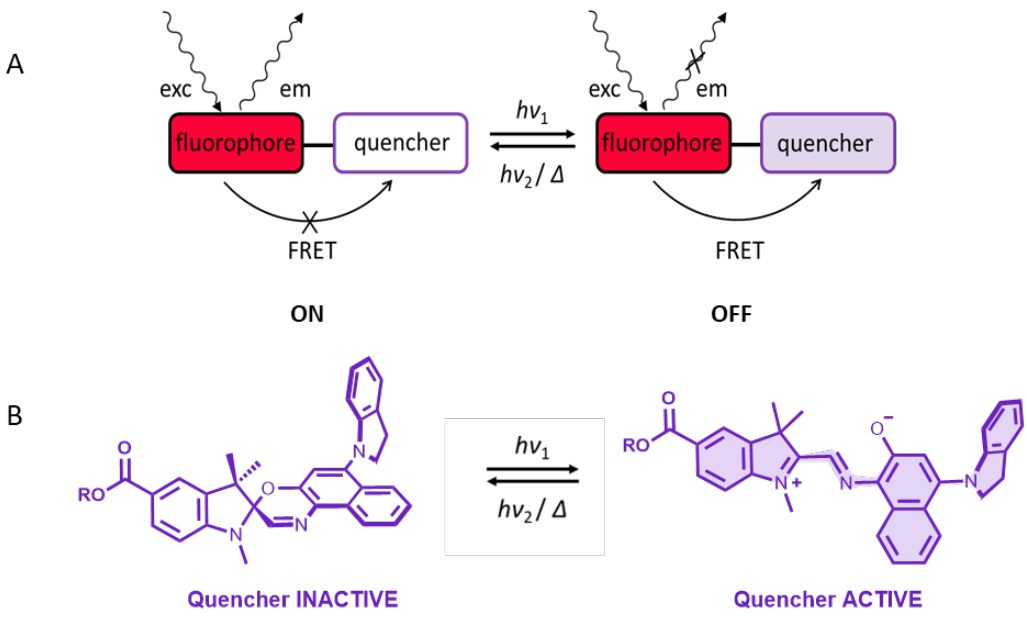


Figure 3.1: (A) Schematic diagram of a photoswitchable FRET dyad where a fluorophore is covalently linked to a reversibly switchable quencher. (B) The structures of the closed (inactive) and open (quenching) forms of the spironaphthoxazine photoswitch.

One of the main limitations of these systems is the fatigue that occurs in the photoswitch throughout the repeated isomerisation cycles. In cuvette studies of the switch, 10% photodegradation was observed after 100 switching cycles in CH_2Cl_2 (Figure 3.2A).[1] Comparable fatigue was observed under microscope conditions when the photoswitch was incorporated into

dyads, where approximately 15% degradation was observed over 100 imaging cycles of the dyad in vesicle membranes, with worse fatigue for higher laser power at 405 nm (Figure 3.2B).[2]

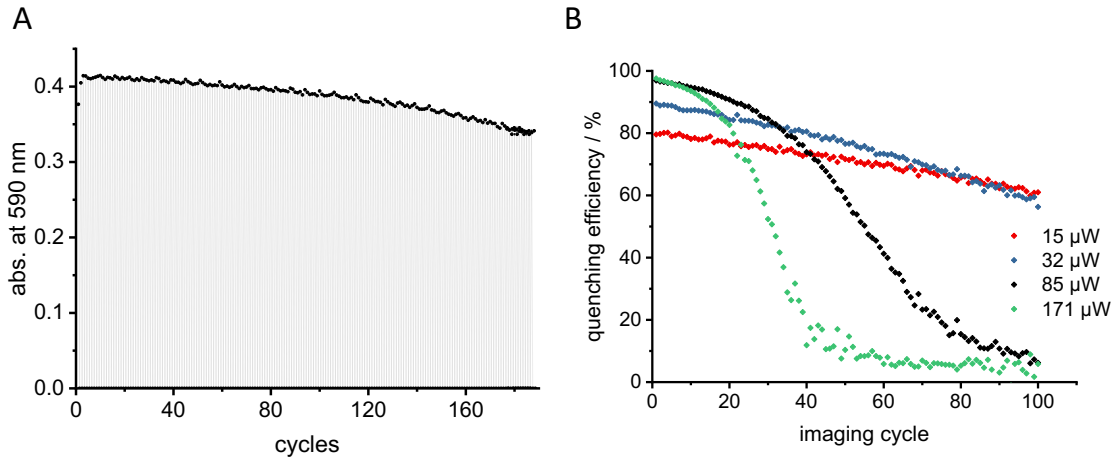


Figure 3.2: Fatigue curves of (A) spironaphthoxazine, measured by photoswitching in dichloromethane and (B) spironaphthoxazine as part of a cyanine-based dyad, measured at different 405 nm laser powers over 100 imaging cycles, in vesicles, by confocal microscopy.

As also outlined in the Introduction (Chapter 1, Section 2.4), the requirements for an effective photoswitch for a FRET quenching RESOLFT dyad include (i) visible light switching in both directions, (ii) high photostationary state distributions of both forms - a result of spectral separation of absorption bands, and the ratio of extinction coefficients and quantum yields of isomerisation, and (iii) a large change in absorption maximum upon switching, leading to optimal FRET overlap with a fluorophore in one form but not the other.

1.2 Choosing a photoswitch

Azobenzenes are commonly-used photoswitches that display high fatigue resistance, due to the absence of side reactions in the excited state.[3] Although unsubstituted azobenzene is isomerised with UV light, there are many substitutions that can lead to the absorption bands being moved into the visible region. In unsubstituted azobenzene, the difference between the relative absorption in the UV π - π* transition (stronger for *Z*) and the visible n - π* (stronger for *E*) gives rise to the ability to enrich isomers selectively (Figure 3.3).[4] There are two main strategies employed to make visible-light switching azobenzenes. These are (i) red-shifting the *E* isomer π - π* transition from the UV

into the blue region of the spectrum, and (ii) separating the normally overlapping n-π* transitions of the *E* and *Z* isomers in the visible region.[5]

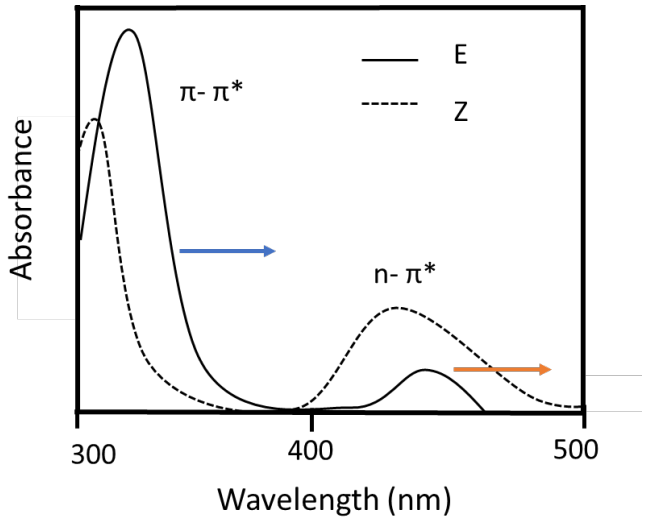


Figure 3.3: Representative spectra of *E* and *Z* azobenzenes, with π - π* and n - π* transitions marked. Design strategies to make azobenzenes addressable by visible light in both directions include (i) shifting the π - π* transition into the visible (blue arrow), and (ii) separating the n - π* transitions from each other (orange arrow).

Some examples of azobenzenes and their absorption maxima in each form are shown in Figure 3.4. Synthetic motifs that employ the first strategy include installing electron donor groups or donor/acceptor groups at the *para* positions (e.g. Figure 3.4, A),[6] and extending the π conjugation (Figure 3.4, B).[7] These strategies facilitate *E* to *Z* isomerisation with visible light, however often the π - π* transition of the *E* form begins to overlap with the n - π* of the *Z* form, so the two isomers can no longer be addressed selectively.[4] These substitutions can also destabilise the *Z* isomer, so it thermally relaxes back to *E* with a half-life on the timescale of milliseconds to seconds.[6]

Tetra-*ortho* substitution is the main strategy used to separate n - π* transitions, with the tetra-fluoro analogue showing very favourable photostationary state distributions in both directions (Figure 3.4, C),[8] although tetra-methoxy,[9] tetra-thiol,[10] and other halogen and chalcogen[11] derivates have also been reported. Finally, *ortho* ethylene linkers give well separated n - π* bands in diazocines (Figure 3.4, D).[12]

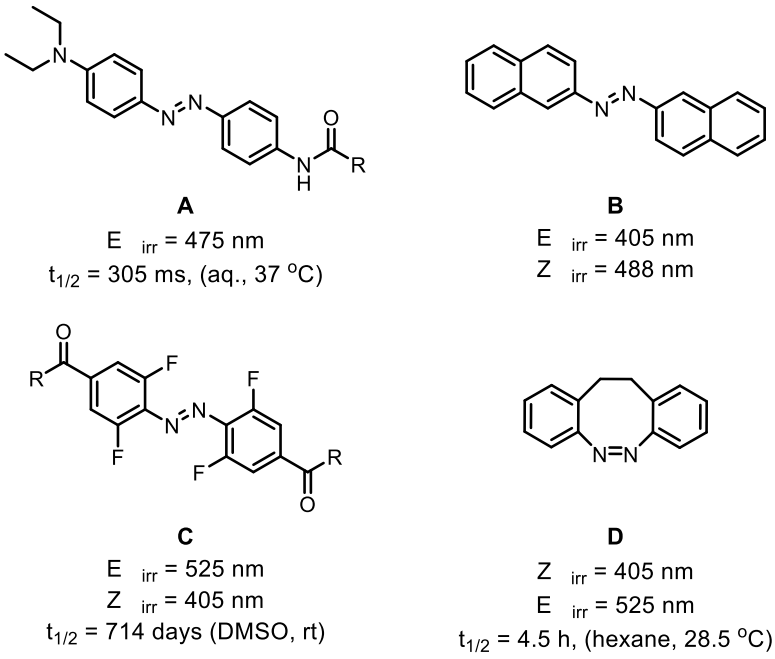


Figure 3.4: Examples of visible-light switching azobenzenes with the wavelength each isomer can be irradiated to induce isomerisation: (A) push-pull *para* substituted,[6] and (B) extended conjugation[7] push the π - π* transition into the visible region, whereas (C) tetra-*ortho* substituted azobenzenes[8] and (D) *ortho*-bridged diazocines[12] separate the n-π* visible transitions.

In addition to these classes, there are a large variety of heteroaryl-azobenzenes, some with absorption pushing into the visible region.[3,13,14] They are a relatively newer class of photoswitch however, and there are few derivatives that have been developed with very high photostationary state distributions and visible light switching in both directions, as well as convenient points of attachment for incorporation into materials.

Of the visible light switching azobenzenes discussed, diazocines in particular have well-separated absorption bands, with approximately 90 nm between the absorption maxima for the *Z* and *E* forms.[12] This feature lends itself well to separating the bright 'on' and dark 'off' state of a FRET-quenched dyad, as it is easier to find a fluorophore with spectral overlap with only one form of the photoswitch (Figure 3.5). The geometric constraints of the ethylene linker are responsible for shifting the relative energies of the n - π* transitions.[4] The ring strain also results in the *Z* form of the switch being the most thermally stable, which is unusual for azobenzenes (Figure 3.4).

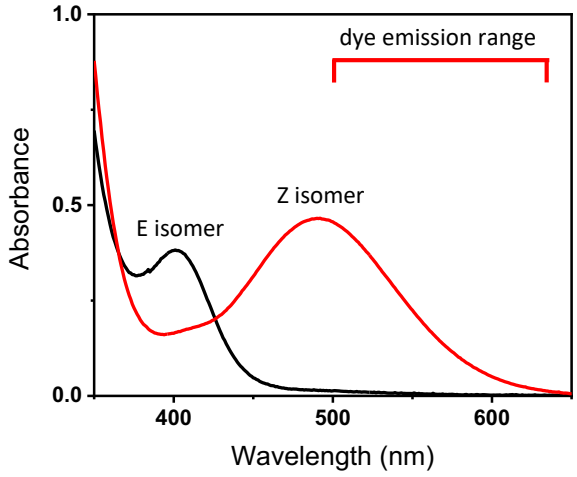


Figure 3.5: Absorption bands of example diazocine in *E* (black) and Z (red), showing ideal range for dye emission.

In addition to the fatigue resistance, visible light switching, and well separated absorption bands, diazocines have high photostationary state distributions in both directions (100% *Z* with 525 nm irradiation and up to 88% *E* with 405 nm irradiation).[15] This combination of properties makes them ideal candidates for incorporation into a dyad for super-resolution RESOLFT imaging. We envisaged attaching an orange-red emitting dye to a diazocine photoswitch, and reversibly activating FRET quenching by isomerisation to the more red-shifted *E* form (Figure 3.6).

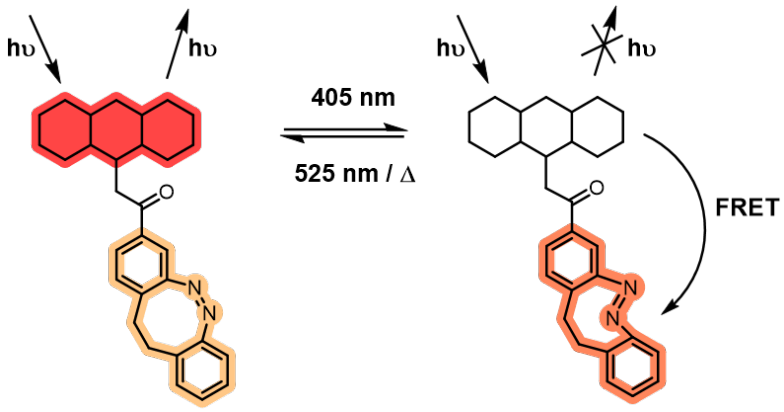


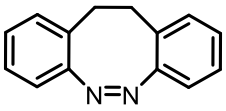
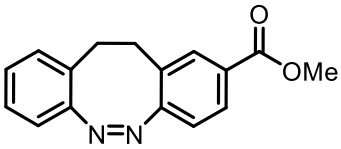
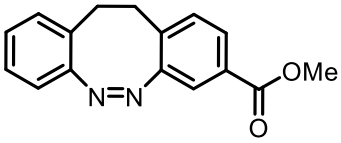
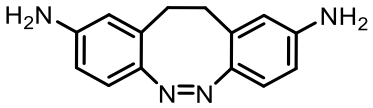
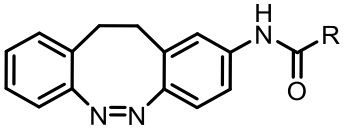
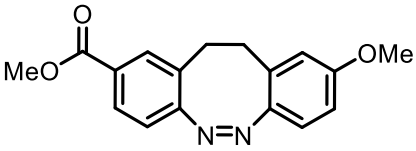
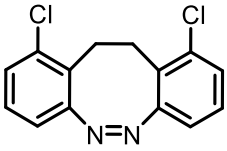
Figure 3.6: Schematic showing reversible FRET quenching of dyes with diazocine as photoswitchable quencher.

In order to link a fluorescent dye to the diazocine, we needed to choose a derivative with a synthetic handle which would not adversely impact the properties of the switch. The effects of various

substituents on the photophysical and photochemical properties of diazocines have been explored in the literature (for representative examples, see Table 3.1). Most substitution patterns either have little effect on the photophysical properties, or trade slightly red-shifted absorption maxima for much lower percentage composition of the *E* isomer at the photostationary state.[16] Electron-withdrawing substituents do not influence the PSS compared to the parent compound when installed at a variety of positions (Table 3.1, entry 2 and 3),[15] whereas more electron rich substituents have very detrimental effects on the PSS[17] (entry 4). This effect can be reduced by amidation (i.e. lowering the electron-donating ability of the substituent) but the PSS remains worse than using electron-withdrawing groups (entry 5).[16] Donor-acceptor systems were similarly poorly tolerated (entry 6), and the rarer *ortho*-ethylene substitution pattern (entry 7) appears to tolerate halogens but not more electron-donating substituents.[18] Alkyl chain substituents were shown to maintain the photophysical properties of the unsubstituted parent switch, however require considerably more synthetic effort to install on the diazocine core than other functional groups.[17] In all these examples, 100% recovery to the *Z* form is possible with green/red irradiation.

For these reasons, an ester-substituted photoswitch (entry 2) was chosen as the target FRET quencher, due to its favourable properties, ease of synthesis, and the ease of functionalising with a dye *via* an amide coupling.

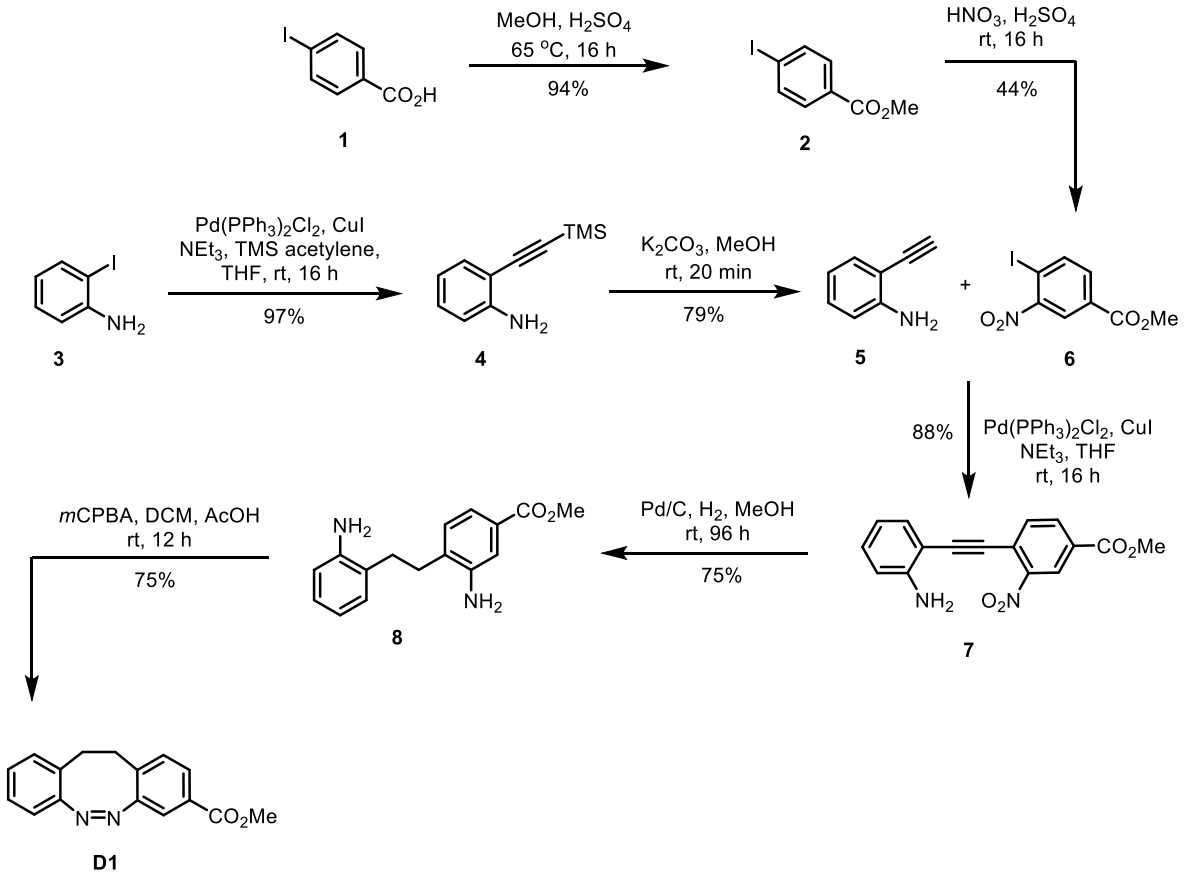
Table 3.1: Example diazocines and their photophysical properties.

Entry	Structure	λ_{max} *Z*	λ_{max} *E*	PSD (% E)	Solvent
1[15]		405	495	88	DMSO
2[15]		400	495	86	DMSO
3[15]		400	490	86	DMSO
4[17]		400	475	25	MeCN
5[16]		400	475	52	HEPES buffer
6[15]		410	500	45	DMSO
7[18]		400	490	78	MeOH

2. Results and Discussion

2.1 Photoswitch synthesis and characterisation

The photoswitch **D1** was made according to Scheme 3.1, following a literature procedure for the oxidative coupling of ethynyl-linked anilines.[15] In this synthesis, building block **6** was prepared from 4-iodobenzoic acid **1**, which was protected as the ester and nitrated at the 3-position. Building block **5** was prepared from 2-iodoaniline **3**, which underwent a Sonogashira reaction with TMS-acetylene to install an alkyne, and subsequent deprotection of the TMS group. A second Sonogashira coupling of **5** with **6** gave compound **7**, which was globally reduced to furnish the ethane-linked dianiline **8**. Finally, *m*CPBA-mediated oxidation, as reported by the Trauner group,[15] gave photoswitch **D1** in good overall yields.



Scheme 3.1: Synthesis of photoswitch **D1.**

The photophysical properties of photoswitch **D1** were characterised in DMSO both for solubility, and for easy comparison to the literature.[15] UV-Vis switching experiments showed the photoswitch isomerises reversibly between the *Z* and *E* forms with blue (405 nm – to E enriched) and green (525 nm – to *Z* enriched) LEDs (Figure 3.7A). The photostationary state under 525 nm irradiation contains 100% *Z* isomer, whereas the photostationary composition under 405 nm irradiation is 72% *E* isomer, verified by proton NMR of an irradiated sample. This is slightly lower than the reported 86% with 390 nm irradiation, due to the slightly different ratio of extinction coefficients of each isomer at this wavelength. The thermally stable *Z* isomer is a pale-yellow colour, while the E isomer is orange (Figure 3.7B). Quantum yields of photoswitching were measured using the initial slope method[19] (see Section 4.4), for the E→Z and Z→E isomerisations, and are reported in Table 3.2. They are significantly lower than the values reported by Herges (50 and 72% respectively) ,[12] although these values were measured in a different solvent (MeCN rather than hexane) and using a different method, which assumes the forming product does not absorb at the switching wavelength (untrue in this case).

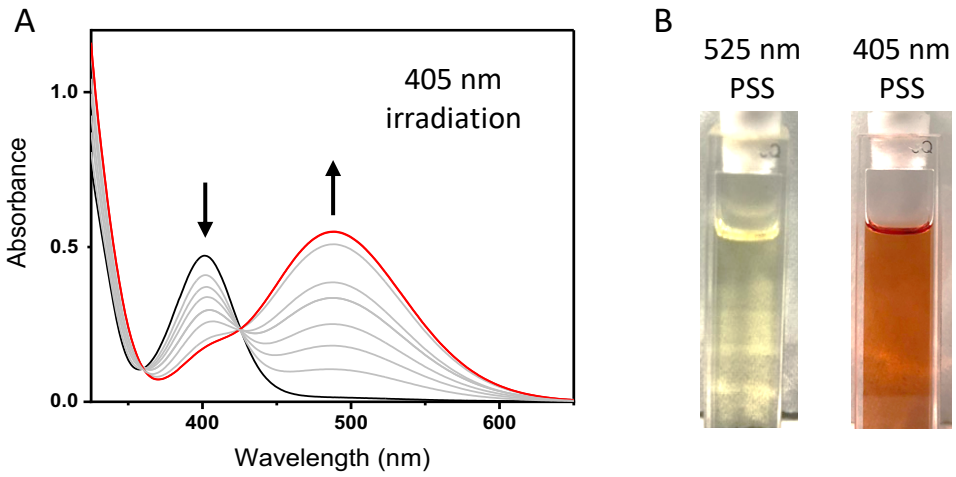


Figure 3.7A: Absorption spectra of photoswitch **D1** upon irradiation with a blue (405 nm) LED light in DMSO. The spectral changes were reversible upon irradiation with a green (525 nm) LED. B: A solution of photoswitch **D1** in DMSO at 405 nm and 525 nm PSSs.

Table 3.2: Photophysical properties of photoswitch **D1** in DMSO.

Photoswitch	**D1**
Z λ_{max}, (ε, M^{-1} cm^{-1})	404 (762)
E λ_{max}, (ε, M^{-1} cm^{-1})	493 (1040)
PSS 405 nm (% *E*)	72
PSS 525 nm (% *Z*)	100
$\Phi_{E\rightarrow Z}$	15
$\Phi_{Z\rightarrow E}$	35

2.2 Choosing a fluorophore

With the photoswitch in hand, we considered various rhodamine dyes as fluorescent partners for the **D1** quencher. These were Rhodamine 110, Sulforhodamine B, Rhodamine B, Atto590 and Silicon Rhodamine (Figure 3.8A), which had varying degrees of spectral overlap with the photoswitch (Figure 3.8B). As discussed in the Introduction (Chapter 1, Section 3.2), efficient FRET quenching requires good spectral overlap, spatial proximity, and aligned dipole moments of the donor and acceptor.

To make the best choice of dye for incorporation into the dyad, the efficiency of FRET quenching was calculated for each donor/acceptor pair, using the equations for FRET outlined in the Introduction (Chapter 2, section 3.2). Initially, Förster radii (R_0) were calculated using Equation 1:

$$R_0 = 0.2108 \left[\frac{\kappa^2 \varphi_D J(\lambda)}{n^4}\right]^{\frac{1}{6}} \qquad \text{(Equation 1)}$$

where κ^2 is the dipole orientation factor (assumed to be 2/3 given free rotation between the donor and acceptor), φ_D is the fluorescence quantum yield of the donor, *n* is the refractive index of the solvent (1.479 for DMSO), and $J(\lambda)$ is the spectral overlap integral, which is given by Equation 2.

$$J(\lambda) = \int f_D \varepsilon_A(\lambda) \lambda^4 \, d\lambda \qquad \text{(Equation 2)}$$

where f_D is the normalised donor emission spectrum, $\varepsilon_A(\lambda)$ is the acceptor molar extinction coefficient at wavelength λ. The data for each dye/switch pair are shown in Table 3.3. It can be seen that the more red-shifted the dye emission is, the shorter the R_0 becomes, as the overlap with the switch absorption reduces and FRET becomes less favoured.

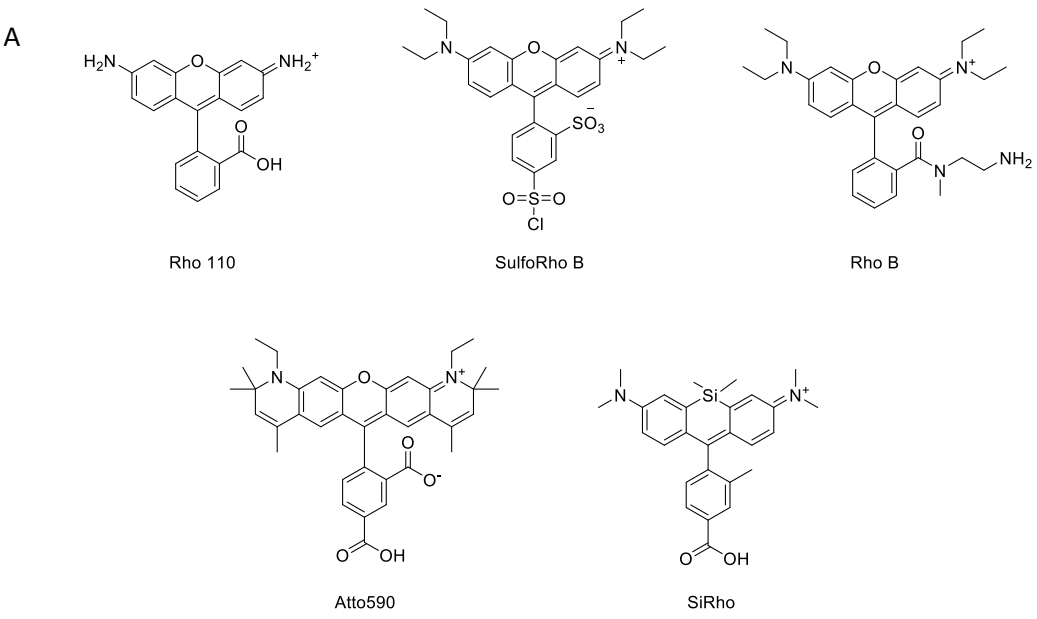


Figure 3.8A: Structures of candidate dyes. B: Calculated spectrum of photoswitch **D1** in 100% *trans* form, and measured emission spectra of candidate dyes in DMSO.

The efficiency of the FRET process, *E*, can be calculated from the Förster radius R_0, and the distance between the donor and acceptor, *r*, according to Equation 3.

$$E = \frac{1}{1+(\frac{r}{R_0})^6} \quad \text{(Equation 3)}$$

Table 3.3: Calculated Förster distances and FRET efficiencies for various donor dyes with acceptor **D1**. D-A distances are estimated from UFF forcefield energy minimised structures.

Dye	R_0 (Å)	D-A distance (Å)	FRET efficiency *E* (%)
Rho110	23.6	11.3	98.8
SulfoRho B	19.4	16.5	72.3
Rho B	17.2	11.3	92.6
Atto590	15.1	16.5	37.1
SiRho	10.6	16.5	6.8

When the distance between the donor and acceptor is considered in the FRET efficiency calculation, the order of dye suitability changes (Table 3.3). This is because some dyes have attachment points in the *ortho* position of the bottom rhodamine ring, and others at the *para* position, leading to differences in how close the donor and acceptor can get to one another. This difference (approximately 11.3 Å for *ortho* vs. 16.5 Å for *para*, assuming a short 2-carbon diamide linker, Figure 3.9) means that Rhodamine 110 and Rhodamine B are both good candidates for a FRET dyad, while despite good spectral overlap, SulfoRhoB would not be a good choice. There will be a degree of flexibility in these predicted distances but it is expected that the *ortho* substitution holds the switch significantly closer.

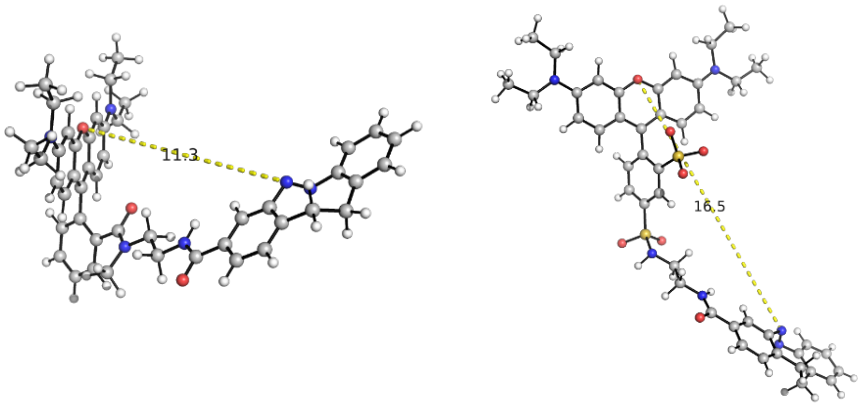


Figure 3.9: Example dyads with Rho B (left) and SulfoRho B (right), showing the distance between donor and acceptor for the *ortho* and *para* attachment points, minimised with UFF forcefield in Avogadro.

Both Rhodamine B and Rhodamine 110 have predicted FRET efficiencies over 90%, however Rhodamine B has an absorption spectrum better suited for excitation with our available 594 nm laser, which is red-shifted enough to avoid unwanted isomerisation of the photoswitch. Rhodamine B was therefore chosen as the best fluorophore candidate for this FRET dyad.

2.3 Dyad synthesis

One design consideration for rhodamine dyes with attachment *via* the ortho carboxylic acid is that primary and secondary amides can ring-close and form a non-fluorescent lactam, depending on the pH (Figure 3.10). The ratio of this equilibrium depends on both the nature of the xanthene group[20] and also the electronic and steric[21] character of the substituents on the amide nitrogen. By incorporating a tertiary amide, lactamisation can no longer occur and the fluorophore remains in a fluorescent state.[22]

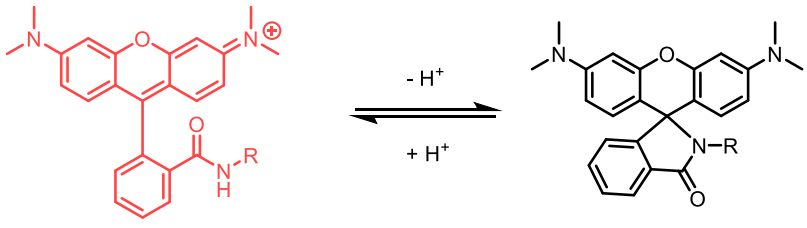
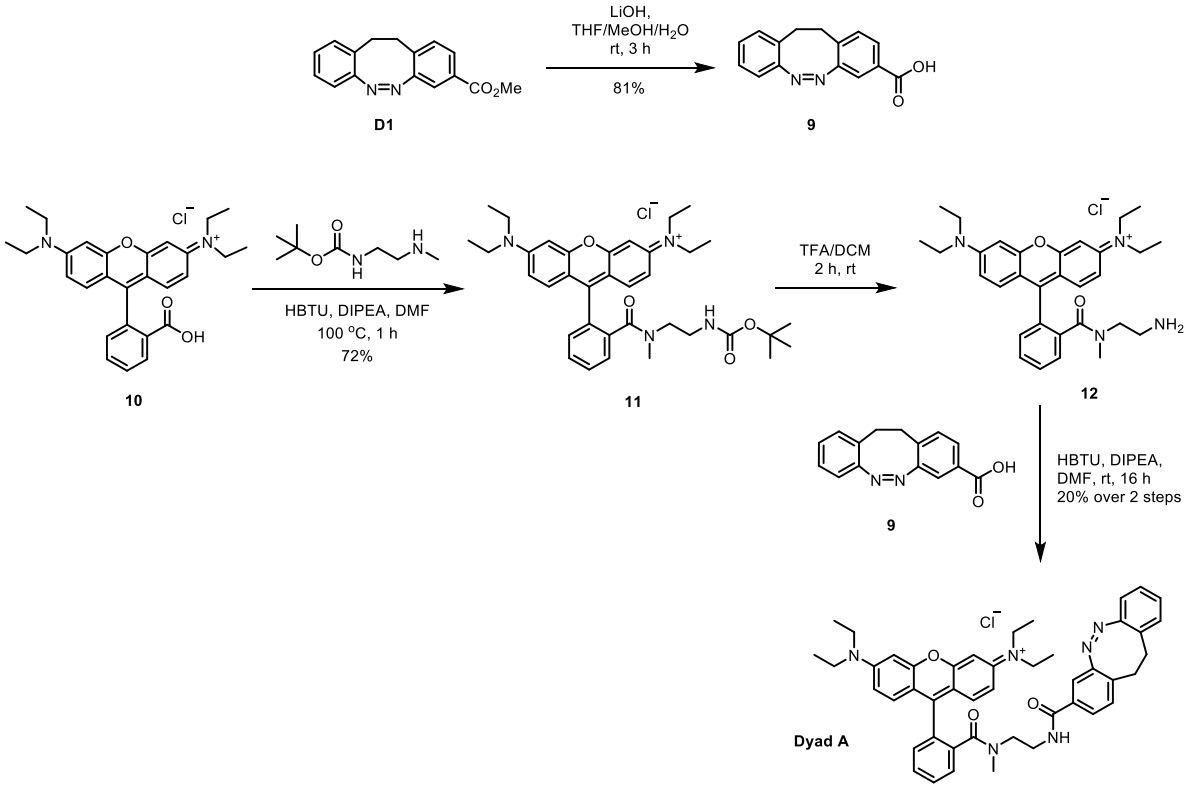


Figure 3.10: pH-dependent spirolactamisation of rhodamine derivatives causes switching between a fluorescent, coloured form and a non-fluorescent, colourless form.

Therefore, a tertiary amide was incorporated into the design of the dyad. Target **Dyad A** was synthesised according to Scheme 3.2. The *ortho* position of Rhodamine B (**11**) was coupled to boc-protected N-methyl-ethylene diamine to give a tertiary amide linker, which was then deprotected with trifluoroacetic acid (TFA). The **D1** ester was hydrolysed to the acid and amide coupling of the two fragments was performed using HBTU to give **Dyad A**.



Scheme 3.2: Synthesis of **Dyad A**.

Both the NMR spectrum of Rhodamine dye **11** and **Dyad A** in DMSO-d_6 showed evidence of *cis* and *trans* amide rotamers. A variable temperature NMR experiment of dye **11**, was conducted. The composition of the rotamers at room temperature (298 K) was approximately 70:30 *trans*:*cis* amide (the dominant conformation as drawn above). When the solution was warmed in 10-15 degree increments, the peaks showed coalescence between 345 and 355 K (Figure 3.11). The k_{exch} at this temperature was 67 Hz.

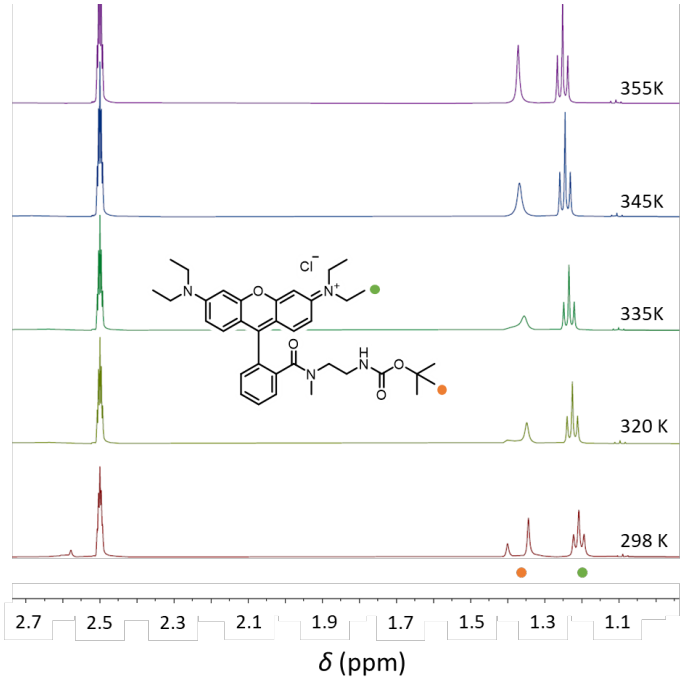


Figure 3.11: Variable temperature ^{1}H-NMR (500 MHz) of dye **11** in DMSO-d_6.

2.4 Dyad testing

The photophysical properties of **Dyad A** were measured in DMSO for comparison to the switch. The spectral features of the absorption and emission of the dyad are dominated by the dye contribution (Figure 3.12A), with the switch absorption not visible.

A switching experiment was then undertaken to see if the fluorescence spectrum of **Dyad A** could be turned off and on by isomerisation of the photoswitch. The fluorescence emission of a sample of **Dyad A** in DMSO was recorded (Figure 3.12B, spectrum 0, black). The sample was then irradiated with 405 nm light in order to isomerise the photoswitch, as in the analogous experiment on **D1** (Figure 3.7, above). After irradiation, the emission spectrum was recorded again (spectrum 1, red), showing a small (7%) reduction in the emission intensity. Further irradiation with 405 nm light did not increase the extent of quenching, and if a second spectrum was recorded immediately after the first, the intensity was restored to its original maximum (spectrum 2, grey).

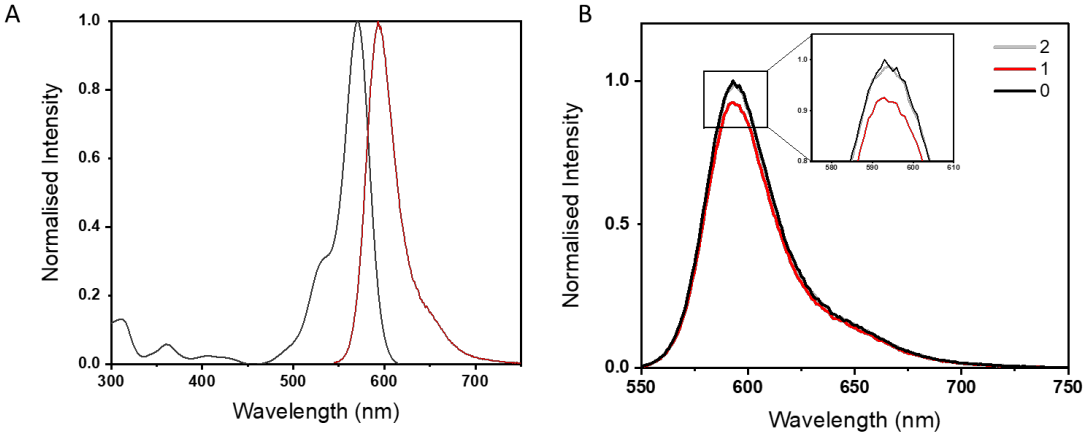


Figure 3.12A: Normalised absorption and emission spectra of **Dyad A** in DMSO at 298 K (λ_{exc} = 530 nm). B: Emission intensity of a sample of **Dyad A** in DMSO (0, black), after irradiation with blue (405 nm) LED light (1, red) and again after measurement 1 (2, grey) (λ_{exc} = 540 nm).

This result was unexpected, as the high calculated FRET efficiency, and a PSS dominated by the *E* isomer of **D1**, had indicated that the observed quenching would be approximately 70% under our LED isomerisation conditions. We also tested the switching behaviour on the microscope by staining DOPC vesicle membranes with **Dyad A** (Chapter 2, Section 4.4). Rather than irradiate with a donut-shaped laser to switch most of the dyes off and measure resolution, we used the 405 nm laser without the donut phase plate to switch off all dyes in the laser spot and measure the quenching efficiency. We imaged each vesicle first with 594 nm excitation, then irradiated with 405 nm, and imaged a second time with 594 nm excitation (Figure 3.13).

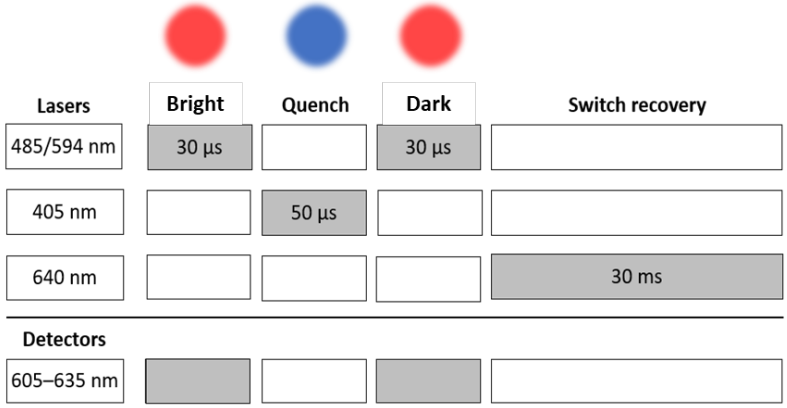


Figure 3.13: Laser sequence for microscope imaging of **Dyad A**, without the donut phase plate.

In a dyad which is able to turn off, the second image should be very dark, however we observed identical images before and after 'switching off' with 405 nm (Figure 3.14).

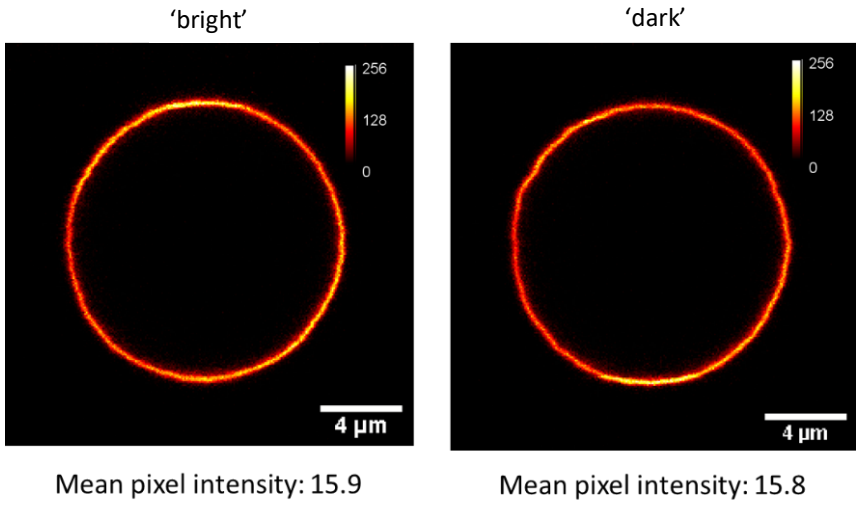


Figure 3.14: Example "dark" and "bright" microscopy images show no difference in mean pixel intensity across the image.

The mean pixel intensity of pairs of images stayed consistent as we varied 405 nm laser power, with a maximum of 12% quenching observed with 12 mW 405 nm irradiation power (Figure 3.15). It also stayed the same as we changed the irradiation sequence order (pixel-by-pixel, line-by-line or image-by-image), and the excitation wavelengths (485, 594 nm) and recovery times.

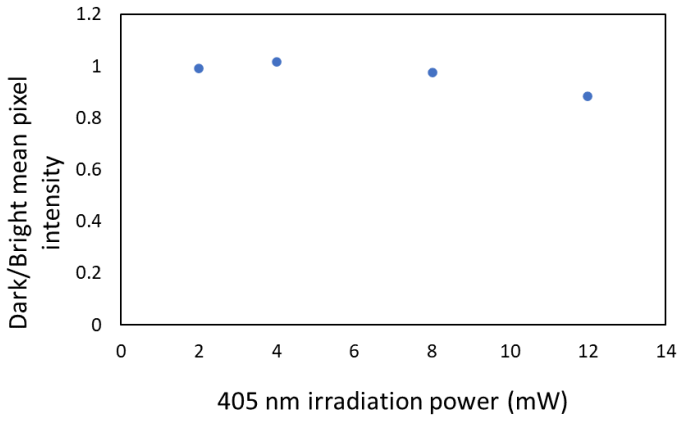


Figure 3.15: Quenching as a ratio of the mean pixel intensity in the dark image over a bright image with varying 405 nm laser power, in images of DOPC vesicles stained with **Dyad A**.

There are a number of possible explanations for the lack of fluorescence switching in **Dyad A**, which were investigated systematically. The first reason could be that the photoswitch is being isomerised

to the *E* form upon 405 nm irradiation, but then relaxing back thermally before the quenched fluorescence emission can be observed (Figure 3.16A). The second is that the photoswitch is being isomerised to the *E* form, but is then not able to participate in FRET, meaning the dye is always emissive (Figure 3.16B). The third is that irradiation with 405 nm is not causing isomerisation of the photoswitch at all, meaning the quenching form is never accessed (Figure 3.16C). The fourth is that once isomerised to the *E* form, the dye is also being excited by the 405 nm irradiation, and efficiently undergoing FRET, which photoisomerises the switch back to the *Z* form, leading to a greatly altered photostationary state in the dyad compared to the switch alone (Figure 3.16D).

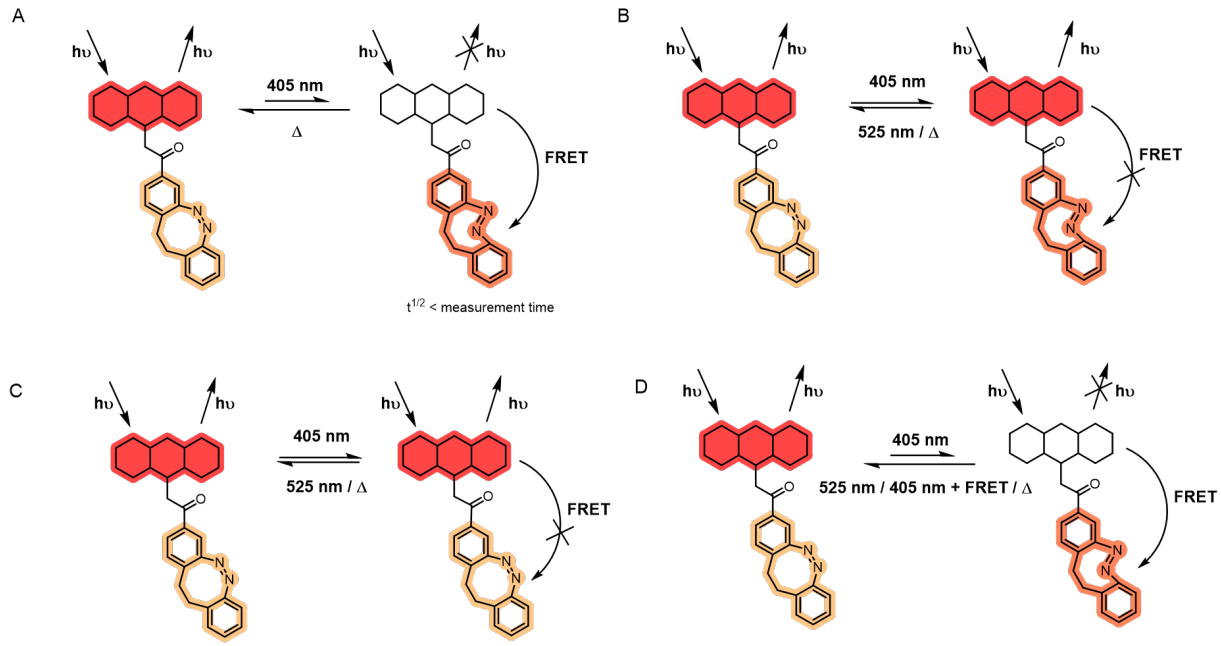


Figure 3.16: Different models for the lack of fluorescence quenching observed in **Dyad A** after isomerisation with 405 nm light. (A) Thermal relaxation occurs faster than the quenched form is able to be measured. (B) FRET is not able to occur to the *E* isomer of the photoswitch. (C) The photoswitch is not isomerised. (D) Dye excitation and subsequent FRET occurs so efficiently that the equilibrium composition does not contain very much *E* diazocine.

In order to investigate the first hypothesis, the rate of thermal relaxation of **D1** after irradiation with 405 nm light was measured by ^{1}H NMR spectroscopy. The disappearance of the *E* form was fitted with a mono-exponential decay (Figure 3.17). The half-life was found to be 10.9 hours at 298 K in DMSO, which is on a similar timescale (hours) to many reported diazocine derivatives.[12] It is

not expected that modification of the methyl ester in diazocine **D1** to an amide in **Dyad A** would significantly change the half-life, based on the available data for similar molecules,[15] indicating that this is unlikely to be the reason the quenched form is not visible in the fluorescence experiments.

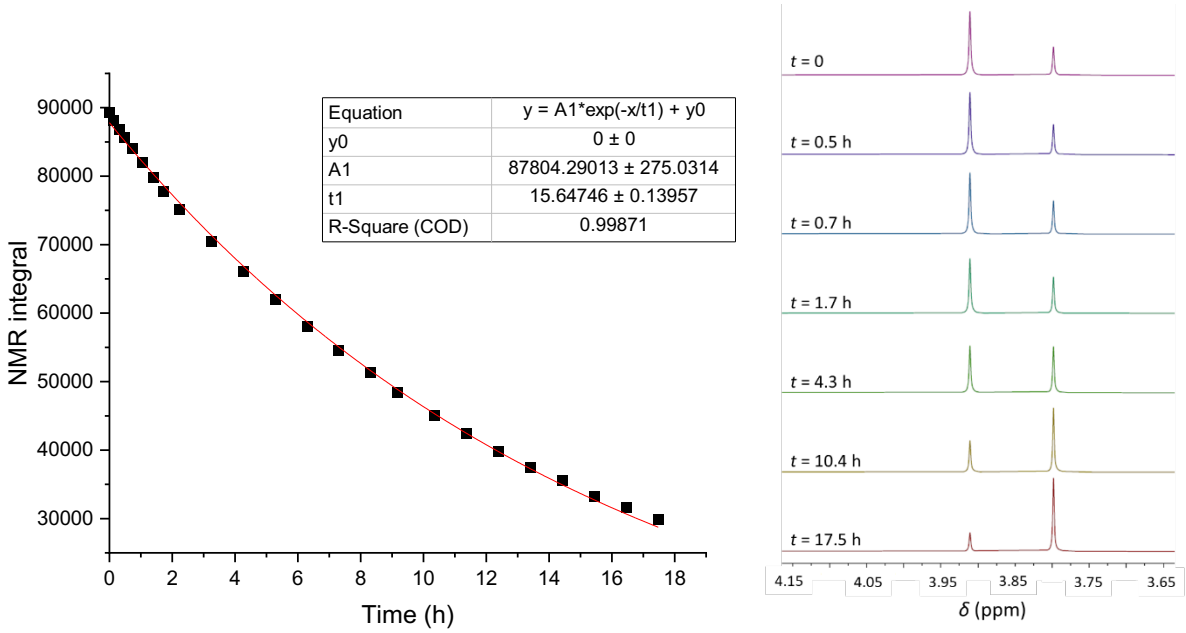


Figure 3.17: Thermal relaxation (measured by NMR) of *E* switch (left); k = 0.0638 h^{-1} and $t^{1/2}$ = 10.9 h. Selected ^{1}H NMR (500 MHz) spectra of methyl ester proton change over time (right). Spectra were recorded at 298 K in DMSO.

The second case, where the switch is successfully isomerised but is not capable of FRET quenching was investigated through an NMR experiment, where a sample of **Dyad A** is irradiated with blue light, and a ^{1}H NMR spectrum is recorded. When this experiment was performed, there was no change observed in the NMR spectrum. Furthermore, there were no peaks in the region expected for the *E* form of **D1** (Figure 3.18). A control experiment with a sample of the same concentration of **D1** in DMSO and irradiated with the same light source in the same type of NMR tube gave substantial switching. This indicates that the second hypothesis is unlikely to be the reason the quenched form of **Dyad A** is not visible in the fluorescence experiments, because the photoswitch is not isomerising.

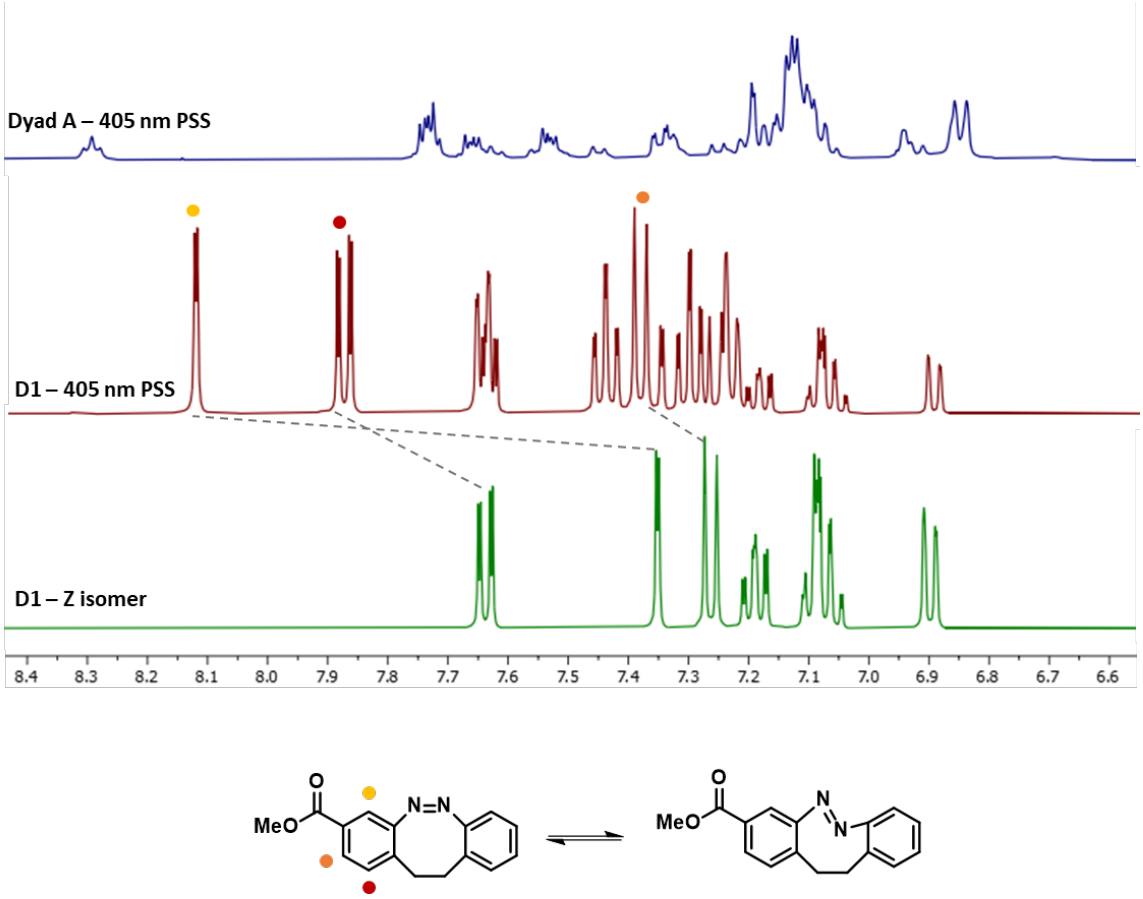


Figure 3.18: ^{1}H NMR spectra of switch **D1** (bottom) in the thermally-stable Z form, and at the 405 nm PSS (middle), showing appearance of diagnostic aromatic protons between 7.8 and 8.2 ppm, and Dyad A (top), after irradiation with 405 nm light showing no evidence of *E* isomer, and identical to the thermally-relaxed sample. NMR spectra in DMSO-d_6 at 293 K.

The third and fourth hypotheses are difficult to discriminate, however there is no obvious reason that the photoswitch should no longer isomerise under 405 nm light when it is incorporated into the dyad. Possible slower absorption due to, for example, competition from the rhodamine dye absorption should only increase the time taken to get to the photostationary state rather than change the PSS, however this would be unlikely to apply under the dilute conditions of a fluorescence experiment. Continuous irradiation with 405 nm light for one hour did not increase the amount of quenching, which implies the sample had reached a photo-equilibrium. This timescale was selected as switching experiments on the **D1** switch alone were all complete in ten minutes at similar concentrations and LED powers.

The fourth hypothesis – that is that the photoswitch is being isomerised but then returned to the *Z* form more efficiently due to energy transfer from the fluorophore – is the most logical based on the way the dyad has been designed, as the FRET process is expected to be highly efficient. Additionally, when you measure dyad emission again immediately after recording it in the quenched form (spectrum 1, Figure 3.12B), it returns to the original experimental maximum (spectrum 2). This indicates that the process of measuring the emission spectrum is changing the sample, and that exciting the dye is causing it to change. A control experiment was performed where **D1** at its 405 nm PSS was subjected to the fluorometer conditions used to acquire the emission spectra of **Dyad A** (λ_{exc} = 540 nm, as in Figure 3.12, above) and the absorption measured to monitor the *E*/*Z* composition. In the absence of the dye, the photoswitch did not relax back to the *Z* form under these conditions, implying that it is the dye absorption that is responsible for the isomerisation.

As the dye also absorbs light at 405 nm (ε_{405} = 2071 M^{-1} cm^{-1} vs 749 M^{-1} cm^{-1} for **D1**), irradiation at 405 nm will also excite the dye, leading to energy transfer, and an increased rate of isomerisation back to the *Z* form of any photoswitch in the *E* form. This is expected to alter the photostationary state under constant irradiation compared to that observed for the switch in isolation. A mathematical description of this process is outlined below.

2.5 A model for dyad switching

In photoswitch **D1**, the ratio of the two isomers under constant irradiation at a given wavelength (λ) can be expressed as an equilibrium state K_λ, which is the ratio of the rate of the forward and reverse isomerisation reactions:

$$K_\lambda = \frac{\varepsilon_Z \varphi_{Z\to E}}{\varepsilon_E \varphi_{E\to Z}} \qquad \text{(Equation 4)}$$

where ε is the extinction coefficient at the irradiation wavelength (in this case, 405 nm LED) and φ is the quantum yield of isomerisation at the same wavelength. K_λ relates to the PSS at that wavelength:

$$PSS_\lambda = \frac{K_\lambda}{1+K_\lambda} \quad \text{(Equation 5)}$$

For photoswitch **D1**, the PSS = 0.72 under 405 nm irradiation. However, when a dye is attached, the equation for K_λ changes as the dye can also absorb photons at the wavelength, then undergo energy transfer to the switch and increase the rate of reverse isomerisation, according to equation 6:

$$K_\lambda = \frac{\varepsilon_Z \varphi_{Z\to E}}{\varepsilon_E \varphi_{E\to Z} + \varepsilon_{dye} \varphi_{E\to Z} \psi_{FRET}} \quad \text{(Equation 6)}$$

where ψ_{FRET} is the FRET efficiency between the dye and switch. Taking into account the contribution to the rate of back isomerisation from the antenna dye, the $K_\lambda$expression for **Dyad A** is:

$$K_\lambda = \frac{749\ \mathrm{M^{-1}cm^{-1}} \times\ 0.15}{331\ \mathrm{M^{-1}cm^{-1}} \times\ 0.35\ + 2071\ \mathrm{M^{-1}cm^{-1}}\ \times 0.35\ \times 0.93}$$

$$K_\lambda = 0.142$$

And therefore:

$$PSS_\lambda = 0.125$$

This value of 13% *E* isomer at the PSS, is much closer to the 7% observed in the laboratory. While this does not take into account every excited state process that could occur, it provides a good model for the results we obtained with **Dyad A**. It is also possible that some FRET from the excited switch to the dye occurs, accounting for the lower experimental PSS of the dyad. These processes are summarised in Figure 3.19.

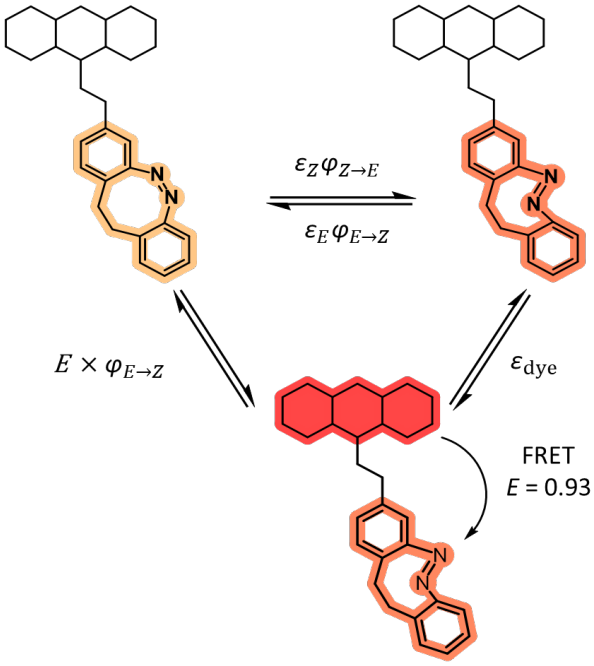


Figure 3.19: An expanded model for dyad switching, showing energy transfer from the dye under 405 nm irradiation contributing to the lower observed photostationary state of E isomer.

This issue has not been observed in the previous dyads made by the group, or specifically reported in the literature. We hypothesise that this is because the quantum yields of isomerisation for the diazocines are much higher than for the spironaphthoxazine.[1] Crucially, the quantum yield for switching from the quenching form back to the bright form is 1.1% for the spironaphthoxazine, which means it can absorb roughly 100 photons from the dye before returning the dyad to a bright fluorescent form. In the diazocine, this value is 35%, which means it can only absorb roughly 3 photons before returning the dyad to its bright form. Using the values for the spiroxazine with Atto590 Rhodamine in the above model, the PSS of the open photoswitch in the Dyad is 90%, compared to 97% alone, showing that the recovery isomerisation quantum yield of 1.1% for the spiroxazine is low enough that including the FRET pathway in its reverse isomerisation does not materially impact its PSS under 405 nm irradiation.

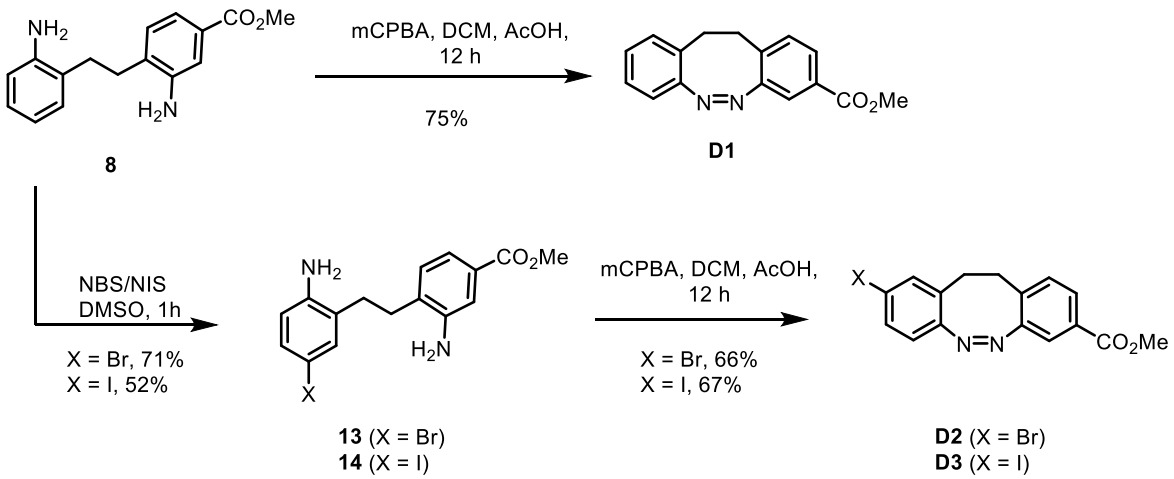
Based on this model, the best way to prevent this issue would be to use photoswitches with low quantum yields of isomerisation, in order to slow down unwanted reverse isomerisation, or to use

dyes with minimal absorption at the switching wavelength (405 nm), in order to selectively drive photoswitching without significant dye excitation.

2.6 Switch modifications

We investigated whether we could synthetically modify the diazocine photoswitch in order to lower its photoswitching quantum yields. Diazocines have some of the highest photoisomerisation quantum yields of all synthetic photoswitches.[23] Most synthetic derivatives of diazocine maintain these high quantum yields, including those with extended and freely-rotating aromatic substituents,[24] and heteroatom substitutions on the ethylene bridge.[25,26] Restricting their conformational flexibility further has also led to even higher isomerisation quantum yields (up to 80-90%), by removing access to inversions that lead to unproductive relaxation.[23]

We wanted to use halogenation of the diazocine core as a means to promote unproductive triplet state populations through an increased rate of intersystem crossing. The mechanism of diazocine switching is currently unknown, with few computational or experimental studies on the topic. However, the heavy atom effect is known to increase triplet populations in organic chromophores,[27] and the use of triplet sensitisation has been applied in other photoswitches such as diarylethenes to the detriment of the photoisomerization quantum yields.[28] Therefore, we envisaged a similar effect may be observed in diazocines, by favouring the rate of intersystem crossing and then non-radiative decay from the triplet state (see Jablonksi diagram in Introduction – Chapter 1, Section 1.1). Bromo- and iodo-substituted derivatives (**D2** and **D3** respectively) were synthesised according to Scheme 3.3 from a common intermediate in the synthesis of **D1**.



Scheme 3.3: Synthesis of diazocine photoswitch D1, and halogenated derivates D2 and D3.

The photophysical and photochemical properties of **D2** and **D3** were measured and compared to **D1**. The properties of the halo-substituted switches were mostly unchanged compared to the unsubstituted switch, with absorption spectra, PSSs, extinction coefficients, photochemical quantum yields showing similar values (Table 3.4), as do their spectral features (Figure 3.20). In particular, the photoisomerisation quantum yield was higher in the *E*→*Z* direction (the one of interest) for **D3**, but lower for **D2**. This suggests that either diazocines switch *via* the triplet excited state, or that switching in the singlet excited state is so fast that intersystem crossing does not compete even in **D3.** While the *E*→*Z* photoisomerization quantum yields vary by a factor of 2, this difference is not big enough to significantly reduce the rate of the unwanted reverse switching pathway if incorporated in a dyad.

Table 3.4: Photochemical quantum yields, photostationary states and maximum absorption coefficients for switches **D1-3** measured in DMSO at 293 K.

	D1	D2	D3
$\Phi_{Z\rightarrow E}$ (%)	15	13	10
$\Phi_{E\rightarrow Z}$ (%)	35	23	48
$PSS_{405\ nm}$ (%)	72	70	70
$PSS_{525\ nm}$ (%)	100	100	100
$\varepsilon_{\lambda max,\ Z}$ ($M^{-1}\ cm^{-1}$)	762	984	604
$\varepsilon_{\lambda max,\ E}$ ($M^{-1}\ cm^{-1}$)	1040	917	1063

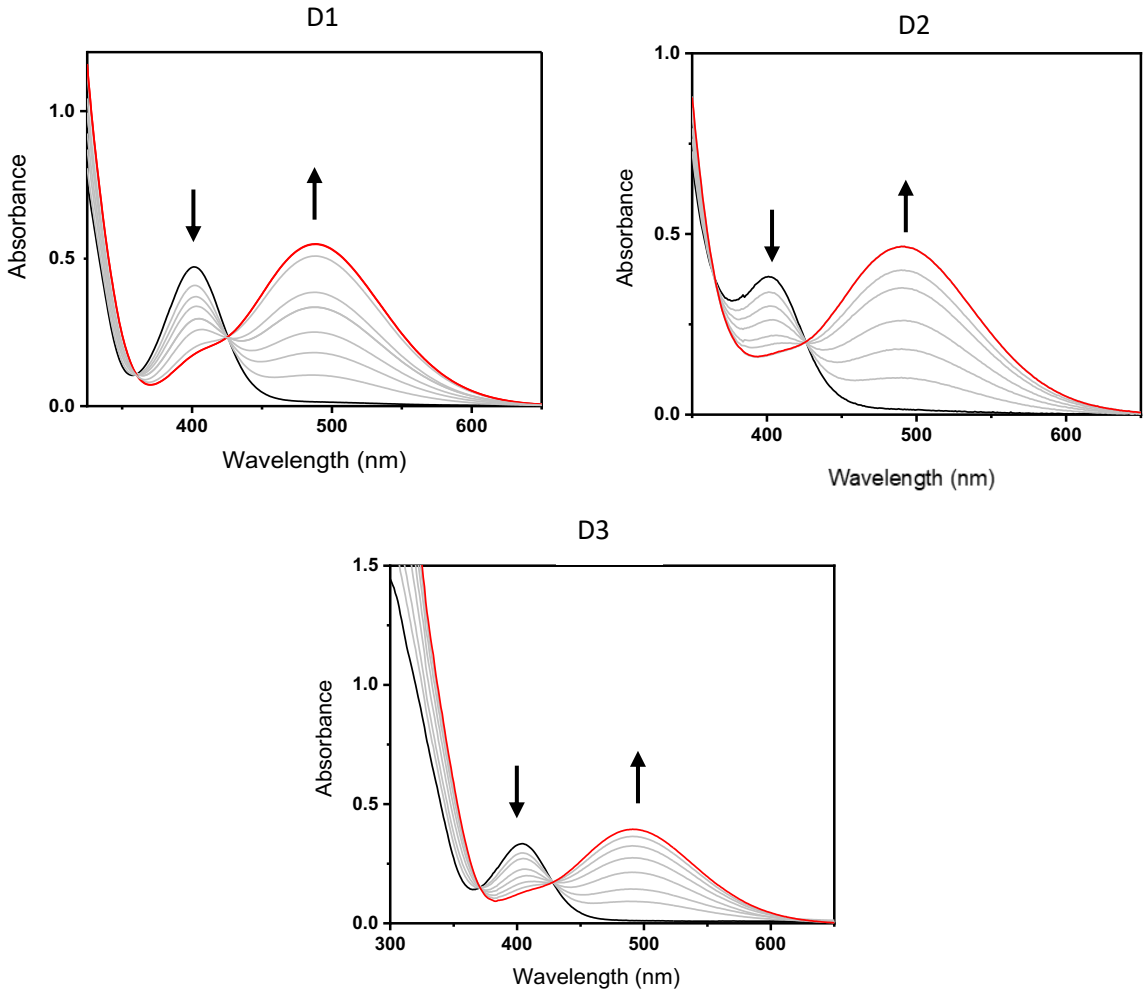


Figure 3.20: Absorption spectra of photoswitch **D1, D2,** and **D3** upon irradiation with a blue (405 nm) LED light in DMSO. The spectral changes were reversible upon irradiation with a green (525 nm) LED.

As the switching properties were not significantly changed, these photoswitches were not incorporated into dyads as it was anticipated they wouldn't have significantly different quenching behaviour. Further synthetic modifications could be undertaken, however introducing non-productive excited state pathways to lower the switching quantum yields is a difficult strategy without a more thorough understanding of the switching mechanism and energy levels in diazocines.

3. Conclusions and Future Work

In this project a new generation of FRET-quenched photoswitchable dyads has been investigated, with the aim of improving on the switching fatigue observed in previous designs.[1,2] The dyad was designed around a diazocine, a type of azobenzene photoswitch with excellent fatigue resistance.[12] This photoswitch was matched with Rhodamine B, which was predicted to have excellent FRET overlap, and favourable properties for imaging on the RESOLFT microscope.

The dyad was successfully synthesised, and its switching properties investigated. Surprisingly, it did not exhibit the on/off switching of fluorescence intensity that was expected. Several hypotheses were investigated to understand the reason for this, including fast thermal relaxation, poor FRET quenching, and a lack of photoswitching in the first place. These hypotheses were eliminated, leading us to conclude that the dye was acting as an antenna for the photoswitch at the switching irradiation wavelength, and shifting the equilibrium by increasing the rate of the reverse isomerisation. The effect of this is that the PSS of the switch in the dyad differed from the PSS of the switch alone.

A model was developed to describe this process using the quantum yields of switching and FRET efficiency, so that this reverse reaction contribution could be anticipated in the design of future FRET-switchable dyads. This analysis is consistent with the behaviour of a previously successful dyad, with good agreement with the observed and calculated photostationary states of the switch within a dyad. It was concluded that in order to minimise the effect of the dye increasing the reverse photoswitching reaction, switches with low quantum yields of photoswitching in this direction should be chosen, in combination with dyes that have very low molar exctinction coefficients at the wavelength of forward isomerisation.

Synthetic modifications of the diazacine photoswitch were undertaken in order to attempt to reduce the quantum yield of isomerisation in the reverse direction. Bromine and iodine susbtituents were installed on the diazocine in an attempt to reduce the quantum yield of

isomerisation by increasing the competing intersystem crossing excited state pathway via the heavy atom effect. This was ultimately unsuccessful, as the isomerisation quantum yields appear to be heavily dominated by the strained ring structure, and not sensitive to heavy atom Br or I substituents.

In the future, designs for FRET-quenched dyads should take into account this extra requirement for efficient photoswitchable quenching. The high quantum yields of photoswitching present in most azobenzene derivatives indicate that this is not an effective class of photoswitch for this type of FRET-quenching design. Photoswitches such as diarylethenes, which have some reported derivatives with up to an order of magnitude difference between the quantum yields in each direction,[29,30] as well as large changes in absorption spectrum on cyclisation, could be good candidates for further investigation. A balance, however, is needed between reducing unwanted reverse isomerisation, and still being able to return the switch to the dyad's 'on' form when irradiating at green/red wavelengths for iterative imaging cycles.

It would be advantageous to separate the role of the photoswitch from the role of the quencher in dyad design, so that there wasn't a need to balance so many different photophysical properties in one molecule, particularly as the choice of possible photoswitches is fairly limited. Exploring other mechanisms of quenching, such as photoinduced electron transfers, which are much more sensitive to the distance between a fluorophore and quencher than FRET, could allow us to harness the geometric change between photoswitch isomers rather than the spectral one. In this way the photoswitch is no longer directly required to quench the fluorophore, and their properties can be optimised separately. This idea is further expanded in Chapter 4.

4.Experimental Methods

4.1 General Synthetic Methods

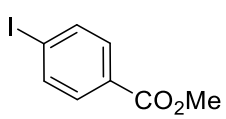
All reagents were purchased from commercial sources and used as received. Normal phase flash column chromatography was carried out using SiO_2 (60 Å pore size, 40–63 µm particle size, Aldrich, UK) as the stationary phase.

NMR spectra were acquired on a Bruker AVII400, AVIII400, or AVII500 instrument at 298 K. NMR chemical shifts are reported in ppm relative to $SiMe_4$ (δ = 0) and were referenced internally with respect to residual solvent protons. Coupling constants are reported in Hz. Multiplicity is denoted by s (singlet), sb (broad singlet), d (double), t (triplet), dd (doublet of doublet), dt (doublet of triplets), q (quartets). Electrospray mass spectrometry was carried out on a Waters Micromass LCT Premier XE spectrometer using 90:10 MeOH:H_2O (+0.1% formic acid) as the mobile phase. High-resolution mass spectra (HRMS) were obtained on a Bruker µTOF instrument or a Waters GCT.

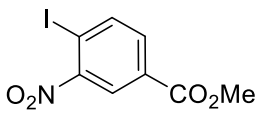
4.2 mCPBA titration

This titration was performed as described in the literature.[15] An unknown amount of I^- is oxidised to I_2 by mCPBA of unknown concentration. This is then reduced back to I^- with a known concentration of $Na_2S_2O_3$. Starch is used as the indicator whereby the final amounts of I_2 are made more vibrantly coloured when bound by starch. To a mixture of 5 wt% aqueous sulfuric acid (50 mL) and 10 wt% aqueous potassium iodide (1–2 mL) at 0 °C was added a solution of mCPBA in acetic acid (500 µL). The mixture was titrated with 0.1 M aqueous sodium thiosulfate until the brown color almost disappeared, then 1 wt% aqueous starch (1–2 mL) was added. The titration with sodium thiosulfate was continued until the black-blue color disappeared and a white suspension was obtained. The concentration of the solution of mCPBA directly corresponds to the necessary total volume of sodium thiosulfate solution ($VNa_2S_2O_3$) by the following relation: c(mCPBA) = ($VNa_2S_2O_3$ / 10 mL) * mol/L.

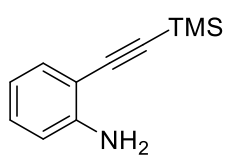
4.3 Synthesis and Characterisation



Methyl 4-iodobenzoate (2) Conc. sulfuric acid (215 µL, 4.03 mmol) was added to a suspension of 4-iodobenzoic acid (10.0 g, 40.3 mmol) in methanol (40 mL) and heated at reflux overnight, after which time the solids were fully dissolved. The reaction mixture was cooled to room temperature and saturated aqueous $NaHCO_3$ solution (50 mL) was added. The resulting suspension was extracted with ethyl acetate (2 × 50 mL), and the combined organic layers dried over anhydrous Na_2SO_4. The solvent was removed under reduced pressure to give compound **2** as a white crystalline solid (9.78 g, 93%) with spectra matching the literature.[31] **^{1}H NMR** (400 MHz, $CDCl_3$) *δ* 7.80 (d, *J* = 8.7 Hz, 2H), 7.74 (d, *J* = 8.7 Hz, 2H), 3.91 (s, 3H); **^{13}C NMR** (101 MHz, $CDCl_3$) δ 166.7, 138.1, 130.8, 129.7, 100.8, 52.4.

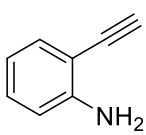


Methyl 4-iodo-3-nitrobenzoate (6) Conc. nitric acid (15.0 mL) was added dropwise to a solution of methyl 4-iodobenzoate **2** (8.7 g, 33.2 mmol) in conc. sulfuric acid (15 mL) at 0 ˚C. The reaction mixture was warmed to room temperature and stirred overnight, then poured over ice water. The resulting suspension was filtered, and the solids recrystallised from ethanol to give compound **6** as a pale yellow crystalline solid (4.50 g, 44 %) with spectra matching the literature.[32] **^{1}H NMR** (400 MHz, $CDCl_3$) δ 8.44 (d, *J* = 2.0 Hz, 1H), 8.14 (d, *J* = 8.2 Hz, 1H), 7.87 (dd, *J* = 8.2, 2.0 Hz, 1H), 3.96 (s, 4H); **^{13}C NMR** (101 MHz, $CDCl_3$) **ESI-MS** $[M+H]^+$ 308.0.

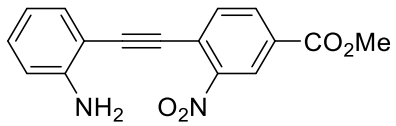


2-((Trimethylsilyl)ethynyl)aniline (4) was synthesised according to an adapted literature procedure.[15] Copper(I) iodide (68 mg, 358 µmol) was added to a degassed suspension of 2-iodoaniline **3** (3.14 g, 14.3 mmol), $Pd(PPh_3)_2Cl_2$ (252 mg, 358 µmol), triethylamine (4.0 mL, 28.7 mmol), and trimethylsilylacetylene (3.06 mL, 21.5 mmol) in anhydrous THF (30 mL). The reaction mixture was stirred overnight, then the volatiles

removed under reduced pressure. The solids were suspended in petrol ether (100 mL) and sonicated, then filtered and washed with further petrol ether (2 × 50 mL). The combined filtrate was evaporated under reduced pressure, and the crude residue was dissolved in dichloromethane and filtered through a silica plug. The solvent was removed under reduced pressure to give compound **4** as a dark red oil (2.63 g, 97%) with spectra matching the literature.[15] **^{1}H NMR** (400 MHz, $CDCl_3$) δ 7.33 (dd, *J* = 7.9, 1.6 Hz, 1H), 7.14 (td, *J* = 7.3, 1.6 Hz, 1H), 6.71 – 6.65 (m, 2H), 4.26 (sb, 2H), 0.32 (s, 9H); **^{13}C NMR** (101 MHz, $CDCl_3$) δ 148.4, 132.3, 130.0, 117.8, 114.3, 107.8, 102.0, 99.8, 0.3; **ESI-MS** $[M+H]^+$ 190.1.

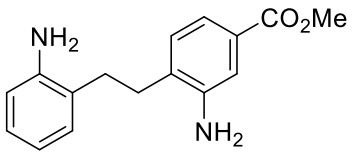


2-Ethynylaniline (5) was synthesised according to literature procedure.[15] Potassium carbonate (2.03 g, 14.7 mmol) was added to a solution of **4** (2.78 g, 14.7 mmol) in methanol (33 mL) and stirred at room temperature for 30 min, until the starting material was consumed (monitored by TLC). The reaction mixture was then diluted with dichloromethane (100 mL), and filtered. The filtrate was washed with water (50 mL), and then the aqueous wash extracted with dichloromethane (50 mL). The combined organic layers were dried over anhydrous Na_2SO_4, and the solvent removed under reduced pressure. The crude residue was purified with flash silica chromatography (20% ethyl acetate in petrol ether) to give compound **5** as a red oil (1.15 g, 67%) with spectra matching the literature. [15] **^{1}H NMR** (400 MHz, CDCl3) δ 7.38 (dd, *J* = 7.6, 1.3 Hz, 1H), 7.18 (td, *J* = 7.6, 1.7 Hz, 1H), 6.81 – 6.59 (m, 2H), 4.27 (sb, 2H), 3.43 (s, 1H); **^{13}C NMR** (101 MHz, $CDCl_3$) δ 148.6, 132.6, 130.2, 117.8, 114.4, 106.6, 82.6, 80.7; **ESI-MS** $[M+H]^+$ 118.0.

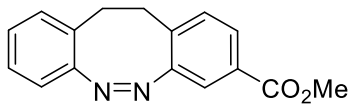


Methyl 4-((2-aminophenyl)ethynyl)-3-nitrobenzoate (7) was synthesised according to adapted literature procedure.[15] Copper(I) iodide (37 mg, 194 µmol) was added to a degassed suspension of compound **5** (1.00 g, 8.54 mmol), compound **6** (2.38 g 7.76 mmol), $Pd(PPh_3)_2Cl_2$ (136 mg, 194 µmol), and triethylamine

(2.16 mL, 15.5 mmol) in dry THF (20 mL). The reaction mixture was stirred overnight, then the volatiles removed under reduced pressure. The crude residue was dissolved in dichloromethane, then washed with water. The organic layer was dried over anhydrous Na_2SO_4, and the solvent removed under reduced pressure. The residue was then recrystallised from toluene to give compound **7** as a red crystalline solid (2.02 g, 88%) with spectra matching the literature.[15] **^{1}H NMR** (400 MHz, $CDCl_3$) δ 8.79 (d, J = 1.7 Hz, 1H), 8.23 (dd, J = 8.2, 1.7 Hz, 1H), 7.78 (d, J = 8.2 Hz, 1H), 7.39 (dd, *J* = 7.7, 0.5 Hz, 1H), 7.21 (ddd, *J* = 8.2, 7.3, 1.6 Hz, 1H), 6.77 – 6.65 (m, 2H), 3.98 (s, 3H); **^{13}C NMR** (101 MHz, $CDCl_3$) δ 164.8, 150.1, 148.2, 134.6, 133.6, 132.9, 131.9, 129.8, 126.4, 123.6, 117.7, 114.6, 105.8, 99.2, 91.0, 53.0; **ESI-MS** $[M+H]^+$ 297.1.

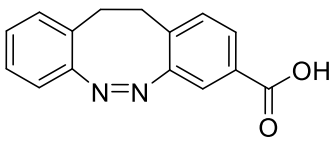


Methyl 3-amino-4-(2-aminophenethyl)benzoate (8) was synthesised according to adapted literature procedure.[15] Hydrogen gas was added to an evacuated flask of **7** (50 mg, 0.2 mmol) and Pd/C (10%, 20 mg) in MeOH (2 mL) and stirred for 4 days. The flask was then evacuated and re-filled with nitrogen, and the reaction mixture diluted with dichloromethane, then filtered over Celite. The solvent was removed under reduced pressure and the crude residue was purified with flash silica column chromatography (20% ethyl acetate in dichloromethane) to give **8** (34 mg, 75%) as a white solid with spectra that matched the literature.[15] **^{1}H NMR** (400 MHz, $CDCl_3$) δ 7.40 (dd, *J* = 7.8, 1.7 Hz, 1H), 7.34 (d, *J* = 1.7 Hz, 1H), 7.11 (d, *J* = 7.8 Hz, 1H), 7.08 – 7.00 (m, 2H), 6.75 (td, *J* = 7.4, 1.2 Hz, 1H), 6.70 (dd, *J* = 7.9, 1.3 Hz, 1H), 3.88 (s, 3H), 3.41 (s, 4H), 3.05 – 2.67 (m, 4H); **^{13}C NMR** (101 MHz, $CDCl_3$) δ 167.3, 144.4, 143.9, 131.5, 129.7, 129.6, 129.1, 127.5, 126.0, 120.3, 119.4, 116.7, 116.2, 52.0, 31.0, 30.7; **ESI-MS** $[M+H]^+$ 271.1.

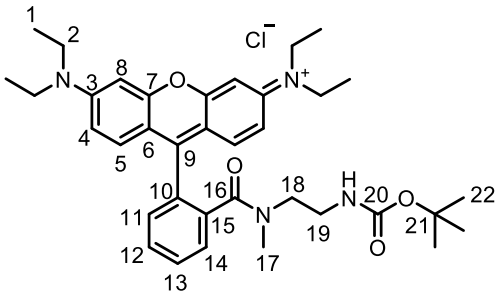


Methyl diazocine-3-carboxylate (D1) was synthesised according to literature procedure.[15] A freshly prepared and titrated (0.52 M, see

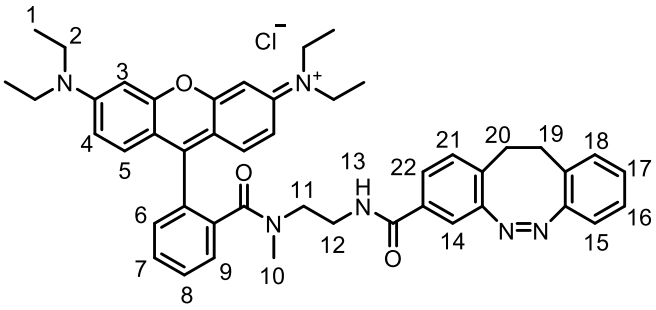
Section 4.2) solution of mCPBA (481 µL, 250 µmol) in acetic acid was added by syringe pump over a period of 12 hours under rapid stirring to a solution of the 2,2'-ethylenedianiline substrate **8** (34 mg, 125 µmol) in acetic acid/dichloromethane = 1/3 (3.1 mL). After the complete addition of the mCPBA solution, the mixture was stirred for 3 hours. The solvent was then removed under reduced pressure, the residue taken up in ethyl acetate (10 mL) and washed with saturated, aqueous sodium hydrogen carbonate (2 × 5 mL), followed by saturated aqueous sodium chloride (5 mL). The solution was dried over sodium sulfate, the solvent was removed under reduced pressure and the residue was purified by column chromatography (20% ethyl acetate in hexanes) to afford compound **9** (25 mg, 75%) as a yellow solid.**^{1}H NMR** (400 MHz, $CDCl_3$) δ 7.68 (dd, *J* = 7.9, 1.7 Hz, 1H), 7.49 (d, *J* = 1.7 Hz, 1H), 7.13 (td, *J* = 7.5, 1.6 Hz, 1H), 7.05 (d, *J* = 8.0 Hz, 1H), 7.03 – 6.95 (m, 2H), 6.84 (dd, *S* = 7.8, 1.3 Hz, 1H), 3.85 (s, 3H), 3.13 – 2.93 (m, 2H), 2.90 – 2.72 (m, 2H); **^{13}C NMR** (101 MHz, $CDCl_3$) δ 166.3, 155.4, 155.4, 133.8, 123.0, 129.7, 129.0, 128.2, 127.6, 127.4, 127.1, 120.2, 118.9, 52.3, 32.0, 31.5; **ESI-MS** $[M+H]^+$ 266.1.



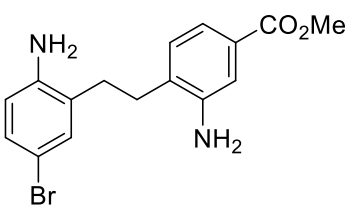
Diazocine-3-carboxylic acid (9) was synthesised according to literature procedure.[15] Compound **D1** (52 mg, 0.20 mmol) was dissolved in THF (0.5 mL), then methanol (0.5 mL), water (0.5 mL) and lithium hydroxide (13 mg, 0.55 mmol) were added. The mixture was sonicated and the solution stirred for 3 hours at room temperature. The mixture was then acidified with 2 M HCl (0.3 mL), and the precipitate collected *via* filtration, washed with water, and dried to give compound **10** (40 mg, 81%). Removal of the methyl ester was confirmed by proton NMR, and the compound used in the next step without further purification. **^{1}H NMR** (400 MHz, DMSO-d_6) δ 13.09 (s, 1H), 7.60 (dd, *J* = 7.9, 1.8 Hz, 1H), 7.31 (d, *J* = 1.7 Hz, 1H), 7.27 – 7.15 (m, 2H), 7.14 – 7.02 (m, 2H), 6.89 (dd, *J* = 7.7, 1.2 Hz, 1H), 3.05 – 2.77 (m, 4H).



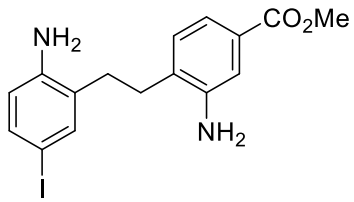
Rhodamine B-ethylenediamine linker (11). Tert-butyl (2-(methylamino)ethyl)carbamate (175 mg, 1.00 mmol) was added to a pre-stirred solution of Rhodamine B HCl salt (437 mg, 913 µmol), HBTU (521 mg, 1.37 mmol), and DIPEA (318 µL, 1.83 mmol) in DMF (10 mL) at 100 °C. The reaction mixture was stirred for 3 hours and then cooled to room temperature. Ethyl acetate (100 mL) was added, and the organic layer washed with brine (6 × 50 mL). The organic solution was dried over anhydrous sodium sulfate, then the solvent removed under reduced pressure. The crude residue was purified by flash silica column chromatography (5% MeOH in dichloromethane), then precipitated from petrol ether to give compound **11** as a dark iridescent solid (420 mg, 72%). The NMR spectrum was complicated by the presence of rotamers around the amide bond. Some protons are split into two environments, with the *trans* as the major isomer (as drawn), and *cis* as the minor isomer (approximately 30:70 ratio). When the peaks are split in the proton NMR, the major environment is assigned HX, and the minor environment is assigned HX'. **^{1}H NMR** (600 MHz, DMSO) δ 7.81 – 7.64 (m, H11, H12, H13), 7.59 (d, *J* = 7.4 Hz, 11H'), 7.56 – 7.52 (m, H14), 7.50 – 7.47 (d, *J* = 7.0 Hz, H14'), 7.22 – 7.09 (m, H4, H5), 6.99 (t, *J* = 5.9 Hz, NH'), 6.96 – 6.93 (m, H8), 6.67 (t, *J* = 5.9 Hz, NH), 3.82 – 3.57 (m, H2), 3.18 – 3.13 (m, H18'), 3.09 (t, *J* = 6.9, H18), 3.06-3.01 (m, H19'), 2.94 (s, H17), 2.63 – 2.59 (m, H19), 2.58 (s, H17'), 1.40 (s, H22'), 1.34 (s, H22), 1.21 (t, *J* = 7.0 Hz, H1); **^{13}C NMR** (151 MHz, DMSO) δ 168.0 (16'), 167.5 (16), 157.1 (9), 157.0 (7), 155.7 (10), 155.6, 155.5 (20'), 155.4 (20), 155.1 (3), 136.1 (10), 136.0 (10'), 131.9, 131.7 (5), 130.5, 130.2, 130.2, 129.7, 129.6, 129.4, 129.3, 127.4 (14), 114.1 (4), 113.0 (6), 95.9 (8), 95.8 (8'), 78.0 (21'), 77.7 (21), 50.1 (18'), 46.5 (18), 45.3 (2), 37.9 (19'), 37.7 (17), 36.3 (19), 31.8 (17'), 28.2 (22), 12.4 (1); **HR-ESI-MS** [M^{+}] $[C_{36}H_{47}N_4O_4]^+$ found: 599.3594 predicted: 599.3592; **MP** decomposition 134 – 137 °C; **IR** ν (cm^{-1}) 2979, 2934, 1589, 1468, 1413, 1338, 1275, 1248, 1181, 1134, 1074, 840, 684.



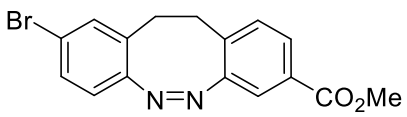
Dyad A. Compound **11** (96 mg, 0.16 mmol) was stirred in a 1:9 TFA:dichloromethane mixture (2 mL) for 2 h at room temperature, and then the solvent was removed under reduced pressure. The crude deprotected dye was added to a pre-stirred solution of compound **9** (37 mg, 0.15 mmol), HBTU (83 mg, 0.22 mmol), and DIPEA (51 µL, 0.29 mmol) in DMF (3 mL). The reaction mixture was stirred at room temperature overnight, then ethyl acetate (50 mL) was added, and the organic layer washed with brine (6 × 30 mL). The solution was dried over anhydrous sodium sulfate, then the solvent removed under reduced pressure. The crude residue was purified by flash silica column chromatography (10% MeCN in dichloromethane) to give **Dyad A** (20 mg, 18%) as a purple solid. The NMR spectrum was complicated by the presence of rotamers around the amide bond. Some protons are split into two environments, with the *trans* as the major isomer (as drawn), and *cis* as the minor isomer (34:66 ratio). The major has been assigned in the proton NMR. All peaks observed in the carbon NMR are reported. **^{1}H NMR** (600 MHz, DMSO) δ 8.28 (t, *J* = 5.7 Hz, H13), 7.75 – 7.70 (m, H7, H8), 7.67 – 7.65 (m, H9), 7.57 – 7.51 (m, H6), 7.35 (dd, *J* = 8.0, 2.0 Hz, H17), 7.23 – 7.04 (m, H4, H5, H15, H16, H21, H22) 6.88 – 6.82 (m, H18, H3), 3.64 (m, H2), 3.28 – 3.17 (m, H11), 2.96 (s, H10), 2.93 – 2.89 (m, H12), 2.88 – 2.80 (m, H20, H19), 1.20 (t, *J* = 7.1 Hz, H1); **^{13}C NMR** (151 MHz, DMSO) δ 167.8, 164.8, 157.0, 157.0, 155.6, 155.1, 155.0, 154.7, 136.1, 132.7, 132.5, 131.7, 131.4, 130.5, 130.3, 130.1, 129.9, 129.8, 129.7, 129.4, 129.2, 127.7, 127.3, 127.3, 126.9, 125.8, 125.5, 118.3, 117.2, 114.1, 112.9, 95.8, 49.5, 46.0, 45.3, 37.6, 37.3, 36.0, 32.0, 30.9, 30.6, 30.5, 12.4; **HR-ESI-MS** [M^+] [$C_{46}H_{49}N_6O_3$]$^+$ found: 733.3877 predicted: 733.3861. **MP** decomposition 178 – 182 ^{o}C; **IR** ν (cm^{-1}) 2976, 1589, 1413, 1337, 1275, 1247, 1181, 1133, 1075, 841, 757, 684.



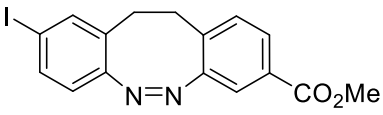
Methyl 3-amino-4-(2-amino-5-bromophenethyl)benzoate (13) was synthesised according to a literature procedure.[15] **8** (50 mg, 185 µmol) was stirred in DMSO (0.5 mL) at room temperature with N-bromo-succinimide (33 mg, 185 µmol) for 2 h. Dichloromethane (50 mL) was added and the solution washed with saturated aqueous NaCl (3 × 20 mL), and then dried over sodium sulfate. The organic solvent was removed under reduced pressure and the crude residue purified with column chromatography (0 - 20% ethyl acetate in dichloromethane), and then used in the next step without further purification (46 mg, 71%). Dominant species in **^{1}H NMR**: (400 MHz, $CDCl_3$) δ 7.40 (dd, *J* = 7.8, 1.7 Hz, 1H), 7.35 (d, *J* = 1.7 Hz, 1H), 7.16 (d, *J* = 2.4 Hz, 1H), 7.13 (dd, *J* = 8.3, 2.4 Hz, 1H), 7.07 (d, *J* = 7.8 Hz, 1H), 6.54 (d, *J* = 8.3 Hz, 1H), 3.88 (s, 3H), 3.74 (sb, 2H), 3.60 (sb, 2H), 2.88 – 2.70 (m, 4H).



Methyl 3-amino-4-(2-amino-5-iodophenethyl)benzoate (14) was synthesised according to a literature procedure.[15] **8** (50 mg, 185 µmol) was stirred in DMSO (0.5 mL) at room temperature with N-iodo-succinimide (42 mg, 185 µmol) for 2 h. Dichloromethane (50 mL) was added and the solution washed with saturated aqueous NaCl (3 × 20 mL), and then dried over sodium sulfate. The organic solvent was removed under reduced pressure and the crude residue purified with column chromatography (0 - 20% ethyl acetate in dichloromethane), and then used in the next step without further purification (38 mg, 52%). Dominant species in **^{1}H NMR**: (400 MHz, $CDCl_3$) δ 7.40 (dd, *J* = 7.8, 1.7 Hz, 1H), 7.36 (d, *J* = 1.7 Hz, 1H), 7.34 (d, *J* = 2.1 Hz, 1H), 7.31 (dd, *J* = 8.2, 2.1 Hz, 1H), 7.08 (d, *J* = 7.8 Hz, 1H), 6.44 (d, *J* = 8.2 Hz, 1H), 3.89 (s, 3H), 3.73 (sb, 2H), 3.61 (sb, 2H), 2.91 – 2.68 (m, 4H).



Methyl 9-bromo-diazocine-3-carboxylate (D2) was synthesised according to literature procedure.[15] A freshly prepared and titrated (0.52 M) solution of mCPBA (507 µL, 263 µmol) in acetic acid was added by syringe pump within a period of 12 hours under rapid stirring to a solution of **13** (46 mg, 132 µmol) in acetic acid/dichloromethane = 1/3 (3.1 mL). After the complete addition of the mCPBA solution, the mixture was stirred for at least one more hour. The solvent was then removed under reduced pressure, the residue taken up in ethyl acetate (10 mL) and washed with saturated, aqueous sodium hydrogen carbonate (2 × 5 mL), followed by saturated, aqueous sodium chloride (5 mL). The solution was dried over sodium sulfate, the solvent was removed under reduced pressure and the residue was purified by column chromatography (0 - 10% ethyl acetate in hexanes) to afford compound **D2** (30 mg, 66%) as a yellow solid**. ^{1}H NMR** (400 MHz, $CDCl_3$) δ 7.72 (dd, *J* = 7.9, 1.8 Hz, 1H), 7.49 (d, *J* = 1.7 Hz, 1H), 7.29 – 7.22 (m, 1H), 7.13 (d, *J* = 2.1 Hz, 1H), 7.08 (d, *J* = 7.9 Hz, 1H), 6.73 (d, *J* = 8.4 Hz, 1H), 3.87 (s, 3H), 3.04 - 2.95 (m, 2H), 2.84 – 2.71 (m, 2H). **^{13}C NMR** (101 MHz, $CDCl_3$) δ 166.0, 155.1, 154.0, 133.0, 132.4, 130.1, 130.0, 129.8, 129.2, 128.4, 120.7, 120.6, 120.1, 52.3 31.5, 31.3. **ESI HR-MS** $[C_{16}H_{14}O_2N_2Br+H]^+$ found: 345.0234 predicted: 345.0233. **MP** 156 – 159 °C; **IR** ν (cm^{-1}) 2945, 2917, 2849, 1716, 1435, 1297, 1282, 1260, 1121, 849, 805, 761.



Methyl 9-iodo-diazocine-3-carboxylate (D3) was synthesised according to literature procedure.[15] A freshly prepared and titrated (0.52 M) solution of mCPBA (369 µL, 192 µmol) in acetic acid was added by syringe pump within a period of 12 hours under rapid stirring to a solution of **14** (38 mg, 96 µmol) in acetic acid/dichloromethane = 1/3 (3.1 mL). After the complete addition of the mCPBA solution, the mixture was stirred for at least one more hour. The solvent was then removed under reduced pressure, the residue taken up in ethyl acetate (10 mL) and washed with saturated, aqueous sodium hydrogen carbonate (2 × 5 mL), followed by saturated, aqueous sodium chloride (5 mL). The

solution was dried over sodium sulfate, the solvent was removed under reduced pressure and the residue was purified by column chromatography (0 - 10% ethyl acetate in hexanes) to afford compound **D3** (25 mg, 67%) as a yellow solid**.** **^{1}H NMR** (400 MHz, $CDCl_3$) δ 7.72 (dd, *J* = 7.9, 1.8 Hz, 1H), 7.49 (d, *J* = 1.8 Hz, 1H), 7.45 (dd, *J* = 8.3, 1.8 Hz, 1H), 7.33 (d, *J* = 1.8 Hz, 1H), 7.08 (d, *J* = 8.0 Hz, 1H), 6.60 (d, *J* = 8.3 Hz, 1H), 3.87 (s, 3H), 3.09 – 2.91 (m, 2H), 2.91 – 2.64 (m, 2H). **^{13}C NMR** (101 MHz, CDCl3) δ 166.2, 155.3, 154.8, 138.4, 136.1, 133.1, 130.1, 130.0, 129.3, 128.6, 120.9, 120.2, 92.2, 52.4, 31.6, 31.3. **ESI HR-MS** $[C_{16}H_{14}O_2N_2I+H]^+$ found: 393.0094 predicted: 393.0094. **MP** 154 – 157 °C; **IR** ν (cm^{-1}) 3727, 3629, 2646, 1721, 1436, 1419, 1292, 1120, 807, 762, 668.

4.4 Photophysical characterisation

All spectroscopic measurements were conducted in HPLC grade solvents using fused silica cuvettes (10 mm path length, Starna Scientific Ltd, UK). UV-vis absorption spectra were acquired on a Perkin Elmer Lambda 20 spectrometer. Unless otherwise stated, all absorption spectra were recorded at 298 K, with temperature control by a PTP-1 Peltier unit from Perkin Elmer. Fluorescence spectra were acquired at 298 K using an Edinburgh Instruments FS5 spectrofluorometer operating Fluoracle® software, and equipped with a xenon arc lamp (providing 230–1000 nm excitation range), a thermostatic sample holder (SC-20) and an R13456 PMT detector (200–950 nm spectral coverage, Hamamatsu).

Photostationary state distribution measurements were performed by irradiating a dilute NMR sample under either 405 nm or 525 nm LED light, and subsequently measuring the ^{1}H NMR spectrum repeatedly until no further change was observed. The percentage composition was determined by integration.

Photochemical quantum yields of switching were measured by followed the change in concentration of each form of isomer upon irradiation with either a blue (405 nm) or green (525 nm) LED, using either UV-Vis or NMR spectroscopy. Concentration changes over time were plotted

and the linear region fitted using Equation 7, where [*A*] is the concentration of the predominant isomer, *I* is the photon flux (s^{-1}), *V* is the volume of the solution, N_A is Avogadro's number and t_{irr} is the irradiation time (s).[19] An example of this measurement for the Z to *E* switching quantum yield for an azobenzene is shown in Figure 3.21.

$$[A] = [A_0] - \frac{\varphi_A \cdot I}{N_A \cdot I} \cdot t_{irr} \qquad \text{(Equation 7)}$$

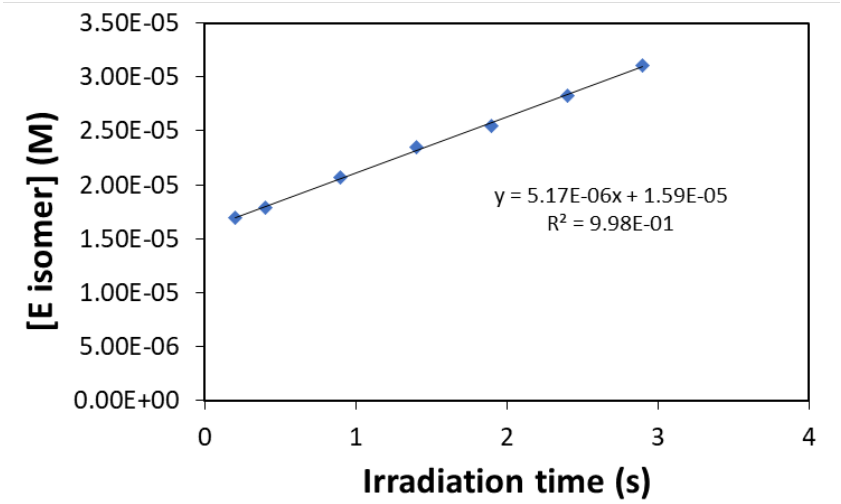


Figure 3.21: Increase in concentration of E isomer with irradiation with 405 nm LED over time for the diazocine **D1** switch in DMSO. The initial slope is estimated with a linear fit and the gradient used in Equation 7.

4.4 Preparation of GUVs for imaging

See Chapter 2, Section 4.4.

4.5 RESOLFT microscopy

See Chapter 2, Section 4.7.

5. References

1. Y. Xiong, A. Vargas Jentzsch, Johannes W. M. Osterrieth, E. Sezgin, I. V. Sazanovich, K. Reglinski, S. Galiani, A. W. Parker, C. Eggeling and H. L. Anderson, *Chem. Sci.*, **2018**, *9*, 3029.
2. A. T. Frawley, V. Wycisk, Y. Xiong, S. Galiani, E. Sezgin, I. Urbančič, A. Vargas Jentzsch, K. G. Leslie, C. Eggeling and H. L. Anderson, *Chem. Sci.*, **2020**, *11*, 8955.
3. S. Crespi, N. A. Simeth and B. König, *Nat. Rev. Chem.*, **2019**, *3*, 133.
4. D. Bléger and S. Hecht, *Angew. Chem. Int. Ed.*, **2015**, *54*, 11338.
5. M. Gao, D. Kwaria, Y. Norikane and Y. Yue, *Nat. Sci.*, **2023**, *3*, e220020.
6. A. Mourot, M. A. Kienzler, M. R. Banghart, T. Fehrentz, F. M. E. Huber, M. Stein, R. H. Kramer and D. Trauner, *ACS Chem. Neurosci.*, **2011**, *2*, 536.
7. S. Malkin and E. Fischer, *J. Phys. Chem.*, **1962**, *66*, 2482.
8. D. Bléger, J. Schwarz, A. M. Brouwer and S. Hecht, *J. Am. Chem. Soc.*, **2012**, *134*, 20597.
9. S. Samanta, A. A. Beharry, O. Sadovski, T. M. McCormick, A. Babalhavaeji, V. Tropepe and G. A. Woolley, *J. Am. Chem. Soc.*, **2013**, *135*, 9777.
10. S. Samanta, T. M. McCormick, S. K. Schmidt, D. S. Seferos and G. A. Woolley, *Chem. Commun.*, **2013**, *49*, 10314.
11. A. Kerckhoffs, K. E. Christensen and M. J. Langton, *Chem. Sci.*, **2022**, *13*, 11551.
12. R. Siewertsen, H. Neumann, B. Buchheim-Stehn, R. Herges, C. Näther, F. Renth and F. Temps, *J. Am. Chem. Soc.*, **2009**, *131*, 15594.
13. J. Calbo, A. R. Thawani, R. S. L. Gibson, A. J. P. White and M. J. Fuchter, *Beilstein J. Org. Chem.*, **2019**, *15*, 2753.
14. J. Calbo, C. E. Weston, A. J. P. White, H. S. Rzepa, J. Contreras-García and M. J. Fuchter, *J. Am. Chem. Soc.*, **2017**, *139*, 1261.
15. M. S. Maier, K. Hüll, M. Reynders, B. S. Matsuura, P. Leippe, T. Ko, L. Schäffer and D. Trauner, *J. Am. Chem. Soc.*, **2019**, *141*, 17295.
16. E. R. Thapaliya, J. Zhao and G. C. R. Ellis-Davies, *ACS Chem. Neurosci.*, **2019**, *10*, 2481.
17. W. L. Moormann, D.; Herges, R., *Beilstein J. Org. Chem.*, **2019**, *15*, 727.
18. F. Klockmann, C. Fangmann, E. Zender, T. Schanz, C. Catapano and A. Terfort, *ACS Omega*, **2021**, *6*, 18434.
19. K. Stranius and K. Börjesson, *Sci. Rep.*, **2017**, *7*, 41145.
20. S.-n. Uno, M. Kamiya, T. Yoshihara, K. Sugawara, K. Okabe, M. C. Tarhan, H. Fujita, T. Funatsu, Y. Okada, S. Tobita and Y. Urano, *Nat. Chem.*, **2014**, *6*, 681.
21. L. Yuan, W. Lin and Y. Feng, *Org. Biomol. Chem.*, **2011**, *9*, 1723.
22. T. Nguyen and M. B. Francis, *Org. Lett.*, **2003**, *5*, 3245.
23. W. Moormann, T. Tellkamp, E. Stadler, F. Röhricht, C. Näther, R. Puttreddy, K. Rissanen, G. Gescheidt and R. Herges, *Angew. Chem. Int. Ed.,* **2020**, *59*, 15081.
24. Q. Zhu, S. Wang and P. Chen, *Org. Lett.*, **2019**, *21*, 4025.
25. P. Lentes, E. Stadler, F. Röhricht, A. Brahms, J. Gröbner, F. D. Sönnichsen, G. Gescheidt and R. Herges, *J. Am. Chem. Soc.*, **2019**, *141*, 13592.
26. P. Lentes, P. Frühwirt, H. Freißmuth, W. Moormann, F. Kruse, G. Gescheidt and R. Herges, *J. Org. Chem.*, **2021**, *86*, 4355.
27. J. R. Lakowicz, *Principles of fluorescence spectroscopy*, Springer Science & Business Media, **2013**.
28. S. Fredrich, R. Göstl, M. Herder, L. Grubert and S. Hecht, *Angew. Chem. Int. Ed.*, **2016**, *55*, 1208.
29. T. Sumi, Y. Takagi, A. Yagi, M. Morimoto and M. Irie, *Chem. Commun.*, **2014**, *50*, 3928.
30. K. Morimitsu, S. Kobatake and M. Irie, *Mol. Crystals Liq. Crystals*, **2005**, *431*, 451.
31. E. Speckmeier, C. Padié and K. Zeitler, *Org. Lett.*, **2015**, *17*, 4818.

32. H. Kakuta, N. Yakushiji, R. Shinozaki, F. Ohsawa, S. Yamada, Y. Ohta, K. Kawata, M. Nakayama, M. Hagaya, C. Fujiwara, M. Makishima, S. Uno, A. Tai, A. Maehara, M. Nakayama, T. Oohashi, H. Yasui and Y. Yoshikawa, *ACS Med. Chem. Lett.*, **2012**, *3*, 427.

Chapter 4

Photoswitchable PET quenching for RESOLFT dyads

1. Introduction

Designing high-performance FRET-quenched photoswitchable dyads like those described in the preceding chapters is difficult due to the large number of demands placed on the photoswitch. It must play the role of both switch and quencher, remaining stable to constant photoswitching cycles. Tuning the many properties required for these two functions can be a difficult task given the fairly limited number of high-performance photoswitch scaffolds. For example, in Chapter 3, I discussed the use of a visible-light switching cyclic azobenzene as a FRET-quenching photoswitch, which was chosen for its notable fatigue resistance, in an attempt to improve the performance of previous spironaphthoxazine-based dyads. Unfortunately, its quantum yield of photoswitching was too high and its absorption too low compared to the competing dye excitation for it to remain in its quenching form for long enough to be applied to imaging. The fundamental problem with this FRET-dyad design is that FRET to the switch will cause it to isomerise, meaning the quenching and switching processes are not independent.

A possible solution to this problem is to explore alternative quenching mechanisms that would allow the separation of the role of photoswitch and quencher. One quenching mechanism for photoswitchable dyads which is under-explored in the literature is photoinduced electron transfer (PET). Unlike FRET where the quenching efficiency decreases with distance R with the relationship $\frac{1}{R^6}$, PET rates decay exponentially, and become negligible over short (<1 nm) distances. A change in distance, rather than spectral overlap, could therefore be used to modulate fluorescence emission. This would allow the use of photoswitches that do not have a large change in absorption between two forms, but instead trigger a geometric change upon isomerisation, such as azobenzenes. If a PET-quencher and fluorophore were attached to opposite ends of an azobenzene, isomerisation to the *Z* isomer could be expected to bring them much closer together (Figure 4.1).

This kinetic-based switching (manipulating the rate of electron transfer by changing the distance between quencher and photoswitch) is distinct from a thermodynamic-based PET switching. In a thermodynamic mechanism, photoswitch isomerisation leads to a change in its HOMO and LUMO energy levels, modulating the thermodynamic driving force for electron transfer with the dye. This is similar to the previous FRET-based designs as it does not utilise a separate quencher. It is also more suited to photoswitches with large changes in conjugation and absorption spectra between isomers, as this leads to larger changes in the orbital energy levels (for example in diarylethenes).

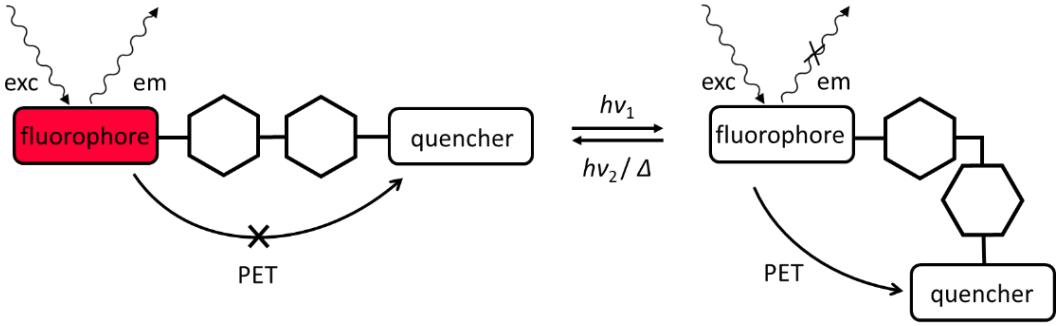


Figure 4.1: Design for distance-dependent photoswitchable dyads, where fluorescence emission is modulated by PET.

Despite the extensive use of PET quenching as a design concept for fluorescent sensors,[1,2] very few systems exist where PET quenching has been exploited to make photoswitchable dyads, and none are reported for RESOLFT microscopy. Of those that are reported, the mechanism tends to rely on the thermodynamic driving force change described above, and therefore diarylethenes are a commonly-employed photoswitch.[3] The Irie group has investigated a system involving a diarylethene photoswitch conjugated to a perylene bisiimide fluorophore as a reversible read-out memory device (Figure 4.2A).[4,5] A brief analysis of the change in HOMO energy between the two forms of the switch was presented as the rationale for this design, in which the switch would act as the electron donor. Experimentally, a reversible decrease in fluorescence to 14% of the original value through switching of the diarylethene to the closed form was observed.[4] Solvent-dependency studies gave evidence that the mechanism was PET, as the quenching was more efficient with increasing dielectric constant.

The Würthner group reported similar systems around the same time,[6,7] and went on to additionally make a terrylene derivative that operates under the same design (Figure 4.2B).[8] The PET-quenching mechanism was rationalised by quantifying the thermodynamic driving force with the Weller equation (see Introduction, Chapter 1, Section 3.3), undertaking polarity-dependence studies, and several ultrafast transient absorption spectroscopy experiments to demonstrate electron transfer. Fluorescence emission was quenched to between 20 and 50% of the original intensity, depending on the solvent system used.

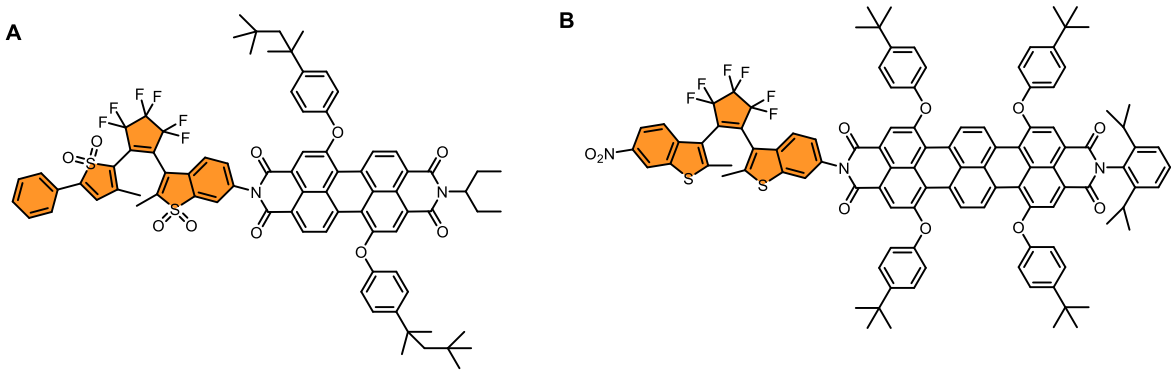


Figure 4.2: Diarylethene-based switchable fluorescent systems from the Irie group (A) and the Würthner group (B).

The Raymo group has also developed switchable fluorescent molecules based on a conjugate between a spiropyran photoswitch and a BODIPY fluorophore (Figure 4.3).[9] The isomerisation of the spiropyran to its merocyanine form reduced the fluorescence of the BODIPY by 54%, which was attributed to an electron transfer from the excited dye to the switch. Issues with fatigue were addressed in follow-up work that encapsulated the BODIPY and spiropyran molecules in amphiphilic polymer assemblies which allowed the separate components to interact closely within a hydrophobic environment and be transferred into biological aqueous environments.[10] Similar effects were observed in this intermolecular interaction to what had been demonstrated in the dyad, and this supramolecular assembly was shown to switch in cellulo. Thermodynamic analysis for this system was undertaken to show the favourability of the electron transfer in the open form and not the closed, however the potential for a contributing FRET mechanism was not discounted by the authors.

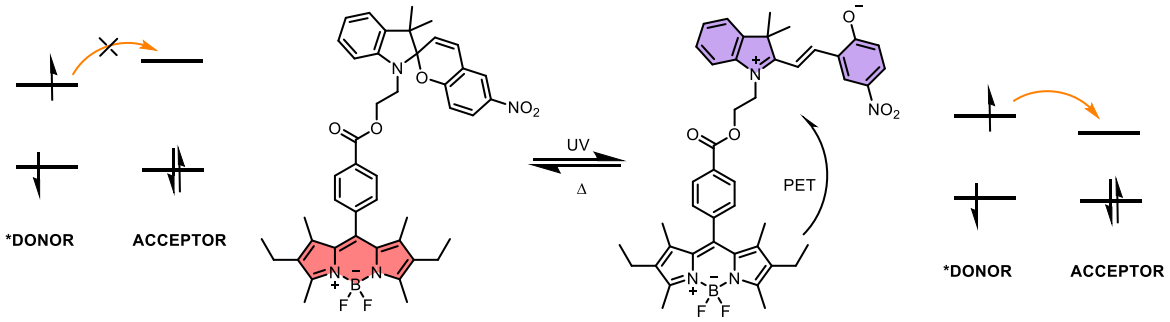


Figure 4.3: A switchable fluorescent BODIPY-spiropyran conjugate.

One example of an azobenzene photoswitch observed to participate in PET was with conjugated naphthyl fluorophore units which underwent fluorescence enhancement upon isomerisation to the *Z* form (Figure 4.4).[11] It was hypothesised that in the *E* form, PET quenching was inhibiting fluorescence, and that isomerisation to the *Z* form changed the extent of conjugation and therefore disfavoured PET. Protonation experiments showed a similar fluorescence enhancement, indicating that the azo lone pairs are involved in the electron transfer, however no further investigation into the mechanism was undertaken.

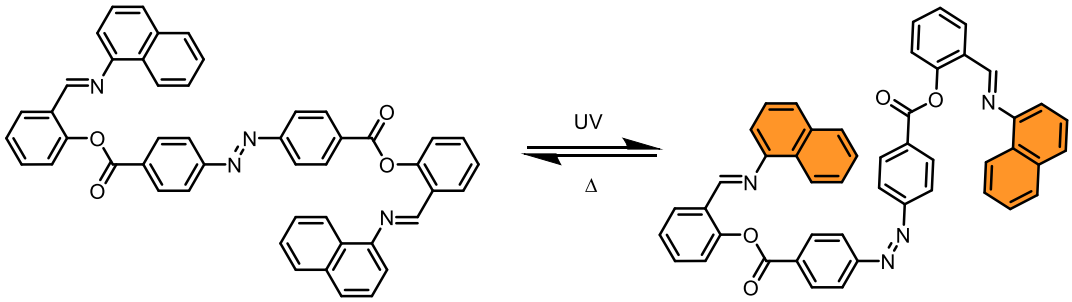


Figure 4.4: The structure of a switchable fluorescent naphthyl-azobenzene.

There are even fewer examples of photoswitchable dyads which attempt to change the distance between a PET donor and acceptor, moderating the kinetics of an electron transfer with a change in geometry. One example is a porphyrin-azobenzene triad, where isomerisation brought an electron-poor porphyrin closer to a more electron-rich one, resulting in a 55% quenching of emission intensity (Figure 4.5A).[12] Another porphyrin-based system used an axially-coordinated pyridine-derived stilbene to modulate the proximity of a quencher, causing a moderate decrease in the fluorescence emission intensity.[13] An interesting system that does not involve PET quenching but showcases photoswitching geometry change was a pyrene-thioindigo triad reported in 1992.

This compound showed a change in the fluorescence emission wavelength, assigned to the excitation of a pyrene excimer complex, rather than a change in intensity, upon thioindigo isomerisation (Figure 4.5B).[14]

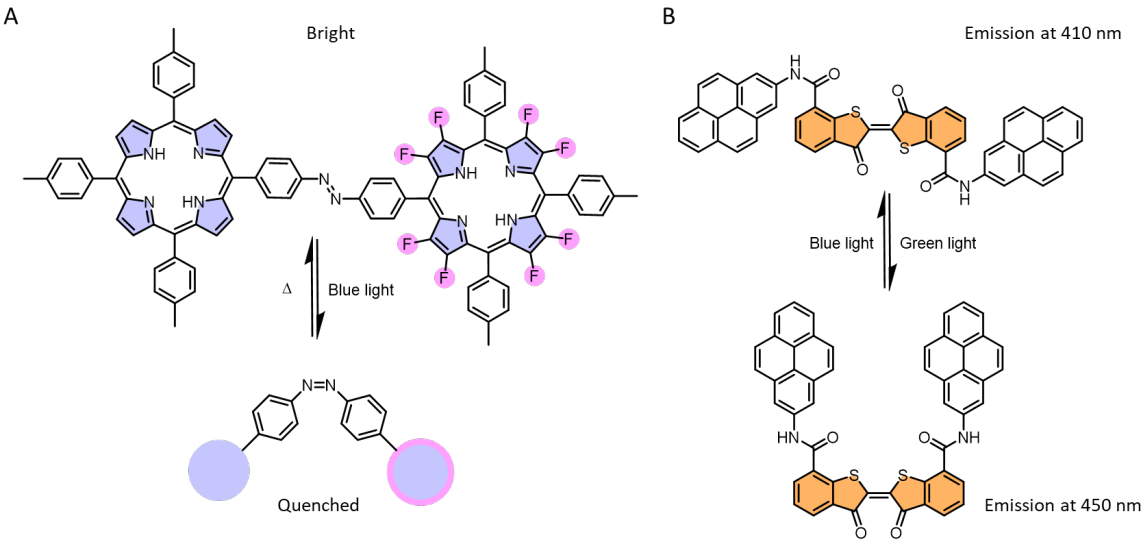


Figure 4.5A: Isomerisation of azobenzene-linked porphyrins induces fluorescence emission quenching by electron transfer to the fluorinated porphyrin. B: Pyrene excimer formation upon thioindigo isomerisation red-shifts the emission wavelength.

Although these systems provide interesting proof-of-concept results, they are clearly not designed for biological applications, using weakly emissive, blue-shifted, and often insoluble fluorophores, and UV-switching photoswitches. In contrast to the PET-based systems discussed above, the aim of this chapter is to explore designs that emphasise visible light switching in both directions, solubility, photostability, and complete quenching in the off state, in order to develop tools that are useful for RESOLFT super-resolution microscopy. We will therefore choose visible-light photoswitches and high-performance fluorophores, and attempt to rationally-design PET-quenched systems based on their thermodynamic driving force and geometric changes.

2. Results and Discussion

2.1 First design phase

2.1.1 Photoswitch synthesis and characterisation

Azobenzenes were identified as good potential candidates for a photoswitch for this project, due to the large change in geometry between their *E* and *Z* isomers. As outlined in Chapter 3 (Section 1.2), there are several visible-light switching azobenzenes. The tetra-ortho fluorinated diester reported by Stefan Hecht's group (Figure 4.6),[15] was selected as an ideal candidate, as it fulfils the following criteria:

1. Visible light switching in both directions (blue and green light switching)
2. High photostationary state distributions of each isomer (90% *E* and 97% *Z*)
3. Good fatigue resistance (100s of switching cycles with no photodegredation)
4. Absorption at available laser lines (405 nm and 488 nm)
5. A change in geometry between the two forms

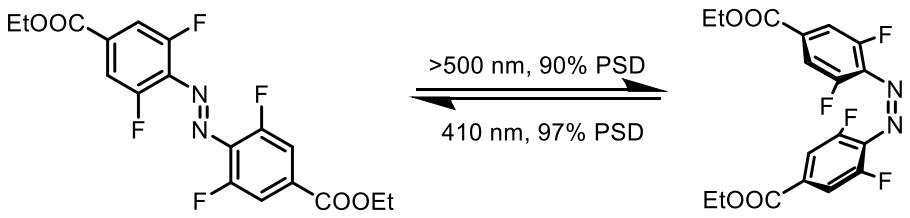


Figure 4.6: The switching properties of tetra-*ortho* fluorinated diester azobenzene.

In most azobenzenes, the n – π* transitions of both isomers lie in the visible region and overlap significantly (see Chapter 3, Section 1.2 for discussion). The twisted *Z* isomer has a higher energy π* orbital as a result of less delocalisation, however the n-orbital is also significantly higher in energy in the *Z* form than the planar *E*, leading to similar transition energies and overlapping absorption bands for the two isomers (Figure 4.7A). The n-orbital can be approximated as the sum of the two nitrogen lone pairs, which interact through mixing with the N-N σ bond in the *E* isomer, however in the *Z* isomer they interact through space. In the tetra-*ortho* fluoroazobenzene, having

ortho inductively electron-withdrawing substituents and *para* mesomerically withdrawing ester groups, removes electron density from the lone pairs, lowering the n-orbital energy more in the *Z* isomer than the *E*. This leads to separation of the n – π* bands and the ability to selectively address each with isomer with visible light (Figure 4.7B).[15]

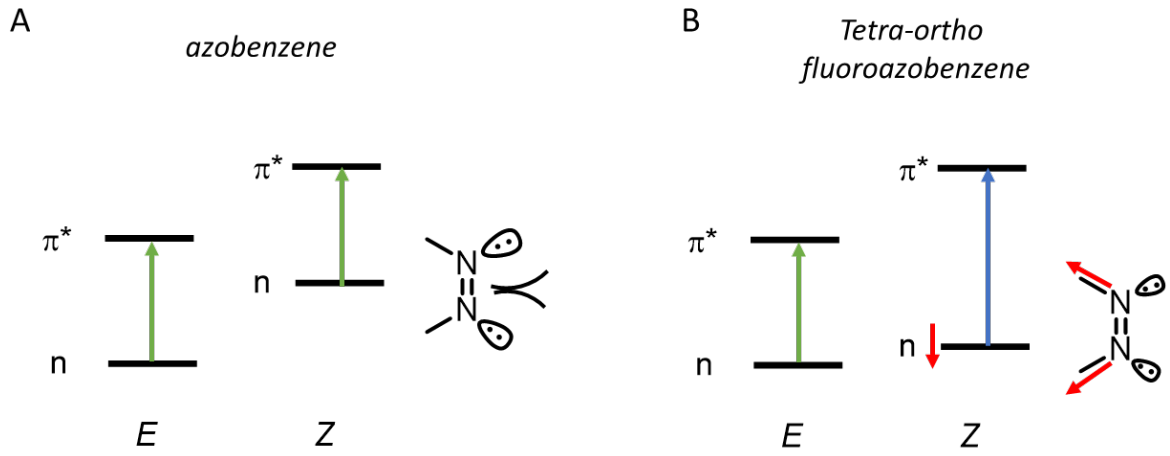
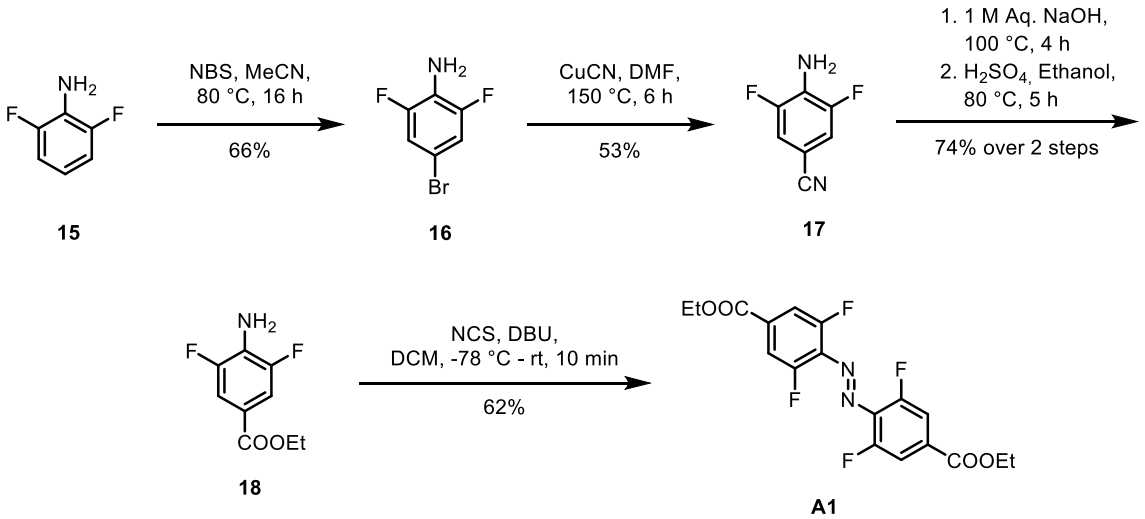


Figure 4.7: Orbital diagrams of n – π* transitions in unsubstituted azobenzenes (A) and the tetra-*ortho* fluoroazobenzene (B). Red arrows indicate the withdrawal of electron density and the lowering of the n-orbital energy.

The photoswitch was synthesised according to published procedures (Scheme 4.1).[15,16] Bromination of 2,6-difluoroaniline gave para-substituted **16**, followed by substitution with copper cyanide gave the nitrile derivative **17**. Hydrolysis to the carboxylic acid, followed by esterification with ethanol gave compound **18**. Oxidative coupling with *N*-chlorosuccinimide and DBU as developed by John and Lin[16] gave the azobenzene **A1** in short reaction times and much higher yields (62%) than the traditional manganese and iron-based oxidative azo-forming methods reported by Hecht et al. (23%).[15]



Scheme 4.1: Synthesis of photoswitch **A1**.

The photophysical properties of this photoswitch **A1** were characterised in acetonitrile for comparison to the literature.[15] UV-Vis switching experiments showed the photoswitch isomerises reversibly between *Z* and *E* forms with green (525 nm – to *Z* enriched) and blue (405 nm – to *E* enriched) light (Figure 4.8A). Irradiation of a sample in deuterated acetonitrile and subsequent ^{1}H NMR experiments showed the PSD at 525 nm to be 88 % *Z* and at 405 nm to be 93 % E (Figure 4.8B). Quantum yields of photoswitching were measured using the initial slope method (see Chapter 3, Section 4.4), and are reported in Table 4.1.

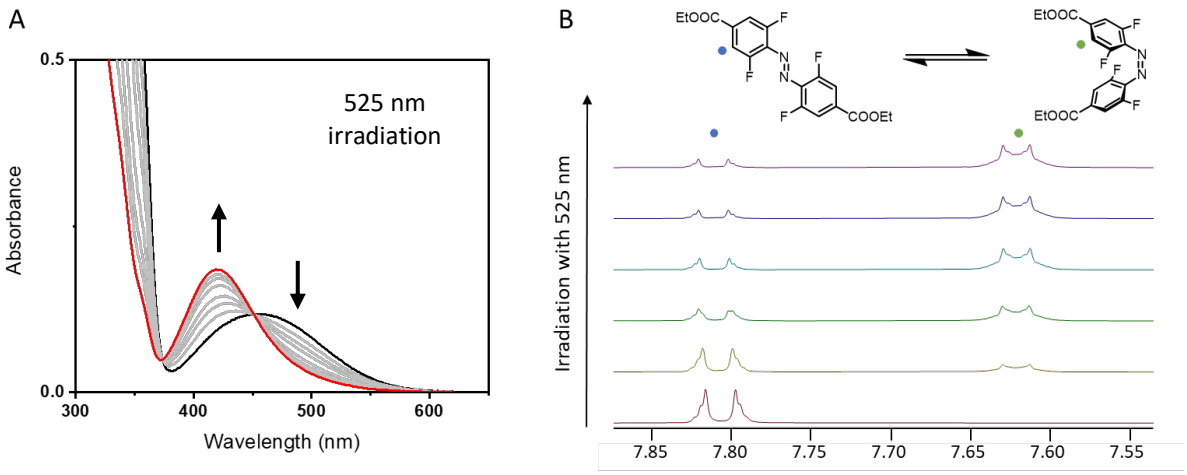


Figure 4.8A: Absorption spectra of photoswitch **A1** upon irradiation with green (525 nm) LED light in MeCN at 298 K. Black is the initial spectrum and red is the PSS. The spectral changes were reversible upon irradiation with a blue (405 nm) LED. B: ^{1}H NMR spectra (400 MHz, 298 K) of photoswitch **A1** in d_3-MeCN after irradiation with a 525 nm LED.

Table 4.1: Photophysical properties of photoswitch **A1** in MeCN.

Photoswitch	**A1**
Z λ_{max} (nm)	420
E λ_{max} (nm)	465
PSS 525 nm (% *Z*)	88
PSS 405 nm (% *E*)	93
$\Phi_{E\rightarrow Z}$	0.03
$\Phi_{Z\rightarrow E}$	0.4

2.1.2 Choosing a fluorophore and quencher

In order to choose a dye to couple with the switch, it had to fulfil the following criteria:

- Absorption λ at (red) microscope laser line
- No spectral overlap with switch to minimise any FRET
- Bright and photostable
- Can be synthetically conjugated to azobenzene
- Appropriate energy levels to be quenched by a small-molecule organic quencher

The electrochemical and photophysical properties of a series of cyanine and rhodamine dyes were characterised for analysis with the Weller equation (Introduction Section 3.3). The singlet excitation energies were measured with UV-Vis spectroscopy (Figure 4.9A) and the reduction and oxidation potentials were measured using square wave voltammetry (Figure 4.9B). All measurements were performed in acetonitrile.

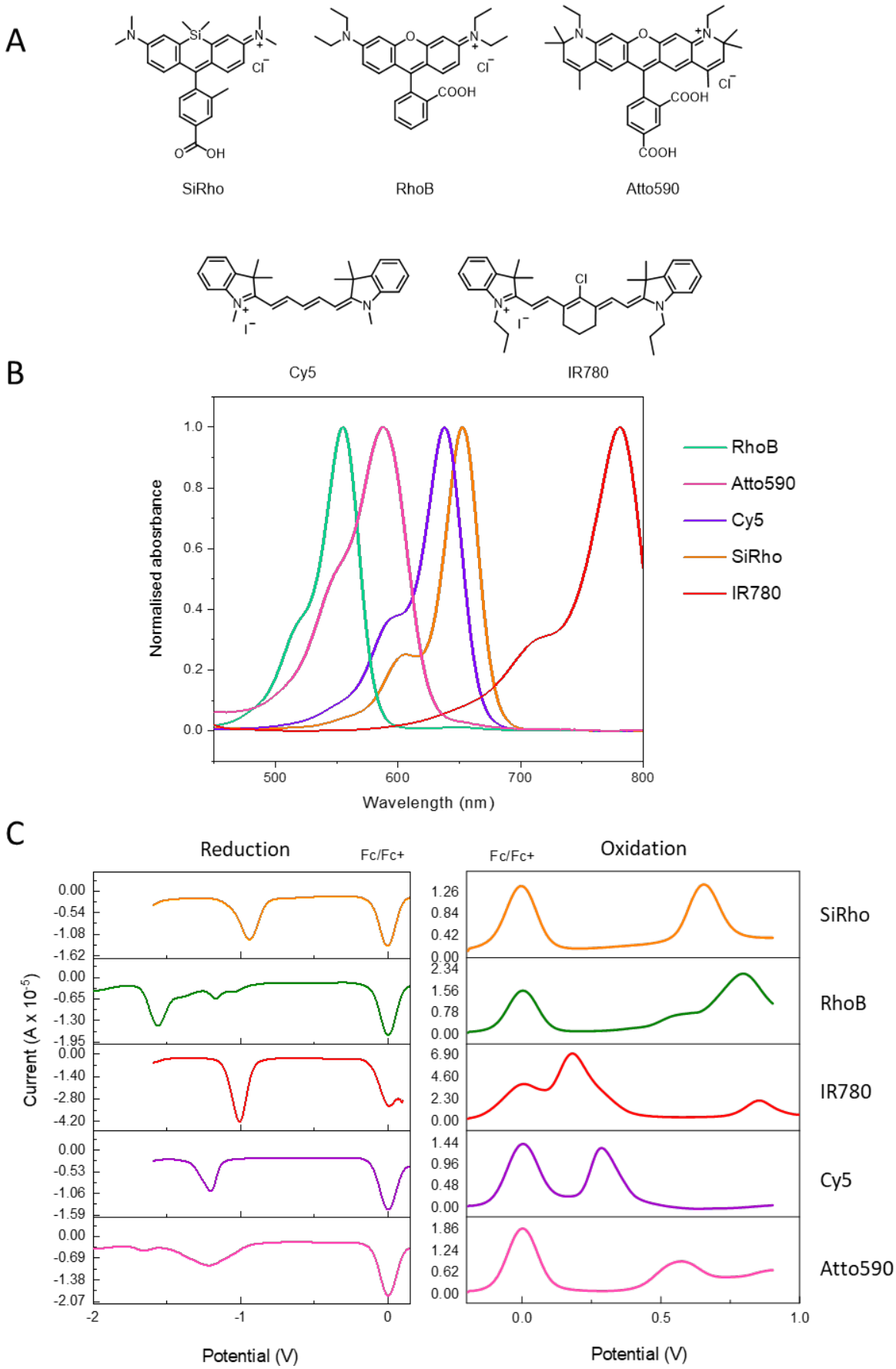


Figure 4.9A: Structures of investigated dyes, B: UV-Vis absorption spectra of the dyes in MeCN at 298 K, C: Square-wave voltammograms of the dyes in 0.1 M Bu_4NPF_6 in MeCN at 298 K.

The values of the redox potentials in volts against the Fc/Fc+ redox couple standard and excitation energies (in eV) for the measured dyes are shown in Table 4.2. The oxidation potentials of a selection of electron-rich substituted benzenes, and the reduction potentials of a selection of electron-poor benzoic acids were also measured in acetonitrile (Figure 4.10). There was a relatively small change in reduction potential between the investigated electron-deficient benzoic acids. 3,5-Dinitrobenzene is the most easily reduced compound measured, but the potentials were all within 0.26 V of each other. Conversely, the oxidation potentials of the electron-rich quenchers varied between -0.28 V for N,N,N',N',tetramethyl-1,4-diaminobenzene, to 0.97 V for 1,4-dimethoxybenzene. An acetyalted dimethyl-diaminobenzene was measured to investigate the impact of using aniline to form an amide bond with the photoswitch. It was observed that although the amide linker did make the compound harder to oxidise than the tetra-methyl analogue, its oxidation potential (0.19 V) was still significantly lower than dimethoxybenzene.

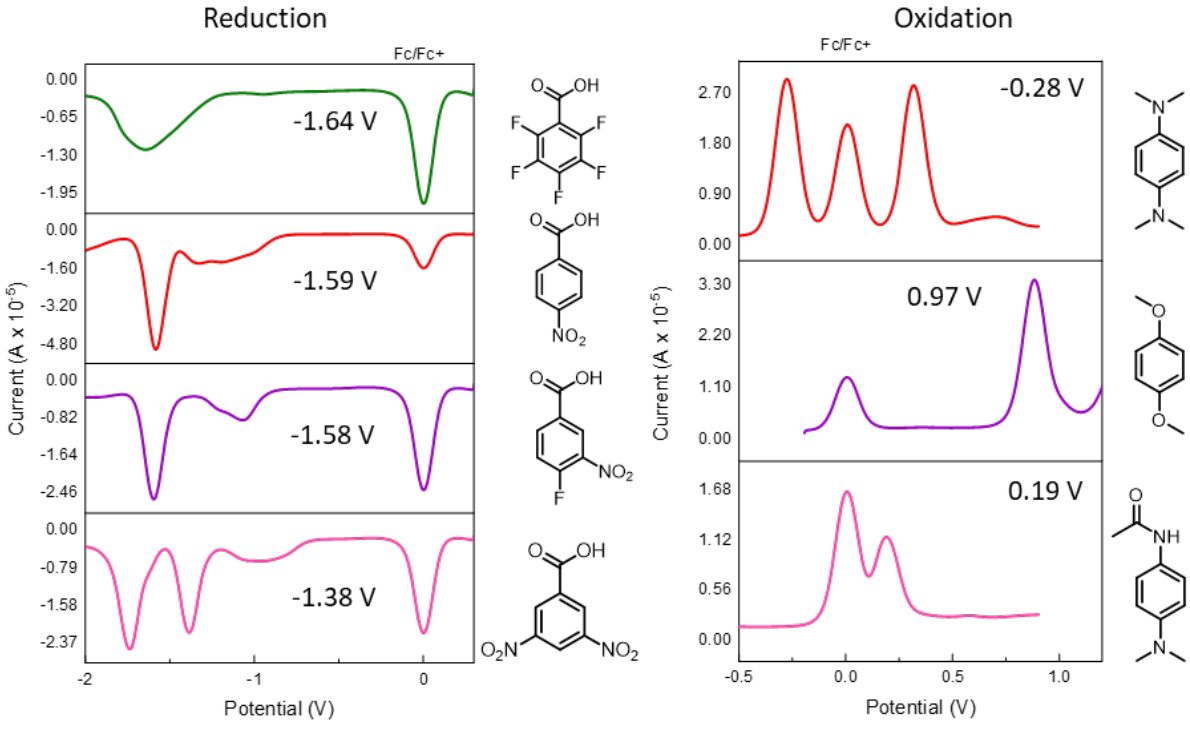


Figure 4.10: Square-wave voltammograms of the investigated small molecule organic quenchers. in 0.1 M Bu_4NPF_6 in MeCN at 298 K.

By taking the most easily reduced electron-poor quencher (3,5-dinitrobenzoic acid) and the acetylated diaminobenzene as example quenchers (bottom pink spectra, Figure 4.10), the ΔG

values for electron transfer between the measured dyes and these two quenchers were calculated using the Weller equations (see Introduction, Chapter 1, section 3.3, Equation 11 and 12). This allows us to analyse the role of the investigated dyes as either electron acceptors (from an aniline donor) or electron donors (to a benzoic acid quencher) (Figure 4.11A and B respectively). The results of this analysis are shown in Table 4.2.

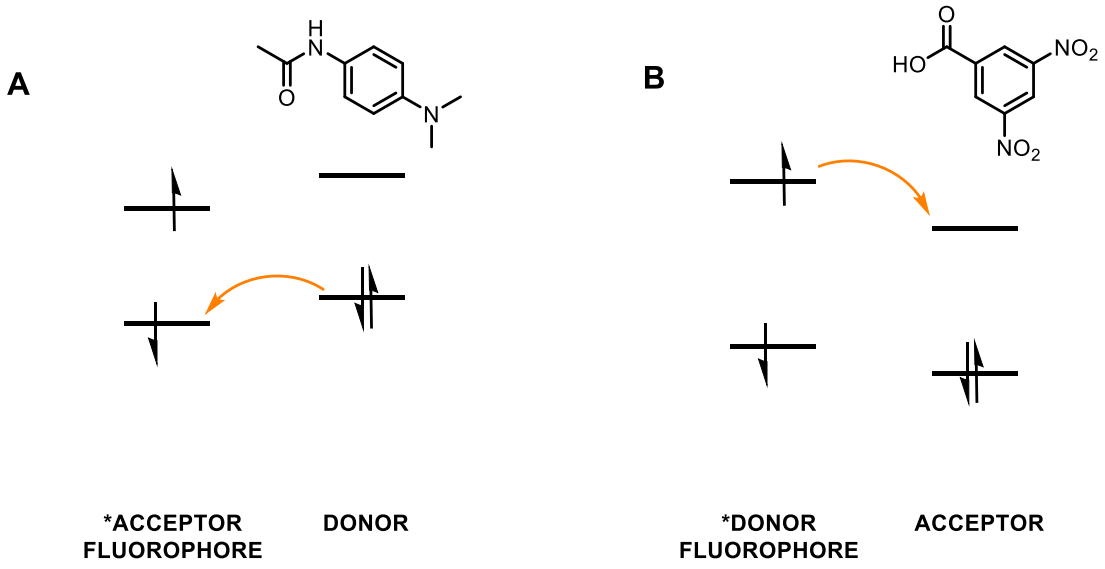


Figure 4.11: Representation of the two PET reactions being investigated, with electron-rich quenchers (A), and electron-poor quenchers (B).

Table 4.2: Reduction, oxidation, and excitation energy values for the investigated dyes, and their Δ*G* values for photoinduced electron transfer when paired with electron-rich donor or electron-poor acceptor quenchers (aniline and benzoic acid pictured above, Figure 4.10).

Dye	E_{RED} **(V)**	ΔE_{S0-S1} **(eV)**	E_{OX} **(V)**	ΔG_{PET} *(with donor quencher)*	ΔG_{PET} *(with acceptor quencher)*
SiRho	-0.93	1.90	0.65	-0.78	0.13
RhoB	-1.56	2.23	0.80	-0.48	-0.10
IR780	-1.02	1.59	0.18	-0.38	-0.03
Cy5	-1.20	1.94	0.29	-0.55	-0.27
Atto590	-1.21	2.11	0.58	-0.71	-0.15

It is evident from this analysis that a larger thermodynamic driving force for electron transfer can be achieved with an electron-rich quencher as a donor and the dye as an acceptor. The Δ*G* values for the dyes acting as electron donors are all quite close to 0, with the exception of Cy5, which is one of the more difficult dyes to synthetically desymmetrise. As the Δ*G* values for dyes acting as an electron acceptor all indicate a favourable thermodynamic process, it was decided to use a Rhodamine B derivative or a silicon rhodamine derivative coupled with an electron-rich aniline in the dyads.

It is also possible that the photoswitch itself could act as a PET quencher when attached to the fluorophores. As the photoswitch is so electron-poor, it is expected that it would participate in a PET reaction as the electron acceptor. Electrochemical analysis of the photoswitch **A1** in 0.1 M Bu_4NPF_6 in MeCN at 298 K found its reduction potential to be -0.83 V vs Fc/Fc^+. A plot of the singlet excitation energy and the oxidation potential of the investigated dyes shows that they could all theoretically be quenched by **A1** acting an electron acceptor, so this competing reaction might be difficult to avoid in any dyad (Figure 4.12).

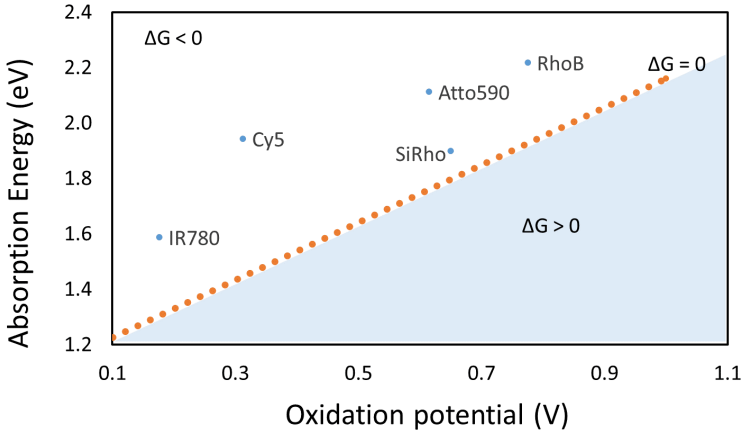


Figure 4.12: The relationship between the absorption energy and oxidation potential for the measured dyes, in relation to the photoswitch **A1** as an electron acceptor. The blue area indicates the region where the ΔG_{PET} is positive, and the dotted line where it is 0. All the dyes lie in the region where a photoinduced electron transfer to **A1** is thermodynamically favourable in MeCN at 298 K.

In order to investigate whether this electron transfer occurs as a background effect in the synthesised dyads, control molecules were synthesised with the dyes (rhodamine B and silicon

rhodamine) and the photoswitch but not the quencher. There was also the possibility that the quencher could participate in PET directly with the photoswitch as well, as the ΔG_{PET} = -1.12 V for this reaction. An additional control molecule of the photoswitch with the quencher attached but not the dyes was synthesised to investigate these effects.

2.1.3 Modelling geometric changes

The final aspect to consider in the design of these systems is the geometry of the compounds in their *E* and *Z* forms. The proximity of the dye to the quencher will probably have a large impact on the rate of electron transfer (discussed in Introduction, Chapter 1, Section 3.3), and therefore how effective the quenching is in the 'off' form. In particular, the flexibility of the linkers joining the chosen dye, switch and quencher components could have a significant impact.

In order to investigate this further, a computational search of the ground state conformations of some potential dyads in their *E* and *Z* forms was undertaken using GFN2-xTB metadynamics.[17] The energies of the resulting conformers were calculated with DFT and the distance between donor and acceptor in each conformer weighted with a Boltzmann distribution according to their relative energy to give an average distance across the whole ground state population (Figure 4.13).

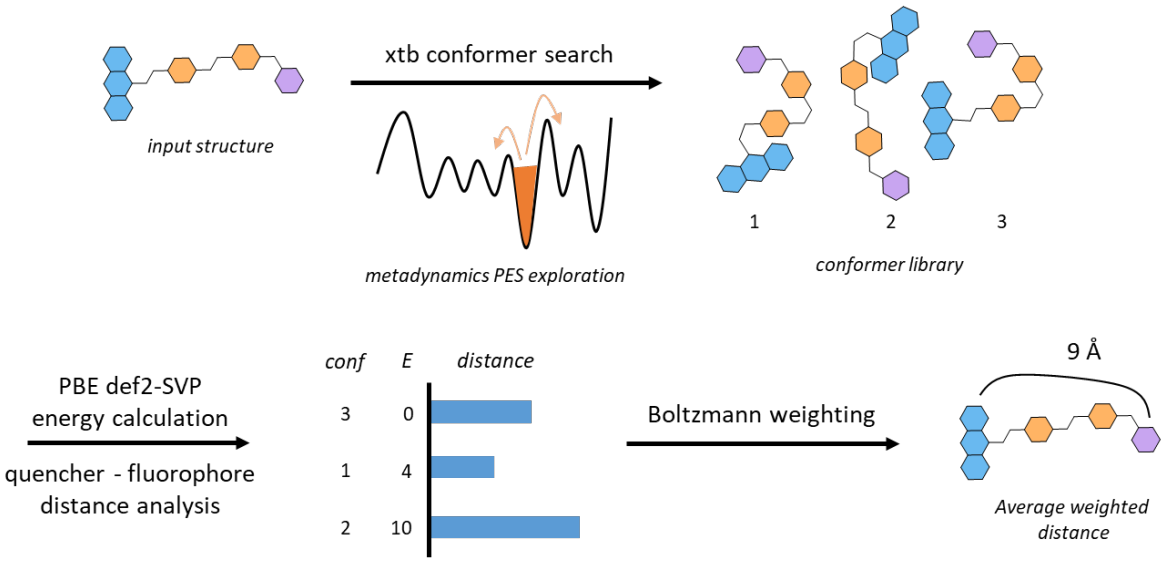


Figure 4.13: Computational workflow for average donor-acceptor distance analysis.

GFN2-xTB is a tight-binding method, which approximates molecular orbitals as linear sums of valence atomic orbitals, and assumes core electron density remains frozen. It then introduces various approximations for neighbouring atom interactions, rather than assessing electron density across a whole molecule like in DFT methods.[18] In the metadynamics conformational exploration implementation, a potential energy surface (PES) is explored by the use of Gaussian function biasing potentials. These apply energy penalties to geometries that have been previously explored through a root-mean-square-deviation (RMSD) analysis.[17] This has the effect of 'filling up' a conformational energy well to push molecules across into different conformational space, leading to a faster and more complete exploration of the PES landscape (Figure 4.13, above).

Through this modelling, it was observed that the introduction of too many flexible linkers led to no difference in the average donor-acceptor distance between the *E* and *Z* isomers, as in the example in Figure 4.13A. This was because the photoswitch could form π stacks with the fluorophore and quencher in both isomers, and so both azobenzene isomers formed tightly-stacked conformers according to xTB. Having too few flexible linkers also prevented close stacking in the *Z* isomer, as in the example of the rigid molecule in Figure 4.13B, where the quencher is still almost 9 Å from the dye in the lowest energy structure. In an example with a single flexible linker between the dye and the photoswitch, the closest stacking in the *Z* form was observed (Figure 4.13C), while maintaining a reasonable difference between the *E* and *Z* forms.

It is evident that getting the balance of flexibility to allow close stacking is quite a nuanced choice. Although this modelling was helpful in ruling out designs which are highly unlikely to work (as in Figure 4.13A and 4.13B), there were some problems with this computational modelling that limited its predictive ability.

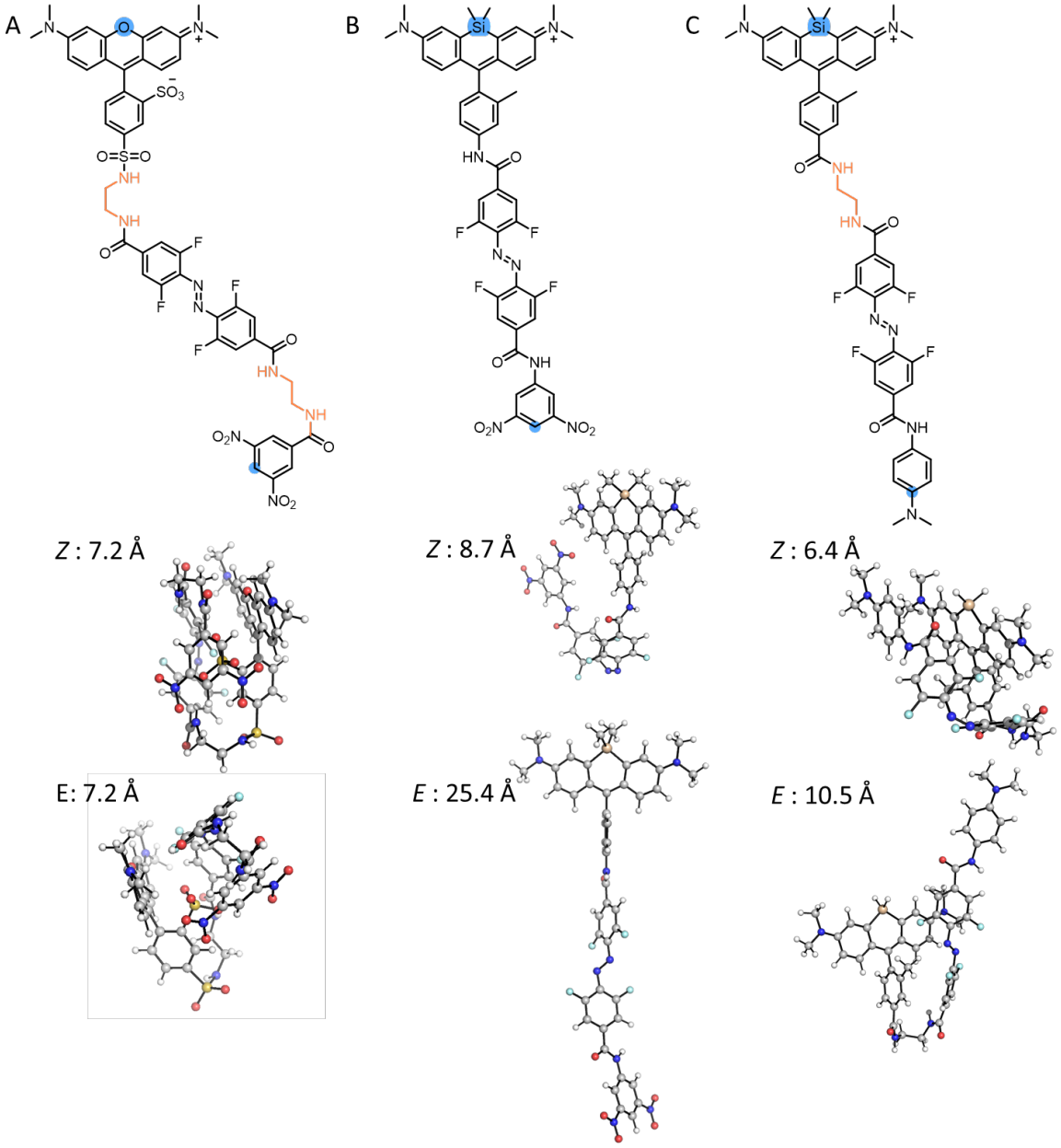


Figure 4.13: Example dyads showing the impact of linker incorporation (shown in orange) on flexibility and Boltzmann-weighted average donor-acceptor stacking distances. Distance was measured from the silicon/oxygen atom to the *4*-position of the dinitroanilide quenchers (highlighted in blue). Representative structures are the minimum energy conformer found using GFN2-xTB metadynamics search, calculated at PBE def2-SVP.

Firstly, the molecules being modelled are charged, as the rhodamine dyes are large aromatic cations, and sulforhodamine B has a sulfonate anion as well. Both xtb and DFT use implicit solvation models, which are less accurate when modelling ionic species,[19] leading to possible errors in the energy calculations and subsequent weightings of different conformers. Secondly, as the molecules are quite flexible and have many degrees of freedom and a fairly flat potential energy surface, small errors in energy calculation may lead to large errors in Boltzmann weighted distances. Relatedly, both xTB and DFT tend to predict highly-folded structures as the lowest energy, emphasising the strength of any possible π-π interactions. This is evident in the example model for a silicon rhodamine-azobenzene dyad (a control compound, discussed further in Section 2.1.4), where the energy of different conformers tends to increase with the distance between the two fragments of the molecule, so that all stretched out conformers are significantly higher in energy (Figure 4.14). Sometimes, this leads the method to predict molecules with multiple *cis* amides to be the lowest energy structures for the sake of maximising π-π stacking. Attempts to validate this model with eg. NOESY NMR experiments were inconclusive, so the results of the modelling were used as guidance rather than absolute predictions.

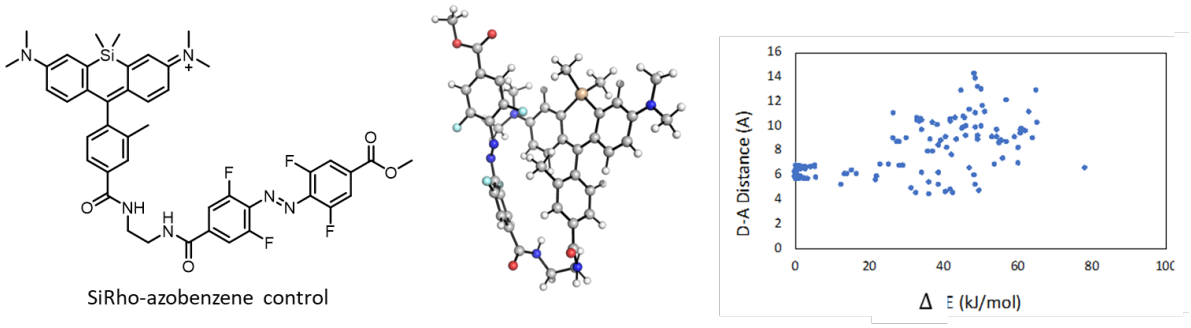


Figure 4.14: The lowest energy conformation of a silicon rhodamine-azobenzene dyad, and a plot showing the relationship between the energy of all the generated conformers and the distance between the silicon rhodamine and the photoswitch (measured as Si atom to N=N double bond).

Despite these problems, the model was informative as to the minimum distance that could be expected between fluorophore and quencher, assuming π-stacking is highly favoured. As the results indicated that the distances in all the *E* forms are quite large, and would all probably prohibit significant PET, it was decided to favour designs that minimise the distance in the *Z* form rather than maximise it in the *E*. As a result of this analysis, two dyads were proposed: **Dyad B** and **Dyad C** (Figure 4.15). They both comprised a diaminobenzene quencher, the tetra-*ortho* fluoroazobenzene and either Sulforhodamine B (a derivative of rhodamine B – **Dyad B**) or silicon rhodamine (**Dyad C**). The predicted properties for both dyads are shown in Table 4.3, including the predicted *ΔG* of the photoinduced electron transfer between the dye and the quencher, and the weighted average distances between the fluorophore and the quencher in both the *E* and *Z* forms.

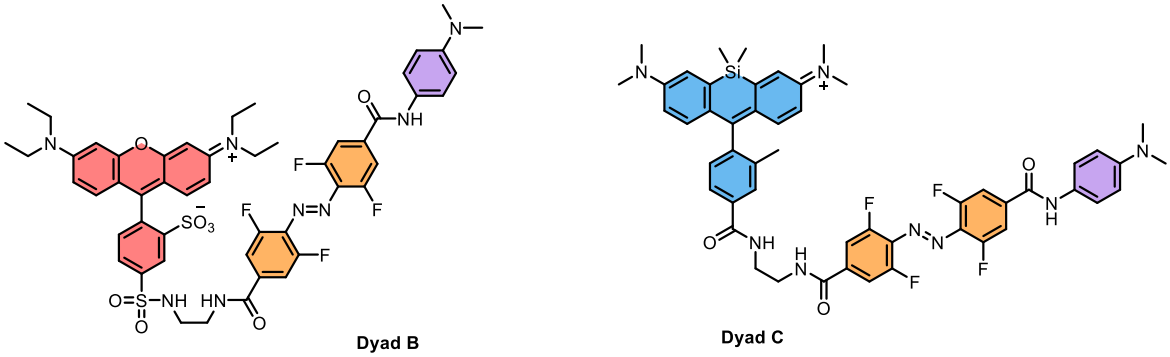


Figure 4.15: Proposed **Dyads B** and **C**.

Table 4.3: Predicted properties for the two proposed Dyads. *ΔG* values are from electrochemical analysis and Weller equation, distances are from Boltzmann-weighted xTB conformational searches for the *Z* and *E* isomer of each Dyad.

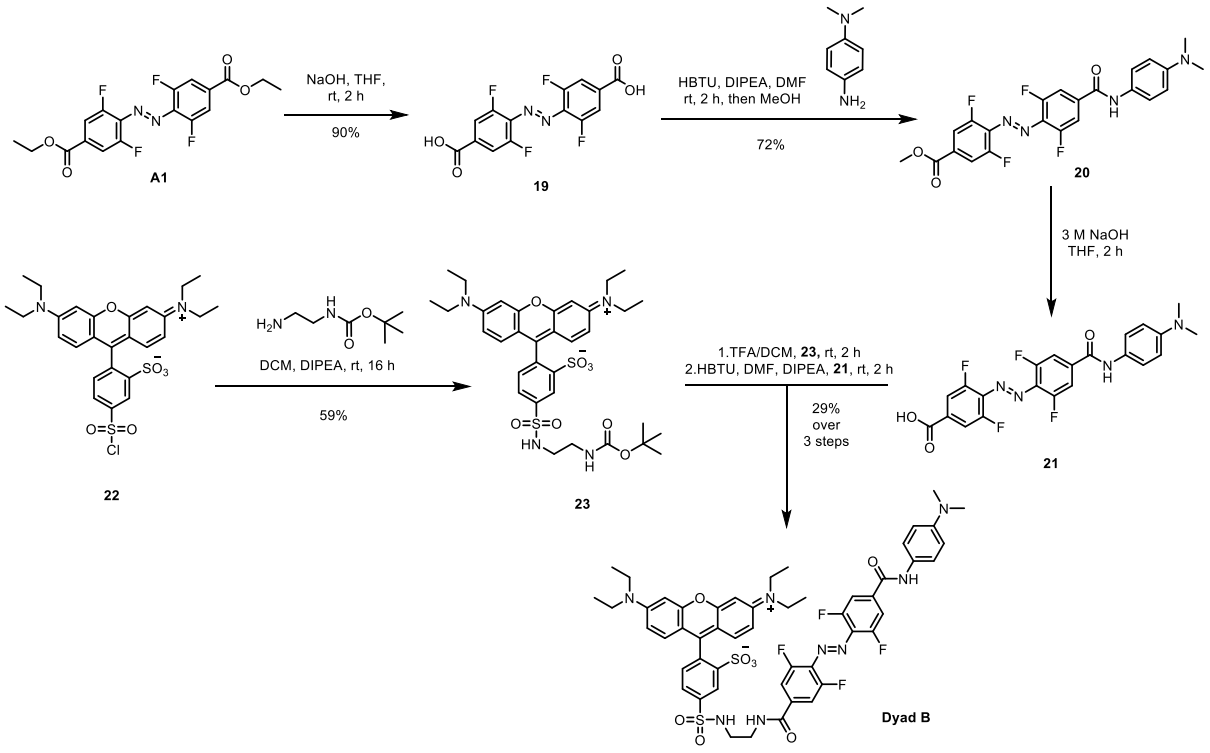
Dyad	ΔG_{PET} (V)	D_Z (Å)	D_E (Å)
B	-0.48	8.0	9.5
C	-0.78	6.4	11.2

2.1.4 Dyad synthesis

Dyads B and **C** were synthesised through successive amide couplings of the photowsitch, quencher, and dye components (Scheme 4.2, 4.3). Photoswitch **A1** underwent ester hydrolysis under basic

conditions to give the diacid photoswitch **19**. This was then coupled with the electron-rich quencher *N*,*N*-dimethyl-1,4-diaminobenzene using HBTU, followed by quenching with methanol to give the asymmetric amide and ester azobenzene **20**. This was achieved in good yield by using an excess of **19** compared to aniline and reclaiming the dimethyl ester byproduct. The photophysical properties of compound **20** were characterised as a control to explore the impact of the quencher on the photoswitching of **A1**.

Sulforhodamine B sulfonyl chloride **22** was substituted with *N*-Boc-ethylenediame to give compound **23**. The Boc protecting group was removed with TFA to give a primary amine, which then underwent amide coupling with the acid **21**, which had been synthesised through hydrolysis of compound **20**. The two deprotections and amide coupling steps gave **Dyad B** in 29% over these three steps.

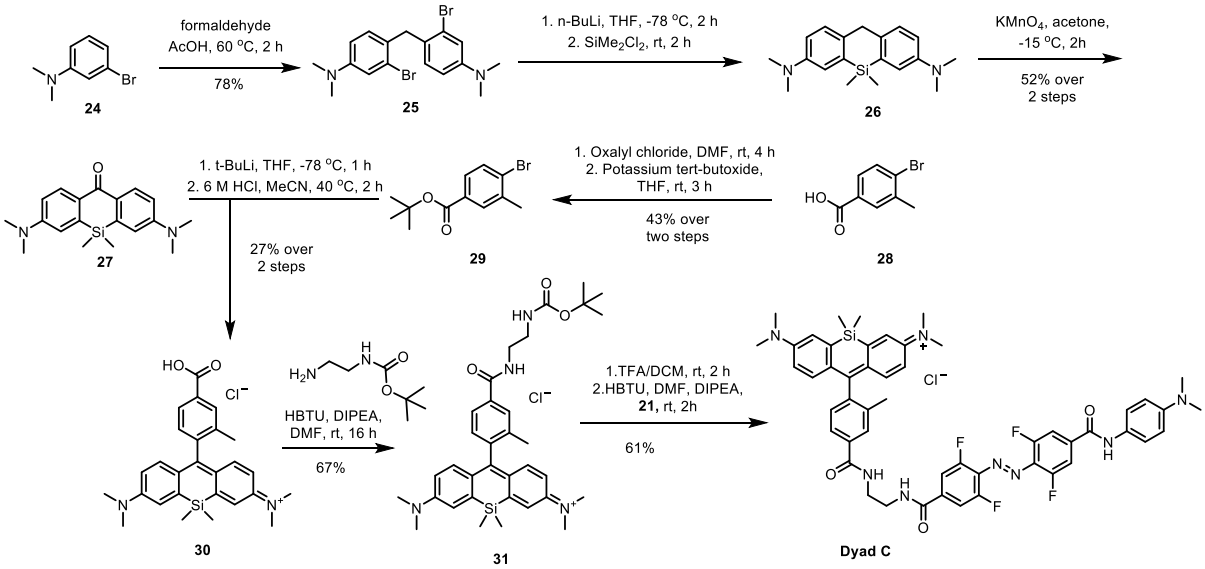


Scheme 4.2: Synthetic route to **Dyad B**.

Silicon rhodamine was synthesised according to literature procedure (Scheme 4.3).[20] Condensation of aniline **24** with formaldehyde gave dianiline **25**, which then underwent lithium halogen exchange

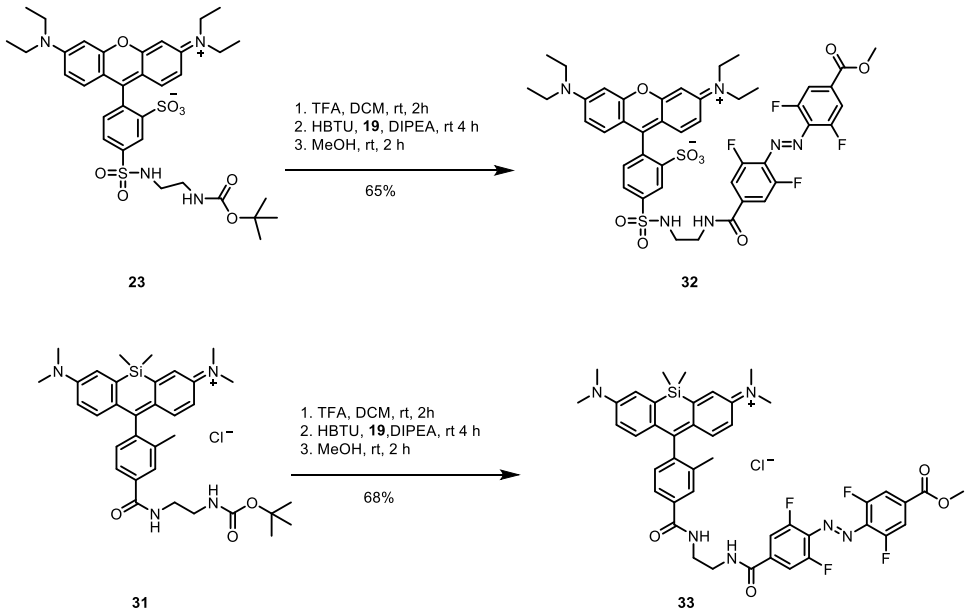
and substitution of dichlorodimethysilane to give **26**. This compound was used immediately in the next oxidation step with potassium permanganate due to its sensitivity to oxygen, to give ketone **27**. Protection of 4-bromo-3-methylbenzoic acid **28** as the tert-butyl ester allowed selective lithium halogen exchange and addition in ketone **27** to give silicon rhodamine. Hydrolysis of the ester with potassium hydroxide gave **30** ready for amide coupling with N-Boc-ethylenediamine to give **31**.

Compound **31** underwent an analogous TFA deprotection and amide coupling with the photoswitch-quencher carboxylic acid **21** to give **Dyad C**.



Scheme 4.3: Synthetic route to **Dyad C**.

In order to investigate the effect of the photoswitch on the photophysical properties of the dye (and vice versa) in isolation from the quencher, control molecules **32** and **33** were synthesised (Scheme 4.4). TFA deprotection of the linker dyes **23** and **31** followed by coupling with an excess of the diacid photoswitch **19** and quenching with methanol gave the control compounds **32** and **33** in good yields.



Scheme 4.4: Synthesis of control molecules **32** and **33**.

2.1.5 Dyad testing

The photophysical properties of the control molecules were investigated first. The photoswitching properties of compound **20**, comprising the photoswitch and the electron-rich aniline quencher were measured in acetonitrile (Figure 4.16A). Upon irradiation with 525 nm light, the most red absorption band intensity reduces, however this is not accompanied by a more intense absorption around 430 nm, as in photoswitch **A1**. This is presumably because the spectral separation is not as good, and there is overlap between the absorption of the *Z* and *E* forms. Nonetheless, the observed changes are reversible upon irradiation with 405 nm light, and NMR experiments confirmed the isomerisation between *E* and *Z* forms (Figure 4.16B). The PSD of *Z* isomer for **20** under 525 nm irradiation is approximately 65% and of *E* isomer under 405 nm irradiation is 88%, which is slightly lower than for **A1**, possibly as a result of the worse spectral separation.

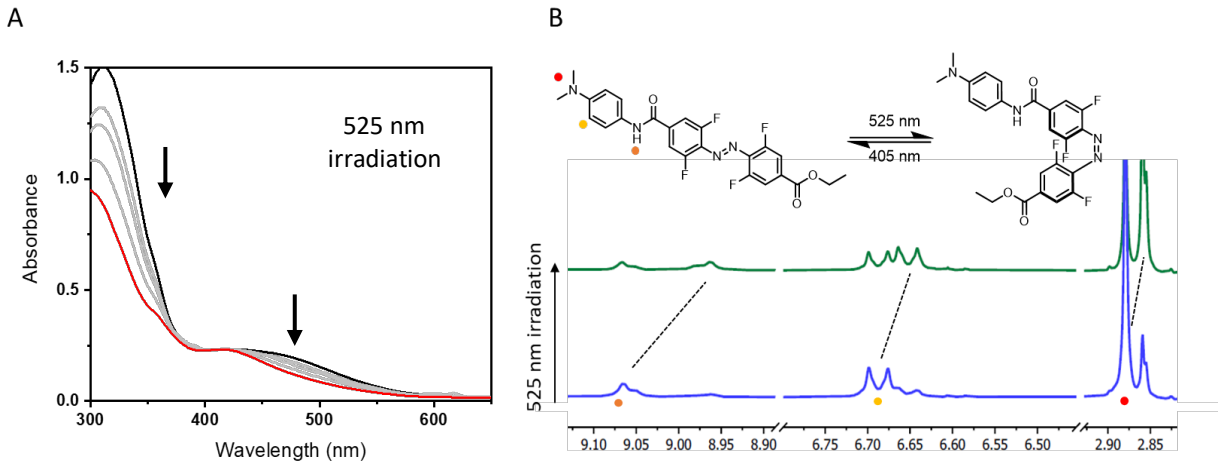


Figure 4.16A: Absorption spectra of photoswitch **20** upon irradiation with green (525 nm) LED light in MeCN. The initial spectrum is in black and the final spectrum is in red. The spectral changes were reversible upon irradiation with a blue (405 nm) LED. B: ^{1}H NMR spectra (400 MHz, 298 K) of photoswitch **20** in d_3-MeCN after irradiation with a 525 nm LED.

The properties of the control molecules **32** and **33**, comprising dyes and switches but no quencher, were then investigated, to understand whether the photoswitch itself will act as a PET quencher to the selected dyes. The absorption and emission spectra were measured in acetonitrile, with the absorption being heavily dominated by the fluorophores, consistent with the much larger molar absorption coefficients of these chromophores compared to the photoswitch (Figure 4.17).

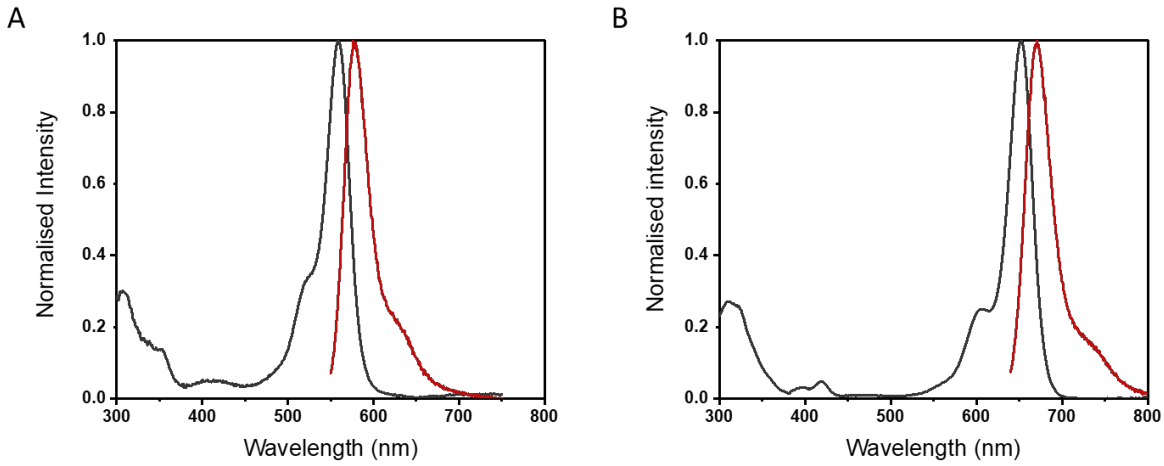


Figure 4.17: Absorption (black) and emission (red) spectra of **32** (A) and **33** (B) in MeCN at 298 K.

The fluorescence quantum yields of these molecules were recorded and compared to the parent dye molecules. Attachment of the photoswitch resulted in significantly lower quantum yields of

fluorescence (Table 4.4, below). This indicates that the photoswitch can act as a fluorescence quencher, presumably by a PET mechanism, as the dye emission (particularly for the SiRho) does not have good overlap with the photoswitch absorption for FRET.

A switching experiment was then undertaken to observe whether the isomerisation of the photoswitch would lead to a modulation in fluorescence emission due to a change in the energy levels of the photoswitch. The fluorescence emission of **32** and **33** were recorded following gradual irradiation with 525 nm light (Figure 4.18). It was shown that the fluorescence emission intensity increased by 36% and 44% respectively upon isomerisation of the photoswitch to the *Z* form. This was an interesting result which is presumably because the photoswitch becomes a poorer electron acceptor in the *Z* form, consistent with a higher energy π* orbital as a result of reduced conjugation, as discussed above. This is a similar mechanism as some of the PET dyads discussed in the introduction (eg. the BODIPY-spiropyran dyad in Figure 4.3, above), which rely on a change in thermodynamic driving force of PET quenching with photoswitch isomerisation to modulate emission intensity, rather than distance between the donor and acceptor.

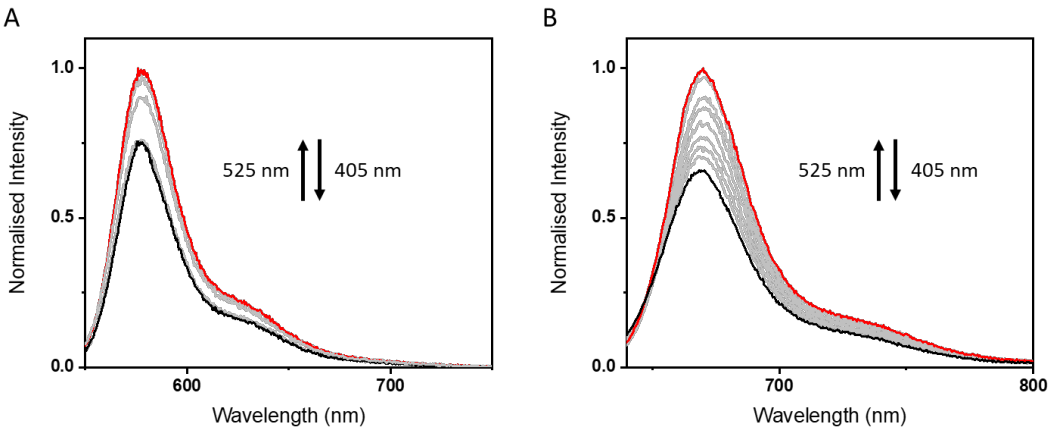


Figure 4.18: Emission spectra of **32** (A, λ_{exc} = 540 nm) and **33** (B, λ_{exc} = 630 nm) upon irradiation with green (525 nm) and blue (405 nm) LED lights in MeCN at 298 K. Black represents the blue PSS and red the green PSS.

This photoswitching result was confirmed by quantum yield analysis, which showed that the reduction in quantum yield associated with attaching the dyes to the photoswitch can be slightly recovered by isomerisation to a more *Z*-enriched photoswitch sample. Proton NMR photoswitching

experiments also showed that although the photostationary states of these dyads were lower than the parent photoswitch **A1**, there is still significant isomerisation between the two forms (Table 4.4).

Table 4.4: Photostationary state distributions of *E* and *Z* forms, and fluorescence quantum yields of dyes and control molecules.

		PSD (%)	ϕ
SiRho		-	0.56
SulfoRho B		-	0.30
A1	*E*	93	-
	Z	88	-
33	*E*	79	0.14
	Z	56	0.17
32	*E*	90	0.13
	Z	70	0.19

Finally, the photophysical properties of **Dyad B** and **Dyad C** were investigated. The absorption and emission spectra were very similar to that of the constituent fluorophores, and that of the control equivalents without the separate quencher (Figure 4.19).

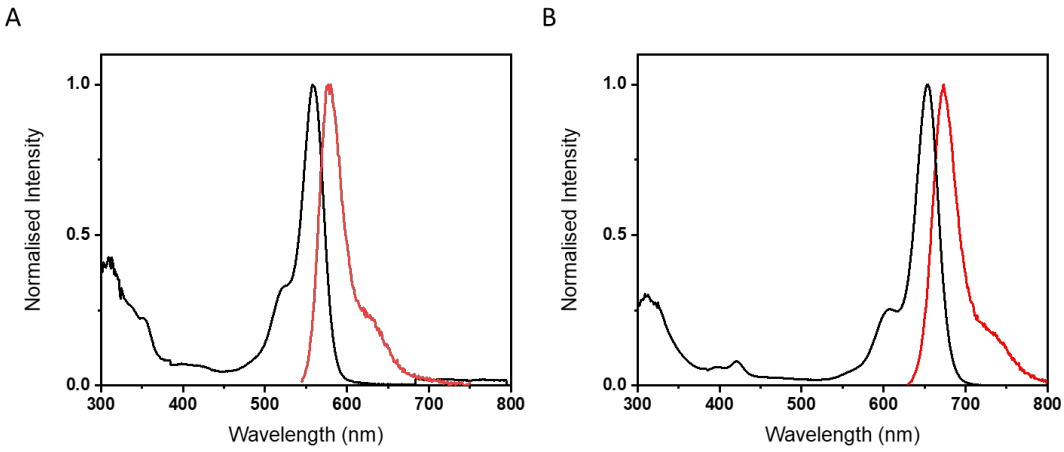


Figure 4.19: Absorption (black) and emission (red) spectra of **Dyad B** (A) and **Dyad C** (B) in MeCN at 298 K.

A switching experiment was then undertaken to observe whether the isomerisation of the photoswitch would lead to any changes in fluorescence emission due to a change in the geometry of the molecule, and the proximity of the quencher. The fluorescence emission of **Dyad B** was recorded following irradiation with 525 nm and 405 nm light for up to 1 hour, however no change in emission intensity was observed (Figure 4.20A). One reason this could be occuring is the photoswitch could no longer switch when incorporated into the dyad. However, proton NMR switching experiments confirmed that the photoswitch is undergoing isomerisation upon irradiation, with PSDs of 86% *Z* and 71% *E* under 405 nm blue and 525 nm green irradiation respectively (Figure 4.20B).

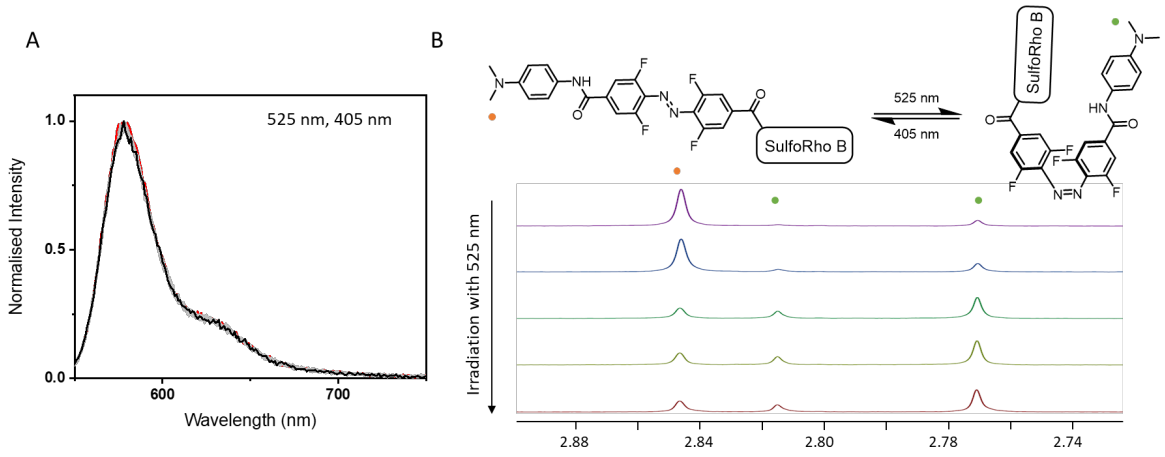


Figure 4.20A: Emission spectra (λ_{exc} = 540 nm) of **Dyad B** upon irradiation with green (525 nm) and blue (405 nm) LED light in MeCN at 298 K. B: ^{1}H NMR spectra (400 MHz, 298 K) of **Dyad B** in d_3-MeCN after irradiation with a 525 nm LED. The *Z* isomer spectrum shows two sets of resonances for each *E* one, suggesting two conformations might be present in solution.

It is interesting that there is no change in fluorescence emission in this molecule, particularly as emission changes were observed in compound **32**, and the presence of two conformers in the *Z* form of **Dyad B** indicates that the quenching unit is potentially stacking on two different sides of the photoswitch, and is spatially close to the dye. This implies, perhaps, that the electron quenching effect to the photoswitch in the *E* form is essentially as efficient as the electron quenching effect from the aniline quencher in the *Z* form, leading to no overall difference in fluorescence quenching between the isomers.

A photoswitching experiment was performed on **Dyad C** in an analogous manner. In this case, isomerisation with 405 nm and 525 nm light did result in modulation of the fluorescence emission in the expected direction, with green light causing a decrease in fluorescence emission as the quencher was brought closer to the fluorophore, and blue light increasing emission again. (Figure 4.21). This corresponds to a 43% increase in emission intensity between the *Z* to *E* photostationary states. Measurement of the fluorescence quantum yield of the dyad at both photostationary states showed this increase to be 0.21 to 0.31, in comparison to the value of 0.56 for silicon rhodamine alone. Surprisingly, neither form of **Dyad C** is as efficiently quenched as control molecule **33**.

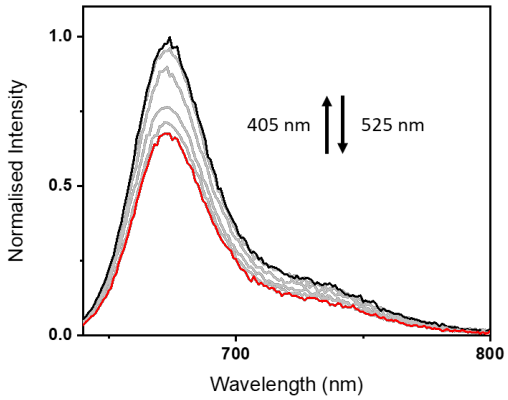


Figure 4.21A: Emission spectra of **Dyad C** (λ_{exc} = 625 nm) upon irradiation with green (525 nm) and blue (405 nm) LED light in MeCN at 298 K.

2.1.6 Conclusions from this design

In this section, I attempted to use the variation in distance between a fluorophore with a PET quencher upon isomerisation of a central azobenzene photoswitch to modulate fluorescence emission. **Dyad B** and **Dyad C** were investigated as candidates for this design, with both having a predicted downhill thermodynamic driving force (ΔG_{PET} = -0.48 V for **Dyad B** and ΔG_{PET} = -0.78 V for **Dyad C**). Additionally, they both had a significant difference between the predicted average quencher – fluorophore distance using a Boltzmann weighting analysis of conformer populations. Both dyads were synthesised alongside control molecules comprising just the dye and tetra-*ortho*-fluoroazobenzene photoswitch. Interestingly, these molecules showed a significant amount of

fluorescence switching without an additional quencher, as the photoswitch itself could act as a PET electron acceptor. Isomerisation to the *Z* form of these molecules was accompanied by a turn-on in fluorescence, as the photoswitch became harder to reduce in its less conjugated form.

When a separate quencher had been introduced on the opposite side of the photoswitch, this fluorescence switching behaviour was reversed in **Dyad C**, and isomerisation to the *Z* form of these molecules was accompanied by a turn-off in fluorescence as the quencher and dye were brought closer together. This change was significant (Φ_{flu} 0.31 in *E* to 0.21 in *Z*) but not high-contrast enough to be useful for super-resolution microscopy. In **Dyad B** however, no change in emission was observed between the two isomers. This is possibly because the magnitude of the quenching from the photoswitch in the *Z* form was similar to the quencher in the *E* form, but could also be due to the sulfonate charge causing unexpected conformations not captured by the modelling.

A similar design strategy was reported around this time with azobenzene dyads comprising a rhodamine fluorophore and an electron-poor quencher (Figure 4.22).[21] A similar extent of quenching was observed in these molecules (around 50%) on isomerisation with UV light. As photostationary state distributions were not reported, it is unclear if the lack of complete quenching in these molecules is due to a low PSD or poor quenching. The mechanism in this report was described as 'contact quenching', and not elaborated beyond this.

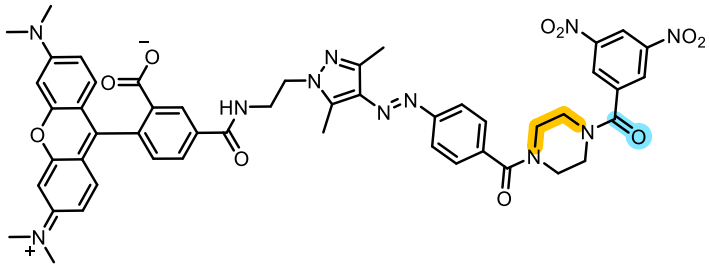


Figure 4.22: Structure of reported photoswitchable contact quenching dyads.[21] Two further molecules were made, with linker groups not including the highlighted atoms.

It is interesting that although the chosen photoswitch, linkers, quencher, and fluorophore were different, the maximum achievable fluorescence quenching was similar. This potentially indicates

that optimisation around this design concept will not drastically improve the system due to some key limitations. Based on my results, I think the key takeaway points from this design are:

1. It is very difficult to balance the amount of flexibility which is necessary to allow close enough contact for PET, without losing the rigidity required for two distinct states. This is particularly true as these molecules are poorly suited to the available computational techniques used to explore ground state conformation, being flexible, charged, and incorporating large π systems, which makes it hard to predict conformation in advance. Perhaps a lesson from this is to design molecules which are inherently less flexible, because if the computational methods are uncertain about the conformation, it is unlikely we will be able to induce precise control over the two different states.
2. The turn-on response is less important than the turn-off one. It would be better for contrast to have a completely dark off state with a moderate turn-on, than a somewhat bright off state with a very large turn-on state. The molecules above are thermally stable in the 'on' form, which makes it harder to optimise the 'off' state for complete quenching. It would be more sensible to design a molecule where the resting state was 'off', with ideal conditions for PET fluorescence quenching, and where isomerisation caused a disturbance that led to emission turn-on.
3. Further to the above point, the photostationary state distributions of **A1** became worse in every single example where something was attached. Perhaps this is due to excited state relaxation pathways introduced by the substituents that compete with isomerisation. Whether this is electron transfer, FRET, or simply more non-radiative decay from higher degrees of freedom, it would be more advantageous to design molecules which relax fully back to the off state, and where a lower PSD in the 'on' direction would affect the brightness but not impact the contrast so much.

2.2 Second Design Phase

In order to address the limitations of the above systems, a new molecular design was pursued which would allow the close stacking of a fluorophore and a quencher in the thermally stable state of a photoswitch. Any isomerisation would disrupt this close stacking, and hopefully allow for a turn-on (rather than a turn-off) of the fluorescence. Diazocines were chosen as a rigid photoswitch, with high quantum yields of photoswitching, and a cyclic structure which would allow two adjacent substituents to be introduced (Figure 4.23).

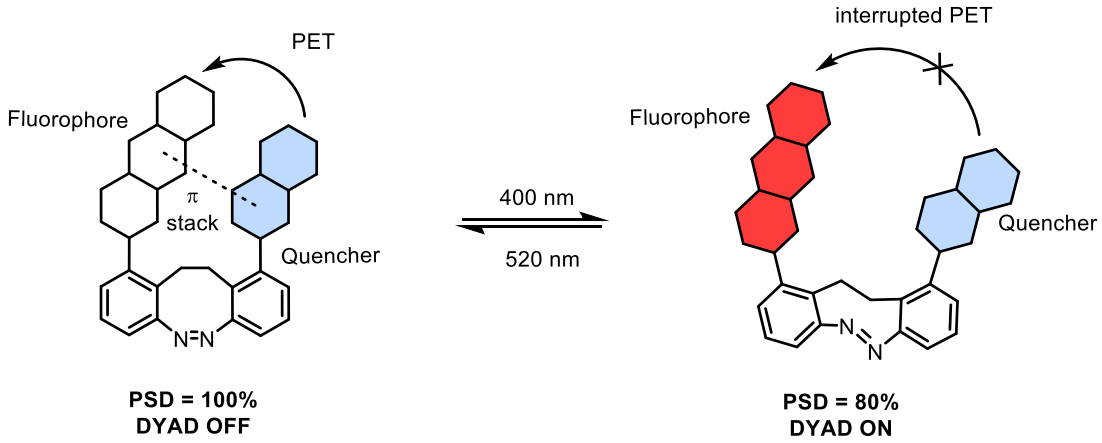
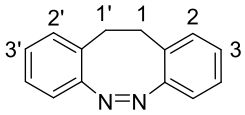


Figure 4.23: Design for diazocine-based dyad with stacked fluorophore and quencher in the resting state.

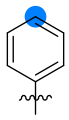
2.2.1 Modelling geometry changes

In order to estimate the geometric relationship between the two substituents upon isomerisation of the diazocine photoswitch, some models were made to investigate the various positions of substitution. Three positions on the bridged azobenzene were considered for functionalisation, with the aim of making a *Z* conformation with close, parallel-stacked fluorophore and quencher units. A simple model with a benzene substituent used to represent both fluorophore and quencher at each position was used (Figure 4.24). Rather than xTB, a starting geometry of the DFT-minimised structure of diazocine[22] was functionalised with the model aryl substituents and minimised using UFF in Avogadro. These results indicated that functionalisation at the 2/2' positions was the most promising for both a minimal quencher-fluorophore distance in the *Z* conformation, and a

maximum distance discrimination to the *E* conformation. While the difference is largest for position 3, the *Z* stacking distance is not close enough for efficient quenching, and position 1 gave little discrimination between the *Z* and *E* forms.



functionalisation positions



model substituent

position	distance *Z* (Å)	distance *E* (Å)	Δ distance (Å)
1/1' (*cis*)	6.6	7.2	0.6
1/1' (*trans*)	9.3	9.6	0.3
2/2'	5.4	8.8	3.4
3/3'	12.3	16.3	4.0

Figure 4.24: A simple model for the different proposed functionalisation positions and their corresponding *Z*/E distance changes. Distance refers to distance between highlighted blue carbons on two model phenyl substituents. Note substituents at 1/1' could be cis or trans to one another.

As well as the distance, the isomerisation impacted the alignment of the two substituents. In the *Z* isomer, the two substituents are essentially parallel, whereas in the *E* form they are no longer well stacked (Figure 4.25).

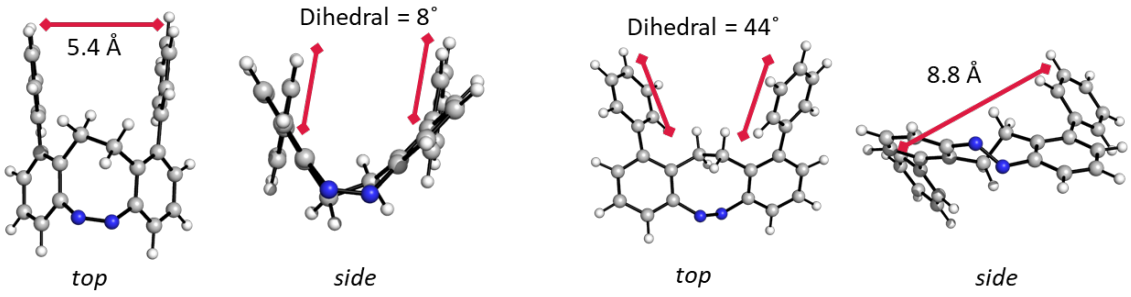


Figure 4.25: Angle and distance between model aryl substituents on a proposed diazocine photoswitch in *Z* (quenched) and *E* (emissive) isomers.

2.2.2 Choosing a dye and quencher

Based on the electrochemical analysis performed in Section 2.1.2, an electron-rich aniline was chosen as a quencher. In order to maximise the geometric overlap with the fluorophore, it was decided to use a dimethylaminonaphthalene. An alkyne linker was chosen both for ease of synthesis, and to include a spacer that would allow good alignment with the xanthene portion of

the fluorophore. Silicon rhodamine was chosen as the fluorophore in order to minimise the chance of FRET, as the absorption of diazocines is red-shifted by ~50 nm compared to **A1**. An example of the di-*ortho* substituted final design is shown in Figure 4.26, although the substituents could also be *ortho* to the azo group, as discussed below.

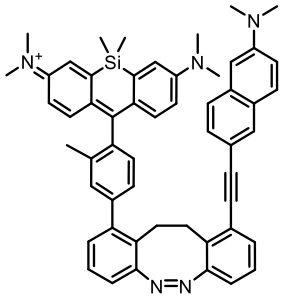
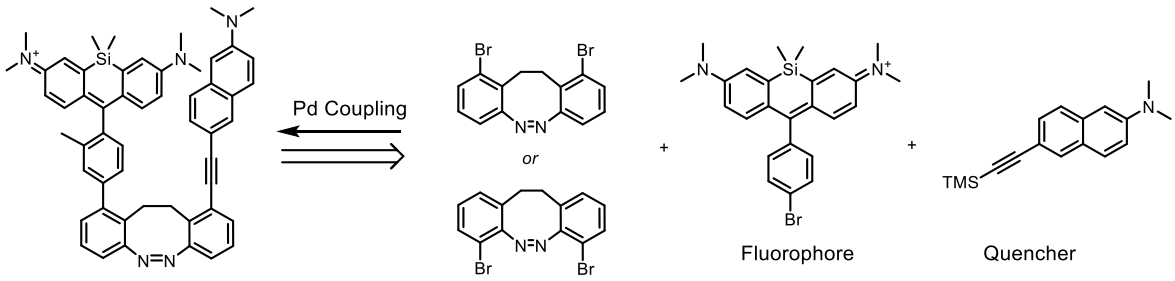


Figure 4.26: The structure of proposed **Dyad D.**

2.2.3 Synthesis of the photoswitch

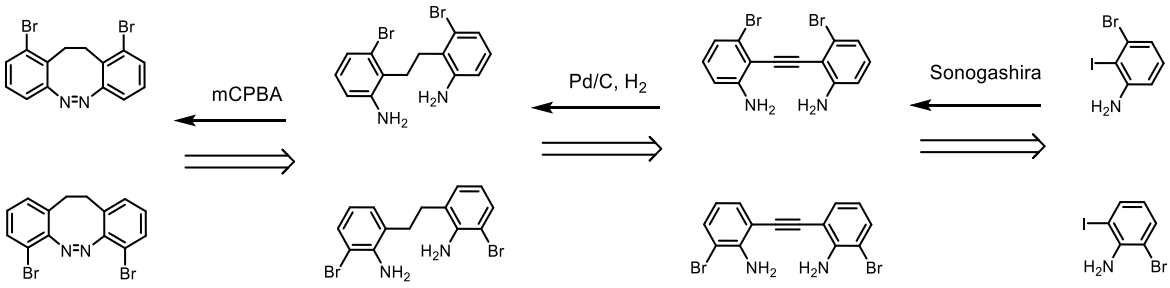
It was envisaged that the quencher and the dye could be coupled to the photoswitch using Suzuki and Sonogashira cross-coupling reactions (Scheme 4.5). This requires a diazocine photoswitch with di-substitution either *ortho* to the ethylene bridge, or *ortho* to the azo group, as both of these positions should give analogous geometry changes.



Scheme 4.5: Synthetic strategy for **Dyad D**.

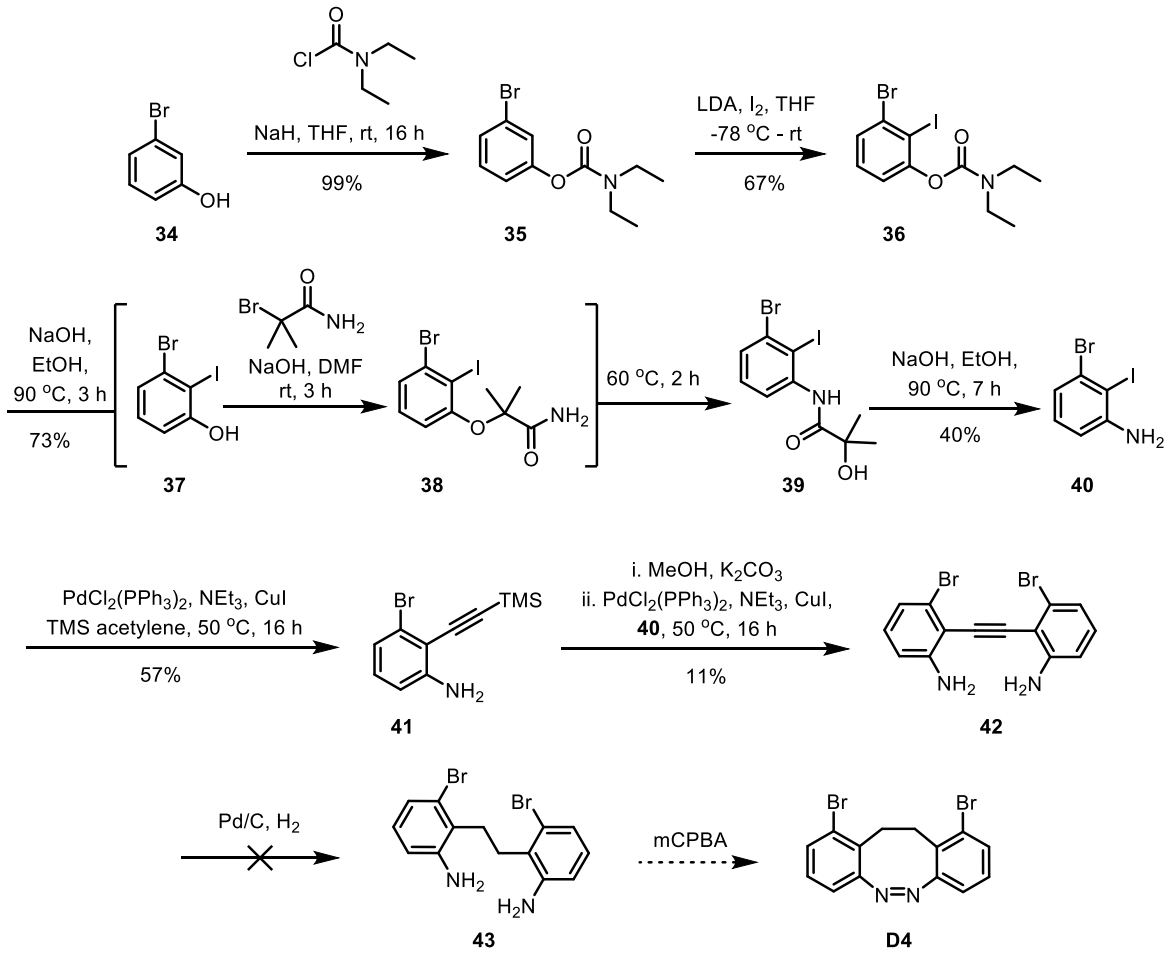
An advantage to this convergent strategy is that many different fluorophore and quencher combinations could be coupled to the photoswitch in order to investigate or iteratively improve the dyad's properties. One effective method of making diazocines is through an intramolecular oxidative cyclisation of a bis-aniline (Scheme 4.6). The ethylene bridge of these molecules is usually

installed by the reduction of an alkyne, which is introduced by Sonogashira coupling of two aryl fragments.



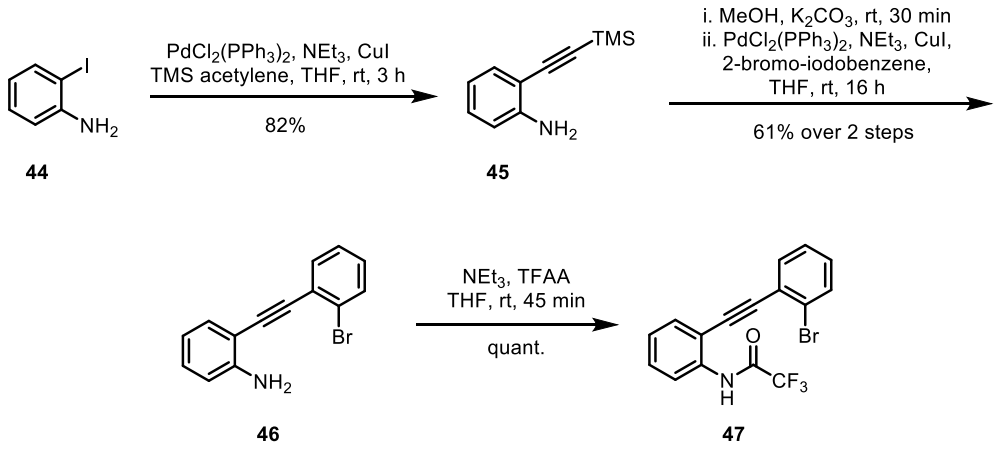
Scheme 4.6: Retrosynthetic analysis for the oxidative formation of diazocines.

In light of this analysis, a route was designed toward dibromodiazocine **D4** *via* the 2,3-substituted aniline **40** (Scheme 4.7). Installation of a single *ortho* and *meta* substituent on aniline requires starting from carbamate-protected 3-bromophenol **35**, and selectively iodinating at the 2-position to give **36**. Cleaving the directing group under basic conditions to give **37**, followed by addition of the Smiles reagent triggers a Smiles rearrangement of the phenol to the anilide **39**. Cleavage to the aniline **40** under basic conditions allowed a subsequent Sonogashira coupling to install TMS acetylene, with selective reaction at the iodine, to give **41**. Alkyne deprotection, and a second Sonogashira coupling with compound **40** gave **42** in low yield, along with a significant amount of starting material and some homo-coupled alkyne. Additionally, compound **42** was poorly soluble, making purification difficult. Subsequent reduction attempts with Pd/C and H_2 were unsuccessful, giving very slow reaction rates, ultimately stalling after ~5% conversion, and the appearance of proto-dehalogenated products.



Scheme 4.7: Proposed route 1 to functionalised diazocine photoswitch.

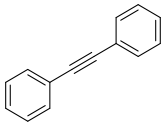
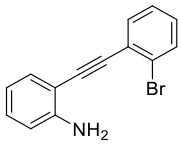
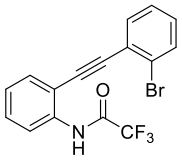
It was hypothesised that the lack of complete reduction observed could be due to the coordination of the aniline groups to the palladium catalyst, or protodehalogenation of the ortho halogen leading to catalyst poisoning. Some test substrates **46** and **47** were synthesised to investigate the impact of the *ortho* halogen and the *ortho* aniline on a variety of reduction conditions (Scheme 4.8). Compound **46** was made by Sonogashira coupling of iodoaniline **44** with TMS acetylene, followed by TMS deprotection and a second Sonogashira reaction with 2-bromoiodobenzene. Subsequent acetylation with trifluoroacetic anhydride gave compound **47** in quantitative yield.



Scheme 4.8: Synthesis of test substituents.

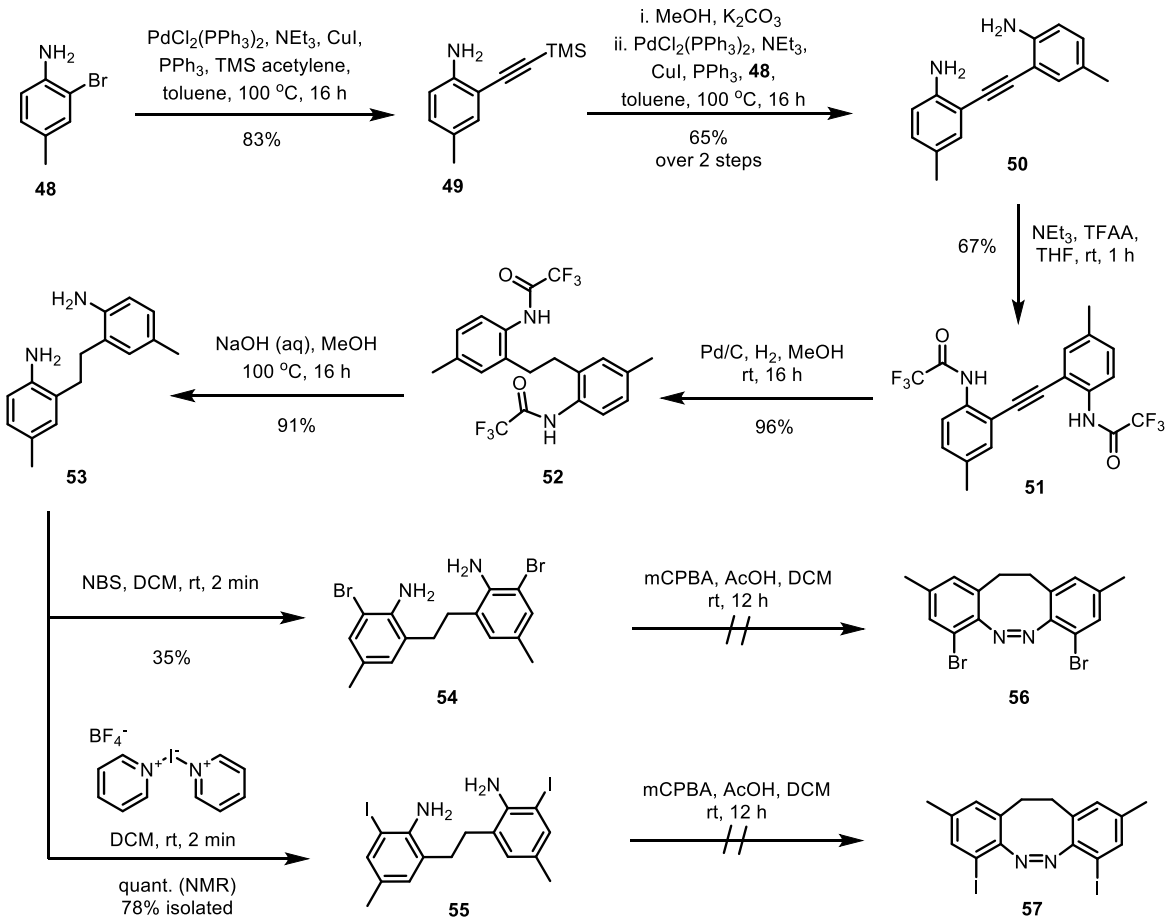
The test substrates, as well as diphenylacetylene, were subjected to various reduction conditions (Table 4.5). Platinum has been used to reduce similar halogenated diphenylacetylene substrates without dehalogenation, however with fluorine *ortho* and bromine *para* to the alkyne.[23] Tosyl hydrazine and sodium acetate have been successfully used to reduce alkenes with *ortho*-bromo phenyl substituents.[24] Diphenylacetylene was quantitatively converted with both Pd/C and PtO_2, but unreactive with the tosyl hydrazide conditions, indicating that these conditions are inappropriate for alkyne reduction. Compound **46** was unreactive with Pd/C, but showed some conversion to product with PtO_2. The conversion stalled over longer reaction times, however, and a significant proportion remained as the partly-reduced *Z* alkene. When the aniline was acetylated in compound **47**, some Pd/C reduction activity returned, however traces of dehalogenated products were observed, along with a significant amount of alkene, but none of the desired product. This indicates that for the Pd/C conditions, interaction of the aniline with the Pd was inhibiting reactivity. Under PtO_2 conditions, conversion was slightly higher after acetylation as well, although almost all reduction stopped at the alkene rather than proceding to the alkane product. It is possible that catalyst poisoning through dehalogenation side reactivity was inhibiting full conversion. My conclusion from this screen was that both the *ortho* aniline and *ortho* halogens were potential problems with this synthetic route, so an alternative route was explored that would allow late-stage introduction of the halogen substituents, after the reduction step.

Table 4.5: Screening conditions for alkyne reduction against different test substrates.

			
	Diphenylacetylene	**46**	**47**
Conditions		**(hours) conversion**	
Pd/C, H_2, MeOH, rt	(3) 100%	(24) 0%	(3) 16% alkene (24) 33% alkene, dehalogenation
PtO_2, H_2 methanol/THF, rt	(3) 100%	(3) 13% alkene, 5% product (24) 23 % alkene, 13% product	(3) 26% alkene, trace product (24) 35% alkene, trace product
Tosyl hydrazide, NaOAc, THF, reflux	(24) 0%	(24) 0%	(24) 0%

The second proposed route was to a photoswitch with halogen substituents *ortho* to the azo group (Scheme 4.9). Starting with 2-bromo-4-methylaniline **48**, the *para* position was blocked for a late-stage halogenation reaction. Sonogashira coupling with TMS acetylene to give **49**, followed by subsequent deprotection of the alkyne and a second Sonogashira coupling with **48** gave **50** in good yield. Direct hydrogenation of this substrate was unsuccessful, so it was decided to protect the anilines as amides, as in the test reactions above above. Acetylation with trifluoroacetic anhydride gave compound **51** which was then cleanly reduced in high yields to give **52**. Hydrolysis of the trifluoroacetyl protecting groups under basic conditions gave bis-aniline **53**, which could then be halogenated with NBS or Barluenga's reagent to give the bromo- and iodo-substituted compounds **54** and **55** respectively. As compound **53** is so electron-rich, reaction with I_2 or NIS gave poly-

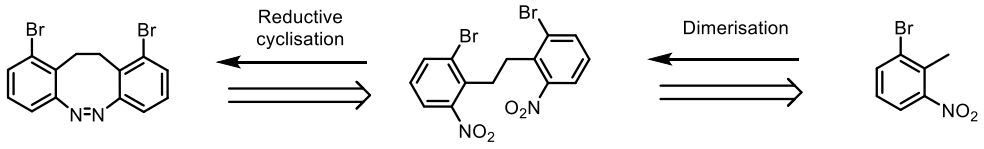
iodinated products, and significant amounts of decomposition, however the less active Barluenga's reagent, known to convert similar substrates cleanly,[25] gave the desired product in quantitative yield. When both compound **54** and compound **55** were subjected to the oxidative mCPBA azo-forming conditions, evidence of the desired product was observed by NMR spectroscopy in the crude reaction mixture. Unfortunately, the product was formed with a large amount of dehalogenated byproducts, presumably due to the proximity of the *ortho*-halogens to the aniline. This mixture of compounds was inseparable under all trialled chromatography conditions.



Scheme 4.9: Alternative route 2 to functionalised diazocine photoswitch.

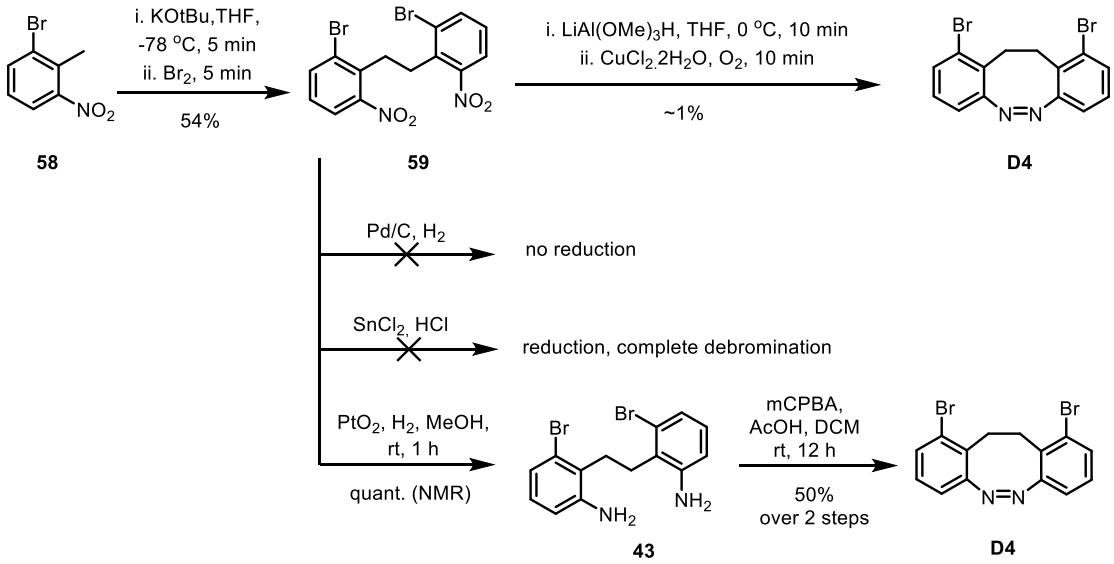
An alternative route towards diazocines was considered, utilising reductive cyclisation methods[26] (Scheme 4.10). A new report[27] showed the synthesis of the target photoswitch **D4** with two bromo substituents (Scheme 4.11), however with low reported low yield (20%) and modified reaction conditions to avoid making dehalogenated by-products, with only moderate success. These

byproducts are inseparable using chromatography, and require vacuum sublimation purification at 120 °C and 10^{-5} mbar.



Scheme 4.10: Retrosynthetic analysis for the oxidative formation of diazocines.

Ultimately, attempts to follow this route (Scheme 4.11), by dimerization of **58** with potassium tert-butoxide and bromine to give **59**, then reduction with $LiAl(OMe)_3H$ to make **D4**, formed a mixture of the desired product, and two byproducts with either one or no bromine substituents. After column chromatography followed by recycling gel permeation chromatography and recrystallisation from THF, the product was isolable in approximately 1% yield, showing this route was not a viable strategy for the formation of **D4** in appreciable yields. However, the reduction of the nitro compound to the aniline, followed by an oxidative cyclisation was envisaged as a work-around (Scheme 4.11). Although it requires inefficient redox manipulation steps, it was pursued as an alternative route to the final product. Reduction with Pd/C gave incomplete conversion and a mixture of products, but no aniline, potentially due to coordination of a reduced intermediate with the Pd. Tin chloride and HCl reduction conditions reduced the nitro groups but also gave complete debromination. However, using the PtO_2 conditions that had been explored for previous routes gave the bis-aniline with quantitative conversion and no dehalogenation. Subsequent oxidative cyclisation gave the photoswitch in reasonable yield and crucially, without the dehalogenation observed under these conditions when the bromine atoms were *ortho* to the azo group.



Scheme 4.11: Synthesis of photoswitch **D4**.

2.2.4 Characterisation of the photoswitch

The photophysical properties of photoswitch **D4** were measured in MeCN. UV-Vis switching experiments showed the photoswitch isomerises reversibly from the *Z* isomer to the *E* isomer and back, with irradiation at 405 nm and 525 nm respectively, displaying similar spectral features to diazocines **D1** – **D3** (Figure 4.27A). The photostationary state under 525 nm irradiation contains 100% *Z* isomer, which can be converted to 68% *E* isomer with 405 nm light (Figure 4.27B).

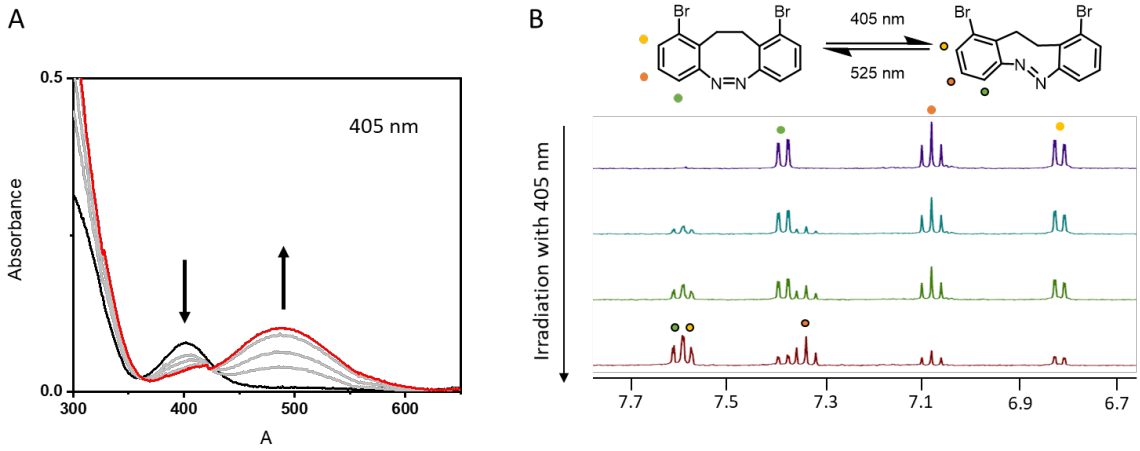
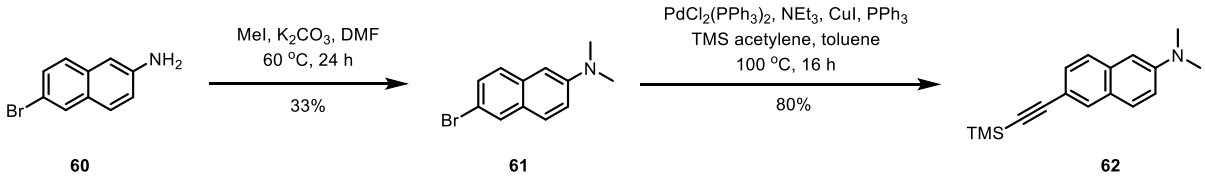


Figure 4.27A: Absorption spectra of photoswitch **D4** upon irradiation with blue (405 nm) LED light in MeCN. The initial spectrum is black and the final spectrum is red. The spectral changes were reversible upon irradiation with a green (525 nm) LED. B: Partial ^{1}H NMR spectra (400 MHz, 298 K) of photoswitch **A1** in d_3-MeCN after irradiation with a 405 nm LED.

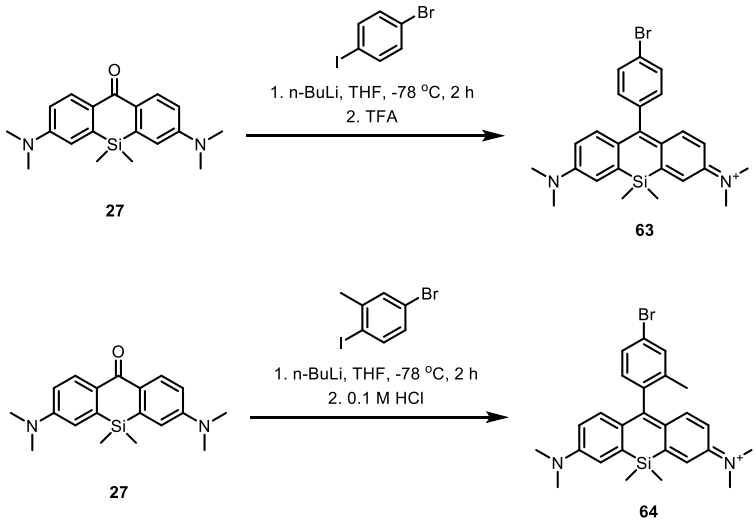
2.2.5 Synthesis of the Dyad

The quenching unit was synthesised from naphthylamine **60**, with methylation to give **61** and a subsequent Sonogashira reaction with TMS acetylene to install the alkyne linker and give **62** (Scheme 4.12).



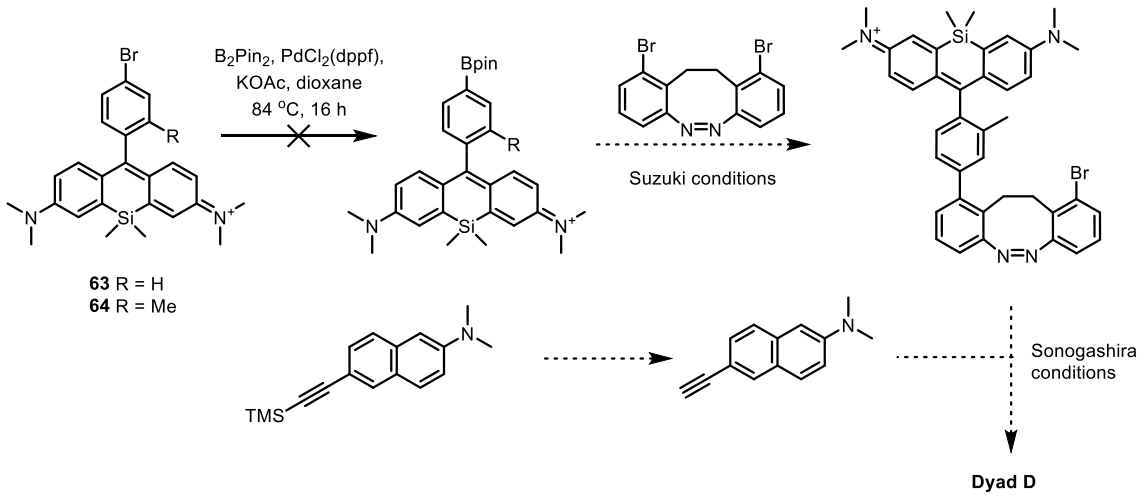
Scheme 4.12: Synthesis of quenching naphthylamine with alkyne linker.

The silicon rhodamine fluorophore was synthesised analogously to **30** above (Scheme 4.3). 4-Bromoiodobenzene was lithiated and added into ketone **27** to give **63** with an aryl bromide handle for further coupling (Scheme 4.13). Compound **64** was synthesised in a similar way with an *ortho* methyl group. It was thought that **63** would give the best stacking with the quencher in the final dyad, however removal of steric bulk around the xanthene is known to make this chromophore susceptible to nucleophilic attack and blinking.[28] Therefore **64** was synthesised as a more stable (although possibly worse stacking) fluorophore for comparison.



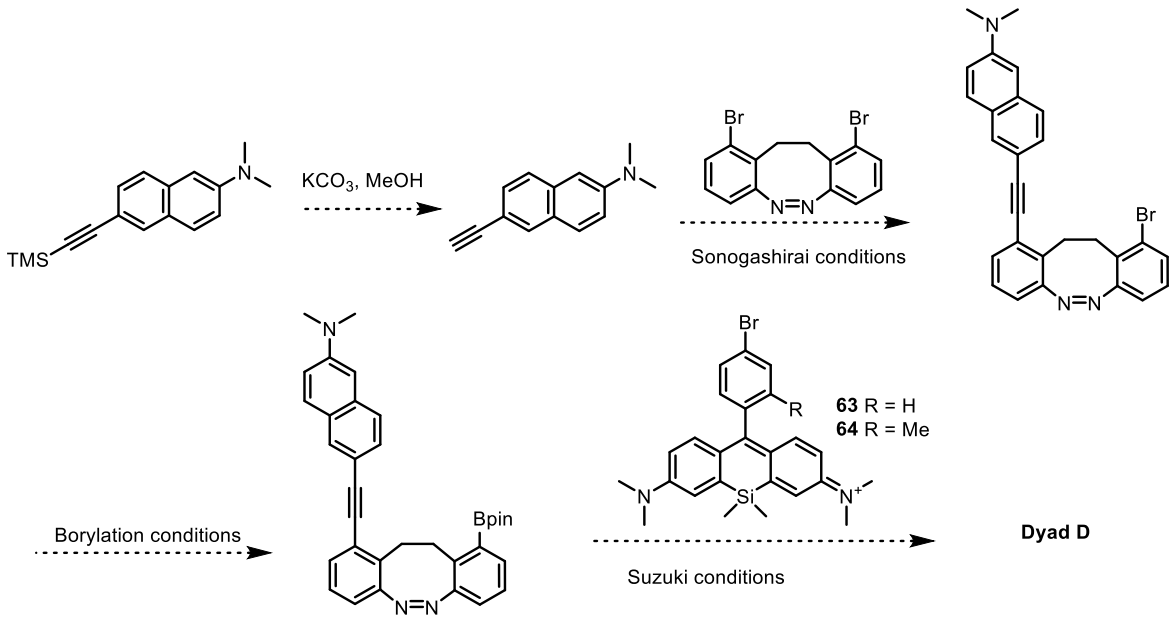
Scheme 4.13: Synthesis of silicon rhodamine fluorophores.

Unfortunately, when it came to assembling the final dyad, several difficulties were found in pursing the proposed coupling reactions. Neither **63** nor **64** were stable to the trialled Miyaura borylation conditions (Scheme 4.14).



Scheme 4.14: First proposed synthesis of **Dyad D**.

One way around this would be building the dyad in the opposite direction in future attempts, coupling of the quencher first, followed by borylation of the photoswitch (Scheme 4.15).



Scheme 4.15: Second proposed synthesised of **Dyad D**.

3. Conclusions and Future Work

In this chapter, using a PET-quenching mechanism for photoswitchable quenchable RESOLFT dyads has been explored. In the first design phase, two dyads were synthesised, **Dyad B** and **Dyad C**. They both comprised a central tetra-*ortho*-fluoroazobenzene photoswitch, which was chosen for its high photostationary states and visible light switching in both directions. The two *para* positions of this azobenzene were functionalised with a sulforhodamine B (**dyad B**) or silicon rhodamine (**Dyad C**) and an electron-rich aniline quencher. The dyads were designed to show a reduction in the fluorescence emission in the *Z* form, as the quencher and fluorophore were brought closer together and PET quenching became faster. **Dyad B** did not show any fluorescence quenching upon isomerisation, however **Dyad C** showed a 44% reduction in emission intensity.

The biggest drawback of this dyad design is that the 'off' state is still reasonably fluorescent, leading to poor contrast between the two states. The thermodynamically stable state of the chosen photoswitch holds the quencher and fluorophore far apart, and is the 'on' state. The dyads also have a high degree of flexibility, which makes the conformation in the *Z* and *E* isomers difficult to predict. This led to the design of a much more rigid diazocine-based dyad. The synthesis of the photoswitch with substituents *ortho* to the ethylene bridge was explored and optimised, allowing large quantities to be synthesised. A fluorophore and quencher were chosen for their electrochemical and geometric properties, and successfully synthesised. However, I was unable to make the final dyad, due to limitations in the stability of the coupling partners. A new synthetic route to the dyad, coupling the components of the dyad in a different order, will be explored in the future to attempt to synthesise this compound, and characterise its photophysical properties.

The major conclusion of this chapter of work is that making an effective PET quenching dyad poses several challenges. Firstly, the close distances required for PET to occur are difficult to design, predict, and control with a photoswitch. This challenge would be aided by more synthetic

approaches to photoswitches, expansion into less obvious substitution patterns, and better computational modelling tools.

Secondly, there are many competing excited state processes which can occur when molecular designs get bigger and more complicated. These are difficult to separate from each other and fully understand, even with control molecules. Advanced methods like time-resolved spectroscopy can help but ultimately it is better to have more simple designs where there are fewer options for competing deactivation pathways. However, this makes it harder to find molecules that can perform multiple functions of the material (emission, quenching, switching), and further emphasises the need for new photoswitchable materials with optimised properties.

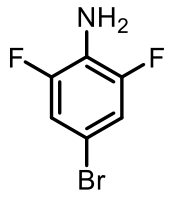
4. Experimental Methods

4.1 General Synthetic Methods

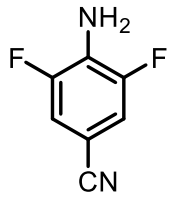
All reagents were purchased from commercial sources and used as received. Normal phase flash column chromatography was carried out using SiO_2 (60 Å pore size, 40–63 µm particle size, Aldrich, UK) as the stationary phase.

NMR spectra were acquired on a Bruker AVII400, AVIII400, or AVII500 instrument at 298 K. NMR chemical shifts are reported in ppm relative to $SiMe_4$ (δ = 0) and were referenced internally with respect to residual solvent protons. Coupling constants are reported in Hz. Multiplicity is denoted by s (singlet), sb (broad singlet), d (double), t (triplet), dd (doublet of doublet), dt (doublet of triplets), q (quartets). Electrospray mass spectrometry was carried out on a Waters Micromass LCT Premier XE spectrometer using 90:10 MeOH:H_2O (+0.1% formic acid) as the mobile phase. High-resolution mass spectra (HRMS) were obtained on a Bruker µTOF instrument or a Waters GCT or a BioAccord High Resolution Spectrometer.

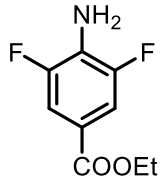
4.2 Synthesis and Characterisation



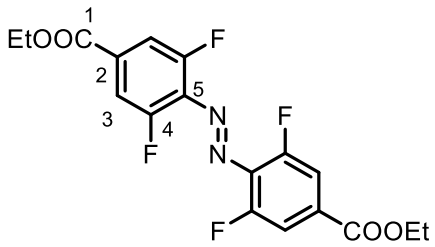
4-Bromo-2,6-difluoroaniline (16) was synthesised according to a known procedure.[15] *N*-Bromosuccinimide (13.8 g, 77.5 mmol) was added to a solution of 2,6-difluoroaniline **5** (10.0 g, 77.4 mmol) in acetonitrile (150 mL) and stirred for 4 h at room temperature. The reaction mixture was diluted with water and extracted with petrol ether (3 × 100 mL). The combined organic extracts were dried over $MgSO_4$, filtered, and evaporated under reduced pressure. The crude residue was purified by flash column chromatography (1:1 CH_2Cl_2 : petrol ether) to give compound **16** as a white solid (10.6 g, 66%) with spectra matching the literature. **^{1}H NMR** (400 MHz, $CDCl_3$): δ 6.99 (dd, *J* = 7.0, 1.4 Hz, 2H, *Ar-H*), 3.72 (sb, 2H, *N-H*); **^{13}C NMR** (101 MHz, $CDCl_3$): δ 153.0, 150.6, 114.7, 107.1; **MP** 56-58 ˚C.



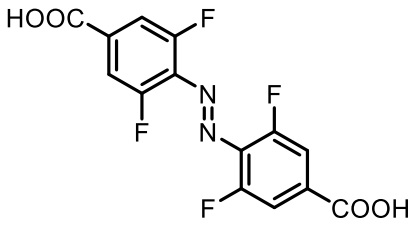
4-Cyano-2,6-difluoroaniline (17) was synthesised according to a known procedure.[15] Copper cyanide (6.33 g, 70.7 mmol) was added to compound **16** (5.0 g, 24.0 mmol) in DMF (50 mL) and stirred at reflux for 4 hours. The reaction mixture was then poured into distilled water, filtered and the precipitate further washed with ethyl acetate. The filtrate was extracted with ethyl acetate (3 × 100 mL), then the combined organic extracts were dried over $MgSO_4$, filtered and evaporated under reduced pressure. The crude residue was purified by flash column chromatography (1:1 CH_2Cl_2 : petrol ether) to give compound **17** as a white solid (1.97 g, 53%) with spectra matching the literature. **^{1}H NMR** (400 MHz, $CDCl_3$): δ 7.14 (dd, *J* = 6.0, 2.3 Hz, 2H, *Ar-H*), 4.27 (sb, 2H, *N-H*); **^{13}C NMR** (101 MHz, $CDCl_3$): δ 150.7 (dd, $^1J_{CF}$ = 244 Hz, $^3J_{CF}$ = 9 Hz), 129.8 (t, $^2J_{CF}$ = 31 Hz), 118.1 (t, $^4J_{CF}$ = 3 Hz), 115.9-115.2 (m), 98.4 (t, $^3J_{CF}$ = 11 Hz). **MP** 103-105 ˚C.



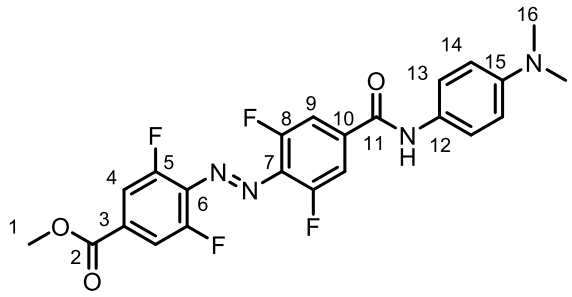
Ethyl 4-amino-3,5-difluorobenzoate (18) was synthesised according to a known procedure.[15] **17** (1.8 g, 11.7 mmol) was stirred at reflux in 1 M NaOH (20 mL) for 4 hours. 1M HCl was then added, and the resulting precipitate extracted into ethyl acetate, dried with $MgSO_4$, and evaporated under reduced pressure. The crude residue was dissolved in ethanol (10 mL), conc. H_2SO_4 (250 µL) was added and the reaction was heated at reflux for 5 hours. The reaction mixture was then cooled, neutralised to pH 7 with sat. $NaHCO_3$ solution, and extracted with CH_2Cl_2 (3 × 100 mL). The combined organic extracts were dried over Na_2SO_4 and evaporated under reduced pressure to give **18** as a white solid (1.75 g, 71% over two steps) with spectra matching the literature. **^{1}H NMR** (400 MHz, $CDCl_3$): δ 7.50 (d, *J* = 7.1 Hz, 2H, *Ar-H*), 4.31 (q, *J* = 7.2, 2H Hz, *CH_2*), 4.19 (sb, 2H, *N-H*), 1.34 (t, *J* = 7.2 Hz, 3H, *CH_3*); **^{13}C NMR** (101 MHz, $CDCl_3$): δ 165.2 (t, $^4J_{CF}$ = 3 Hz), 150.7 (dd, $^1J_{CF}$ = 241 Hz, $^3J_{CF}$ = 8 Hz), 128.9 (t, $^2J_{CF}$ = 16 Hz), 118.4 (t, $^3J_{CF}$ = 8 Hz), 114.4-110.7 (m), 61.0, 14.3. **MP** 61-63 ˚C.



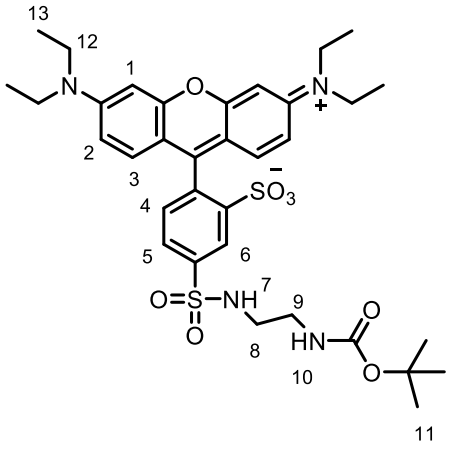
Tetra-*ortho*-fluoro-azobenzene diester (A1) was synthesised according to a known procedure.[16] DBU (2.6 mL, 17.4 mmol) was added to a solution of **18** (1.75 g, 8.7 mmol) in CH_2Cl_2 (100 mL) and stirred for 5 minutes at room temperature. The reaction mixture was then cooled to -78 ˚C, and NCS (2.33 g, 17.4 mmol) was added. The reaction was stirred for 10 minutes, then quenched with the addition of sat. $NaHCO_3$ solution and warmed to room temperature. The organic layer was separated, washed with water (50 mL), 1 M HCl (50 mL), then dried over Na_2SO_4 and evaporated under reduced pressure. The crude residue was purified with flash silica chromatography (1:1 CH_2Cl_2 : petrol ether) to give **A1** as a red solid (1.04 g, 66%), with spectra matching the literature. **^{1}H NMR** (400 MHz, $CDCl_3$): δ 7.77 (d, *J* = 9.6 Hz, 4H, *Ar-H*), 4.42 (q, *J* = 7.1 Hz, 4H, *CH_2*), 1.42 (t, *J* = 7.1 Hz, 6H, *CH_3*); **^{13}C NMR** (101 MHz, $CDCl_3$): δ 163.7 (*C_1*), 155.0 (dd, $^1J_{CF}$ = 263 Hz, $^3J_{CF}$ = 4 Hz, *C_4*), 134.2 (t, $^2J_{CF}$ = 10 Hz, *C_5*), 133.7 (t, $^3J_{CF}$ = 9 Hz, *C_2*), 113.9 (dd, $^2J_{CF}$ = 23 Hz, $^4J_{CF}$ = 3 Hz, *C_3*), 62.2 (*CH_2*), 14.2 (*CH_3*). **ESI-MS** $[M+H]^+$ 399.0.



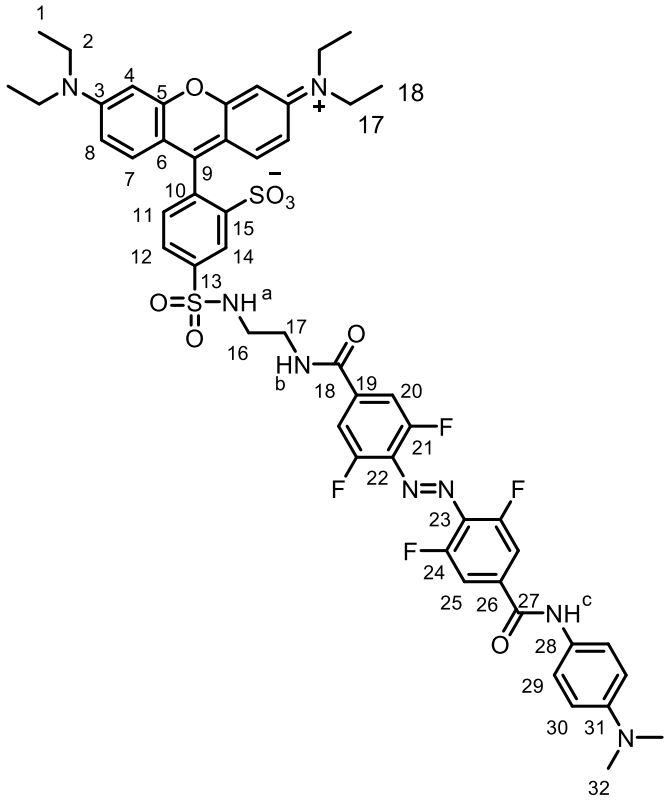
Tetra-*ortho*-fluoro-azobenzene diacid (19). Compound **A1** (510 mg, 1.31 mmol) was stirred at room temperature for 2 h in a mixture of THF (40 mL) and 3 M aqueous NaOH (40 mL). The reaction was then acidified to pH 3 using 1 M HCl, and the resulting suspension was extracted with ethyl acetate (5 × 100 mL), dried over Na_2SO_4, and evaporated under reduced pressure to give **19** as a red solid (400 mg, 90%), with spectra matching the literature.[29] **^{1}H NMR** (400 MHz, DMSO-d_6): δ 7.81 (d, *J* = 9.3 Hz, 4H, *Ar-H*); **^{13}C NMR** (126 MHz, DMSO-d_6): δ 164.6, 154.4 (dd, $^1J_{CF}$ = 265 Hz, $^3J_{CF}$ = 4 Hz), 135.3 (t, $^2J_{CF}$ = 9 Hz), 133.0 (t, $^3J_{CF}$ = 11 Hz), 114.0 (dd, $^2J_{CF}$ = 20 Hz, $^4J_{CF}$ = 4 Hz). **ESI-MS** $[M-H]^-$ 341.0.



Tetra-*ortho*-fluoro-azobenzene diemethylamine anilide (20). Tetra-ortho-fluoro-azobenzene dicarboxylic acid **19** (221 mg, 646 µmol) was pre-stirred with HBTU (491 mg, 1.29 mmol) and DIPEA (225 µL, 1.29 mmol) in DMF (2 mL) for 20 minutes. 2-Amino-N,N-dimethylaniline (22.0 mg, 162 µmol) was then added, and the reaction stirred for 2 h at room temperature. Methanol (3.27 mL, 80.8 mmol) was then added and the reaction stirred for another 30 minutes. Ethyl acetate (100 mL) was added and the organic layer washed with brine (6 × 50 mL), then water (3 × 50 mL). The organic layer was dried over anhydrous sodium sulfate, the solvent was removed under reduced pressure, and the crude residue purified with flash silica column chromatography (0-5% MeOH in DCM) to give compound **20** as a brown solid (76 mg, 79%). **^{1}H NMR** (400 MHz, $CDCl_3$): δ 7.77-7.70 (m, 3H, *H4, NH*), 7.58 (d, *J* = 8.9 Hz, 2H, *H9*), 7.47 (d, *J* = 8.6 Hz, 2H, *H13*), 6.73 (d, *J* = 9.0 Hz, 2H, *H14*), 3.98 (s, 3H, *H1)*, 2.96 (s, 6H, *H16*). **^{13}C NMR** (151 MHz, $CDCl_3$) δ 164.4 (C2), 162.1 (C11), 155.6 (dd, $^{1}J_{CF}$ = 264 Hz, $^{3}J_{CF}$ = 3 Hz, C9), 155.1 (dd, $^{1}J_{CF}$ = 262 Hz, $^{3}J_{CF}$ = 4 Hz, C4), 148.7 (C15), 139.0 (t, $^{3}J_{CF}$ = 9 Hz, C10), 134.5 (t, $^{2}J_{CF}$ = 10 Hz, C7), 133.3 (t, $^{3}J_{CF}$ = 9 Hz, C3), 133.2 (t, $^{2}J_{CF}$ = 10 Hz, C6), 126.7 (C12), 122.4 (C13), 114.1 (dd, $^{2}J_{CF}$ = 21 Hz, $^{4}J_{CF}$ = 3 Hz, C4) 113.0 (C14), 111.8 (d, $^{2}J_{CF}$ = 21 Hz, C9) 53.1 (C1), 40.9 (C16); **HR ESI-MS** $[C_{23}H_{18}F_4N_4O_3 + H]^+$ calculated 475.1388, observed 475.1389, Δ = 0.21 ppm. **MP** 208 – 212 ˚C; **IR** ν (cm^{-1}) 3654,3392,2981,2889, 1707, 1649, 1577, 1530, 1519, 1434, 1339, 1253, 1052, 947, 827, 766.

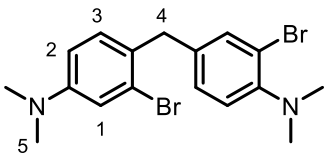


Sulforhodamine B boc-ethylenediamine (23). Compound **23** was synthesised according to a literature procedure.[30] DIPEA (0.3 mL, 1.7 mmol) was added to a mixture of Sulforhodamine B sulfonylchloride **22** (0.2 g, 0.34 mmol) and mono-Boc-ethylenediamine (76 µL, 0.48 mmol) in CH_2Cl_2 (5 mL). The reaction was stirred at room temperature for 16 h, then evaporated to dryness and purified by flash silica column chromatography (5% MeOH in CH_2Cl_2) to give **23** as a pink solid (116 mg, 59%) with spectra matching the literature. **^{1}H NMR** (400 MHz, MeOD): δ 8.64 (d, *J* = 1.9, 1H Hz, H_6), 8.10 (dd, *J* = 8.0, 1.9 Hz, 1H, H_5), 7.51 (d, *J* = 8.0 Hz, 1H, H_4), 7.13 (d, *J* = 9.5 Hz, 2H, H_3), 7.00 (dd, *J* = 9.5, 2.5 Hz, 2H, H_2), 6.93 (d, *J* = 2.5 Hz, 2H, H_1), 3.67 (q, *J* = 7.2 Hz, 8H, H_{12}), 3.23-3.13 (m, 2H, $H_{8/9}$), 3.12-3.03 (m, 2H, $H_{9/8}$), 1.44 (s, 9H, H_{11}), 1.30 (t, *J* = 7.1 Hz, 12H, H_{13}); **^{13}C NMR** (126 MHz, MeOD/$CDCl_3$): δ 158.7, 157.7, 157.5, 156.4, 146.9, 143.1, 134.7, 133.3, 131.4, 128.5, 127.3, 114.7, 114.4, 96.5, 80.0, 48.5, 43.4, 41.0, 28.7, 12.8 **ESI-MS** [M+Na$^+$] 723.2.



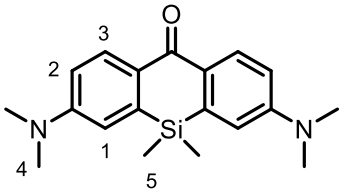
Dyad B. Compound **23** (59 mg, 84 µmol) was stirred at room temperature in a 9:1 DCM:TFA solution for 1.5 h, and then the solvent evaporated. At the same time, compound **20** (510 mg, 1.31 mmol) was stirred at room temperature for 2 h in a mixture of THF (40 mL) and 3 M aqueous NaOH (40 mL). The reaction was then acidified to pH 3 using 1 M HCl, and the resulting suspension was extracted with ethyl acetate (5 × 100 mL), dried over Na_2SO_4, and evaporated under reduced

pressure to give **21** as an orange solid. The crude residue of **23** was added to a pre-stirred solution of HBTU (32 mg, 84 µmol), DIPEA (26 µL, 0.15 mmol) and the crude residue of **21** (35 mg, 76 µmol) in DMF. The reaction was stirred at room temperature for 2 h, then ethyl acetate (100 mL) was added and the organic layer washed with brine (5 × 50 mL), then water (2 × 50 mL). The organic layer was dried over sodium sulfate and solvent removed under reduced pressure to give a crude residue, which was purified with flash silica column chromatography (5-10% MeOH in DCM) to give **Dyad B** as a pink solid (23 mg, 29%). The minor *Z* isomer was neglected in the NMR assignment. **^{1}H NMR** (500 MHz, DMSO) δ 10.26 (s, NHc), 8.94 (t, *J* = 5.6 Hz, NHa/b), 8.45 (d, *J* = 1.9 Hz, H14), 8.19 (t, *J* = 6.1 Hz, NHa/b), 8.03 – 7.87 (m, H12, H20/H25), 7.87 – 7.78 (m, H20/H25), 7.59 (d, *J* = 9.1 Hz, H29), 7.48 (d, *J* = 8.2 Hz, H11), 7.04 (d, *J* = 9.7 Hz, H7), 6.99 (dd, *J* = 9.4, 3.4 Hz, H8), 6.93 (s, H4), 6.75 (d, *J* = 9.2 Hz, H30), 3.70 – 3.54 (m, H2), 3.49 – 3.39 (m, H16), 3.15 – 3.04 (m, H17), 2.89 (s, H32), 1.32 – 1.15 (m, H1); **^{13}C NMR** (126 MHz, DMSO) δ 156.0 (d, $^{1}J_{CF}$ = 263 Hz, C21), 154.3 (d, $^{1}J_{CF}$ = 260 Hz, C24), 148.1 (C31), 132.7 (C8), 130.6 (C11), 126.4 (C12), 125.6 (C14), 121.9 (C29), 113.6 (C3), 113.4 (C7), 112.4 (d, $^{2}J_{CF}$ = 22 Hz, C20), C24 112.3 (C30), 112.4 (d, $^{2}J_{CF}$ = 21 Hz, C25), 95.3 (C4), 45.2 (C2), 41.3 (C17), 40.3 (C32), 39.3 (C16), 12.4 (C1). Other quaternary carbons and carbonyls not observed. **HR ESI-MS** $[C_{51}H_{50}F_4N_8O_8S + H]^+$ calculated 1043.3203, observed 1043.3199, Δ = 0.38 ppm; **MP** > 300 ˚C; **IR** ν (cm^{-1}) 2927, 2362, 2343, 1651, 1592, 1421, 1341, 1264, 1185, 1077, 815.

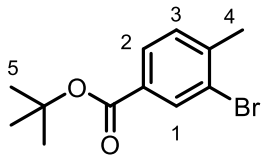


4,4'-Methylenebis(3-bromo-N,N-dimethylaniline) (25) was made according to a published procedure.[31] 3-Bromo-N,N-dimethylaniline (3.0 g, 15 mmol) was dissolved in formaldehyde solution 37% (2.28 mL, 30.6 mmol) in Acetic Acid (21 mL) and stirred at 60 °C for 2 h. After cooling, the acetic acid was evaporated and then saturated aqueous $NaHCO_3$ was added carefully. The aqueous phase was extracted with ethyl acetate, and the combined organic phase was washed with water and brine, dried over anhydrous sodium sulfate, filtered, and evaporated to give **25** as a white solid (2.4 g,

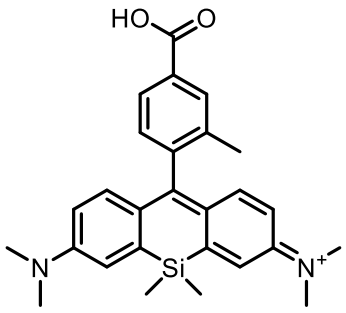
78%). **^{1}H NMR** (400 MHz, $CDCl_3$) δ 6.95 (s, 2H, H_1), 6.86 (d, *J* = 8.5 Hz, 2H, H_3), 6.59 (dd, *J* = 8.6, 2.7 Hz, 2H, H_2), 4.01 (s, 2H, H_4), 2.92 (s, 12H, H_5). **^{13}C NMR** (101 MHz, $CDCl_3$) δ 150.19, 130.91, 127.26, 125.75, 116.42, 112.01, 40.66, 40.01. **ESI-MS** $[M+H]^+$ 413.0.



3,7-Bis(dimethylamino)-5,5-dimethyldibenzo[b,e]silin-10(5H)-one (27) was synthesised according to a published procedure.[31] **25** (3.0 g, 7.28 mmol) was dissolved in dry tetrahydrofuran (THF) (75 mL) and stirred at −78 °C. n-BuLi (1.6 M solution in n-hexane, 10.9 mL, 17.5 mmol) was slowly added over 30 min to the solution and stirred for a further 2 h at the same temperature. $SiMe_2Cl_2$ (1.76 mL, 14.6 mmol) was added to the reaction mixture and it was warmed to room temperature and stirred for 2 h. Then, water was added carefully to the reaction to neutralise the solution, followed by sat. $NaHCO_3$. The THF was evaporated and the resulting aqueous solution was extracted with AcOEt, and the organic phase was washed with saturated aqueous NaHCO3, water, and brine, dried over Na_2SO_4, filtered, and evaporated to obtain the crude including compound **26**, which was used for the next reaction immediately due to its high sensitivity toward oxygen. The residue was dissolved in acetone (40 mL) and stirred at −15 °C. $KMnO_4$ powder was added portion wise (6 × 380 mg) over 30 min, and the reaction stirred for a further 15 mins. The acetone was removed, and dichloromethane was added, then the suspension was filtered through a Celite pad, and the yellow filtrate was evaporated to give compound **27** as a yellow- green solid (1.2 g, 51% over 2 steps). **^{1}H NMR** (400 MHz, $CDCl_3$) δ 8.39 (d, *J* = 9.0 Hz, 2H, H_3), 6.84 (dd, *J* = 9.0, 2.8 Hz, 2H, H_2), 6.79 (d, *J* = 2.8 Hz, 2H, H_1), 3.09 (s, 12H, H_4), 0.46 (s, 6H, H_5). **^{13}C NMR** (101 MHz, $CDCl_3$) δ 185.34, 151.56, 140.57, 131.69, 129.78, 114.35, 113.24, 40.11, -0.89. **ESI-MS** $[M+H]^+$ 325.2.

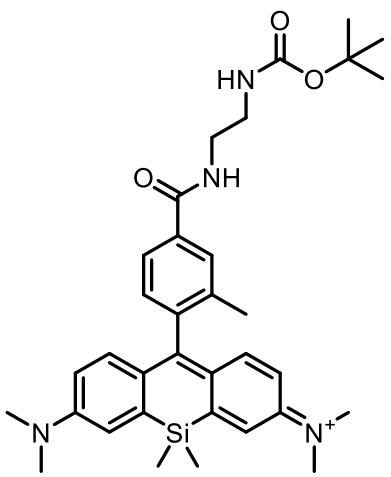


T**ert-butyl 4-bromo-3-methylbenzoate (29)** was synthesised according to a published procedure.[31] 4-Bromo-3-methylbenzoic acid **28** (1.0 g, 4.7 mmol) and oxalyl chloride (611 µL, 6.98 mmol) were dissolved in dry dichloromethane (DCM) (10 mL); then, a catalytic amount of dry DMF (4-5 drops) was slowly added dropwise via a syringe under Ar. The mixture was stirred for 4 h, and DCM was evaporated to obtain the crude, which was used for the next reaction immediately due to its high sensitivity toward moisture. After removal of the solvent, the residue was dissolved in dry THF (30 mL) and cooled to 0 °C under Ar. Potassium t-butoxide (1.04 g, 9.30 mmol) in dry THF (30 mL) was added slowly to the reaction mixture. Upon complete potassium t-butoxide addition, the ice bath was removed, and the solution was stirred at room temperature for 3h. After removal of the solvent, the residue was dissolved in AcOEt. The organic phase was washed with water and brine, dried over anhydrous sodium sulfate, filtered, and evaporated. The residue was purified by silica gel column chromatography to obtain **29** as a clear oil (540 mg, 43%). **^{1}H NMR** (400 MHz, $CDCl_3$) δ 7.81 (d, *J* = 1.3 Hz, 1H, H_1), 7.61 (dd, *J* = 8.3, 2.2 Hz, 1H, H_2), 7.51 (d, *J* = 8.3 Hz, 1H, H_3), 2.39 (s, 3H, H_4), 1.57 (s, 9H, H_5). **^{13}C NMR** (101 MHz, $CDCl_3$) δ 165.16, 137.91, 132.28, 131.56, 131.14, 129.81, 128.20, 81.22, 28.19, 22.87.



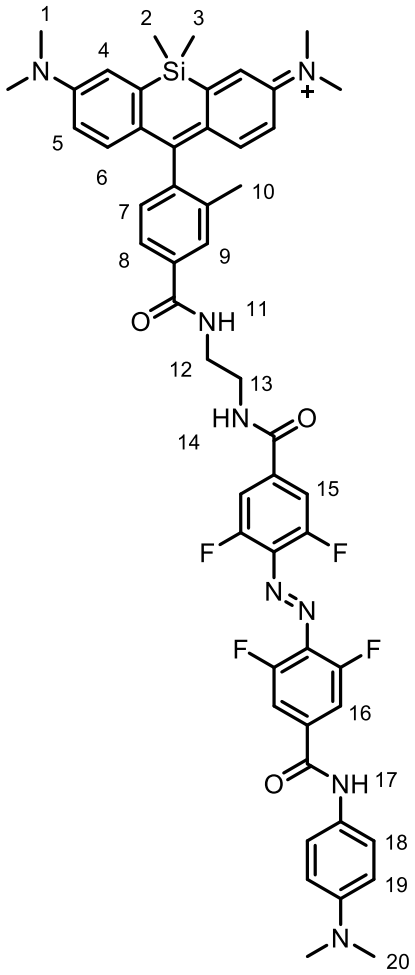
Silicon rhodamine carboxylic acid (30) was synthesised according to a published procedure.[31] Compound **29** (0.50 g, 1.84 mmol) was dissolved in dry THF (15 mL) and cooled to -78 °C. *t*-BuLi (1.14 mL, 1.94 mmol) was slowly added dropwise and the solution was stirred for 1 h under Ar. Compound **27** (598 mg, 1.84 mmol) in dry THF (10 mL) was added dropwise at -78 °C. The solution was warmed to room temp and stirred for 3 h. Then, 0.1 M HCl aq. was added to the reaction mixture, and the resulting intense blue solution was basified with saturated AQUEOUS $NaHCO_3$ and extracted with DCM. The combined organic phase

was washed with brine, dried over Na_2SO_4, filtered, and evaporated to obtain the crude, which was used for the next reaction without further purification. The residue was dissolved in 3 M HCl aq. (50 mL) and acetonitrile (50 mL) and stirred at 40 °C for 3 h, then at room temperature overnight. 2 M aqueous NaOH was added to adjust the pH to 2–3, and the solution was extracted with DCM; the combined organic phase was washed with brine, dried over Na_2SO_4, filtered, and evaporated. The residue was purified by silica gel column chromatography (0:5:95 AcOH:MeOH:CH_2Cl_2 to 2:5:93 AcOH:MeOH: CH_2Cl_2) to obtain **30** as a blue solid (220 mg, 27% over two steps). **^{1}H NMR** (400 MHz, MeOD) δ 8.00 (s, 1H), 7.96 (d, *J* = 7.9 Hz, 1H), 7.36 (d, *J* = 2.8 Hz, 2H), 7.14 (d, *J* = 7.6 Hz, 1H), 7.08 (d, *J* = 9.6 Hz, 2H), 6.77 (dd, *J* = 9.6, 2.8 Hz, 2H), 3.34 (s, 12H), 2.06 (s, 3H), 0.62 (s, 3H), 0.60 (s, 3H); **^{13}C NMR** (126 MHz, MeOD) δ 169.6, 155.8, 149.5, 141.9, 137.6, 132.9, 132.0, 130.5, 128.0, 127.7, 122.3, 115.4, 40.9, 19.4, -1.1, -1.3; **ESI-MS** $[M]^+$ 443.1.

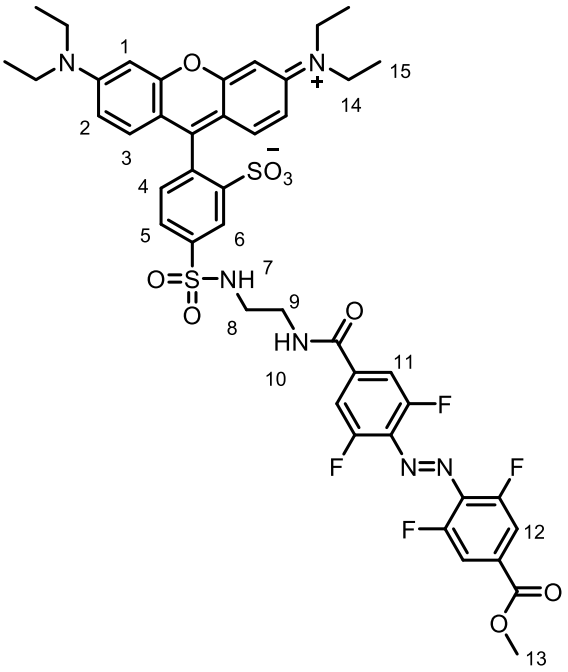


Silicon rhodamine boc-ethylenediamine (31). Tert-butyl (2-aminoethyl)carbamate (32 µL, 200 µmol) was added to a pre-stirred solution of **30** (80.0 mg, 181 µmol), DIPEA (63 µL, 360 µmol) and HBTU (103 mg, 271 µmol) in DMF (5 mL) under nitrogen. The reaction mixture was stirred for 16 h at room temperature, then ethyl acetate (100 mL) was added and the organic layer washed with brine (6 ×50 mL), then water (3 × 50 mL), and dried over Na_2SO_4, filtered, and evaporated to obtain the crude. The crude residue was purified with flash silica column chromatography (5-10% MeOH in CH_2Cl_2), and then further purified by dissolving in a minimum volume of methanol and precipitation from diethyl ether to give **31** as a blue solid (14 mg, 13%). **^{1}H NMR** (400 MHz, $CDCl_3$) δ 7.86 (s, 1H), 7.81 (d, *J* = 7.9 Hz, 1H), 7.55 (sb, 1H), 7.19-7.12 (m, 3H), 7.04 (d, *J* = 9.5 Hz, 2H), 6.59 (dd, *J* = 9.6, 2.7 Hz, 2H), 3.66-3.58 (m, 2H), 3.52-3.42 (m, 2H), 3.35 (s, 12H), 2.07 (s, 3H), 1.45 (s, 9H), 0.61 (s, 3H), 0.59 (s, 3H). **^{13}C NMR** (101 MHz,

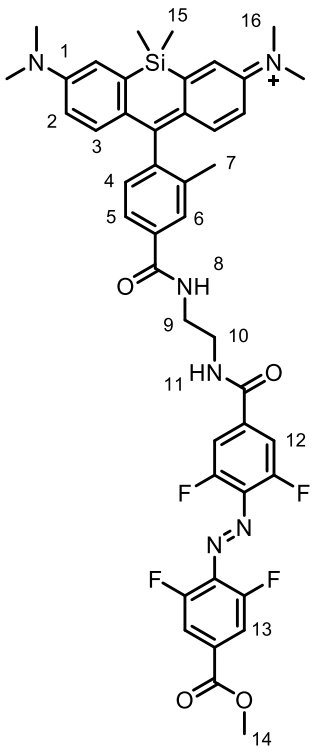
$CDCl_3$) δ 167.8, 157.6, 154.2, 148.5, 141.6, 141.5, 136.4, 135.1, 129.2, 129.1, 127.1, 124.5, 120.9, 114.1, 79.9, 42.0, 40.9, 40.3, 28.5, 19.4, -1.0, -1.2; **ESI-MS** $[M]^+$ 585.1.



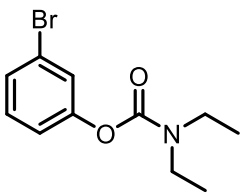
Dyad C. Compound **20** (13.0 mg, 27.4 μmol) was stirred in 50/50 THF/3 M aqueous NaOH (3 mL) for 2 h. The reaction mixture was neutralised to pH 7 with aqueous HCl, and extracted with ethyl acetate. The combined organic fractions were dried over Na_2SO_4 and the solvent removed under reduced pressure to give the crude acid **21**. Meanwhile, compound **31** (14.6 mg, 24.9 μmol) was stirred in a 9:1 DCM:TFA solution (5 mL) at room temperature for 2 h. The solvent was removed under reduced pressure and the crude residue was added to a pre-stirred solution of the acid **21**, HBTU (14.2 mg, 37.4 μmol) and DIPEA (8.68 μL, 49.8 μmol) in DMF. The reaction was stirred for 16 h, then ethyl acetate (100 mL) was added and the organic layer washed with brine (6 ×50 mL), then water (3 × 50 mL), and dried over Na_2SO_4. The solvent was removed under reduced pressure and the crude residue purified with flash silica column chromatography (5-10% MeOH in DCM) to give **Dyad C** as a blue solid (14 mg, 61%). **^{1}H NMR** (400 MHz, MeOD) δ 8.76 (sb, NH), 7.88 (s, H9), 7.84 (d, *J* = 7.8 Hz, H8), 7.78 (d, *J* = 9.7 Hz, H15/16), 7.68 (d, *J* = 9.3 Hz, H16/15), 7.59 (d, *J* = 8.7 Hz, H18), 7.36 (d, *J* = 2.9 Hz, H4), 7.25 (d, *J* = 7.9 Hz, H7), 7.03 (d, *J* = 9.7 Hz, H6), 6.95-6.88 (m, H19), 6.76 (dd, *J* = 9.7, 2.5 Hz, H5), 3.34 (s, H1), 2.99 (s, H20), 2.09 (s, H10), 0.62 (s, H2/H3), 0.60 (s, H3/H2); **HR ESI-MS** $[C_{51}H_{51}O_3N_8F_4Si]^+$ theoretical 927.3784, observed 927.3774, Δ = 1.01 ppm; **MP** decomposition at 220 °C; **IR** ν (cm^{-1}) 2363, 2343, 1578, 1359, 1320, 1163, 847.



Control 32. A solution of **23** (20 mg, 29 µmol) was stirred at rt in a mixture of TFA: CH_2Cl_2 (1 mL, 1:9) for 2 h. The solvent was completely evaporated, and the deprotected dye added to a solution of **19** (49 mg, 142 µmol), HBTU (108 mg, 285 µmol) and DIPEA (60 µL, 0.34 mmol) in DMF (3 mL). The reaction was stirred for 4 h then methanol (3 mL) added, and the reaction stirred again for 2 h. Ethyl acetate (300 mL) was added, and the organic layer washed with brine (6 ×50 mL) and distilled water (3 × 50 mL). The solvent was removed under reduced pressure and the crude residue purified with flash silica chromatography (5-10% MeOH in CH_2Cl_2, to give **32** as a red solid (18 mg, 65%).**^{1}H NMR** (500 MHz, MeOD/$CDCl_3$): δ 8.67 (d, *J* = 1.9 Hz, 1H, H_6), 8.06 (dd, *J* = 8.0, 1.9 Hz, 1H, H_5), 7.73 (d, *J* = 8.8 Hz, 2H, $H_{11/12}$), 7.65 (d, *J* = 9.3 Hz, 2H, $H_{12/11}$), 7.35 (d, *J* = 7.9 Hz, 1H, H_4), 7.13 (d, *J* = 9.5 Hz, 2H, H_3), 6.87 (dd, *J* = 9.6, 2.5 Hz, 2H, H_2), 6.78 (d, *J* = 2.4 Hz, 2H, H_1), 3.96 (s, 3H, H_{13}), 3.64-3.55 (m, 8H, H_{14}), 3.53 (t, *J* = 6.1, 2H, $H_{8/9}$), 3.25 (t, *J* = 6.1 Hz, 2H, $H_{9/8}$), 1.29 (t, *J* = 7.2 Hz, 12H, H_{15}). **^{13}C NMR** (126 MHz, MeOD/$CDCl_3$): δ 165.9, 165.0, 158.6, 157.4, 156.3, 155.8 (dd, $^1J_{CF}$ = 263 Hz, $^3J_{CF}$ = 4 Hz), 155.6 (dd, $^1J_{CF}$ = 263 Hz, $^3J_{CF}$ = 4 Hz), 146.9, 143.0, 138.8 (t, $^3J_{CF}$ = 9 Hz), 134.9 (t, $^3J_{CF}$ = 9 Hz), 134.7, 133.9 (t, $^3J_{CF}$ = 9 Hz), 133.6 (t, $^3J_{CF}$ = 9 Hz), 133.2, 131.5, 128.5, 127.3, 114.7, 114.5 (dd, $^2J_{CF}$ = 21 Hz, $^4J_{CF}$ = 4 Hz), 114.4, 112.6 (dd, $^2J_{CF}$ = 21 Hz, $^4J_{CF}$ = 4 Hz), 96.4, 53.4, 46.4, 42.6, 40.9, 12.8; **HR ESI-MS** $[C_{44}H_{42}O_9N_6F_4S_2 + H]^+$ theoretical 939.2464, observed 939.2451, Δ = 1.38 ppm; **MP** decomposition at 200 ˚C; **IR** ν (cm^{-1}) 2981, 2929, 2360, 2341, 1729, 1649, 1591, 1435, 1338, 1246, 1181.

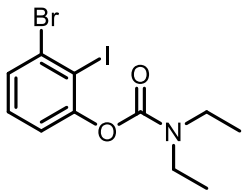


Control 33. A solution of **31** (50 mg, 0.085 mmol), was stirred at rt in a mixture of TFA: CH_2Cl_2 (1 mL, 1:9) for 2 h. The solvent was completely evaporated, and the deprotected dye added to a solution of **19** (146 mg, 0.43 mmol) HBTU (323 mg, 0.85 mmol) and DIPEA (178 µL, 1.02 mmol) in DMF (5 mL). The reaction was stirred for 4 h then methanol (3 mL) added, and the reaction stirred again for 2 h. Ethyl acetate (300 mL) was added, and the organic layer washed with brine (6 × 50 mL) and distilled water (3 × 50 mL). The solvent was removed under reduced pressure and the crude residue purified with flash silica chromatography (5-10% MeOH in CH_2Cl_2, to give **33** as a blue solid (50 mg, 68%). **^{1}H NMR** (500 MHz, $CDCl_3$): δ 7.96 (dd, *J* = 7.5, 2.3 Hz, 1H, H_5), 7.73 (d, *J* = 10.0 Hz, 2H, $H_{13/12}$), 7.60 (s, 1H, H_6), 7.55 (d, *J* = 10.0 Hz, 2H, $H_{12/13}$) 7.43 (d, *J* = 8.1 Hz, 1H, H_4), 7.11 (d, *J* = 2.8 Hz, 2H, H_1), 7.06 (d, *J* = 9.6 Hz, 1H, H_3), 6.61 (dd, *J* = 9.6, 2.8 Hz, 2H, H_2), 3.99 (s, 3H, H_{14}), 3.77-3.71 (m, 2H, $H_{9/10}$), 3.71-3.66 (m, 2H, $H_{9/10}$), 3.32 (s, 12H, H_{16}), 2.07 (s, 3H, H_7), 0.59 (s, 3H, $H_{15'}$), 0.56 (s, 3H, $H_{15''}$); **^{13}C NMR** (126 MHz, MeOD/$CDCl_3$): δ 169.3, 168.7, 164.7, 164.4, 155.4 (dd, $^1J_{CF}$ = 262 Hz, $^3J_{CF}$ = 4 Hz), 155.0 (dd, $^1J_{CF}$ = 262 Hz, $^3J_{CF}$ = 4 Hz), 154.3, 148.5, 141.8, 139.4, 138.6, 138.4 (t, $^3J_{CF}$ = 9 Hz), 134.4 (t, $^3J_{CF}$ = 9 Hz), 133.1 (t, $^3J_{CF}$ = 9 Hz), 132.8 (t, $^3J_{CF}$ = 9 Hz), 132.1, 130.7, 128.2, 127.8, 127.7, 120.6, 114.4, 114.0 (dd, $^2J_{CF}$ = 22 Hz, $^4J_{CF}$ = 3 Hz), 111.9 (dd, $^2J_{CF}$ = 22 Hz, $^4J_{CF}$ = 3 Hz), 53.2, 41.7, 40.8, 40.0, 19.5, 1.2, -0.7, -1.4. **HR ESI-MS** $[C_{44}H_{43}O_4N_6F_4Si]^+$ theoretical 823.3046, observed 823.3036, Δ = 1.21 ppm; **MP** decomposition at 147 ˚C; **IR** ν (cm^{-1}) 2928, 2360, 1728, 1574, 1354, 1315, 1244, 1157.

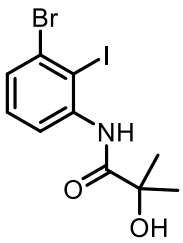


3-Bromophenyl diethylcarbamate (35) was synthesised according to literature procedure.[32] A solution of 3-bromophenol (10.0 g, 57.8 mmol) in THF (20 mL) was added to a suspension of sodium hydride (60% dispersion,

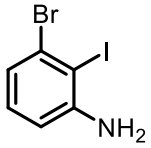
4.6 g, 116 mmol) in THF (80 mL) dropwise at room temperature. After stirring for 2 h, a solution of *N,N*-diethylcarbamoyl chloride (8.06 mL, 63.6 mmol) in THF (10 mL) was added. The reaction was stirred overnight, then quenched by a slow addition of water. The THF was removed under reduced pressure, and the crude reaction mixture separated between water and EtOAc. The organic layer was washed with brine, and dried with sodium sulfate, then the EtOAc removed under reduced pressure to give compound **35** as a pale orange oil (15.6 g, 99%) with spectra matching the literature. **^{1}H NMR:** (400 MHz, $CDCl_3$) δ 7.37 – 7.25 (m, 2H), 7.18 (t, J = 8.0 Hz, 1H), 7.06 (m, 1H), 3.37 (m, 6H), 1.19 (m, 9H). **^{13}C NMR** (101 MHz, $CDCl_3$) δ 153.6, 152.1, 130.2, 128.2, 125.3, 122.1, 120.7, 42.4, 42.0, 14.3, 13.4; **ESI-MS** $[M + Na]^+$ 294.0



3-Bromo-2-iodophenyl diethylcarbamate (36) was synthesised according to literature procedure, with concentration adjustments.[33] n-BuLi (39.4 mL, 1.6 M, 63.1 mmol) was added to a solution of i-Pr_2NH (9.71 mL, 68.8 mmol) in THF (320 mL) at 0 ^{o}C. After 30 min, the LDA solution was cooled to –78 ^{o}C and a solution of **35** (15.6 g, 57.3 mmol) in THF (20 mL) was added.The resulting solution was stirred for 30 min at –78 ºC and then a solution of iodine (14.5 g, 57.3 mmol) was added. After 30 min at low temperature the reaction mixture was allowed to warm to room temperature, H_2O was added and THF evaporated under reduced pressure. The aqueous phase was extracted with EtOAc (3 × 25 mL) and the combined organic layers were washed with 1 M HCl, dried over anhydrous Na_2SO_4, and evaporated under reduced pressure. The crude was purified by recrystallisation from 10% EtOAc in petrol to give **36** as white crystals (16.4 g, 72% yield). **^{1}H NMR** (400 MHz, $CDCl_3$) δ 7.48 (dd, *J* = 8.0, 1.4 Hz, 1H), 7.22 (t, *J* = 8.0 Hz, 1H), 7.09 (dd, *J* = 8.1, 1.4 Hz, 1H), 3.53 (q, *J* = 7.1 Hz, 2H), 3.40 (q, *J* = 7.1 Hz, 2H), 1.32 (t, *J* = 7.1 Hz, 3H), 1.23 (t, *J* = 7.1 Hz, 3H). **^{13}C NMR** (101 MHz, $CDCl_3$) δ 153.5, 152.9, 130.7, 130.0, 129.6, 121.8, 99.9, 42.5, 42.2, 14.5, 13.4; **ESI-MS** $[M + H]^+$ 397.8

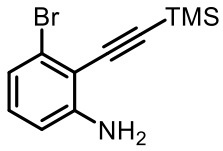


N-(3-bromo-2-iodophenyl)-2-hydroxy-2-methylpropanamide (39) was synthesised according to literature procedure.[33] To a solution of **36** (1 g, 2.51 mmol) in EtOH (25 mL) NaOH (1.00 g, 25.1 mmol) was added, and the mixture was heated at reflux for 2 h, until complete by TLC. After the mixture was cooled to room temperature, most of the EtOH was removed under reduced pressure and the residue was diluted with Et_2O and water. The organic phase was rejected and then the aqueous solution was carefully neutralized with a 1 M HCl solution. The aqueous phase was extracted with Et_2O (3 × 30 mL), and the combined organic layers were washed with brine, dried over anhydrous Na_2SO_4, and evaporated under reduced pressure. Without further purification, the crude phenol **37** was dissolved in anhydrous DMF (5 mL) under a nitrogen atmosphere and NaOH (300 mg, 7.54 mmol) was added to the mixture. After 1 h at room temperature, 2-bromo-2-methylpropanamide (1.25 g, 7.54 mmol) was added and the reaction was stirred for 2 h at room temperature. NaOH (904 mg, 22.6 mmol) was then added and the mixture was heated at 60 ^oC for 2 h. The reaction was quenched with H_2O and filtered to give compound **39** was recovered as a white solid (700 mg, 73%). **^{1}H NMR** (400 MHz, $CDCl_3$) δ 9.30 (s, 1H), 8.25 (dd, *J* = 8.3, 1.4 Hz, 1H), 7.42 (dd, *J* = 8.0, 1.5 Hz, 1H), 7.26-7.21 (m, 1H), 2.26 (m, 1H), 1.59 (s, 6H). **^{13}C NMR** (101 MHz, $CDCl_3$) δ 174.9, 130.4, 130.1, 128.5, 119.4, 98.2, 74.7, 28.1. **ESI-MS** $[M + H]^+$ 383.8.

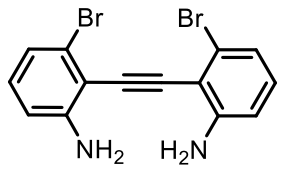


3-Bromo-2-iodoaniline (40) was synthesised according to literature procedure.[33] A mixture of **39** (2.0 g, 5.21 mmol) and NaOH (5.0 M in H_2O, 10 mL, 50 mmol) in EtOH (56 mL) was heated at reflux for 7 h. The mixture was diluted with EtOAc and H_2O. The resulting mixture was extracted with EtOAc. The combined organic layer was washed with brine, dried over Na_2SO_4, filtered, and concentrated in vacuo. The residue was purified by column chromatography on silica gel with hexane/EtOAc (8:2) to give compound **40** as a white solid (650

mg, 42%). **^{1}H NMR** (400 MHz, $CDCl_3$) δ 7.07 – 6.92 (m, 2H), 6.64 (dd, *J* = 7.5, 1.9 Hz, 1H), 4.33 (s, 2H). **^{13}C NMR** (101 MHz, $CDCl_3$) δ 149.25, 130.63, 129.93, 122.20, 112.43, 91.19. **ESI-MS** $[M + H]^+$ 297.8

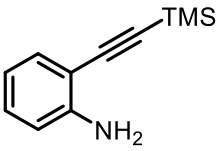


3-Bromo-2-((trimethylsilyl)ethynyl)aniline (41). A mixture of **40** (848 mg, 2.85 mmol), bis(triphenylphosphine)palladium(II) chloride (200 mg, 285 µmol), triethylamine (2.0 mL, 14.2 mmol), ethynyltrimethylsilane (591 µL, 4.27 mmol) and CuI (54.2 mg, 285 µmol) in THF (3.50 mL) was stirred under Ar at 50 °C for 16 h. The mixture was then diluted with water (20 mL) and extracted with ethyl acetate (2 × 15 mL). The combined organic extracts were washed with brine, dried over sodium sulfate, and concentrated. The crude residue was purified with flash silica column chromatography (20% EtOAc in petrol) to give **41** as a dark oil (431 mg, 57%). **^{1}H NMR** (400 MHz, $CDCl_3$) δ 6.97 – 6.85 (m, 2H), 6.61 (dd, *J* = 6.6, 2.5 Hz, 1H), 4.36 (sb, 2H), 0.29 (s, 9H). **^{13}C NMR** (101 MHz, $CDCl_3$) δ 149.8, 130.2, 125.9, 121.5, 112.7, 110.2, 104.9, 100.1, 0.2; **ESI-MS** $[M + H]^+$ 269.9 ; **MP** 35-38 ˚C; **IR** ν (cm^{-1}) 3487, 3385, 2960, 3256, 2341, 2150, 1610, 1559, 1461, 1449, 1251.

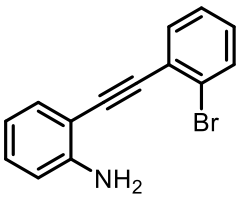


2,2'-(Ethyne-1,2-diyl)bis(3-bromoaniline) (42). Potassium carbonate (70 mg, 503 µmol) was added to a solution of compound **41** (135 mg, 503 µmol) in methanol (2 mL) and stirred for 1 h. The reaction mixture was diluted with CH_2Cl_2 and filtered. The filtrate was concentrated in vacuo and used directly in the next step. The crude residue was added to a mixture of compound **40** (228 mg, 765 µmol), bis(triphenylphospine)palladium)II) chloride (36 mg, 51 µmol), triethylamine (355 µL, 2.55 mmol), and CuI (10 mg, 51 µmol) under Ar, and the reaction mixture was heated to 50 °C for 16 h. The reaction mixture was then cooled, and diluted with water (20 mL), and extracted with EtOAc (2 × 15 mL). The combined organic extracts were washed with brine, dried over Na_2SO_4, and concentrated in vacuo. The crude residue was purified with flash silica chromatography (10% EtOAc

in petrol) to give compound **7** as an orange solid (20.0 mg, 11%). **^{1}H NMR** (500 MHz, $CDCl_3$) δ 7.03 (t, *J* = 8.1 Hz, 2H), 6.88 (dd, *J* = 7.8, 1.0 Hz, 2H), 6.78 (dd, *J* = 8.3, 1.0 Hz, 2H), 5.72 (s, 4H); **^{13}C NMR** (126 MHz, $CDCl_3$) δ 151.0, 131.0, 124.2, 119.5, 113.0, 107.7, 94.5. **ESI-MS** $[M + H]^+$ 366.9.

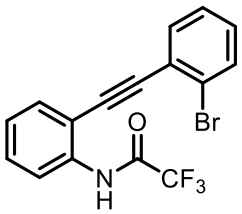


2-((Trimethylsilyl)ethynyl)aniline (5). 2-iodoaniline (500 mg, 2.28 mmol) was added to a mixture of trimethylsilylacteylene (226 mg, 3.42 mmol), bis(triphenylphosphine)palladium(II) chloride (160 mg, 228 µmol), copper(I) iodide (44 mg, 228 µmol) and triethyl amine (1.59 mL, 11.4 mmol) in THF (15 mL) under Ar, and stirred at room temperature for 3 h. The reaction mixture was then diluted with water (20 mL) and extracted with EtOAc (3 × 15 mL). The combine organic extracts were dried over Na_2SO_4, and concentrated in vacuo. The crude residue was purified with flash silica chromatography (10% EtOAc in petrol ether) to give **45** (354 mg, 82%) as an orange oil. **^{1}H NMR** (400 MHz, $CDCl_3$) δ 7.31 (dd, *J* = 7.6, 1.6 Hz, 1H), 7.12 (ddd, *J* = 8.1, 7.3, 1.6 Hz, 1H), 6.72 – 6.64 (m, 2H), 4.24 (sb, 2H), 0.28 (s, 9H); **^{13}C NMR** (101 MHz, $CDCl_3$) δ 148.4, 132.4, 130.0, 117.8, 114.3, 107.9, 101.9, 99.8, 0.3; **ESI-MS** $[M + H]^+$ 190.1.

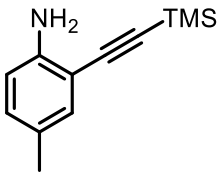


2-((2-Bromophenyl)ethynyl)aniline (46). Potassium carbonate (212 mg, 1.53 mmol) was added to a solution of **45** (290 mg, 1.53 mmol) in MeOH (3 mL) and stirred at room temperature for 30 mins. The reaction mixture was then diluted with CH_2Cl_2 (50 mL) and filtered. The filtrate was evaporated to give the crude residue, which was added directly to a mixture of 1-bromo-2-iodoabenzene (433 mg, 1.53 mmol), bis(triphenylphosphine)palladium(II) chloride (107 mg, 153 µmol), copper(I) iodide (29 mg, 153 µmol) and triethyl amine (1.1 mL, 7.7 mmol) in THF (10 mL) under Ar, and stirred at room temperature for 16 h. The reaction mixture was then diluted with water (20 mL) and extracted with EtOAc (3 × 15 mL). The combine organic extracts were dried over Na_2SO_4, and concentrated in

vacuo. The crude residue was purified with flash silica chromatography (10% EtOAc in petrol ether) to give **46** (255 mg, 61%) as a pale brown solid. **^{1}H NMR** (400 MHz, $CDCl_3$) δ 7.62 (dd, *J* = 8.1, 1.2 Hz, 1H), 7.57 (dd, *J* = 7.7, 1.7 Hz, 1H), 7.39 (dd, *J* = 7.6, 1.6 Hz, 1H), 7.31 (td, *J* = 7.6, 1.2 Hz, 1H), 7.23 – 7.11 (m, 2H), 6.82 – 6.67 (m, 2H), 4.49 (s, 2H). **^{13}C NMR** (101 MHz, $CDCl_3$) δ 148.6, 133.1, 132.5, 132.2, 130.3, 129.3, 127.3, 125.7, 125.2, 117.9, 114.5, 107.4, 93.5, 91.2; **ESI-MS** $[M + H]^+$ 271.9.

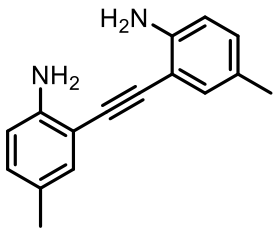


***N*-(2-((2-Bromophenyl)ethynyl)phenyl)-2,2,2-trifluoroacetamide (47).** Trifluoroacetic anhyrdride (27 µL, 193 µmol) was added dropwise to a solution of **46** (40.5 mg, 193 µmol) and triethyl amine (38 µL, 276 µmol) in THF (0.5 mL) at 0 °C. The reaction mixture was warmed to room temperature and stirred for 1 h, then partitioned between ethyl acetate (20 mL) and water (10 mL). The organic layer was dried over Na_sSO_4 and the solvent removed in vacuo to give **47** (65 mg, 96%) as a white solid. **^{1}H NMR** (400 MHz, $CDCl_3$) δ 8.88 (sb, 1H), 8.41 (dd, *J* = 8.4, 1.1 Hz, 1H), 7.66 (dd, *J* = 8.1, 1.2 Hz, 1H), 7.61 (dd, *J* = 7.7, 1.6 Hz, 1H), 7.58 (dd, *J* = 7.7, 1.7 Hz, 1H), 7.49 – 7.41 (m, 1H), 7.35 (td, *J* = 7.6, 1.2 Hz, 1H), 7.29 – 7.20 (m, 2H). **^{13}C NMR** (101 MHz, $CDCl_3$) δ 154.9 (q, $^{2}J_{CF}$ = 38), 136.4, 133.4, 132.7, 132.5, 130.5, 130.4, 127.5, 125.7, 124.3, 120.1, 115.8 (q, $^{1}J_{CF}$ = 289), 113.2, 96.1, 87.6; **ESI-MS** $[M + Na]^+$ 389.9.

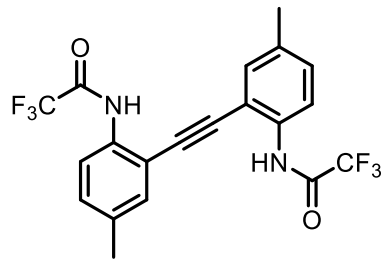


4-Methyl-2-((trimethylsilyl)ethynyl)aniline (49) was synthesised according to literature procedure.[34] 2-Bromo-4-methylaniline (5.00 g, 26.9 mmol) was added to a mixture of bis(triphenylphosphine)palladium(II) chloride (472 mg, 672 µmol), triethylamine (7.49 mL, 53.7 mmol), trimethylsilylacetylene (5.74 mL, 40.3 mmol) and CuI (128 mg, 672 µmol) in toluene (15 mL) under Ar, and heated to 100 °C for 16 h. The reaction mixture was then cooled, and diluted with water (20 mL), and extracted with EtOAc (2 × 15 mL). The combined organic extracts were washed with brine, dried over Na_2SO_4, and concentrated in

vacuo. The crude residue was purified with flash silica chromatography (5% EtOAc in petrol) to give compound **49** as an orange oil. **^{1}H NMR** (400 MHz, $CDCl_3$) δ 7.13 (dd, *J* = 1.4, 0.7 Hz, 1H), 6.93 (dd, *J* = 8.3, 2.1 Hz, 1H), 6.60 (d, *J* = 8.3 Hz, 1H), 4.07 (s, 2H), 2.20 (s, 3H), 0.28 (s, 9H); **^{13}C NMR** (101 MHz, $CDCl_3$) δ 146.1, 132.4, 130.8, 127.0, 114.4, 107.8, 102.2, 99.4, 20.2, 0.2; **ESI-MS** $[M + H]^+$ 204.1.

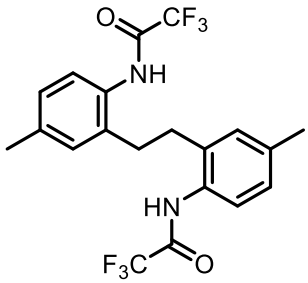


2,2'-(Ethyne-1,2-diyl)bis(4-methylaniline) (50) was synthesised according to literature procedure.[34] Potassium carbonate (502 mg, 3.63 mmol) was added to a solution of compound **49** (738 mg, 3.63 mmol) in methanol (5 mL) and stirred for 1 h. The reaction mixture was diluted with CH_2Cl_2, and filtered. The filtrate was concentrated in vacuo and used directly in the next step. The crude residue was added to a mixture of 2-bromo-4-methylaniline (0.54 mL, 4.35 mmol), bis(triphenylphospine)palladium)II) chloride (12.7 mg, 18.1 μmol), triethylamine (4.05 mL, 29.0 mmol), CuI (6.9 mg, 36.3 μmol), and triphenylphospine (28.6 mg, 109 μmol) under Ar, and the reaction mixture was heated to 100 °C for 16 h. The reaction mixture was then cooled and filtered to give compound **50** as a brown solid (20.0 mg, 11%). **^{1}H NMR** (400 MHz, DMSO-d_6) δ 7.11 (d, *J* = 2.1 Hz, 2H), 6.87 (dd, *J* = 8.2, 2.2 Hz, 2H), 6.64 (d, *J* = 8.2 Hz, 2H), 2.14 (s, 6H); **^{13}C NMR** (101 MHz, DMSO) δ 146.7, 131.8, 130.1, 124.3, 114.2, 106.6, 91.2, 19.8; **ESI-MS** $[M + H]^+$ 237.1.

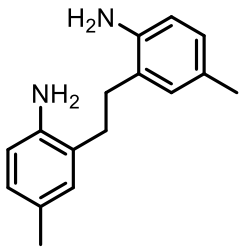


***N,N'*-(Ethyne-1,2-diylbis(4-methyl-2,1-phenylene))bis(2,2,2-trifluoroacetamide) (51).** Trifluoroacetic anhydride (2.04 mL, 14.7 mmol) was added dropwise to a solution of compound **50** (1.65 g, 6.98 mmol) and triethylamine (2.92 mL, 20.9 mmol) in THF (25 mL) at room temperature. The resulting precipitate was isolated by filtration, to give compound **51** (2.0 g , 67%) as a white solid. **^{1}H NMR** (400 MHz, DMSO-d_6) δ 11.18 (s, 2H), 7.47 – 7.17 (m, 6H), 2.32 (s, 6H). **^{13}C NMR** (126 MHz, DMSO) δ 155.2 (q, $^2J_{CF}$ = 35 Hz), 137.2, 133.2, 132.5,

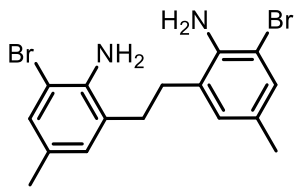
130.5, 126.6, 119.4, 116.0 (q, $^1J_{CF}$ = 273 Hz), 90.3, 20.4; **HR ESI-MS** $[C_{20}H_{14}F_6N_2O_2 + H]^+$ theoretical 429.1032, observed 429.1037, Δ = 1.10 ppm; **MP** sublimation at 260-265 ˚C; **IR** ν (cm^{-1}) 3302, 1707, 1544, 1281, 1167, 1124, 912, 876, 722.



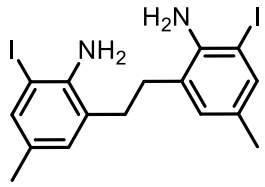
***N,N*'-(Ethane-1,2-diylbis(4-methyl-2,1-phenylene))bis(2,2,2-trifluoroacetamide) (52).** Compound **51** (62 mg, 145 µmol) was stirred with 10% Pd/C (6 mg), in MeOH (20 mL), under an atmosphere of H_2. After 3 h, when the starting material had completely dissolved, the solution was filtered through Celite, and concentrated in vacuo to give compound **52** (60 mg, 96%) as a pale yellow solid. **^{1}H NMR** (400 MHz, $CDCl_3$) δ 7.34 (d, *J* = 8.3 Hz, 2H), 7.16 (d, *J* = 2.1 Hz, 2H), 7.13 (dd, *J* = 8.3, 2.1 Hz, 2H), 6.68 (s, 2H), 2.86 (s, 4H), 2.36 (s, 6H); **^{13}C NMR** (126 MHz, DMSO) δ 155.7 (q, $^1J_{CF}$ = 35 Hz), 136.9, 136.7, 133.3, 129.6, 126.6, 125.7, 117.5 (q, $^1J_{CF}$ = 289 Hz), 32.3, 20.6; **HR ESI-MS** $[C_{20}H_{18}F_6N_2O_2 + H]^+$ theoretical 433.1345, observed 433.1357, Δ = 2.71 ppm; **MP** > 300 ˚C; **IR** ν (cm^{-1}) 3280, 2930, 1703, 1541, 1255, 1225, 1202, 1178, 1163, 915, 819, 713.



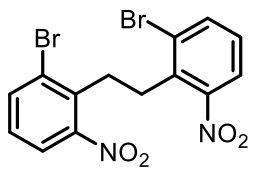
2,2'-(Ethane-1,2-diyl)bis(4-methylaniline) (53). Compound **52** (50 mg, 116 µmol) was stirred in a solution of 3 M aqueous NaOH (3 mL) and MeOH (1.5 mL) at 100 °C for 3 hours. The reaction mixture was then diluted with water (10 mL), and extracted with CH_2Cl_2 (3 × 5 mL). The combined organic extracts were dried with sodium sulfate, and concentrated in vacuo to give **53** (25 mg, 91%). **^{1}H NMR** (400 MHz, $CDCl_3$) δ 6.93 (d, *J* = 1.4 Hz, 2H), 6.88 (dd, *J* = 8.1, 1.4 Hz, 2H), 6.61 (d, *J* = 8.1 Hz, 2H), 3.50 (s, 4H), 2.77 (s, 4H), 2.26 (s, 6H); **^{13}C NMR** (101 MHz, $CDCl_3$) δ 141.9, 130.3, 128.4, 127.8, 126.8, 116.2, 31.5, 20.6; **ESI-MS** $[M + H]^+$ 241.1.



6,6'-(Ethane-1,2-diyl)bis(2-bromo-4-methylaniline) (54). A solution of NBS (84 mg, 470 µmol) in CH_2Cl_2 (1 mL) was added to a solution of **53** in CH_2Cl_2 (1 mL) at 0 °C. The reaction mixture was stirred for 5 mins, then separated between water (10 mL) and CH_2Cl_2. The organic layer was washed with brine and the solvent removed under reduced pressure. The crude residue was purified with flash silica chromatography (10-20% EtOAc in petrol ether) to give **54** (32 mg, 35%) as a pale yellow solid. **^{1}H NMR** (400 MHz, $CDCl_3$) δ 7.17 (d, *J* = 1.2 Hz, 2H), 6.82 (d, *J* = 1.9 Hz, 2H), 4.00 (sb, 4H), 2.76 (s, 4H), 2.22 (s, 6H); **^{13}C NMR** (101 MHz, $CDCl_3$) δ 139.5, 131.0, 129.5, 127.4, 110.7, 32.0, 20.3; **HR ESI-MS** $[C_{16}H_{18}Br_2N_2 + H]^+$ theoretical 396.9910, observed 396.9909, Δ = 0.13 ppm; **MP** 159-161 ˚C; **IR** ν (cm^{-1}) 3437, 3362, 3340, 2926, 2857, 2360, 2341, 1625, 1597, 1485, 1475, 1051, 849.

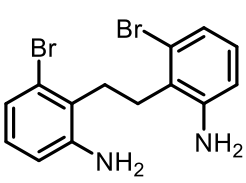


6,6'-(Ethane-1,2-diyl)bis(2-iodo-4-methylaniline) (55). A solution of Barluenga's reagent (34 mg, 91.5 µmol) in CH_2Cl_2 (1 mL) was added dropwise to a solution of **53** in CH_2Cl_2 (1 mL). The reaction was diluted with water (10 mL), and extracted with CH_2Cl_2 (3 × 5 mL). The combined organic extracts were dried with sodium sulfate, and concentrated in vacuo. The crude residue was filtered through a silica plug (50% EtOAc in petrol) to give **54** as a brown solid (10 mg, 45%). **^{1}H NMR** (400 MHz, $CDCl_3$) δ 7.40 (d, *J* = 1.2 Hz, 2H), 6.84 (d, *J* = 2.0 Hz, 2H), 4.02 (s, 4H), 2.76 (s, 4H), 2.20 (s, 6H); **^{13}C NMR** (101 MHz, $CDCl_3$) δ 142.1, 137.6, 130.6, 129.9, 126.4, 86.4, 32.6, 20.0; **HR ESI-MS** $[C_{16}H_{18}I_2N_2 + H]^+$ theoretical 492.9632, observed 492.9641, Δ = 1.76 ppm; **MP** 167-172 ˚C; **IR** ν (cm^{-1})3425, 3347, 2917, 1619, 1597, 1466, 851.

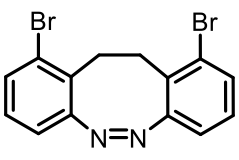


1,2-Bis(2-bromo-6-nitrophenyl)ethane (59) was synthesised according to literature procedure.[27] KOtBu (4.67 g, 41.7 mmol) was slowly added to a solution of 1-bromo-2-methyl-3-nitrobenzene (3.0 g, 13.9 mmol) in THF (70

mL) at -78 °C. The reaction was stirred for 5 minutes, and a dark red colour formed. Br_2 (715 µL, 13.9 mmol) was then added dropwise until the red colour disappeared. The reaction was stirred for a further 5 minutes, then saturated aqueous Na_2SO_4 (20 mL) was added. The THF phase was separated and the aqueous phase further extracted with CH_2Cl_2 (3 × 40 mL). The organic fractions were combined and the solvent removed under reduced pressure. The crude residue was purified with flash silica chromatography (20% EtOAc in petrol ether) to give **59** as a pale yellow solid (1.64 g, 56%). **^{1}H NMR** (400 MHz, $CDCl_3$) δ 7.70 (dd, *J* = 8.0 Hz, 1.3, 2H), 7.59 (dd, *J* = 8.2 Hz, 1.3, 2H), 7.17 (t, *J* = 8.1 Hz, 2H), 3.35 (s, 4H); **^{13}C NMR** (101 MHz, $CDCl_3$) δ 151.7, 137.3, 133.7, 128.6, 127.4, 123.8, 30.7. **ESI-MS** $[M + Na]^+$ 452.8.

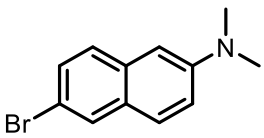


2,2'-(Ethane-1,2-diyl)bis(3-bromoaniline) (43). A mixture of **59** (1.9 g, 4.42 mmol) and PtO_2 (20 mg, 88 µmol) were stirred in MeOH (250 mL) under an atmosphere of hydrogen for 16 h. The reaction mixture was then filtered through Celite, and washed with further MeOH. The solvent was removed under reduced pressure to give to **43** (1.28 g, 78%) as a white solid. **^{1}H NMR** (400 MHz, $CDCl_3$) δ 6.99 (dd, *J* = 7.9, 1.2 Hz, 2H), 6.89 (t, *J* = 7.9 Hz, 2H), 6.63 (dd, *J* = 7.9, 1.2 Hz, 2H), 4.06 (s, 4H), 2.92 (s, 4H). **^{13}C NMR** (101 MHz, $CDCl_3$) δ 146.4, 128.5, 126.0, 124.6, 122.8, 115.1, 29.6. **HR MS** $[C_{14}H_{14}Br_2N_2 + H]^+$ theoretical 368.9597, observed 368.9602, Δ = 1.49 ppm; **MP** 171-175 ˚C; **IR** ν (cm^{-1}) 3399, 3207, 2928, 2365, 1595, 1571, 1466, 1449, 1292, 1086, 866, 778.

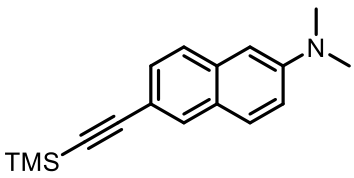


(Z)-1,10-Dibromo-11,12-dihydrodibenzo[c,g][1,2]diazocine (D4) was synthesised by analogy to literature procedure.[35] A solution of mCPBA (2.7 mmol in 4.16 mL) in acetic acid was added by syringe pump over a period of 12 hours under rapid stirring to a solution of the 2,2'-ethylenedianiline substrate **43** (500 mg, 1.35 mmol) in acetic acid/dichloromethane = 1/3 (35 mL). After the complete addition of the mCPBA

solution, the mixture was stirred for 3 hours. The solvent was then removed under reduced pressure, the residue taken up in ethyl acetate (10 mL) and washed with saturated, aqueous sodium hydrogen carbonate (2 × 5 mL), followed by saturated aqueous sodium chloride (5 mL). The solution was dried over sodium sulfate, the solvent was removed under reduced pressure and the residue was purified by column chromatography (20% ethyl acetate in hexanes) to afford **D4** (250 mg, 50%) as a yellow solid. **^{1}H NMR** (400 MHz, $CDCl_3$) δ 7.31 (dd, *J* = 8.0, 1.2 Hz, 2H), 6.98 (t, *J* = 7.9 Hz, 2H), 6.75 (dd, *J* = 7.8, 1.2 Hz, 2H), 3.38 – 3.33 (m, 2H), 2.83 – 2.74 (m, 2H); **^{13}C NMR** (126 MHz, $CDCl_3$) δ 156.1, 131.5, 127.9, 127.7, 125.3, 118.1, 30.5. **ESI-MS** $[M + H]^+$ 366.8.

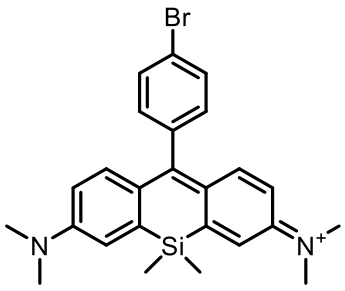


6-Bromo-N,N-dimethylnaphthalen-2-amine (61) was synthesised according to literature procedure.[36] Iodomethane (2.98 mL, 47.7 mmol) was added to a mixture of 6-bromonaphtalen-2-amine (4.24 g, 19.1 mmol) and potassium carbonate (5.28 g, 28.2 mmol) in DMF (76 mL) under N_2 at 60 °C for 24 h. The reaction mixture was then cooled to room temperature and separated between a mixture of ethyl acetate (50 mL) and petrol (25 mL) and water (100 mL). The organic layer was collected, and washed with brine (5 × 50 mL). The solvent was removed under reduced pressure and the crude residue purified by flash silica chromatography (10 % EtOAc in petrol ether) to give **61** (1.57 g, 33 %) as a white solid. **^{1}H NMR** (400 MHz, $CDCl_3$) δ 7.82 (d, *J* = 2.0 Hz, 1H), 7.61 (dd, *J* = 9.0, 0.7 Hz, 1H), 7.58 – 7.48 (m, 1H), 7.41 (dd, *J* = 8.8, 2.0 Hz, 1H), 7.16 (dd, *J* = 9.1, 2.6 Hz, 1H), 6.86 (d, *J* = 2.5 Hz, 1H), 3.05 (s, 7H); **^{13}C NMR** (101 MHz, $CDCl_3$) δ 148.9, 133.6, 129.5, 129.5, 128.0, 127.9, 127.9, 117.2, 115.1, 106.2, 40.8; **ESI-MS** $[M + H]^+$ 249.9.

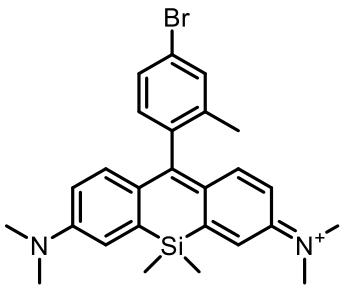


N,N-Dimethyl-6-((trimethylsilyl)ethynyl)naphthalen-2-amine (62). 6-bromo-N,N-dimethylnaphthalen-2-amine (500 mg, 2.00 mmol) was added to a mixture of

bis(triphenylphosphine)palladium(II) chloride (7.0 mg, 10 µmol), triethylamine (2.23 mL, 16 mmol), trimethylsilylacetylene (427 µL, 3.0 mmol), triphenylphosphine (15.7 mg, 60 µmol) and copper(I) iodide (3.8 mg, 20 µmol) in toluene (2 mL) under Ar, and heated to 100 °C for 16 h. The reaction mixture was then cooled, and diluted with water (5 mL), and extracted with EtOAc (2 ×10 mL). The combined organic extracts were washed with brine, dried over Na_2SO_4, and concentrated in vacuo. The crude residue was purified with flash silica chromatography (5% EtOAc in petrol) to give compound **62** as a yellow solid.**^{1}H NMR** (400 MHz, $CDCl_3$) δ 7.87 (s, 1H), 7.64 (d, *J* = 9.3 Hz, 1H), 7.56 (d, *J* = 8.4 Hz, 1H), 7.41 (dd, *J* = 8.5, 1.7 Hz, 1H), 7.14 (dd, *J* = 9.1, 2.6 Hz, 1H), 6.85 (d, *J* = 2.5 Hz, 1H), 3.06 (s, 6H), 0.29 (s, 9H). **^{13}C NMR** (101 MHz, $CDCl_3$) δ 149.2, 134.8, 132.0, 129.1, 128.9, 126.1, 126.0, 116.6, 116.0, 106.5, 106.0, 92.9, 40.7, 0.3; **ESI-MS** $[M + H]^+$ 268.1.



Bromo-silicon rhodamine (63). 1-Bromo-4-iodobenzene (131 mg, 462 µmol, dried in CH_2Cl_2 with Na_2SO_4, filtered and evaporated to dryness before use) was dissolved in dry THF (1.5 mL), and cooled to -78 °C. n-BuLi (1.6 M, 289 µL, 462 µmol) was added dropwise and the solution stirred for 1 h under Ar. Then, a solution of **27** (50 mg, 154 µmol) in dry THF (1.5 mL) was added dropwise at -78 °C, and the solution warmed to room temperature and stirred for 2 h. TFA (~0.2 mL) was then added dropwise to the reaction mixture and the resulting bright blue solution was separated between water (10 mL) and CH_2Cl_2 (20 mL). The organic phase was dried over Na_2SO_4, filtered and evaporated under reduced pressure. The crude residue was purified with flash silica chromatography (5-10% MeOH in CH_2Cl_2) to give **63** as a blue solid (25 mg, 35%) with spectra matching the literature.[37] **^{1}H NMR** (400 MHz, $CDCl_3$) δ 7.66 (d, *J* = 8.3 Hz, 2H), 7.20 (d, *J* = 2.9 Hz, 2H), 7.15 – 7.05 (m, 4H), 6.64 (dd, *J* = 9.6, 2.9 Hz, 2H), 3.40 (s, 12H), 0.60 (s, 6H); **^{13}C NMR** (101 MHz, $CDCl_3$) δ 167.8, 154.1, 148.6, 142.1, 137.9, 131.6, 130.9, 127.8, 123.2, 121.2, 114.0, 41.3, -0.6; **ESI-MS** $[M]^+$ 465.0.



Bromo-methyl-silicon rhodamine (64). 4-bromo-1-iodo-2-methylbenzene (137 mg, 462 µmol, dried in CH_2Cl_2 with Na_2SO_4, filtered and evaporated before use) was dissolved in dry THF (1.5 mL), and cooled to -78 °C. n-BuLi (1.23 M, 376 µL, 462 µmol) was added dropwise and the solution stirred for 1 h under Ar. Then, a solution of **27** (50 mg, 154 µmol) in dry THF (1.5 mL) was added dropwise at -78 °C, and the solution warmed to room temperature and stirred for 2 h. TFA (~0.2 mL) was then added dropwise to the reaction mixture and the resulting bright blue solution was separated between water (10 mL) and CH_2Cl_2 (20 mL). The organic phase was dried over Na_2SO_4, filtered and evaporated under reduced pressure. The crude residue was purified with flash silica chromatography (5-10% MeOH in CH_2Cl_2) to give **64** as a blue solid (75 mg, 91%). **^{1}H NMR** (400 MHz, $CDCl_3$) δ 7.52 (d, *J* = 1.9 Hz, 1H), 7.48 (dd, *J* = 8.0, 2.0 Hz, 1H), 7.24 (d, *J* = 2.8 Hz, 2H), 7.04 (d, *J* = 9.6 Hz, 2H), 6.97 (d, *J* = 8.0 Hz, 1H), 6.63 (dd, *J* = 9.6, 2.8 Hz, 2H), 3.42 (s, 12H), 2.01 (s, 3H), 0.67 (s, 3H), 0.65 (s, 3H); **^{13}C NMR** (126 MHz, $CDCl_3$) δ 167.9, 154.3, 148.7, 141.2, 138.2, 137.6, 133.3, 130.6, 129.1, 127.4, 122.9, 121.4, 114.3, 41.7, 19.5, -0.3, -0.6; **HR ESI-MS** $[C_{26}H_{30}BrN_2Si]^+$ theoretical 477.1356, observed 477.1362, Δ = 1.22 ppm; **MP** decomposition at 230 ˚C; **IR** ν (cm^{-1}) 2360, 2343, 1578, 1380, 1356, 1320, 1260, 1221, 1161, 909.

4.3 Computational Methods

Computational searches of ground state conformations were conducted using GFN2-xTB with simulated annealing, using xTB v6.1.[17] Annealing was run from 298.1 to 1000 K with a 50 ps time step. Single point energy (SPE) caluclations were run using ORCA 4.1,[38] with the PBE functional, def2-SVP basis set,[39] D3 empirical dispersion with Becke-Johnson damping (D3BJ),[40,41] and SMD implicit solvation model. Intra-atomic distance analysis was performed using the *auto dE* package.[42]

4.4 Photophysical Methods and electrochemical methods

See Chapter 3 Section 4.3 for photophysical methods and Chapter 2 Section 4.2 for electrochemical methods.

5. References

1. A. P. de Silva, T. S. Moody and G. D. Wright, *Analyst*, **2009**, *134*, 2385.
2. B. Daly, J. Ling and A. P. de Silva, *Chem. Soc. Rev.*, **2015**, *44*, 4203.
3. T. Fukaminato, S. Ishida and R. Métivier, *NPG Asia Mat.*, **2018**, *10*, 859.
4. Y. Odo, T. Fukaminato and M. Irie, *Chem. Lett.*, **2007**, *36*, 240.
5. T. Fukaminato, T. Doi, M. Tanaka and M. Irie, *J. Phys. Chem. C*, **2009**, *113*, 11623.
6. M. Berberich, A.-M. Krause, M. Orlandi, F. Scandola and F. Würthner, *Angew. Chem. Int. Ed.,* **2008**, *47*, 6616.
7. M. Berberich, M. Natali, P. Spenst, C. Chiorboli, F. Scandola and F. Würthner, *Chem (Weinheim an der Bergstrasse, Germany),* **2012**, *18*, 13651.
8. M. Berberich and F. Würthner, *Chem. Sci.*, **2012**, *3*, 2771.
9. M. Tomasulo, E. Deniz, R. J. Alvarado and F. M. Raymo, *J. Phys. Chem. C*, **2008**, *112*, 8038.
10. I. Yildiz, S. Impellizzeri, E. Deniz, B. McCaughan, J. F. Callan and F. M. Raymo, *J. Am. Chem. Soc.*, **2011**, *133*, 871.
11. P. S. Zacharias, S. Ameerunisha and S. R. Korupoju, *J. Chem. Soc., Perkin Trans. 2*, **1998**, 2055.
12. S. Tsuchiya, *J. Am. Chem. Soc.*, **1999**, *121*, 48.
13. J. Otsuki, A. Suka, K. Yamazaki, H. Abe, Y. Araki and O. Ito, *Chem. Commun.*, **2004**, 1290.
14. T. Saika, T. Iyoda, K. Honda and T. Shimidzu, *J. Chem. Soc., Chem. Commun.*, **1992**, 591.
15. D. Bléger, J. Schwarz, A. M. Brouwer and S. Hecht, *J. Am. Chem. Soc.*, **2012**, *134*, 20597.
16. A. Antoine John and Q. Lin, *J. Org. Chem.*, **2017**, *82*, 9873.
17. S. Grimme, *J. Chem. Theory Comput.*, **2019**, *15*, 2847.
18. C. Bannwarth, S. Ehlert and S. Grimme, *J. Chem. Theory Comput.*, **2019**, *15*, 1652.
19. A. V. Marenich, C. J. Cramer and D. G. Truhlar, *J. Phys. Chem. B*, **2009**, *113*, 6378.
20. Y. Xiong, P. Rivera-Fuentes, E. Sezgin, A. Vargas Jentzsch, C. Eggeling and H. L. Anderson, *Org. Lett.*, **2016**, *18*, 3666.
21. K. Torii, Y. Hori, K. Watabe and K. Kikuchi, *Bull. Chemi. Soc. Japan*, **2020**, *93*, 821.
22. R. Siewertsen, H. Neumann, B. Buchheim-Stehn, R. Herges, C. Näther, F. Renth and F. Temps, *J. Am. Chem. Soc.*, **2009**, *131*, 15594.
23. E. Galán, M. L. Perrin, M. Lutz, H. S. J. van der Zant, F. C. Grozema and R. Eelkema, *Org. Biomol. Chem.*, **2016**, *14*, 2439.
24. T. Yoshida and K. Mori, *Chem. Commun.*, **2017**, *53*, 4319.
25. J. Ezquerra, C. Pedregal, C. Lamas, J. Barluenga, M. Pérez, M. A. García-Martín and J. M. González, *J. Org. Chem.*, **1996**, *61*, 5804.
26. S. Li, N. Eleya and A. Staubitz, *Org. Lett.*, **2020**, *22*, 1624.
27. F. Klockmann, C. Fangmann, E. Zender, T. Schanz, C. Catapano and A. Terfort, *ACS Omega*, **2021**, *6*, 18434.
28. A. Morozumi, M. Kamiya, S.-n. Uno, K. Umezawa, R. Kojima, T. Yoshihara, S. Tobita and Y. Urano, *J. Am. Chem. Soc.*, **2020**, *142*, 9625.
29. B. Heinrich, K. Bouazoune, M. Wojcik, U. Bakowsky and O. Vázquez, *Org. Biomol. Chem.*, **2019**, *17*, 1827.
30. Y. A. Kyriukha, K. Afitska, A. S. Kurochka, S. Sachan, M. Galkin, D. A. Yushchenko and V. V. Shvadchak, *J. Med. Chem.*, **2019**, *62*, 10342.
31. R. Sato, J. Kozuka, M. Ueda, R. Mishima, Y. Kumagai, A. Yoshimura, M. Minoshima, S. Mizukami and K. Kikuchi, *J. Am. Chem. Soc.*, **2017**, *139*, 17397.
32. R. Sanz, M. P. Castroviejo, Y. Fernández and F. J. Fañanás, *J. Org. Chem.*, **2005**, *70*, 6548.
33. R. Sanz, V. Guilarte and N. García, *Org. Biomol. Chem.*, **2010**, *8*, 3860.
34. C. Peng, Y. Wang, L. Liu, H. Wang, J. Zhao and Q. Zhu, *Eur. J. Org. Chem.*, **2010**, *2010*, 818.
35. M. S. Maier, K. Hüll, M. Reynders, B. S. Matsuura, P. Leippe, T. Ko, L. Schäffer and D. Trauner, *J. Am. Chem. Soc.*, **2019**, *141*, 17295.

36. L. E. Johnson, J. S. Kingsbury, D. L. Elder, R. A. Cattolico, L. N. Latimer, W. Hardin, E. De Meulenaere, C. Deodato, G. Depotter, S. Madabushi, N. W. Bigelow, B. A. Smolarski, T. K. Hougen, W. Kaminsky, K. Clays and B. H. Robinson, *Org. Biomol. Chem.*, **2019**, *17*, 3765.
37. C. Fischer and C. Sparr, *Angew. Chem. Int. Ed.*, **2018**, *57*, 2436.
38. F. Neese, *Software update: the ORCA program system, version 4.0*, Wiley, 2018.
39. F. Weigend and R. Ahlrichs, *Phys. Chem. Chem. Phys.*, **2005**, *7*, 3297.
40. S. Grimme, S. Ehrlich and L. Goerigk, *J. Comp. Chem*, **2011**, *32*, 1456.
41. S. Grimme, J. Antony, S. Ehrlich and H. Krieg, *J. Chem. Phys.*, **2010**, *132*, 154104.
42. T. A. Young, J. J. Silcock, A. J. Sterling and F. Duarte, *Angew. Chem. Int. Ed.*, **2020**, *60,* 4266.